



FACULTEIT WETENSCHAPPEN

DEPARTEMENT FYSICA

***Ab initio* description of multicomponent
superconductivity in bulk to atomically thin
materials**

***Ab initio* beschrijving van multicomponent
supergeleiding in bulk en atomair dunne materialen**

*Proefschrift voorgelegd tot het behalen van de graad van
doctor in de wetenschappen: fysica
aan de Universiteit Antwerpen
te verdedigen door*

Jonas BEKAERT

Promotoren:

Prof. dr. Milorad V. MILOŠEVIĆ

Prof. dr. Bart PARTOENS

Antwerpen, mei 2018

Members of the jury:

Chairman

Prof. Dr. Nick Van Remortel, Universiteit Antwerpen, Belgium

Advisors

Prof. Dr. Milorad Milošević, Universiteit Antwerpen, Belgium

Prof. Dr. Bart Partoens, Universiteit Antwerpen, Belgium

Members

Prof. Dr. Jacques Tempère, Universiteit Antwerpen, Belgium

Prof. Dr. Dimitri Roditchev, ESPCI-ParisTech, France

Dr. Alex Aperis, Uppsala University, Sweden

Contact information

Jonas Bekaert

Groenenborgerlaan 171

2020 Antwerpen

Belgium

jonas.bekaert@uantwerpen.be

jonasdbekaert@gmail.com

*Felix, qui potuit rerum
cognoscere causas.*

*Happy the Man, who,
studying Nature's Laws,
Thro' known Effects can
trace the secret Cause.*

– *Publius Vergilius Maro,*
Georgica (Book II),
translation by John Dryden.

Acknowledgements

First and foremost I want to express my utmost gratitude to my advisors, Prof. Milorad Milošević and Prof. Bart Partoens. I am very thankful that they proposed such an exciting, timely topic for me to work on, that they guided and supported me throughout the whole process, and that they generously shared their insights, based on their respective strong expertise in superconductivity and in *ab initio* methods. I am equally grateful that they gave me the liberty to pursue the pathways for this research that I considered promising. However, their support has not been limited to purely scientific advice: they have always been prepared to walk the extra mile to help me establish a career in scientific research. On a lighter note, on many occasions we shared a good laugh during lunchtime or while traveling to conferences (e.g., while browsing catalogues with ludicrous stuff being sold on planes, such as the *perfect pencil* for only \$1200; it has a built-in eraser! Makes us realize, though, how lucky we are to be able to put our minds to the sciences).

Next, I want to acknowledge the members of my PhD jury for their constructive and very supportive feedback, and especially the chairman, Prof. Nick Van Remortel, for directing the defense process. I am also very grateful to Prof. Jacques Tempère for teaching me the basics of superconductivity theory in two excellent Master courses (which have provided much inspiration for Chapter 1 of this thesis), for regular stimulating discussions during the four years of my research, and for defending the ‘special needs’ of the lighter chemical elements.

Another heartfelt thanks goes to all the collaborators involved in this work. Thank you, Dr. Alex Aperis and Prof. Peter Oppeneer (Uppsala University) for our crucial and pleasant collaboration on Migdal-Eliashberg theory and regular research visits. I’ve learnt so much from working with Alex! Thank you, Prof. Petra Rudolf and group (University of Groningen), Dr. Cinzia Cepek and Dr. Andrea Goldoni and collaborators (IOM and Elettra Sincrotrone Trieste) for providing experimental evidence for our calculations concerning multigap superconductivity in magnesium diboride, and Prof. Ruslan Prozorov (Iowa State University) for the collaboration on osmium diboride. I am also grateful to Prof. Irina Grigorieva (University of

Manchester) for interesting discussions within the framework of an ongoing collaboration on 2D transition metal dichalcogenides.

I also want to thank all of the people in our research unit *Condensed Matter Theory* (CMT), for interesting discussions and for the nice working environment. A special thanks to Annelinde Strobbe and to Mikhail Petrov, who both have recently started working on related topics, for the nice joint work that we are doing. I want to thank Annelinde in particular for style advice, e.g., to make grant proposals look even more grand, and Mikhail for teaching me the correct pronunciations of the names of many Russian scientists that have put their marks on superconductivity research. Another special thanks goes to Dr. Rolando Saniz, for guiding my first steps in *ab initio* calculations during my Master thesis research, and for indispensable advice concerning the electron-phonon coupling at the start of my doctorate study. I also want to acknowledge stimulating discussions on condensed matter theory in general with Dr. Lucian Covaci, Prof. Dirk Lamoen and Prof. David Neilson, and with Dr. Ben Van Duppen, specifically on the topic of reaching broader audiences with our research. Another thanks goes to my long-time office mate Jeroen Mulkers for discussions on physics, but also for listening to my complaints about unreasonable referees (usually being the closest person when the email arrives), and for radiating a Zen attitude. Last, but not least, I want to thank Prof. François Peeters, the head of CMT, for regularly proposing new ideas and topics to investigate.

Next, I want to thank the services and people that enabled carrying out the research. First, the Flemish Supercomputer Centre VSC, for providing the indispensable high-performance computing infrastructure to carry out the *ab initio* calculations, as well as the local support team CalcUA for the smooth installation of our codes. I would also like to acknowledge the ABINIT project and all its contributors for sharing their code under the GNU license. ICT support from Nikolas Garofil is gratefully acknowledged, as well as the occasional comic relief. Also a big thanks for great help in administrative matters to, among others, Hilde Evans and Véronique Van Herck.

I also want to send my gratitude to the past and current members of the Antwerp European Physical Society ‘Young Minds’ team (I’m happy to say the list has become too long to name everyone here) for all the nice events –

colloquia, alumni evenings, etc. – that we have organized together, to offer a broader outlook on physics to our fellow researchers and to the wider public. A special thanks goes to Wout Van Alphen, for taking over the ‘burden’ of the leadership from me – when I lacked the time, in the final stage of my PhD study – in a very professional (but nevertheless ever-cheerful) manner. Owing to the excellent atmosphere in the team I may very well remain a ‘Young Mind’ even after my defense, at least until a too apparent *contradictio in terminis* will start to emerge.

Finally, I want to thank my family and in particular my parents Marc and Gerd for their support throughout my life and my studies, and for stimulating my curiosity from a young age. Among many other things, also a big thanks for providing me with a nice house to live in during my doctorate study years – including the garden, where from time to time I can take my mind off my work on physics, while performing physical labor. *Il faut cultiver notre jardin*, as Voltaire said. Moreover, it is at a perfect biking distance from the university, to keep brain and body balanced. *Van harte bedankt!* Last, but not least, I want to wish my grandmother Anny, who turned 90 earlier this year, good health in the years to come.

Finally, I want to thank you, the reader, for taking an interest in my work. Enjoy!

Jonas Bekaert
Antwerpen, May 2018

This research was supported financially by the TOP BOF programme of the University of Antwerp and by Research Foundation-Flanders (FWO).

Abstract

In this thesis, an *ab initio* description of superconducting condensates consisting of multiple components is developed. Such multicomponent superconductivity can originate from a multiband electronic structure, from spin degrees of freedom, additional interactions, and so on. The description starts from a full characterization of the structural, electronic and vibrational properties of a material, obtained from density functional theory. This is coupled here to a quantum-field theory of the superconducting state mediated by the electron-phonon interaction, called Eliashberg theory. This methodology enables the discovery of new properties of multicomponent superconductors of sizes ranging from bulk to atomically thin. First, we explore how band condensates stemming from distinct electronic bands of compound superconductors are coupled, and how this affects the temperature evolution of the superconducting state, and its interaction with an applied magnetic field. Subsequently, a novel approach is elaborated to describe systems hosting not only lattice vibrations but also spin fluctuations, as a result of a competing magnetic state. This provides new insights into multicomponent superconductivity in recently discovered iron-based superconductors, where superconductivity is proven to be conventional yet strongly depleted due to ferromagnetic spin fluctuations. In the second part of this thesis multicomponent superconductivity in atomically thin materials is investigated. Here, the superconducting spectrum is found to be enriched by emergent surface states, leading to the discovery of a three-gap superconducting state in a monolayer material, which can be profoundly changed by the addition of extra layers. The critical temperature of this new monolayer three-gap superconductor is relatively high, owing to multigap effects, and is shown to be enhanced further by means of strain and adatoms. Finally, atomically thin materials are investigated where the superconducting state coexists with other novel quantum states, leading to new physics emerging from the interplay between the states. This thesis thus contributes to a better understanding of the role of atomic-scale interactions in emergent multicomponent superconductivity, and their evolution with dimensionality.

Abstract – Nederlandse versie

In deze thesis wordt een *ab initio* beschrijving van supergeleidende condensaten bestaande uit meerdere componenten ontwikkeld. Zulke multicomponent supergeleiding kan voortkomen uit een elektronische structuur met meerdere banden, uit spinvrijheidsgraden, het aanwezig zijn van verschillende interacties, enzovoort. Het startpunt voor deze beschrijving is een volledige karakterisatie van de structurele, elektronische en vibrationele eigenschappen van een bepaald materiaal, bekomen met dichtheidsfunctionaaltheorie. Dit wordt in deze thesis gekoppeld aan een kwantumveldentheorie voor de supergeleidende toestand ontstaan uit elektron-fonon interactie, Eliashbergtheorie genaamd. Deze methodologie maakt het mogelijk om nieuwe eigenschappen van multicomponent supergeleiders, met afmetingen die variëren van bulk tot atomair dun, te ontdekken. Om te beginnen onderzoeken we hoe de bandcondensaten van een samengestelde stof, afkomstig van verschillende elektronische banden, gekoppeld zijn en hoe dit de temperatuursevolutie van de supergeleidende toestand en de interactie met een aangelegd magnetisch veld beïnvloedt. Vervolgens wordt er een nieuwe aanpak ontwikkeld om systemen te beschrijven waarin niet enkel roostertrillingen maar ook spinfluctuaties, ten gevolge van een concurrerende magnetische fase, een rol spelen. Dit biedt nieuwe inzichten in de multicomponent supergeleiding van recent ontdekte supergeleiders gebaseerd op het element ijzer, waarvoor bewezen wordt dat de supergeleiding conventioneel van aard is, maar sterk verzwakt door ferromagnetische spinfluctuaties. In het tweede deel van deze thesis wordt multicomponent supergeleiding in atomaire dunne materialen onderzocht. Hiervoor werd gevonden dat het supergeleidende spectrum verrijkt is door een in deze limiet tevoorschijn komende oppervlaktetoestand, wat geleid heeft tot ontdekking van een supergeleidende toestand met drie bandkloven in een monolaag, waarvan de eigenschappen diepgaand veranderen wanneer er extra lagen toegevoegd worden. De kritische temperatuur van deze nieuwe monolaag driecomponentsupergeleider is relatief hoog, dankzij de koppeling tussen de componenten, en we bewijzen hier dat deze nog verhoogd kan worden door middel van deformatie van het kristalrooster ('strain') en van adatomen. Ten slotte worden atomair dunne materialen geëxploreerd waarin de

supergeleidende toestand samen voorkomt met andere nieuwe kwantumtoestanden, wat tot nieuwe fysica leidt ten gevolge van de wisselwerking tussen de toestanden. Samenvattend draagt deze thesis bij tot een beter begrip van de rol van interacties op de atomaire schaal in de opkomende multicomponent supergeleiding, en hoe deze evolueert als functie van de dimensionaliteit.

Contents

Acknowledgements	iv
Abstract	vii
Abstract – Nederlandse versie	viii
Abbreviations	xvii
1 Introduction	1
1.1 Brief historical survey and key aspects of superconductivity	1
1.1.1 Discovery	1
1.1.2 Meissner effect and London theory	2
1.1.3 Ginzburg-Landau theory	5
Landau theory of phase transitions.	5
Ginzburg-Landau equations.	5
Superconducting coherence.	6
Interaction with magnetic field.	7
Flux quantization.	9
Other applications of Ginzburg-Landau theory.	10
1.1.4 Towards a microscopic theory	10
1.1.4.1 Key experiments	10
1.1.4.2 Bardeen-Cooper-Schrieffer theory	12
The model.	12
Symmetries of the theory.	13
Diagonalizing the BCS Hamiltonian.	15
Bogoliubov spectrum.	16
Superconducting density of states.	17
Band gap equation.	17
Critical temperature.	19
Critical magnetic field.	20
1.1.4.3 Superconductors with unconventional coupling mechanisms	21

	Timeline of conventional superconductors. . . .	21
	Heavy fermion superconductors.	22
	Cuprate superconductors.	23
	Iron-based superconductors.	26
	Other.	28
1.2	Recent breakthroughs	29
1.2.1	Multigap superconductivity	30
1.2.1.1	Discovery and further experiments	30
1.2.1.2	Mean-field theory	33
	Multicomponent Ginzburg-Landau theory. . . .	33
	Reconstructed multiband Ginzburg-Landau theory.	34
	Extended Ginzburg-Landau theory.	37
1.2.1.3	First-principles theory	38
	Quasiparticle interband scattering.	39
1.2.1.4	New physics in multigap superconductors . .	40
	Novel vortical states.	40
	Interband phase phenomena.	40
1.2.2	Superconductivity in atomically thin materials	43
	The realization of atomically thin materials. . .	43
	Superconductivity in two dimensions.	46
	Atomically thin elemental metal films.	48
	Cuprate superconducting films.	51
	2D electron gas at insulator interfaces.	52
	Atomic sheets.	52
	Monolayer FeSe on a SrTiO ₃ substrate.	55
	Superconducting strength as a function of thickness.	55
1.3	Applications	56
1.3.1	Large-scale applications	56
1.3.2	Small-scale applications	57
1.3.2.1	Sensors	58
1.3.2.2	Communication and computing	59
1.3.2.3	The prospect of atomically thin superconducting devices	62
1.4	Motivation and organization of the thesis	63
2	Electronic structure theory	67
2.1	Introduction	67
2.2	The many-body problem in solids	68
2.2.1	Born-Oppenheimer approximation	68

2.2.2	Hartree-Fock approximation	70
2.3	The fundamentals of Density Functional Theory	72
2.3.1	The Hohenberg-Kohn theorems	73
2.3.2	The Kohn-Sham equations	75
2.3.2.1	Derivation	75
2.3.2.2	Total electronic energy	77
2.4	Exchange-correlation functionals	79
2.4.1	Local density approximation	79
2.4.2	Generalized gradient approximation	80
2.4.3	Limitations of the local approximations	80
2.5	Geometry optimization using the Hellmann-Feynman theorem	82
2.6	Practical calculations	83
2.6.1	The Bloch theorem	84
2.6.2	Plane wave basis set	84
2.6.3	Integration over the first Brillouin zone: the k-point grid	85
2.6.4	Pseudopotentials	86
2.6.5	Projector augmented waves	88
2.7	Implementations	90
3	Phonons, electron-phonon interaction and Migdal-Eliashberg theory	93
3.1	Introduction	93
3.2	Phonons	94
3.2.1	Phonons in 2D materials	95
3.3	Electron-phonon interaction	97
3.4	First-principles calculations	99
3.4.1	Calculating phonons	99
3.4.2	Calculating the electron-phonon interaction	100
3.4.3	Frozen-phonon method	100
3.4.4	Density functional perturbation theory (DFPT)	101
3.4.4.1	Formalism	101
3.4.4.2	Computational approach and challenges	102
	Projectors and iterations.	102
	Acoustic sum rule.	103
	Implementation in ABINIT.	104
	Computational cost.	104
3.5	Migdal-Eliashberg theory	105
3.5.1	Nambu spinor formulation	105
3.5.2	Migdal's theorem	107
3.5.3	Eliashberg equations	109
3.5.4	Coulomb repulsion	112

3.5.5	Isotropic approximations	113
3.5.6	Quasiparticle DOS in the superconducting state.	114
3.5.7	Uppsala superconductivity code (UppSC)	114
3.5.7.1	Interpolation of the electron-phonon coupling	114
3.5.7.2	Numerical treatment	115
3.5.8	Density functional theory for superconductors (SCDFT)	116
3.5.9	Nuclear quantum effects and phonon anharmonicity	116
4	Anomalous multiband superconductivity in osmium diboride	117
4.1	Introduction	118
4.2	Crystal structure	119
4.3	Electronic properties	120
4.4	Shubnikov-de Haas oscillations	122
4.4.1	Theory behind Shubnikov-de Haas oscillations	122
4.4.2	Shubnikov-de Haas oscillations in OsB ₂	123
	Extension to iron selenide.	124
4.5	Phonons and electron-phonon interaction	125
4.6	Anisotropic superconducting gap and anomalous superfluid density	128
4.7	Superconducting length scales and type-I behavior	132
4.8	Conclusions	135
5	Coexisting lattice vibrations and spin fluctuations, with application to iron tetraboride	137
5.1	Introduction	138
5.2	Methodology	140
5.3	Application to FeB ₄	143
5.3.1	Crystal structure	143
5.3.2	Electronic structure	144
5.3.3	Electron-phonon interaction	146
5.3.4	Ferromagnetic spin fluctuations and their coupling to electrons	147
5.3.4.1	Susceptibility	147
5.3.4.2	Stoner interaction strength	148
5.3.4.3	Coupling of electrons to ferromagnetic spin fluctuations	150
5.3.5	Superconducting properties	150
5.4	Conclusions	153
6	Multigap superconductivity in the atomically thin limit: magnesium diboride	157
6.1	Introduction	158

6.2	Crystal structure	160
6.3	Properties of the monolayer	162
6.3.1	Electronic structure	162
6.3.2	Electron-phonon interaction	163
6.3.3	Superconducting properties	165
6.4	Evolution with added monolayers	167
6.4.1	Evolution of the superconducting gap spectrum	167
6.4.2	Evolution of the superconducting length scales	170
6.5	Influence of a magnesium substrate	172
6.5.1	Structural properties	172
6.5.2	Electronic properties	174
6.6	ARPES experiments	175
6.6.1	Sample growth	176
6.6.2	Normal-state electronic properties	177
6.6.3	Superconducting properties	178
6.6.4	Theoretical interpretation	178
6.6.5	Path to experimental realization of superconductivity in the thinnest limit	181
6.7	Conclusions	182
7	Strain- and adatom-enhanced superconductivity in mono- layer magnesium diboride	185
7.1	Introduction	186
7.2	Strain-enhanced superconductivity	188
7.2.1	The effect of strain on the electron-phonon interaction	188
7.2.2	The effect of strain on the superconducting properties	192
7.3	Superconductivity enhanced by hydrogen adatoms	194
7.3.1	Structural properties	194
7.3.2	Electronic properties	195
7.3.3	Electron-phonon interaction and superconducting prop- erties	197
7.3.4	Additional enhancement with strain	199
7.4	Conclusions	200
8	Interplay of superconductivity and novel quantum states in 2D transition metal dichalcogenides	203
8.1	Introduction	204
8.2	Crystal structure	207
8.3	Electronic structure	208
8.4	Phonons, electron-phonon coupling and Eliashberg theory . .	210
8.4.1	Issue of the overestimated superconducting strength . .	210

8.5	The Ising state	212
8.5.1	Spin expectation values	212
8.5.2	The crucial role of symmetry	213
8.5.3	Rashba effect and spin-valley locking	214
8.5.4	<i>Ab initio</i> description	215
8.6	<i>Ab initio</i> description of the charge density wave state	216
8.7	Interplay between the states	219
8.7.1	Tailoring the interplay	220
8.8	Conclusions	221
9	Summary and outlook	223
9.1	Summary	223
9.2	Outlook	228
10	Samenvatting en toekomstperspectieven	231
10.1	Samenvatting	231
10.2	Toekomstperspectieven	236
A	Computational details	239
A.1	Calculations of Chapter 4	239
A.2	Calculations of Chapter 5	240
A.3	Calculations of Chapter 6	241
A.4	Calculations of Chapter 7	242
A.5	Calculations of Chapter 8	243
B	Shubnikov-de Haas analysis of bulk iron selenide	245
C	Relation between susceptibility and nesting in metals	249
	Bibliography	253
	Publication list	285
	Curriculum vitæ	287

Abbreviations

1,2,3D	one-, two-, three-dimensional
ARPES	Angle-Resolved Photoemission Spectroscopy
BCS	Bardeen-Cooper-Schrieffer
BLG	Bilayer graphene
BO	Born-Oppenheimer
BZ	Brillouin Zone
CGA	conjugate gradient algorithm
DFPT	density functional perturbation theory
DFT	density functional theory
DOS	density of states
e-ph	electron-phonon
FSFs	ferromagnetic spin fluctuations
f.u.	formula unit
GGA	generalized gradient approximation
GL	Ginzburg-Landau
hcp	Hexagonal Closed Packed
HF	Hartree-Fock
HK	Hohenberg-Kohn
IBZ	irreducible Brillouin zone
KS	Kohn-Sham
LDA	local density approximation
ML	Monolayer
PAW	projector augmented wave
PBE	Perdew-Burke-Ernzerhof
PDOS	projected density of states
PHDOS	phonon density of states
PP	pseudopotential

RPA	random phase approximation
SC	self-consistent
SEM	scanning electron microscopy
STM	scanning tunnelling microscopy
STS	scanning tunnelling spectroscopy
SOC	spin-orbit coupling
TRS	time-reversal symmetry
TRSB	time-reversal symmetry breaking
VASP	Vienna <i>Ab initio</i> Simulation Package
XC	exchange-correlation

Chapter 1

Introduction

1.1 Brief historical survey and key aspects of superconductivity

1.1.1 Discovery

The discovery of superconductivity can be traced back to the cryogenic research (i.e., at extremely low temperatures) at the beginning of the 20th century. At the same time, it presents a remarkable example of a serendipitous discovery. The Dutch experimental physicist Heike Kamerlingh Onnes, whose lab was situated in the University of Leiden, had for the first time liquefied helium in 1908 [1, 2]. He achieved this by cooling below 4.2 K, the boiling point of helium at a pressure of 1 bar. To attain these very low temperatures, he first cooled compressed helium to the freezing point of hydrogen (14 K), followed by Joule-Thompson expansion, which is based on temperature lowering in expanding gases [3].

This breakthrough in low-temperature research enabled Onnes to investigate the behavior of metals at low temperatures. A crucial discovery followed in 1911, when Onnes investigated the conductivity of mercury (Hg), cooled by liquid helium. The data of the first measurement that revealed zero resistivity in mercury is depicted in Fig. 1.1. The prime characteristic of superconductivity showing here is the resistance drop to zero, within the experimental margin (“nagenoeg nul” as Onnes stated in Dutch). Onnes originally coined

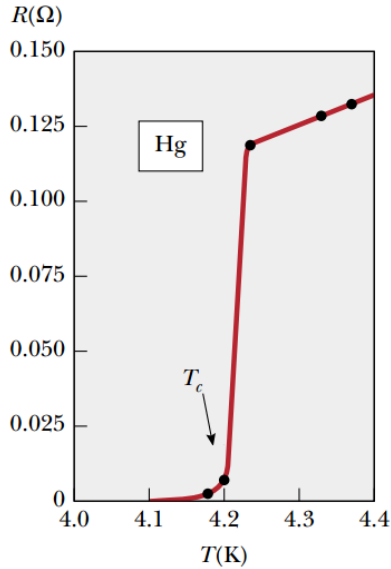


FIGURE 1.1: *Data from the original measurement of Kamerlingh Onnes revealing superconductivity in mercury in 1911 [2].*

this phenomenon *supraconductivity*, but later adopted the more logical term *superconductivity*¹. Clearly visible in Fig. 1.1, the transition from a normal metal to a superconductor appears as a critical phenomenon, that takes place at a critical temperature (T_c), which in the case of Hg is 4.2 K. In 1912, Onnes investigated a superconducting ring made of tin (Sn), and demonstrated that the resistance in a superconductor is indeed exactly zero, and not just undetectably small. Onnes simply cooled the ring below its critical temperature in an external magnetic field, thus inducing a current in the ring once the field was removed. This current in the superconducting ring did not decay after several days, and this *persistent current* yielded the proof Onnes needed. Onnes was awarded the 1913 Nobel prize in physics for “his investigations on the properties of matter at low temperatures which led, inter alia, to the production of liquid helium”.

1.1.2 Meissner effect and London theory

Subsequently, in 1933, a second important characteristic of the superconducting state was discovered by Walther Meissner and Robert Ochsenfeld.

¹The original term by Onnes lives on, though, in the French term “supraconductivité”.

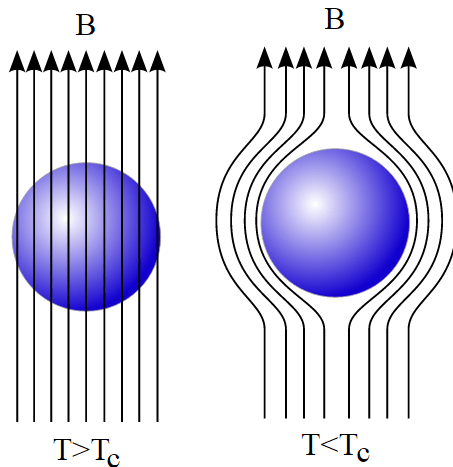


FIGURE 1.2: *The Meissner effect for a spherical superconducting sample: the applied magnetic field \mathbf{B} is expelled from the superconductor below critical temperature T_c .*

They discovered that below its critical temperature, a superconductor expels external magnetic fields, as depicted in Fig. 1.2. This phenomenon can be exploited in order to levitate magnets above superconductors. The expulsion of the magnetic field by the superconductor leads to a repulsive force between superconductor and magnet that can overcome gravity. In certain types of superconductors (‘type-II’ superconductors), the levitation is more stable than in others, because the magnet is pinned by penetrating flux lines. We will have to go further in our study of superconductivity to fully appreciate this. In a first attempt to explain these unconventional properties of superconductors, the brothers Fritz and Heinz London proposed a phenomenological theory of superconductivity in 1935. The London brothers had the tremendous intuition that the superconducting state is a quantum mechanical one, and moreover the ground state, such that the expectation value of its canonical momentum vanishes, $\langle \hat{\mathbf{p}} \rangle = 0$ [4]. The canonical momentum being given by $\hat{\mathbf{p}} = m\hat{\mathbf{v}} + q\hat{\mathbf{A}}(\hat{\mathbf{r}})$, where m is mass, q is charge, and \mathbf{A} is the magnetic vector potential, one obtains in the proposed model for the superconductor that the expectation value of the velocity of the superconducting particles is $\langle \hat{\mathbf{v}}_s \rangle = -\frac{q}{m}\mathbf{A}$. The resulting supercurrent is thus found by $\langle \hat{\mathbf{v}}_s \rangle$ multiplied with the charges that are flowing, $n_s q$, where n_s is the

density of superconducting carriers, such that²

$$\mathbf{J}_s = n_s q \langle \hat{\mathbf{v}}_s \rangle = -\frac{n_s q^2}{m} \mathbf{A} \Rightarrow \mathbf{A} = -\frac{m}{n_s q^2} \mathbf{J}_s . \quad (1.1)$$

This is a remarkable result since it is at odds with Ohm's law for normal conductors stating that $\mathbf{J} = \sigma \mathbf{E}$, where σ is the conductivity. Another important result of the London brothers is that Maxwell's laws retain their validity in superconductors. As a result, the relation between the supercurrent, the electric field and the magnetic field generated by the superconductor can be obtained as

$$\begin{aligned} \mathbf{E} &= -\frac{\partial}{\partial t} \mathbf{A} = \frac{m}{n_s q^2} \frac{\partial}{\partial t} \mathbf{J}_s , \\ \mathbf{B} &= \nabla \times \mathbf{A} = -\frac{m}{n_s q^2} \nabla \times \mathbf{J}_s . \end{aligned} \quad (1.2)$$

This set of equations is called the *London equations*. These are able to describe the Meissner effect. Suppose a semi-infinite superconductor (for $z > 0$), with an interface to a vacuum (for $z < 0$), where a magnetic field is applied parallel to the interface, i.e. $\mathbf{B}_a = B_a \hat{\mathbf{y}}$. We start from the 4th Maxwell equation, $\nabla \times \mathbf{B} = \mu_0 (\mathbf{J} + \epsilon_0 \frac{\partial}{\partial t} \mathbf{E})$, where in the static case we are considering $\frac{\partial}{\partial t} \mathbf{E} = 0$. This yields that in the superconductor ($z > 0$)

$$\nabla \times (\nabla \times \mathbf{B}) = \nabla (\nabla \cdot \mathbf{B}) - \nabla^2 \mathbf{B} = \mu_0 \nabla \times \mathbf{J}_s , \quad (1.3)$$

where $\nabla \cdot \mathbf{B} = 0$ according to the second Maxwell equation. By applying the London equations, 1.2, we obtain the following differential equation for the magnetic field in the superconductor, and its solution, using the boundary condition $\mathbf{B}(0) = \mathbf{B}_a$,

$$\frac{\partial^2}{\partial x^2} \mathbf{B} = \frac{\mu_0 n_s q^2}{m} \mathbf{B} \Rightarrow \mathbf{B} = \mathbf{B}_a e^{-\frac{x}{\lambda_L}} , \quad (1.4)$$

where $\lambda_L = \sqrt{\frac{m}{\mu_0 n_s q^2}}$ has the units of length and is called the *London penetration depth*. This result shows that an applied magnetic field decreases *exponentially* in the superconductor, with the London penetration depth as the characteristic length scale. This magnetic field screening occurs under

²Note the gauge transformation, $\mathbf{A} \rightarrow \mathbf{A} + \nabla f$. The London equations are valid within the choice of gauge $\nabla \cdot \mathbf{A} = 0$, called 'London gauge' or 'Coulomb gauge', such that the continuity equation $\frac{\partial n_s}{\partial t} + \nabla \cdot \mathbf{J}_s = 0$ is fulfilled in the static case, $\frac{\partial n_s}{\partial t} = 0$.

the influence of the superconducting current, and lies at the origin of the Meissner effect.

1.1.3 Ginzburg-Landau theory

Landau theory of phase transitions. In 1950 another, although more deeply rooted, phenomenological theory of superconductivity saw the light of the day, namely *Ginzburg-Landau (GL) theory* [5]. It is based on the more general, very successful Landau theory of second order phase transitions (i.e., whereby the order parameter changes continuously). In GL theory, the quantum mechanical nature of the superconducting state is explicitly taken into account, as it is formulated using the wave function in the superconducting state, $\psi(\mathbf{r})$. GL theory of phase transitions states that around its minimum, the free energy functional of the superconducting state can be expanded as

$$\mathcal{F}_s = \mathcal{F}_n + \int d\mathbf{r} \left[\alpha |\psi(\mathbf{r})|^2 + \frac{\beta}{2} |\psi(\mathbf{r})|^4 + \frac{1}{2M} \psi^*(\mathbf{r}) |i\hbar\nabla + Q\mathbf{A}(\mathbf{r})|^2 \psi(\mathbf{r}) + \frac{\mathbf{B}^2(\mathbf{r})}{2\mu} \right]. \quad (1.5)$$

Here, \mathcal{F}_n is the free energy in the normal state, and since it is a constant it plays no role in the following. The mass $M = 2m_e$ and the charge $Q = -2e$ are characteristic of the *Cooper pairing* between two electrons, which is the microscopic mechanism behind superconductivity (as I will discuss in more depth further on). Notice that in Eq. 1.5 only even powers of the superconducting wave function $\psi(\mathbf{r})$ come into play, as an expansion is made in close vicinity to the minimum. Moreover, the series is cut off at the fourth power, which is also a reasonable approximation in this case. The third term of the integral is the kinetic energy of the Cooper pair, and the fourth term is simply the free energy due to the magnetic field (no different from classical electromagnetism).

Ginzburg-Landau equations. Minimization of this functional with respect to the order parameter $\psi(\mathbf{r})$, $\frac{\delta\mathcal{F}_s}{\delta\psi^*(\mathbf{r})} = 0$, yields the *first GL equation*

$$\frac{-\hbar^2}{2M} \left[\nabla - \frac{iQ}{\hbar} \mathbf{A}(\mathbf{r}) \right]^2 \psi(\mathbf{r}) + \alpha\psi(\mathbf{r}) + \beta |\psi(\mathbf{r})|^2 \psi(\mathbf{r}) = 0. \quad (1.6)$$

This first GL equation is the equivalent of the Gross-Pitaevski equation for Bose-Einstein condensates [6]. There are two unknown functions to be obtained, namely $\psi(\mathbf{r})$ and $\mathbf{A}(\mathbf{r})$, so that an extra condition is required. It can be obtained through the variational form of the fourth Maxwell equation (static case), combined with Eq. 1.5, yielding

$$\mathbf{J}_s = -\frac{\delta\mathcal{F}_s}{\delta\mathbf{A}(\mathbf{r})} = \frac{iQ\hbar}{2M} [\psi^*(\mathbf{r})\nabla\psi(\mathbf{r}) - \psi(\mathbf{r})(\nabla\psi(\mathbf{r}))^*] - \frac{Q^2}{M} |\psi(\mathbf{r})|^2 \mathbf{A}(\mathbf{r}) . \quad (1.7)$$

According to the same Maxwell law (again the static case), $\nabla \times \mathbf{B} = \nabla \times (\nabla \times \mathbf{A}) = \mu (\mathbf{J}_{\text{ext}} + \mathbf{J}_s)$, where \mathbf{J}_{ext} is an external, injected current. This yields

$$\frac{1}{\mu} \nabla \times (\nabla \times \mathbf{A}(\mathbf{r})) = -\frac{\delta\mathcal{F}_s}{\delta\mathbf{A}(\mathbf{r})} = \frac{iQ\hbar}{2M} [\psi^*(\mathbf{r})\nabla\psi(\mathbf{r}) - \psi(\mathbf{r})(\nabla\psi(\mathbf{r}))^*] - \frac{Q^2}{M} |\psi(\mathbf{r})|^2 \mathbf{A}(\mathbf{r}) + \mathbf{J}_{\text{ext}} . \quad (1.8)$$

This constitutes the *second GL equation*. In combination with the first GL equation it can be used to self-consistently solve for $\psi(\mathbf{r})$ and $\mathbf{A}(\mathbf{r})$.

Superconducting coherence. Ginzburg-Landau theory has been very successful in its description of the superconducting length scales and the interaction of superconductors with applied magnetic fields. In ultracold gases, the length scale describing the restoration of Bose-Einstein condensation in the vicinity of an impurity, an interface with another state, or after a perturbation is called the healing length [6]. In superconductors an equivalent length scale arises from Ginzburg-Landau theory, called the *coherence length*, ξ . In the microscopic Bardeen-Cooper-Schrieffer theory, which we will review further on, it can be identified with the characteristic length scale of the Cooper pair (sometimes called its ‘size’). Within GL theory the coherence length of the superconducting condensate can be extracted in its most elementary form by treating again the superconducting half-space for $z > 0$, just like we derived the London penetration depth, but in this case without applied magnetic field. In this case, the first GL equation, 1.6, reduces to

$$-\frac{\hbar^2}{2M} \nabla^2 \psi(\mathbf{r}) + \alpha \psi(\mathbf{r}) + \beta |\psi(\mathbf{r})|^2 \psi(\mathbf{r}) = 0 . \quad (1.9)$$

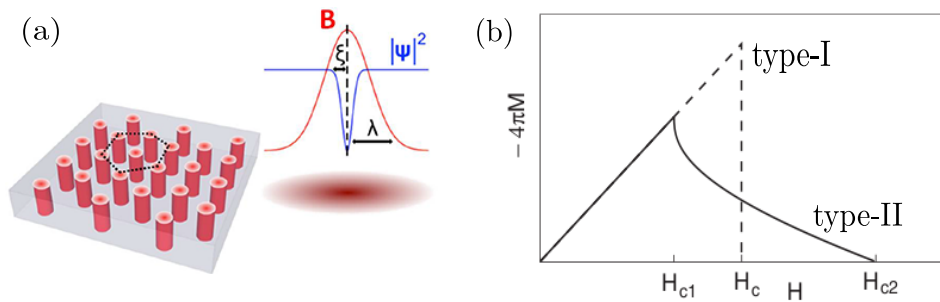


FIGURE 1.3: *Types of superconductivity under applied magnetic field. (a) Abrikosov vortices forming a triangular lattice [7]. The evolution of the magnetic field, \mathbf{B} , and the modulus squared of the condensate wave function $|\psi|^2$ around a vortex. (b) Magnetization M as a function of applied magnetic field H , showing type-I vs. type-II superconducting behavior.*

The solution to this differential equation must have the form $\psi(z) = \sqrt{n_s}f(z)$, where $n_s = \sqrt{-\frac{\alpha}{\beta}}$ is the density of superconducting particles at $z \rightarrow \infty$, such that Eq. 1.9 becomes

$$\frac{-\hbar^2}{2M} \frac{\partial^2 f(z)}{\partial z^2} + f(z) - f^3(z) = 0. \quad (1.10)$$

One can check that the solution to this equation is given by $f(z) = \tanh\left(\frac{z}{\xi}\right)$ with $\xi = \sqrt{\frac{\hbar^2}{2M\alpha}}$ the coherence length.

Interaction with magnetic field. Ginzburg-Landau theory can equally be employed to study the interaction of superconductors with applied magnetic fields more deeply. This analysis was first performed by A. Abrikosov [8–10]. In a first approximation, one can consider making a hole of cross-sectional area A in a superconductor, by means of an applied magnetic field. The energy that is gained is then given by the product of the volume $\lambda_L A$ and the energy density, i.e., $\lambda_L A \frac{\mathbf{B}_c^2}{8\pi}$. The energy that is needed to destroy the superconducting state, on the other hand, depends on its coherence length ξ , namely $\xi A \frac{\mathbf{B}_c^2}{8\pi}$. Therefore, the net energy that is needed to create the interface between an area in the normal state and the rest of the superconductor is to a first approximation the surface energy $E_S = (\xi - \lambda_L) A \frac{\mathbf{B}_c^2}{8\pi}$. As a result, if

$\xi \gg \lambda_L$, this surface energy is positive, and thus it is not beneficial to create the interface. When the critical magnetic field is applied, superconductivity will be destroyed, the sample turning to the normal state, following a *first order phase transition*. This type of interaction of a superconductor with magnetic field is called *type-I*. On the other hand, if $\xi \ll \lambda_L$ such interfaces become beneficial to form. In this case there is an intermediate state where the normal and superconducting states coexist in the sample. The normal state forms a collection of holes in the superconductor, which are named *vortices*. They also exist in Bose-Einstein condensates, where they can be formed by, e.g., rotating the condensate [6]. Abrikosov showed that these vortices, in sufficiently high densities, form a triangular, thus hexagonal closed packed (hcp) lattice, the eponymous *Abrikosov lattice*, shown in Fig. 1.3(a). At the core of the vortex, $\psi(\mathbf{r})$ is depleted. The condensate wave function $\psi(\mathbf{r})$ heals, as we have derived earlier, as $\tanh\left(\frac{r}{\xi}\right)$. Therefore, the characteristic length scale of the core of the vortex is the superconducting coherence length, ξ . The magnetic field decays away from the vortex core according to $e^{-\frac{r}{\lambda_L}}$. Therefore, the size of the vortex as a magnetic object can be identified with the London penetration depth λ_L .

The difference between type-I and type-II superconductors is thus determined by the ratio of λ_L and ξ , called the Ginzburg-Landau parameter $\kappa = \frac{\lambda_L}{\xi}$. The analysis of the types presented above ignores the specific evolution of \mathbf{B} and ψ , and is therefore only valid when $\xi \gg \lambda_L$ and $\xi \ll \lambda_L$. A more detailed calculation of the surface energy than presented here, which can be found in Ref. 11, shows that the transition between type-I and type-II superconductivity occurs at $\kappa = \frac{1}{\sqrt{2}}$ (the Bogomolny point).

The difference between type-I and type-II superconductors becomes apparent in the magnetization curve of superconductors as a function of applied magnetic field, shown in Fig. 1.3(b). For small H both types behave in the same way, namely $M \propto H$, i.e., perfect diamagnetism, according to the Meissner effect. In a type-I superconductor, there is one critical magnetic field at which the first-order transition occurs, namely the *thermodynamic critical field* H_c . In a type-II superconductor, on the other hand, there are two critical field. At H_{c1} , the perfect diamagnetism ceases, yet the superconducting state is not entirely lost. This is the intermediate (or mixed) state

where vortices coexist with the superconducting state. At the *upper critical field*, H_{c2} , superconductivity is entirely destroyed. We will focus on the types of superconductivity under applied magnetic field in Chapter 4, where I will present my discovery of a rare, new type-I superconducting compound, namely OsB₂.

Flux quantization. Importantly, the flux through vortices is quantized. The root cause of this *flux quantization* is the *phase*, ϕ , of the superconducting condensate wave function $\psi(\mathbf{r}) = \sqrt{n_s(\mathbf{r})}e^{i\phi(\mathbf{r})}$. According to Eq. 1.7, the supercurrent is given by

$$\mathbf{J}_s = -\frac{Q\hbar}{M}n_s\nabla\phi - \frac{Q^2}{M}n_s\mathbf{A}(\mathbf{r}) . \quad (1.11)$$

The second term is the supercurrent that we already saw arising in the London theory, while the new, first term is due to gradients in the phase. When one integrates this equation around a closed path \mathcal{C} in the superconductor³, one obtains

$$\oint_{\mathcal{C}} d\mathbf{l} \cdot \mathbf{A} + \frac{M}{n_s Q^2} \oint_{\mathcal{C}} d\mathbf{l} \cdot \mathbf{J}_s = -\frac{\hbar}{Q} \oint_{\mathcal{C}} d\mathbf{l} \cdot \nabla\phi . \quad (1.12)$$

Stokes' theorem yields $\oint_{\mathcal{C}} d\mathbf{l} \cdot \mathbf{A} = \int d\mathbf{S} \cdot \mathbf{B}$, i.e. the standard magnetic flux. The whole left hand side can be proven to be a conserved quantity, namely the London fluxoid,

$$\Phi = \int d\mathbf{S} \cdot \mathbf{B} + \frac{M}{n_s Q^2} \oint_{\mathcal{C}} d\mathbf{l} \cdot \mathbf{J}_s , \quad (1.13)$$

with $\frac{\partial\Phi}{\partial t} = 0$, from the London equation [11]. The second term is the contribution of the supercurrent. Continuity of the superconducting wave function requires that $\oint_{\mathcal{C}} d\mathbf{l} \cdot \nabla\phi = 2\pi n$, where n is an integer number. As such, the London fluxoid is $\Phi = n\frac{\hbar}{|Q|}$, where $\frac{\hbar}{|Q|} := \Phi_0$ is the elementary flux quantum, hence the name *fluxoid*. This implies that magnetic flux through a superconductor is quantized, including the vortices.

The interest in superconducting vortices has peaked in recent years, with notable new vortex states such as multiquantum or giant vortices ($n > 1$) in

³This is valid both when the superconductor does and does not contain normal holes, i.e., is singly or multiply connected in topological terms.

mesoscopic samples [12], fractional vortices (in inhomogeneous systems, such as a weak link Josephson junction between two superconductors [13], or in multicomponent superconductors [14]). Moreover, in new superconductors with two-dimensional characteristics, such as the iron chalcogenide FeSe, the symmetry breaking from fourfold to twofold symmetry, resulting from strong correlations, and the resulting nematic ordering, have been observed to lead to elongated vortices and corresponding anisotropic vortex lattices [15], at odds with the elementary Abrikosov vortex lattice.

Other applications of Ginzburg-Landau theory. GL theory can be generalized to include dynamical properties, as first done to investigate dissipation in thin superconducting filaments, due to the presence of the normal phase as a result of applied current [16]. The resulting time-dependent GL theory (TDGL) can, for instance, be used to study vortex movement, pinning and unpinning of vortices, etc. GL theory is also a useful formalism to study the vortex matter in nanostructured superconductors, e.g., with artificial pinning centers [17]. The major limitation inherent to GL theory is its limited applicability range with respect to temperature.

1.1.4 Towards a microscopic theory

1.1.4.1 Key experiments

Crucial for the construction of the microscopic theory of conventional superconductors were a series of experiments that each hold a clue as to the microscopic origin of superconductivity. They reveal that superconductivity arises as a *boson-like coupling* between *pairs of electrons*, mediated by the *crystal lattice*, and leading to the opening of a *superconducting gap*.

The key experiments were as follows:

1. *Microwave absorption*

When electromagnetic waves are shone on a superconductor, the absorption has been found to be absent for the lower energy range, starting only at a certain threshold value. This value is usually in the range of a few tens of GHz for elemental superconductors (i.e. the μeV range).

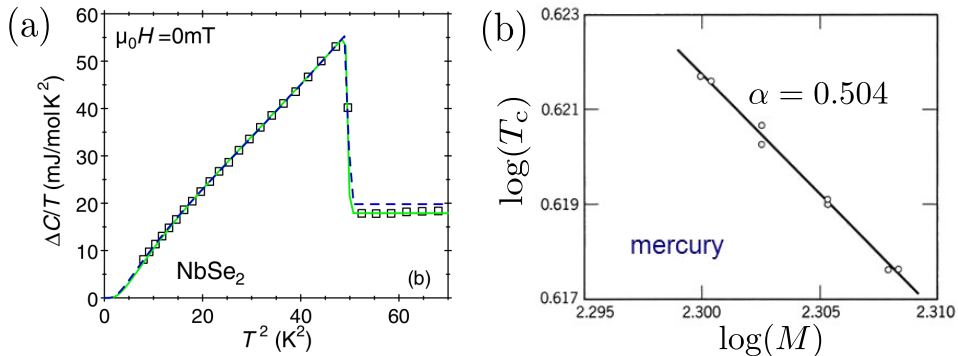


FIGURE 1.4: *Key experiments for the microscopic theory of superconductivity. (a) The peak in the specific heat of a superconductor (i.c. NbSe₂ [18]) around T_c , indicating the bosonic character of the superconducting state. (b) The isotope effect in mercury, yielding $\alpha = 0.504$ in $M^\alpha T_c = \text{const.}$ [19].*

This experiment indicates that there is an *energy band gap* in the superconducting state.

2. Flux quantization

We already studied quantization of magnetic flux through a superconductor and saw that the quantum of flux depends on the charge carriers, namely $\Phi = n \frac{h}{|Q|}$. Experiments carried out on superconducting cylinders revealed that $Q = -2e$, indicating that electrons pair up in the superconducting state [20].

3. Specific heat peak

The specific heat, C , in a superconductor peaks around T_c . As an example, we show the specific heat of NbSe₂ in Fig. 1.4 (a) [18]. In the normal state, the specific heat of an electron gas decreases linearly with T , as also evidenced in the figure far enough below T_c . The peak in C , however, is characteristic for bosonic quantum condensates, e.g., Bose-Einstein condensates [6]. This experiment thus indicates that electrons pair up to form a bosonic state.

4. Isotope effect

In this effect, the critical temperature of a crystal lattice of the same superconducting element, e.g., mercury, is found to depend on the specific isotope. An example of this dependence is shown in Fig. 1.4 (b), for mercury [19]. It is found that $M^\alpha T_c = \text{const.}$, with M the isotope

mass, such that lighter isotopes produce a higher T_c , and α is moreover found to be around $\frac{1}{2}$ in most elemental superconductors (that can be described by Bardeen-Cooper-Schrieffer theory as discussed in the following section). It became thus evident that superconductivity in many materials originates from interactions with the crystal lattice, and the quantitative description was initiated by, among others, H. Fröhlich [21].

1.1.4.2 Bardeen-Cooper-Schrieffer theory

The model. J. Bardeen, L. Cooper and J. Schrieffer brought the microscopic theory of superconductivity to a successful conclusion in 1957, hence the theory is called Bardeen-Cooper-Schrieffer (BCS) theory [22]. BCS theory starts from a series of successful assumptions. The first assumption is that only electrons with energy $-\hbar\omega_D \leq \xi_{\mathbf{k}} \leq \hbar\omega_D$, where $\hbar\omega_D$ signifies the *Debye energy* – the characteristic energy scale of (acoustic) phonons – participate in the *Cooper pairing*. This energy range is also known as the *Debye window*, and we will denote the wave vectors that comply with it as $\mathbf{k} \in \mathcal{D}$. The second assumption for BCS theory is that electrons with *opposite momentum and opposite spin* form the superconducting pair. These states with quantum numbers $(\mathbf{k}, \sigma = \uparrow)$ and $(-\mathbf{k}, \sigma = \downarrow)$ are related by *time-reversal symmetry*. As such, the pair wave function has zero momentum and zero net spin, the latter making it a boson state.

In a normal metal conduction electrons gradually lose their energy as a result of collisions with the lattice. In the superconducting state, however, electrons thus condense into Cooper pairs adopting a superfluid state that can carry electric current without dissipation. Since the energy spectrum of the Cooper pair is gapped, a minimum amount of energy is required to break the Cooper pairs into their single-particle excitations (by means of thermal energy, applied current or magnetic field).

With these assumptions as the starting point, the BCS Hamiltonian can be written as

$$\hat{H}_{\text{BCS}} = \sum_{\mathbf{k}, \sigma} \xi_{\mathbf{k}} \hat{c}_{\mathbf{k}, \sigma}^\dagger \hat{c}_{\mathbf{k}, \sigma} - \tilde{V} \sum_{\mathbf{k}, \mathbf{k}' \in \mathcal{D}} \hat{c}_{\mathbf{k}, \uparrow}^\dagger \hat{c}_{-\mathbf{k}, \downarrow}^\dagger \hat{c}_{-\mathbf{k}', \downarrow} \hat{c}_{\mathbf{k}', \uparrow}, \quad (1.14)$$

where \tilde{V} is the effective attractive potential between the electrons pairs. The ladder operators $\hat{c}_{\mathbf{k},\uparrow}$ and $\hat{c}_{-\mathbf{k},\downarrow}$ annihilate electrons with corresponding quantum numbers. In order to proceed BCS applied the following mean-field approximation to the Hamiltonian

$$\begin{aligned} \hat{H}_{\text{BCS}}^{\text{mf}} = & \sum_{\mathbf{k},\sigma} \xi_{\mathbf{k}} \hat{c}_{\mathbf{k},\sigma}^{\dagger} \hat{c}_{\mathbf{k},\sigma} - \tilde{V} \sum_{\mathbf{k},\mathbf{k}' \in \mathcal{D}} \left[\langle \hat{c}_{\mathbf{k},\uparrow}^{\dagger} \hat{c}_{-\mathbf{k},\downarrow}^{\dagger} \rangle \hat{c}_{-\mathbf{k}',\downarrow} \hat{c}_{\mathbf{k}',\uparrow} \right. \\ & \left. + \hat{c}_{\mathbf{k},\uparrow}^{\dagger} \hat{c}_{-\mathbf{k},\downarrow}^{\dagger} \langle \hat{c}_{-\mathbf{k}',\downarrow} \hat{c}_{\mathbf{k}',\uparrow} \rangle - \langle \hat{c}_{\mathbf{k},\uparrow}^{\dagger} \hat{c}_{-\mathbf{k},\downarrow}^{\dagger} \rangle \langle \hat{c}_{-\mathbf{k}',\downarrow} \hat{c}_{\mathbf{k}',\uparrow} \rangle \right] , \end{aligned} \quad (1.15)$$

where $\langle \dots \rangle$ is the expectation value. Defining the following expectation value

$$\Delta = -\tilde{V} \sum_{\mathbf{k} \in \mathcal{D}} \langle \hat{c}_{\mathbf{k},\uparrow} \hat{c}_{-\mathbf{k},\downarrow} \rangle , \quad (1.16)$$

the mean-field Hamiltonian becomes

$$\hat{H}_{\text{BCS}}^{\text{mf}} = \sum_{\mathbf{k},\sigma} \xi_{\mathbf{k}} \hat{c}_{\mathbf{k},\sigma}^{\dagger} \hat{c}_{\mathbf{k},\sigma} + \sum_{\mathbf{k} \in \mathcal{D}} \left(\Delta^* \hat{c}_{-\mathbf{k},\downarrow} \hat{c}_{\mathbf{k},\uparrow} + \Delta \hat{c}_{\mathbf{k},\uparrow}^{\dagger} \hat{c}_{-\mathbf{k},\downarrow}^{\dagger} \right) + \frac{|\Delta|^2}{\tilde{V}} . \quad (1.17)$$

Symmetries of the theory. Eq. 1.17 is an important result, since it implies *gauge field symmetry breaking* in BCS theory. The gauge transformation in question is $\hat{c} \rightarrow e^{i\theta} \hat{c}$. It leaves all terms of the form $\hat{c}^{\dagger} \hat{c}$ invariant, as well as those of the form $\hat{c}^{\dagger} \hat{c}^{\dagger} \hat{c} \hat{c}$, etc. This symmetry is called U(1) symmetry, denoting the symmetry of the unitary group of degree 1, i.e., rotations on the unit circle. However the Hamiltonian in Eq. 1.17, specifically the term of the form $\Delta^* \hat{c} \hat{c} + \Delta \hat{c}^{\dagger} \hat{c}^{\dagger}$, does not obey U(1) symmetry. Only $\theta = 0$ and $\theta = \pi$ leave the Hamiltonian invariant under the transformation $\hat{c} \rightarrow e^{i\theta} \hat{c}$. This group with two elements $\{0, \pi\}$ is denoted \mathbb{Z}_2 . The fact that there are two values derives microscopically from symmetry between the valence and conduction bands (particle-hole symmetry). Therefore, the microscopic coupling mechanism leading to the BCS state is accompanied by a $\text{U}(1) \rightarrow \mathbb{Z}_2$ symmetry breaking.

According to Goldstone's theorem, every continuous symmetry that is *spontaneously broken*⁴ results in the appearance of an associated boson. In case

⁴Spontaneously broken denotes that the Hamiltonian of the system obeys a certain symmetry, however, the ground state does not. Here, it is clear that the Hamiltonian in Eq. 1.14 obeys U(1) symmetry, however, the mean-field Hamiltonian of Eq. 1.17, which we

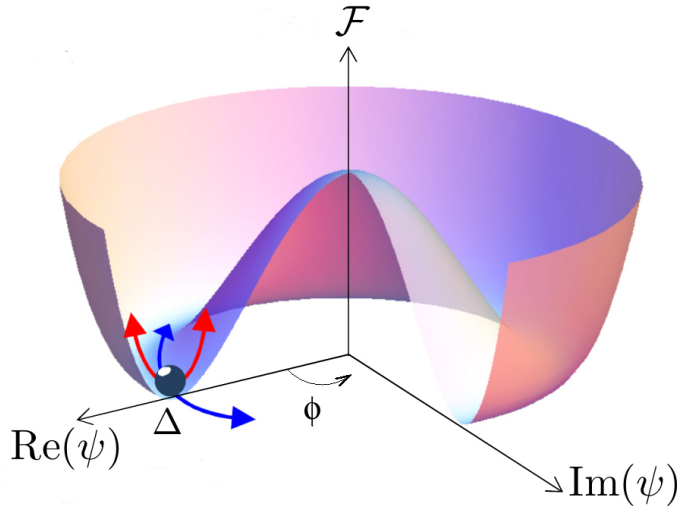


FIGURE 1.5: The free energy of a superconductor, \mathcal{F} as a function of the condensate wave function ψ . For the superconducting ground state $\psi = \Delta e^{i\phi}$ with $\Delta > 0$. Fluctuations in the amplitude of the condensate wave function are indicated here with red arrows, and lead to Anderson-Higgs modes, while fluctuations in the phase are indicated with blue arrows, and give rise to Nambu-Goldstone modes.

the broken symmetry is a *gauge symmetry*, like U(1) in this case, the resulting boson is *massive*, according to the *Anderson-Higgs mechanism* [23]. The gauge that is broken for superconductors is the electromagnetic gauge, which can be understood as the carrier boson of the electromagnetic interaction, the photon, acquiring a mass. This mass, as described by Proca theory, accompanies the transition from an Ohmic conductor to a superconductor obeying London theory, and in particular causes the Meissner effect [23].

The symmetry breaking can also be seen from a different angle, as in Fig. 1.5. It represents the free energy functional, \mathcal{F} , shaped as a Mexican hat. In the normal state $\Delta = 0$ and $\phi \in [0, 2\pi]$, and thus it has U(1) symmetry. In the superconducting state, on the other hand, \mathcal{F} minimizes for a ring of minima with a particular value for $\Delta \neq 0$ and arbitrary phase ϕ . When a state is adopted, however, the phase ϕ becomes a fixed value, thus the state has a lower symmetry than the functional it obeys. Therefore, U(1) symmetry is indeed spontaneously broken in the superconducting state.

will show describes the ground state, does not. This is a case of spontaneous symmetry breaking.

When we introduced the mean-field Hamiltonian in Eq. 1.15, we discarded second order terms in the deviations between the operator products and their expectation values, i.e., of the form

$$[\hat{c}_{-\mathbf{k},\downarrow}\hat{c}_{\mathbf{k},\uparrow} - \langle\hat{c}_{-\mathbf{k},\downarrow}\hat{c}_{\mathbf{k},\uparrow}\rangle] \left[\hat{c}_{\mathbf{k},\uparrow}^\dagger\hat{c}_{-\mathbf{k},\downarrow}^\dagger - \langle\hat{c}_{\mathbf{k},\uparrow}^\dagger\hat{c}_{-\mathbf{k},\downarrow}^\dagger\rangle \right]. \quad (1.18)$$

These higher order contributions, neglected in BCS theory, are called *fluctuations*. As indicated in Fig. 1.5, both the wave function amplitude and the phase can be subject to fluctuations, the former giving rise to Anderson-Higgs (AH) modes and the latter to Nambu-Goldstone (NG) modes. The main difference is that AH modes are accompanied by changes in \mathcal{F} (they are massive), while this is not the case for NG modes (they are massless).

In a multigap superconductor, with different Cooper pair condensates stemming from separate parts of the Fermi surface (discussed in Sec. 1.2.1), an additional type of fluctuations exists, namely collective fluctuations of inter-band phase differences [24, 25].

Diagonalizing the BCS Hamiltonian. To proceed with studying the predictions of BCS theory, we wish to rewrite the BCS Hamiltonian in a diagonalized form. The first step towards this goal employs *Nambu spinors* of the form $\bar{c}_{\mathbf{k}}^\dagger = (\hat{c}_{\mathbf{k},\uparrow}^\dagger, \hat{c}_{-\mathbf{k},\downarrow})$. Then, in terms of the Nambu spinors, the BCS mean-field Hamiltonian, Eq. 1.17, can be written very succinctly as

$$\hat{H}_{\text{BCS}}^{\text{mf}} = \sum_{\mathbf{k} \notin \mathcal{D}, \sigma} \xi_{\mathbf{k}} \hat{c}_{\mathbf{k},\sigma}^\dagger \hat{c}_{\mathbf{k},\sigma} + \sum_{\mathbf{k} \in \mathcal{D}} \left(\bar{c}_{\mathbf{k}}^\dagger H_{\mathbf{k}} \bar{c}_{\mathbf{k}} \right) + \sum_{\mathbf{k} \in \mathcal{D}} \xi_{\mathbf{k}} + \frac{|\Delta|^2}{\tilde{V}}, \quad (1.19)$$

where

$$H_{\mathbf{k}} = \begin{pmatrix} \xi_{\mathbf{k}} & \Delta \\ \Delta^* & -\xi_{-\mathbf{k}} \end{pmatrix}. \quad (1.20)$$

This *Bogoliubov* Hamiltonian plays a crucial role in *Bogoliubov-de Gennes* theory, wherein non-homogeneous superconductors can be studied via the spatial dependence in $\Delta(\mathbf{r})$ [26]. The first term in Eq. 1.19 simply expresses the energy of the electrons outside the Debye window ($\mathbf{k} \notin \mathcal{D}$). Since it is identical in the normal and the superconducting state, and thus unimportant for our investigations, we will simply refer to it as E_0 .

In order to diagonalize $H_{\mathbf{k}}$ first its eigenvalues need to be sought. They are $\pm E_{\mathbf{k}}$ with $E_{\mathbf{k}} = \sqrt{\xi_{\mathbf{k}}^2 + |\Delta|^2}$. The signs denote that this so-called *Bogoliubov spectrum* has solutions for both electrons (+) and holes (-). As the eigenvalues are always symmetric there is a *particle-hole symmetry*. We will get back to the interpretation of the Bogoliubov spectrum further on.

Based on the corresponding eigenvectors the unitary transformation matrix diagonalizing the Hamiltonian $H_{\mathbf{k}}$ is obtained as

$$B_{\mathbf{k}} = \begin{pmatrix} u_{\mathbf{k}} & v_{\mathbf{k}} \\ -v_{\mathbf{k}} & u_{\mathbf{k}} \end{pmatrix}. \quad (1.21)$$

with $u_{\mathbf{k}} = \sqrt{(E_{\mathbf{k}} + \xi_{\mathbf{k}})/(2E_{\mathbf{k}})}$ and $v_{\mathbf{k}} = \sqrt{(E_{\mathbf{k}} - \xi_{\mathbf{k}})/(2E_{\mathbf{k}})}$, such that

$$B_{\mathbf{k}} \cdot H_{\mathbf{k}} \cdot B_{\mathbf{k}}^{\dagger} = \begin{pmatrix} E_{\mathbf{k}} & 0 \\ 0 & -E_{\mathbf{k}} \end{pmatrix}. \quad (1.22)$$

Bogoliubov spectrum. The preceding steps can be formalized by means of the *Bogoliubov transformation*,

$$\hat{\alpha}_{\mathbf{k},\sigma} = u_{\mathbf{k}}^* \hat{c}_{\mathbf{k},\sigma} - \sigma v_{\mathbf{k}} \hat{c}_{-\mathbf{k},-\sigma}^{\dagger} \iff \hat{c}_{\mathbf{k},\sigma} = u_{\mathbf{k}} \hat{\alpha}_{\mathbf{k},\sigma} + \sigma v_{\mathbf{k}} \hat{\alpha}_{-\mathbf{k},-\sigma}^{\dagger}. \quad (1.23)$$

The Bogoliubov annihilation operators $\hat{\alpha}_{\mathbf{k},\sigma}$ reduce the BCS wave function,

$$|\Psi_{\text{BCS}}\rangle = \prod_{\mathbf{k}} \left[u_{\mathbf{k}}^* + v_{\mathbf{k}} \hat{c}_{\mathbf{k},\uparrow}^{\dagger} \hat{c}_{-\mathbf{k},\downarrow}^{\dagger} |0\rangle \right], \quad (1.24)$$

$|0\rangle$ being the electron vacuum, to zero. As such one finds $\hat{\alpha}_{\mathbf{k},\sigma} |\Psi_{\text{BCS}}\rangle = 0$, thus explaining their usefulness.

Finally, the mean-field Hamiltonian of Eq. 1.19 reads in diagonalized form

$$\hat{H}_{\text{BCS}}^{\text{mf}} = E_0 + \sum_{\mathbf{k} \in \mathcal{D}} (\xi_{\mathbf{k}} - E_{\mathbf{k}}) + \frac{|\Delta|^2}{\tilde{V}} + \sum_{\mathbf{k} \in \mathcal{D}, \sigma} E_{\mathbf{k}} \hat{\alpha}_{\mathbf{k},\sigma}^{\dagger} \hat{\alpha}_{\mathbf{k},\sigma}. \quad (1.25)$$

The first three terms describe the system at $T = 0$, while the fourth term is only at play at nonzero temperatures. It describes Cooper pair breaking, where the broken Cooper pairs carry energy $E_{\mathbf{k}} = \sqrt{\xi_{\mathbf{k}}^2 + |\Delta|^2}$. As such, the smallest energy needed to create an excitation is $E_{\mathbf{k}} = |\Delta|$. This justifies the

interpretation of the superconducting gap, $|\Delta|$ as the *binding energy* of the Cooper pair that needs to be exceeded in order to break the pair.

Superconducting density of states. Since the superconducting pairs have a dispersion different from their normal state counterparts, their density of states (DOS) is also altered. With a homogeneous distribution of these states in \mathbf{k} -space, the conservation of the number of states between the superconducting (left hand side) and the normal (right hand side) states yields $N_S dE = N_F d\xi$, with N_F the normal-state DOS at the Fermi level. Thus, the DOS in the superconducting state is

$$N_S(E) = N_F \frac{E}{\sqrt{E^2 - |\Delta|^2}}, \quad (1.26)$$

provided that $|E| > |\Delta|$. Within the gap energy, $|E| < |\Delta|$, the superconducting DOS vanishes, $N_S(E) = 0$.

Result 1.26 is depicted in Fig. 1.6(a). The sharp peaks at $E = |\Delta|$ are very characteristic of the superconducting state. The superconducting DOS can be measured using low-temperature scanning tunneling microscopy (STM) or spectroscopy (STS) [27, 28]. In a realistic measurement at nonzero T , the peaks will of course have a finite height and will be broadened due to thermal fluctuations. Moreover, in a multigap material, e.g. MgB₂, there are several peaks related to the different superconducting gaps [27, 28].

Band gap equation. Minimizing the first three terms of Hamiltonian 1.25 with respect to $|\Delta|$ one obtains the superconducting gap equation at $T = 0$,

$$\frac{\tilde{V}}{2} \sum_{\mathbf{k} \in \mathcal{D}} \frac{1}{\sqrt{\xi_{\mathbf{k}}^2 + |\Delta|^2}} = 1. \quad (1.27)$$

It is reasonable to assume that the electronic density of states is constant in the Debye window, as $\hbar\omega_D$ is very small ($\sim 10 - 100$ meV) compared with the electronic energy scale (Fermi energy $E_F \sim 1 - 10$ eV). Thus, Eq. 1.27

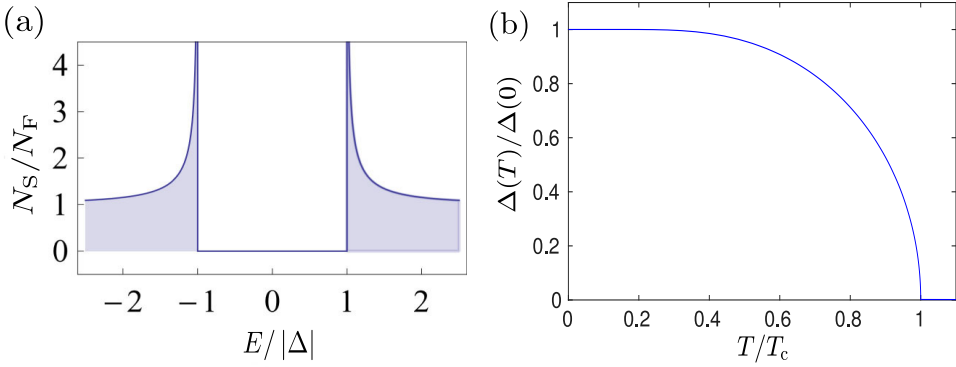


FIGURE 1.6: *Results of the BCS theory. (a) The density of states in the superconducting state, N_S , showing the opening of the gap for $-\Delta \leq E \leq \Delta$, and the divergence at $\pm\Delta$. (b) The evolution of the superconducting gap with temperature, $\Delta(T)$, obtained from numerical solution of the gap equation.*

can be put in infinitesimal form as

$$\int_0^{\hbar\omega_D} \frac{1}{\sqrt{\Delta^2 + \xi^2}} d\xi = \frac{1}{N_F \tilde{V}} \Rightarrow \Delta(0) = \frac{\hbar\omega_D}{\sinh\left(1/(N_F \tilde{V})\right)}. \quad (1.28)$$

This is the BCS result for the superconducting gap at $T = 0$. In many elemental superconductors, the electron-phonon coupling is weak, i.e., $\lambda = N_F \tilde{V} \ll 1$. In this case $\Delta(0) \simeq 2\hbar\omega_D e^{-1/\lambda}$.

To find out the value of Δ at nonzero temperatures, we need to return to the full Hamiltonian, including Bogoliubov excitations. With the help of the Bogoliubov transformation and the fermionic anticommutation relations of the Bogoliubov ladder operators,

$$\{\hat{\alpha}_{\mathbf{k},\sigma}, \hat{\alpha}_{\mathbf{k}',\sigma'}^\dagger\} = \delta_{\mathbf{k}-\mathbf{k}'} \delta_{\sigma\sigma'}, \quad (1.29)$$

the band gap equation, Eq. 1.16, becomes

$$\Delta = \tilde{V} \sum_{\mathbf{k} \in D} \left[(u_{\mathbf{k}} v_{\mathbf{k}} - u_{-\mathbf{k}} v_{-\mathbf{k}}) \left(\langle \hat{\alpha}_{\mathbf{k},\uparrow}^\dagger \hat{\alpha}_{\mathbf{k},\uparrow} \rangle + \langle \hat{\alpha}_{-\mathbf{k},\downarrow}^\dagger \hat{\alpha}_{-\mathbf{k},\downarrow} \rangle \right) \right]. \quad (1.30)$$

Here, $n_{\mathbf{k},\uparrow} = \langle \hat{\alpha}_{\mathbf{k},\uparrow}^\dagger \hat{\alpha}_{\mathbf{k},\uparrow} \rangle$ and $n_{-\mathbf{k},\downarrow} = \langle \hat{\alpha}_{-\mathbf{k},\downarrow}^\dagger \hat{\alpha}_{-\mathbf{k},\downarrow} \rangle$ represent the number of broken Cooper pairs with the corresponding quantum numbers. These are

determined by the Fermi-Dirac distribution,

$$n_{\mathbf{k},\uparrow} = n_{-\mathbf{k},\downarrow} = \frac{1}{e^{\beta E_{\mathbf{k}}} + 1} , \quad (1.31)$$

where $\beta = 1/(k_{\text{B}}T)$. Using this, Eq. 1.30 yields the T -dependent superconducting gap equation

$$\frac{\tilde{V}}{2} \sum_{\mathbf{k} \in D} \frac{1}{\sqrt{\xi_{\mathbf{k}}^2 + \Delta^2}} \tanh \left(\frac{\beta \sqrt{\xi_{\mathbf{k}}^2 + \Delta^2}}{2} \right) = 1 . \quad (1.32)$$

By numerical integration one can obtain $\Delta(T)$ shown in Fig. 1.6 (b). It shows $\Delta(T) \sim \Delta(0)$ until $0.5T_{\text{c}}$, decreasing more rapidly for higher T , until it vanishes at $T = T_{\text{c}}$.

Critical temperature. Taking the limit $\Delta \rightarrow 0$, such that $T \rightarrow T_{\text{c}}$, Eq. 1.32 becomes in infinitesimal form

$$N_{\text{F}} \tilde{V} \int_0^{\hbar\omega_{\text{D}}} d\xi \frac{\tanh \left(\frac{\xi}{2k_{\text{B}}T_{\text{c}}} \right)}{\xi} = 1 . \quad (1.33)$$

With $\Delta(0)/(\hbar\omega_{\text{D}}) \ll 1^5$, the approximate solution reads [29]

$$k_{\text{B}}T_{\text{c}} \simeq 1.13 \hbar\omega_{\text{D}} e^{-1/\lambda} . \quad (1.34)$$

One notices that $k_{\text{B}}T_{\text{c}} \propto \hbar\omega_{\text{D}} \propto 1/\sqrt{M}$, with M the atomic mass, corresponding to the isotope effect with $\alpha = 0.5$. It should be stressed that this value is not universal for all superconductors, even not within the category of superconductors based on conventional electron-phonon coupling. For example, in MgB_2 a lower value of $\alpha = 0.3$ is obtained [30, 31], and in PdH_x even an *inverse isotope effect* with $\alpha = -0.3$ is observed [32]. The latter can likely be attributed to anharmonic phonon effects due to hydrogen [32, 33].

⁵The band gap, $\Delta(0)$, is typically of the order of 0.1 to 1 meV for elemental superconductors, and $\hbar\omega_{\text{D}}$ of the order of 10 to 100 meV. This means that the ratio $\frac{\Delta(0)}{\hbar\omega_{\text{D}}}$ is in the order of 0.1 to 0.001.

Material	$2\Delta(0)/(k_{\text{B}}T_{\text{c}})$ (d.u.)
Al	3.37 ± 0.1
Cd	3.20 ± 0.1
Hg	4.60 ± 0.1
In	3.63 ± 0.1
Nb	3.84 ± 0.06
Pb	4.29 ± 0.04
Sn	3.46 ± 0.1
Ta	3.60 ± 0.1

TABLE 1.1: *The ratio $2\Delta(0)/k_{\text{B}}T_{\text{c}}$ from tunnelling measurements for a selection of superconducting materials [34]. BCS theory predicts a material-independent ratio of 3.53.*

Combining Eqs. 1.28 and 1.34, we obtain in the weak coupling limit

$$\frac{2\Delta(0)}{k_{\text{B}}T_{\text{c}}} \simeq 3.53 . \quad (1.35)$$

As such this ratio is, in principle, material independent. In Table 1.1 experimental values of this ratio are listed [34]. One concludes that BCS theory gives a rather good account of this ratio, given the relative simplicity of the model.

Critical magnetic field. The critical magnetic field can be directly calculated from the band gap. Namely, as the Meissner effect destroys superconductivity, the energy of the applied field must match the energy difference between the superconducting, BCS state and the normal state. To a first approximation, when $\Delta/(\hbar\omega_{\text{D}}) \ll 1$, this energy difference can be estimated by means of the superconducting DOS, shown in Fig. 1.6(a). In the superconducting state, $N_{\text{F}}\Delta$ electrons condense, each going to an energy state $-\Delta/2$ below the energy of the normal state. Therefore, the energy difference between the BCS and the normal state is roughly

$$E_{\text{BCS}} - E_{\text{N}} \simeq -\frac{1}{2}N_{\text{F}}\Delta^2 . \quad (1.36)$$

The energy density of the magnetic field acting on a material is $H^2/(8\pi)$. Thus, we find that superconductivity is destroyed by the field when

$$H_c^2/(8\pi) = \frac{1}{2}N(0)\Delta^2 \Rightarrow H_c(T) = \sqrt{4\pi N_F}\Delta(T) , \quad (1.37)$$

so that the critical field completely follows the gap within BCS theory.

The extension of the BCS theory to include realistic electron-phonon coupling, instead of the simplified Debye window and Coulomb interaction is called *Migdal-Eliashberg theory*, and will be the subject of Chapter III of this thesis.

1.1.4.3 Superconductors with unconventional coupling mechanisms

Timeline of conventional superconductors. Although the BCS theory accounts for superconductivity in many elemental metals, and compounds, it was realized a few decades ago that it does not properly describe all experimentally discovered superconductors. Superconductors that do not fall within the BCS theory are called *unconventional* superconductors. Fig. 1.7 presents a time line of experimentally discovered superconductors. It starts, of course, with the discovery of superconductivity in mercury (Hg) by Kamerlingh Onnes in 1911, and other elemental superconductors, such as Pb, that followed soon after. After that, compound superconducting materials – crystals comprised of more than one atomic species – were synthesized. These include NbN, Nb₃Sn, etc., and ultimately led to a relatively high T_c of 23 K in Nb₃Ge in 1973. The coupling mechanism between the electrons is still the electron-phonon coupling, described within the BCS theory. As such, it was believed the maximal attainable T_c for superconductivity was about reached in Nb₃Ge. It held record T_c until 1986, when the high- T_c cuprate superconductors emerged. Much later, in 2001, a material with a much higher T_c of 39 K was discovered, though with a conventional coupling mechanism [35]. This material is magnesium diboride (MgB₂), whose high T_c originates from its two-gap character [27, 28, 36–39]. It can be described successfully by multiband Migdal-Eliashberg theory, the extension of BCS theory mentioned above. In this thesis, the atomically thin limit of MgB₂ is investigated for the first time.

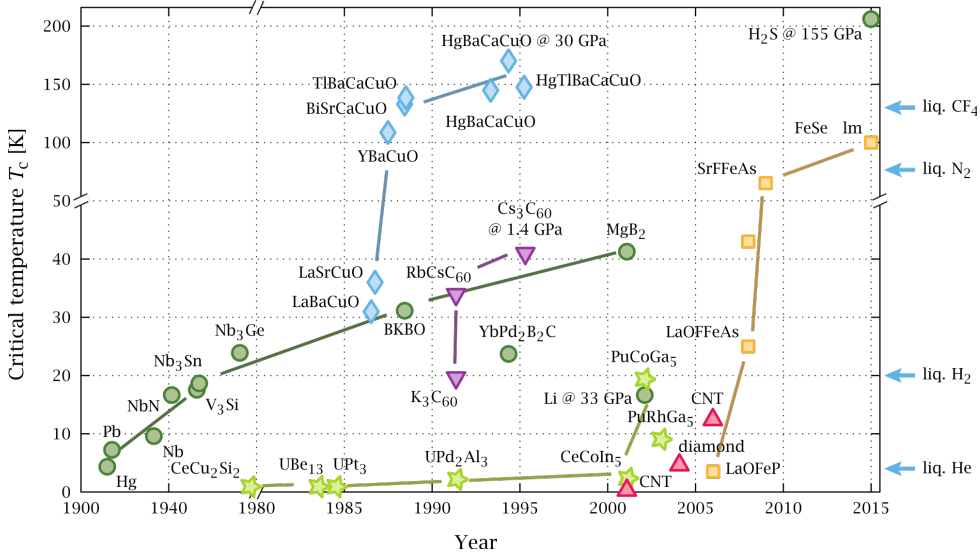


FIGURE 1.7: *Chronological overview of discoveries of superconductors, and their critical temperatures [40]. The symbols denote the families of the superconductors. Dark green circles denote conventional, electron-phonon coupled superconductors, light green stars heavy fermion compounds, blue rhombi cuprate superconductors, purple triangles fullerene superconductors, red triangles other C-based materials, and orange squares the most recent category of Fe-based superconductors.*

Other families of superconductors depicted in Fig. 1.7, where the coupling mechanism is conventional include carbon-based superconductors, such as doped fullerenes (K_3C_{60} , Cs_3C_{60} , etc.), which can reach T_c 's up to 40 K under pressure, and (metallic) carbon nanotubes (CNT). The most striking addition to conventional superconductivity is that of sulfur hydride under ultrahigh pressure of 155 GPa, generated with diamond anvil cells, in 2015 [41]. The high pressure is needed to make the material metallic. This was predicted by *ab initio* calculations on a very similar compound, dense molecular hydrogen [42]. The very light mass of H renders its phonon modes extremely hard, thus strongly boosting the Debye window and, hence, T_c , reaching the *absolute record value* of 203 K in the experiment. The conventional nature of the coupling mechanism was convincingly proven by means of the isotope effect.

Heavy fermion superconductors. In 1978, the first unconventional superconductor, $CeCu_2Si_2$, was discovered [43]. It is a *heavy fermion* material,

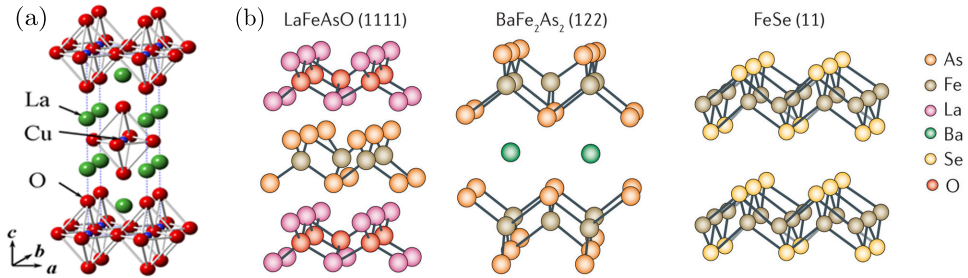


FIGURE 1.8: *Crystal structures of unconventional superconductors. (a) Crystal structure of the prototype cuprate superconductor La_2CuO_4 . (b) Crystal structures of a selection of Fe-based superconductors [45], from left to right the oxypnictide LaFeAsO , the pnictide BaFe_2As_2 , and the chalcogenide FeSe .*

in which the electrons have very high effective masses. In a heavy fermion superconductor, there are 4f or 5f electrons present at the Fermi level, stemming from heavy elements such as cerium (Ce) and uranium (U). Despite the low T_c of CeCu_2Si_2 , 0.5 K, its coupling mechanism cannot be described by the BCS theory. The reason is that the localized f levels are mutually strongly correlated, so that the electrons cannot be considered to be occupying single-particle states in the normal (i.e., non-superconducting) state. Thus, one of the starting points of the BCS theory breaks down in these materials. Moreover, these materials display antiferromagnetism and antiferromagnetic spin fluctuations, that can be the mediators of unconventional pairing [44].

Cuprate superconductors. In 1986, the discovery of superconductivity with $T_c \sim 30$ K in Ba-doped La_2CuO_4 by Bednorz and Müller, by far exceeding the $T_c = 23$ K of Nb_3Ge , shook physics [47]. This discovery was awarded the Nobel prize already in the next year, 1987. Later in 1986, superconductivity in Sr-doped La_2CuO_4 with $T_c \sim 35$ K was achieved. In 1987, the discovery of the related compound $\text{YBa}_2\text{Cu}_3\text{O}_{7-x}$ (YBCO) followed. Much like in doped La_2CuO_4 , its T_c depends on the doping level, in this case by means of oxygen vacancies introducing holes in YBCO. Optimal doping for superconductivity is reached when there are 0.16 holes per CuO_2 layer, and the corresponding $T_c \sim 100$ K. Thus, YBCO was the first superconductor with a T_c exceeding the boiling point of liquid nitrogen. As a result, this discovery enabled many new possibilities for applications. Subsequent

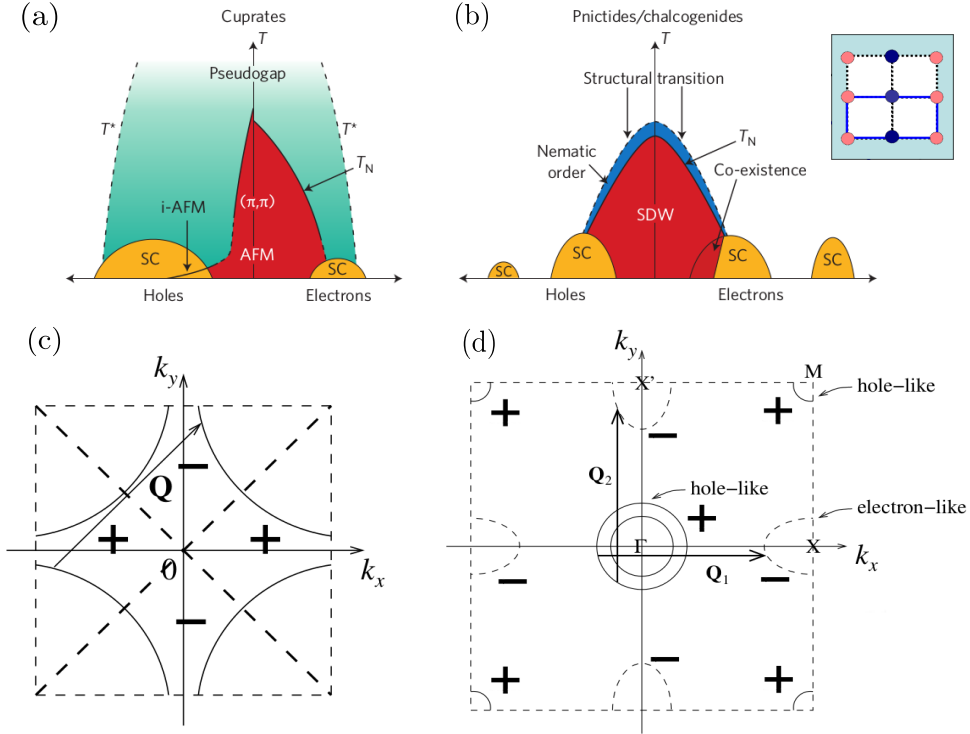


FIGURE 1.9: *Unconventional superconductors: cuprate and Fe-based superconductor (pnictides and chalcogenides). (a) General phase diagram of cuprate superconductors as a function of doping and temperature [46]. (b) Idem for the Fe-based superconductors. The inset shows the real-space magnetic pattern in the SDW state, which is ferromagnetic in one direction and anti-ferromagnetic in the other. (c) The Fermi surface and symmetry of the superconducting gap of cuprate superconductors. The signs denote $\Delta < 0$ (-) and $\Delta > 0$ (+). (d) Idem for the Fe-based superconductors.*

record T_c 's were obtained in $\text{Tl}_2\text{Ba}_2\text{Ca}_2\text{Cu}_3\text{O}_{10}$ (~ 130 K) in 1988, and in $\text{HgBa}_2\text{Ca}_2\text{Cu}_3\text{O}_{8+x}$ in 1993. The latter to date holds the record $T_c \sim 135$ K *at ambient pressure*, but it can be boosted to above 150 K at high pressure, as shown in Fig. 1.7.

The common crystal structure of the cuprate superconductor family is depicted in Fig. 1.8(a), specifically for La_2CuO_4 . It is a tetragonal, layered, and quasi-2D structure of the perovskite type, characterized by oxygen octahedra with Cu in the center. In particular the CuO_2 planes have been shown to develop superconductivity. The cuprates belong to the family of ceramic

materials, i.e., inorganic, mostly non-metallic oxides, nitrides and carbides. These materials are brittle, they can withstand much compression but not shear and tension.

Superconductivity is only one of the many phenomena occurring in the cuprates. Fig. 1.9(a) depicts a typical phase diagram of the cuprates. Another phenomenon is the *pseudogap state*, characterized by partial gapping of the Fermi surface. As a result the Fermi surface consists of *Fermi arcs* instead of the usual closed Fermi contours. When the temperature is lowered the gap states ultimately reduce to the four points cutting the diagonals of the Brillouin zone (depicted in Fig. 1.9(c)). At lower temperatures, below the Néel temperature (T_N), and with low doping the cuprates develop magnetic order. The characteristic wave vector of this order (for which the susceptibility diverges) is (π, π) , corresponding to an *antiferromagnetic*, checkerboard (Néel) pattern [46, and references therein].

The superconducting phase emerges upon electron and/or hole doping. There is a boundary regime where superconductivity and antiferromagnetism (AFM) coexist. This points at a close relation between both phenomena. Although there is no consensus for the coupling mechanism ('glue') between electrons in the cuprates, the general viewpoint is that other bosons than phonons mediate this interaction. The prime candidates for unconventional coupling mechanisms are collective density wave excitations of the charges or the spins [46]. These mediate a repulsive interaction between electrons, but once renormalized by the screening of the full electron cloud and the exchange interaction between the electrons, the coupling becomes a complex function of reciprocal space, and is thus attractive for some wave vectors.

In the cuprates, specifically antiferromagnetic spin fluctuations are conjectured to be at play [46, and references therein]. The resulting superconducting gap should thus contain gap nodes where $\Delta = 0$, as it switches sign. These nodes are well established in cuprate superconductors, as they have been detected directly by means of angle-resolved photoemission spectroscopy (ARPES) [46, and references therein]. These nodes occur at the diagonals of the Brillouin zone, exactly like the pseudogap state right before its disappearance, as mentioned above. The resulting symmetry of the superconducting gap is depicted in Fig. 1.9(c). The 2D projection of the

Fermi surface (containing all vital information, since the structure is quasi-2D) consists of a single sheet centered around the Brillouin zone boundary. The coupling mediated by antiferromagnetic spin fluctuations is most attractive when $\mathbf{Q} = \mathbf{k} - \mathbf{k}' \rightarrow 0$, and most repulsive when $\mathbf{Q} \rightarrow (\pi, \pi)$, hence the gap nodes occur at the diagonals. The resulting sign of Δ has the same symmetry as the electronic d orbital (albeit in reciprocal space, not in real space, in case of the superconducting state), specifically the $d_{x^2-y^2}$ orbital with $\Delta_{\mathbf{k}} = \Delta_0 (\cos(k_x a) - \sin(k_y a))$, where a is the lattice parameter. Hence, this type of superconducting pairing is called *d-wave pairing*.

Iron-based superconductors. As can be seen in Fig. 1.7, another major discovery followed in 2006, namely, that of superconductivity in Fe-based materials. This is all the more remarkable, since iron (Fe) as a ferromagnetic element is detrimental to the coupling strength in terms of conventional superconductivity. It is thus said that superconductivity moved from the copper to the iron age in 2008 [46]. The first Fe-based superconductor to be discovered was the oxypnictide LaOFeP, otherwise known as a (1111) pnictide, with $T_c \sim 4$ K [48]. The name ‘oxypnictide’ denotes that the compound contains both oxygen and a pnictogen atom, i.e., an atom of group V (N, P, As, Sb, and Bi). In 2008, the discovery of another compound of this family followed, namely $\text{LaO}_{1-x}\text{F}_x\text{FeAs}$, with a rather high $T_c \sim 26$ K. In 2009, samarium-doped SrFFeAs (a non-oxypnictide) with record $T_c \sim 56$ K within the ferropnictides was synthesized [49]. Ferropnictides exist in other compositions, like the (122) structures, of which BaFe_2As_2 is a prime example.

The structure of these materials is generally tetragonal and layered with planar layers of iron sandwiched in layers of tetrahedrally coordinated pnictogen atoms [50]. These layers are stacked together with ‘buffer’ layers of alkali (Li, Na, K,...), alkaline-earth (Sr, Ba,...), or rare-earth elements (Ce, La, Sm,...), optionally joined by oxygen or fluorine. Two examples of ferropnictide structures are depicted in Fig. 1.8(b), namely the (1111) structure LaOFeAs, and the (122) structure BaFe_2As_2 .

Closely related materials are the iron chalcogenides, compounds of iron and a chalcogen atom, i.e., S, Se, or Te. These materials have a (11) composition, such as FeSe. It has the simplest structure among the Fe-based superconductors discovered to date, namely one iron layer per unit cell, with tetrahedrally

coordinated Se atoms on both sides, as shown in Fig. 1.8(b). In its bulk form, FeSe superconducts with $T_c \sim 8$ K at ambient pressure, which can be boosted to 37 K under high pressure (9 GPa) [51]. At ambient pressure, the T_c can also be boosted by Te substitution of Se. The maximal $T_c \sim 15$ K is reached in $\text{FeSe}_{1-x}\text{Te}_x$ at $x \sim 0.35$.

Contrary to the cuprates, no distinct Mott phase (pseudogap) has been found in the Fe-based superconductors, which are (poor) metals at higher temperatures [46, and references therein]. The magnetic order is also different from that of the cuprates, namely, in the iron pnictides there is a tendency for ferromagnetism in one direction and antiferromagnetism in the other – called a spin density wave (SDW) state – as shown in the inset in Fig. 1.9(b) [46, 52]. A prevailing theory proposes that fluctuations of this competing magnetic phase provide the glue between the electrons in the superconducting phase [52]. It is proposed in Ref. 52 that antiferromagnetic spin fluctuations prevail over ferromagnetic ones (which would be pair-breaking in case of spin singlet coupling). Another important phenomenon in the Fe-based family is the structural transition from tetragonal to orthorhombic, indicated in Fig. 1.9(b), and the corresponding nematic phase (where the orbitals align in a rotational symmetry breaking fashion, akin to, and named after the longitudinal ordering of the molecules composing liquid crystals).

Fig. 1.9(d) shows a typical 2D-projected Fermi surface of the Fe-based family. There are usually two hole-like bands at the Brillouin zone center, Γ , and at least one electron-like band around point X^6 , and there can be additional hole-like pockets around point M. While the hole-like pockets are usually circular, the electron-like pockets often are quite ellipsoidal. The electron and hole pockets are usually well nested (nesting is the occurrence of large parallel portions of different Fermi sheets), which drives antiferromagnetic spin fluctuations. This is compatible with an *extended s-wave* order parameter with opposite signs between electron and hole pockets [52], as shown in Fig. 1.9(d). This type of pairing is denoted as s_{\pm} pairing, and evolves as $\Delta_{\mathbf{k}} = \Delta_0 \cos(k_x a) \sin(k_y a)$ throughout the Brillouin zone. It is different from d-wave pairing in that the full symmetry of the lattice is preserved. Some other ($\text{Ba}_{1-x}\text{K}_x\text{Fe}_2\text{As}_2$ and KFe_2As_2 [53]) have Fermi surface sheets at the

⁶Here, we employ the convention of the single-iron Brillouin zone. The Brillouin zone of the whole structure is smaller, and the electron-like pockets are centered around point M in this convention. Both are present in the literature.

corner of the Brillouin zone shaped as a four-bladed propeller, with very little to no nesting at all. Thus, it is currently not clear if this proposed coupling mechanism provides an explanation for all Fe-based superconductors. The fermiology of bulk FeSe is discussed in more detail in Appendix B, in the light of quantum oscillations.

In summary, it is thought, though not proven, that superconductivity in both the cuprate and the Fe-based superconductors is mediated by spin fluctuations. We stress again here that no complete theory for unconventional and high- T_c superconductivity has been established. It is one of the most outstanding open problems in physics to date. The details in the phase diagrams in Figs. 1.9(a) and 1.9(b) reveal that a good understanding of these materials on the atomic level is crucial. First-principles theory, as developed in this thesis, provides thus the most realistic and accurate basis to construct such a microscopic theory.

Atomically thin structures of Fe-based superconductors harbor additional surprises. A monolayer of FeSe grown epitaxially on the insulating substrate SrTiO₃ has $T_c \sim 60 - 70$ K [54], by far exceeding that of its bulk counterpart, and even above 100 K under certain growth conditions [55], as also shown in Fig. 1.7. In this case, the Fermi surface has only got the electron pocket at the Brillouin zone boundary. The hole pocket around the Brillouin zone center has disappeared completely, as a result of electron doping by the substrate, increasing the Fermi level [54]. This fermiology is thus no longer compatible with s_{\pm} pairing. Consequently, this discovery evokes many new questions about the coupling mechanism in the Fe-based superconductors.

In this thesis, we will study an Fe-based superconductor, namely iron tetraboride (FeB₄), with a conventional coupling mechanism, mediated by phonons, albeit with ferromagnetic spin fluctuations as well, that strongly deplete the strength of the superconductivity. FeB₄ stands out from other Fe-based superconductors discussed above since it has a tendency for ferromagnetic spin fluctuations, as a result of its electronic structure.

Other. In view of the richness of unconventional superconductivity, this overview is by no means complete. We wish to touch briefly on two other types of unconventional coupling superconductors. Firstly, candidates for

spin-triplet superconductivity have emerged in recent years. In an ordinary, singlet superconductor the total spin of the pair is $S = 0$, as the electrons have opposite spin. In a spin-triplet superconductor, on the other hand, the pairs have total spin $S = 1$. Ferromagnetic spin fluctuations can induce such triplet superconducting pairing, also called *p-wave pairing* due to the symmetry of the order parameter⁷. The most notable candidate material is Sr_2RuO_4 ($T_c = 1.5$ K) [56], although the question of p-wave superconductivity in this material is still highly debated (see Refs. 57 and 58 for reviews on this topic). Interestingly, Sr_2RuO_4 is isostructural to the cuprate superconductor La_2CuO_4 .

One other recent addition to the list of potentially unconventional superconductors is that in quasi-one-dimensional (1D) organic chain link molecules. These are polymers organized in a chain-like fashion. One notable example is K-doped para-terphenyl, with reported T_c 's in the range 43-123 K [59, and references therein], as obtained from magnetic measurements. It should be stressed that the measurements currently cannot unequivocally be identified as manifestations of superconductivity. In addition, a large superconducting gap of 15 meV opening at 60 K has also been reported [59, and references therein].

1.2 Recent breakthroughs

Here, we review recent breakthroughs in superconductivity research. We will specifically focus on two major developments that are investigated in the thesis, namely multigap superconductivity and superconductivity in atomically thin films. Strong interest in the former emerged in 2001-2002, following the discovery of high- T_c superconductivity in magnesium diboride (MgB_2). Atomically thin superconductivity has gained a very strong interest ever since the realization of superconductivity in a single layer of lead (Pb) and indium (In) on a Si(111) substrate in 2010 [60]. It ought to be mentioned that there are other important new trends that will not be treated here. A prime example is topological superconductivity, i.e., ordinary superconductivity inside the bulk of a material, combined with Majorana fermions at the surface [61].

⁷It is akin to p-wave superfluidity in the fermionic, spin-1/2 He-isotope He-3 (two protons and one neutron) [6].

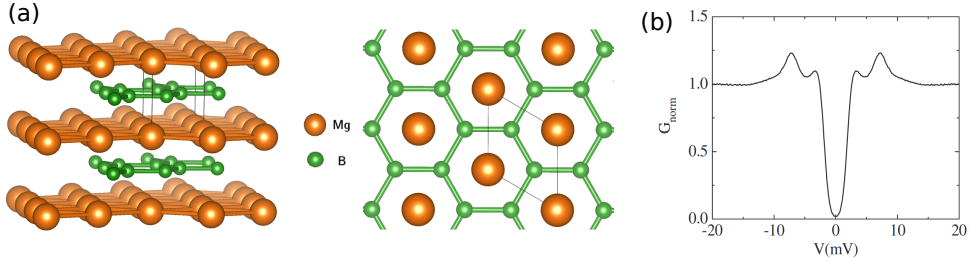


FIGURE 1.10: (a) Crystal structure of bulk MgB_2 in a side view and a top view. (b) Scanning tunneling microscopy spectrum of bulk MgB_2 , normalized conductance as a function of bias voltage, showing the two-gap nature of its superconductivity [28].

1.2.1 Multigap superconductivity

1.2.1.1 Discovery and further experiments

In 2001, an unexpectedly high $T_c = 39$ K was reported in the intermetallic binary compound magnesium diboride (MgB_2) [35]. It is a layered material, as shown in Fig. 1.10(a), with boron (B) arranged in a honeycomb pattern, and magnesium (Mg) sitting above the center of the honeycomb tiles, such that it adopts a hexagonal closed packed (hcp) structure. After this first observation the mechanism for the high T_c was unclear. Among the many competing theories ultimately *two-gap* interactions proved the correct one. This was proven directly by means of scanning tunnelling spectroscopy (STS) [27, 28, 62], which yields the density of states. In the superconducting state the density of states is gapped and peaked at Δ of the superconducting state, as discussed in Sec. 1.1.4.2. Fig. 1.10(b) shows such STS spectrum of bulk MgB_2 [28, 62]. Here, there are two peaks, instead of one, as in a simple, BCS superconductor. This indicates the presence of two different Cooper-pair condensates, yielding *two-gap superconductivity*. Therefore, the glue between the electrons in the condensate is conventional electron-phonon coupling, but the distribution of the order parameter is non-standard. The electron-phonon based nature of superconductivity in MgB_2 was moreover convincingly proven by the measurement of the *B isotope effect* on T_c [30, 31]. It should be noted that the exponent in $T_c \propto M^{-\alpha}$ is in the range $\alpha = 0.26 - 0.32$ [30, 31]. The deviation from the BCS value $\alpha = 0.5$ originates from the multiband nature of superconductivity in MgB_2 . When there are more than two gaps, this concept

can be extended to *multigap superconductivity*. Here, each condensate has an amplitude and a phase, and is weakly coupled to the other condensates.

There is no general consensus on the terminology concerning superconductivity involving more than one band in the literature [63]. In this thesis, we will uphold the following conventions. *Multicomponent* superconductivity is used here as the most general, umbrella term⁸. By this we denote that there is an *increased number of degrees of freedom in the condensate wave function* [64]. This can involve multiple bands, spin degrees of freedom, competing interactions, a combination of different order parameters (e.g., $s+id_{x^2-y^2}$), etc. On the other hand, *multiband* superconductivity denotes specifically that *several electronic bands* are present at the Fermi level, which is the case in most superconductors of interest today. This notion is all the more interesting when the different bands have a different character. An *anisotropic single-gap* superconductor denotes the case when the superconducting gap is spread *continuously* over a range of values. The overlap of the gaps may be accidental, when they have roughly the same intraband coupling, but may also be due to strong interband coupling. Under a *multigap* superconductor we understand that there are stronger and weaker gaps opening on *separate, disconnected* parts of the Fermi surface. They are coupled through weak to intermediate interband coupling.

The coupling between the two Cooper-pair condensates in bulk MgB₂ is responsible for the enhancement of T_c to 39 K. Generally, the critical temperature of a two-gap system is higher than the critical temperature associated with the stronger of the two gaps. This important point was already recognized and proven in 1959 by Suhl, Matthias and Walker [65], as an extension of the BCS theory, that emerged shortly before. In this case only attractive interactions between the bands were considered. However, Kondo realized soon after that superconductivity can even be enhanced by *repulsive* interband interactions if different parts of the Fermi surface support order parameters of opposite sign [66]. Such effect was proposed to be relevant for transition metal superconductors in particular. Subsequently, in 1964 Tilley developed a Ginzburg-Landau description of two-band superconductors based on the Gor'kov procedure [67]. With the discovery of multigap

⁸Note that in some references the term *multicomponent* superconductivity is restricted to a specific case of a multigap superconductor, where the different gaps are all strong, and very weakly coupled [63]. This convention is at odds with ours.

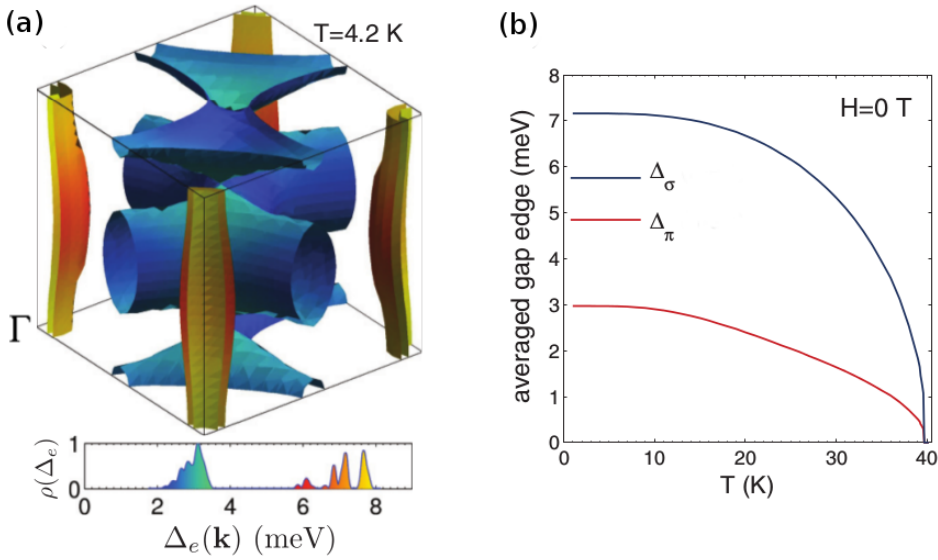


FIGURE 1.11: *The two-gap superconducting gap spectrum of bulk MgB₂, calculated with anisotropic Eliashberg theory [39]. (a) The distribution of the gap on the Fermi surface (calculated at $T = 4\text{ K} \ll T_c = 39\text{ K}$), showing distinct contributions at 2 – 3.5 meV, the π -gap, and 6 – 8 meV, the σ -gap. (b) The evolution of the σ (blue) and π (red) gaps with temperature.*

superconductivity in MgB₂ and possibly in iron based superconductors in the last decade this field has experienced a strong resurgence of interest [63, 64, and references therein].

The different gaps of a multigap superconductor open on distinct parts of the Fermi surface. Several bands can contribute to one condensate. For instance, bulk MgB₂ is a four-band, two-gap superconductor. The different parts of its Fermi surface – called Fermi sheets – derive from its layered structure. The Mg planes dope electrons into the B layers, thus increasing their intrinsic Fermi level (E_F). The electronic states at E_F are localized in the B planes, and couple mainly to B related phonon modes, in particular the E_{2g} mode [36]. Specifically, four bands cross E_F and form thus four sheets of the Fermi surface, as shown in Fig. 1.11(a). The two nested, slightly warped cylindrical sheets centred around Γ stem from in-plane σ bonds between B p_x and p_y states, while the two other bands stem from out-of-plane π bonds between B p_z states. Anisotropic Eliashberg calculations have shown that

the stronger gap opens on the σ bands, $\Delta_\sigma \sim 6 - 8$ meV, while the weaker gap opens on the π bands, $\Delta_\pi \sim 2 - 3$ meV [36, 38, 39]. Fig. 1.11(a) depicts the gap spectrum calculated with Eliashberg theory on the Fermi surface, as well as the distribution of the gap, $\rho(\Delta)$. Two separate domes, the σ dome at higher energy and the π dome at lower energy, are apparent in $\rho(\Delta)$. In Fig. 1.11(b) the temperature evolution of the dome averages are shown, in zero applied magnetic field. Both gaps disappear at $T_c = 39$ K. This result of the distribution of the gaps on the Fermi surface was confirmed with low-temperature ARPES measurements, able to detect the opening of superconducting gaps on different parts of the Fermi surface [68].

In Chapter 6 of this thesis we prove that in two-dimensional MgB₂ structures a surface band, with Mg character, emerges, and that it opens a separate gap. In the thinnest limit, monolayer MgB₂ becomes a three-gap superconductor.

1.2.1.2 Mean-field theory

To study the properties of multigap superconductors more deeply, an appropriate mean-field theory is required. Here, we will present multigap generalizations of Ginzburg-Landau (GL) theory, introduced for ordinary, single-gap superconductors in Sec. 1.1.3. There are several approaches to constructing this multigap GL theory. We will present here the most important modern approaches, namely, multicomponent GL theory, reconstructed multiband GL theory, and Extended GL theory.

Multicomponent Ginzburg-Landau theory. The first approach that was employed is also the simplest one [69]. The different superconducting components are coupled via a simple *Josephson term*, that derives its name from the coupling of two different superconductors through a weak link, i.e. the Josephson effect [4, 6]. The first GL Eqs. are given by the following system of N equations, where N is the number of bands,

$$(\alpha_i + \gamma_{ii} - N_{F,i}\mathcal{A})\Delta_i + \beta_i\Delta_i|\Delta_i|^2 - K_i\nabla^2\Delta_i + \sum_{i \neq j} \gamma_{ij}\Delta_j = 0, \quad (1.38)$$

where α_i , β_i , and K_i are coefficients of the GL expansion, γ_{ij} are the elements of the inverted coupling matrix, $N_{F,i}$ is the electronic DOS at E_F of band i ,

and $\mathcal{A} = \ln\left(\frac{2e^\Gamma \hbar \omega_c}{\pi T_c}\right)$, Γ being the Euler constant and ω_c the characteristic electronic cutoff frequency.

A problem arises with multicomponent GL theory, as originally noted in Refs. 70–72 when carrying out an expansion of the multicomponent order parameter, $\mathbf{\Delta} = (\Delta_1, \Delta_2, \dots, \Delta_N)$ as a function of $\tau = 1 - \frac{T}{T_c}$, i.e., $\mathbf{\Delta} = \mathbf{\Delta}^{(0)} + \mathbf{\Delta}^{(1)} + \mathcal{O}(\tau^{5/2})$, with $\mathbf{\Delta}^{(n)} \propto \tau^{\frac{1}{2}+n}$. Namely, the coefficients of the first and the last term of Eq. 1.38 do not vanish in the limit $\tau \rightarrow 0^9$, and consequently filling in the expansion into Eq. 1.38 leads to solutions for $\mathbf{\Delta}$ containing terms of arbitrarily high order. This result is at odds with the Gor'kov procedure, truncating terms beyond $\tau^{\frac{1}{2}}$ when deriving the GL equations from the BCS theory [11]. As such, the solutions of the multicomponent GL equations exceed the inherent accuracy of the formalism.

Reconstructed multiband Ginzburg-Landau theory. In the reconstructed GL theory the problem described in the previous paragraph is resolved by a systematic perturbation expansion of the GL equation, collecting terms up to order $\tau^{\frac{1}{2}}$ [72]. In this way, the following GL functional is obtained,

$$\mathcal{F}_s = \mathcal{F}_{n0} + \int dr \left[\sum_{\alpha\beta} a_{\alpha\beta} \psi_\alpha^* \psi_\beta + K_{\alpha\beta} \mathbf{D}^* \psi_\alpha^* \mathbf{D} \psi_\beta + \frac{1}{2} \sum_{\alpha\beta\gamma\delta} b_{\alpha\beta\gamma\delta} \psi_\alpha^* \psi_\beta \psi_\gamma^* \psi_\delta + \frac{\mathbf{B}^2}{8\pi} \right], \quad (1.39)$$

where \mathcal{F}_{n0} is the free energy in the normal state in zero applied magnetic field, $\mathbf{D} = \nabla + i \frac{e^*}{\hbar c} \mathbf{A}$ (where \mathbf{A} signifies the vector potential) and $e^* = -2e$ is the Cooper-pair charge. The indices $\alpha, \beta, \gamma, \delta$ run over $1, \dots, M$, where M signifies the number of degenerate solutions of the gap equation to lowest order, $\check{L}\mathbf{\Delta}^{(0)} = 0$ yielding the same maximum T_c . Here, the gap function can be expanded as $\mathbf{\Delta}^{(0)} = \sum_{\alpha=1}^M \psi_\alpha \boldsymbol{\xi}_\alpha$.

Furthermore, the coefficients in the functional can be related to microscopic parameters, (i) the density of states *per band* at the Fermi level, $N_{F,i}$, and

⁹Note that this problem does not occur in the single-band case, where $\gamma_{i \neq j} = 0$ and $\gamma_{ii} = N_{F,i} \mathcal{A}$.

(ii) the average Fermi velocity per band, $v_{F,i}$, by means of [72]

$$\begin{cases} a_{\alpha\beta} &= \sum_i a_i \xi_{\alpha i} \xi_{\beta i} \text{ with } a_i = -N_{F,i} \tau, \\ b_{\alpha\beta\gamma\delta} &= \sum_i b_i \xi_{\alpha i} \xi_{\beta i} \xi_{\gamma i} \xi_{\delta i} \text{ with } b_i = N_{F,i} \cdot \frac{7\zeta(3)}{8\pi^2 T_c^2}, \\ K_{\alpha\beta} &= \sum_i K_i \xi_{\alpha i} \xi_{\beta i} \text{ with } K_i = \frac{b_i}{6} \hbar^2 v_{F,i}^2. \end{cases} \quad (1.40)$$

Thus, microscopic parameters obtained from first-principles calculations can be used directly in GL theory calculations.

It is instructive to apply this framework to a *two-gap superconductor*. In case there are no degeneracies (so, $M = 1$), the first GL equation reads

$$-K\mathbf{D}^2\psi(\mathbf{r}) + a\psi(\mathbf{r}) + b|\psi(\mathbf{r})|^2\psi(\mathbf{r}) = 0. \quad (1.41)$$

This is completely analogous to the single-band GL Eq. 1.6, except that the coefficients are given by Eq. 1.40 in the multiband case. To proceed, we need to solve the gap equation to lowest order, $\check{L}\Delta^{(0)} = 0$. For a two-gap superconductor \check{L} is given by [72]

$$\check{L} = \frac{1}{\Lambda} \begin{pmatrix} \lambda_{22} - \Lambda N_{F,1}\mathcal{A} & -\lambda_{12} \\ -\lambda_{12} & \lambda_{11} - \Lambda N_{F,2}\mathcal{A} \end{pmatrix}, \quad (1.42)$$

where $\Lambda = \lambda_{11}\lambda_{22} - \lambda_{12}^2$ is the determinant of the matrix of coupling constants. The gap equation has non-trivial solutions only if $\det(\check{L}) = 0$, yielding 2 solutions for \mathcal{A} ,

$$\mathcal{A}_{\pm} = \frac{N_{F,1}\lambda_{11} + N_{F,2}\lambda_{22} \pm \sqrt{(N_{F,1}\lambda_{11} - N_{F,2}\lambda_{22})^2 + 4\lambda_{12}^2 N_{F,1}N_{F,2}}}{2N_{F,1}N_{F,2}\Lambda}, \quad (1.43)$$

which is essentially the same result as obtained in pioneering work on multi-gap superconductivity, based on BCS theory [65]. The smallest solution, \mathcal{A}_- , is the true solution minimizing the energy functional, and yields the maximal critical temperature,

$$T_c = \frac{2e^\Gamma \hbar\omega_c}{\pi} \exp(-\mathcal{A}_-). \quad (1.44)$$

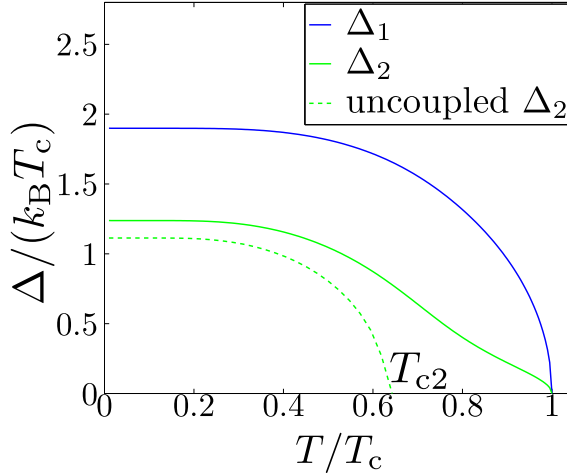


FIGURE 1.12: *The temperature evolution of the gaps of a two-gap superconductor, described by the coupling matrix shown in the inset [73]. The gap profile of the weaker gap, Δ_2 in the absence of interband coupling is also shown (dashed line).*

The gap equation to lowest order, $\check{L}\mathbf{\Delta}^{(0)} = 0$, yields the corresponding eigenvector $\boldsymbol{\xi} = \begin{pmatrix} S^{-1/2} \\ S^{1/2} \end{pmatrix}$ with $S = (\lambda_{22} - \Lambda N_{F,1} \mathcal{A}_-) / \lambda_{12}$, and thus $\mathbf{\Delta}^{(0)}(\mathbf{r}) = \psi(\mathbf{r}) \begin{pmatrix} S^{-1/2} \\ S^{1/2} \end{pmatrix}$. Therefore, this model maps onto a single-band model, so that both gap function components vary on the same length scale [72]. So, this model fails to describe the difference in the spatial profiles of the two condensates. We will see in the next paragraph where differences occur.

Using Eq. 1.40, we find that the coupling of the Ginzburg-Landau coefficient of Eq. 1.41 is given by

$$a = S^{-1}a_1 + Sa_2, \quad b = S^{-2}b_1 + S^2b_2, \quad K = S^{-1}K_1 + SK_2. \quad (1.45)$$

A special case occurs when interband coupling is entirely absent, i.e., λ_{12} . In this case uncoupled (uc) case, Eq. 1.43 reduces to $\mathcal{A}_-^{(uc)} = 1 / (N_{F,1}\lambda_{11})$, where we have chosen $N_{F,1}\lambda_{11} > N_{F,2}\lambda_{22}$, meaning that condensate 1 is the stronger one. Such a situation is depicted in Fig. 1.12, namely, the two-gap model for OsB₂ that we will study further in Chapter 3. In the figure, the situation is shown when the two condensates are completely uncoupled. In this case, the gaps vanish at different temperatures. When the coupling is

turned on, even if it is a very small coupling of $\lambda_{12} = 0.01$ as in the example, the gaps vanish at the same critical temperature. The weaker condensate displays a tail at higher temperatures. The weaker the coupling between the condensates, the more convex the gap profile of the weaker condensate is. The weaker of the two condensates is moreover visibly enhanced in Fig. 1.12 when the coupling is turned on. Similarly, the T_c of the system is enhanced by attractive (positive) interband coupling. Namely, $\mathcal{A}_- < \mathcal{A}_-^{(\text{uc})}$ is always strictly fulfilled (in case of attractive interband coupling), so that $T_c > T_c^{(\text{uc})}$, so the critical temperature of the coupled system is higher than that of the stronger of the two condensates would be if there were no interband coupling. The difference between the two grows as the interband coupling increases. MgB₂ has a considerable interband coupling of $\lambda_{\sigma\pi} \simeq 0.19$ [73, 74]. Thus, T_c of MgB₂ is enhanced to 39 K, indeed the very first sign of its two-gap superconductivity.

Extended Ginzburg-Landau theory. The basic idea behind the Extended GL theory is extending the GL framework to the next order in $\tau = 1 - \frac{T}{T_c}$. As we discussed in the preceding paragraphs, the standard Gor'kov truncation includes terms up to order $\tau^{1/2}$. In Extended GL theory, the next order, $\tau^{3/2}$, is taken into account. It has been applied to both single-gap [75] and two-gap superconductors [71]. In the latter case, the temperature evolution of the gaps generally agrees much better with the original BCS-type result than in the two-component model, especially away from T_c , as a result of extending the perturbation series. A notable exception is the evolution of the weaker gap, away from T_c , in case of weak interband coupling. Furthermore, the identical spatial profiles of the condensates in a two-gap superconductor predicted by multiband GL theory, demonstrated in the previous paragraph, become different in order $\tau^{3/2}$ [71].

Even in the single-band case there are advances in the Extended GL theory. For instance, the thermodynamic critical field, H_c , is extended from order τ to order τ^2 , as $H_c = H_c^{(0)} + \tau H_c^{(1)}$, where $H_c^{(0)} = \sqrt{(4\pi\alpha^2)/\beta}$ and $H_c^{(1)} = -H_c^{(0)} \left(\frac{1}{2} + \frac{\alpha c}{3\beta^2} \right)$ [71]. In an application of this formula in Chapter 3, to OsB₂, we will show that the formula provides a much improved comparison to experimental values, away from T_c [73].

1.2.1.3 First-principles theory

In order to study the gap spectrum of superconductors, and thus to find out whether they are multigap or not, first-principles calculations that start from the basic laws of quantum mechanics, are needed. These calculations are most suited for superconductivity based on electron-phonon coupling, where the coupling mechanism is well understood. Several materials have been investigated in this way, with two main techniques. The first approach, *anisotropic Eliashberg theory*, combined with first-principles calculations of the electron-phonon coupling, is also the path we take in this thesis. The second approach is called *density functional theory for superconductors* (SCDFT), as developed by Gross and coworkers [76–78]. In the latter, three densities enter in the functional at the same time, namely the usual electronic density, the nuclear density matrix, and the superconducting order parameter (in the form of the anomalous density). We will return to a deeper discussion of the first-principles calculation of the electron-phonon coupling, and of the foundations of Eliashberg theory in Chapter 3.

As we mentioned before, through anisotropic Eliashberg theory, solid theoretical evidence for two-gap superconductivity in bulk MgB_2 was delivered [36]. This calculation was later reproduced independently on several occasions [38, 39]. In this thesis I apply anisotropic Eliashberg theory of MgB_2 to the atomically thin limit, including the influence of strain and hydrogen impurities. We find that in this ultrathin limit MgB_2 opens an extra band, a surface band, yielding a third gap. Thus, monolayer MgB_2 becomes a distinctly three-gap superconductor. Very few other three-gap superconductors have been found so far, thus impeding experimental studies of multi-gap superconductivity beyond two-gap. In recent years two other three-gap superconductors were proposed theoretically by Gross and coworkers, using SCDFT. One is molecular hydrogen, which under very high pressure develops three superconducting gaps on different Fermi sheets [42]. However, due to anisotropy two of the gaps strongly overlap. The other material is CaBeSi , a MgB_2 -like compound in which splitting of the π -bands was predicted to give rise to three-gap superconductivity [79], but with impractically low $T_c \cong 0.4$ K.

A similar analysis has led to a revision of the superconducting gap spectrum in even the simplest elemental metals, like bulk lead (Pb), where calculations have shown two different bands play a role in its superconductivity [80]. This was confirmed by low-temperature scanning tunneling microscopy, however, it also showed that the two resulting superconducting gaps differ merely by $150 \mu\text{eV}$ [81], so the condensates are virtually degenerate and multigap effects are expected to be extremely subtle. Several *graphene-based* superconductors have also been studied from first principles. These include Li-doped graphene (LiC_6) [82], Ca-doped graphene (CaC_6) [83], and hole-doped graphene [83], all having a *single, anisotropic gap*. Finally, some *metallic transition metal dichalcogenides* (TMDs), of much recent interest, have equally been investigated in view of their superconducting properties. It was obtained that NbS_2 has a *single, anisotropic gap* [84], a result obtained, however, neglecting charge density waves (CDWs) that can gap part of the Fermi surface, and thus significantly alter the gap spectrum.

In this thesis, we furthermore prove that OsB_2 and FeB_4 , both *multiband borides*, are *anisotropic single-gap* superconductors, in Chapters 4 and 5, respectively.

Quasiparticle interband scattering. In all these descriptions of multigap superconductivity coupling between the condensates is considered to result from phonon exchange between the quasiparticles of the corresponding electronic bands, following the seminal work of Suhl *et al.* [65]. It should be noted that other mechanisms have been proposed, notably scattering of the quasiparticles of a condensate to another band. This effect was first proposed by Moskaleiko *et al.* [85], and later extended by Schopohl and Scharnberg [86]. This would induce superconductivity in the ‘passive’ band in the way of a proximity effect (albeit in reciprocal space), leading to multigap features in the superconducting tunneling spectrum [87, 88]. One example of a material where the multigap signatures in the tunneling spectra can be described within a model of interband quasiparticle scattering is the bulk transition metal dichalcogenide 2H-NbSe_2 , although a possible role of anisotropy of the gap spectrum has currently not been elucidated [87, 88]. The microscopic mechanism behind the quasiparticle interband scattering considered by Moskaleiko *et al.* and Schopohl and Scharnberg was a scattering from impurities. It is currently still under debate whether a similar result can be

obtained in the clean limit from electron-electron interactions [88]. In this thesis only interband coupling resulting from phonon exchange is taken into account, following the successful description of two-gap superconductivity in MgB₂ [36, 38, 39].

1.2.1.4 New physics in multigap superconductors

Novel vortical states. The coupling of the different condensates leads to important changes in their interaction with perturbations and external magnetic fields. It has been reported that vortices in MgB₂ are not necessarily arranged in an Abrikosov-type lattice but can form clusters and stripes [89]. This behavior was dubbed *type-1.5 superconductivity*, as it was reported to result from two different coherence lengths related to the two band condensates, the π condensate with $\kappa_\pi < 1/\sqrt{2}$ (type-I) and the σ condensate with $\kappa_\sigma > 1/\sqrt{2}$ (type-II). This interpretation has stirred a discussion, related to the existence of two different coherence lengths or not, in the multiband GL theory – as discussed in paragraph 1.2.1.2 [70, 90]. A different mechanism that gives rise to the same phenomenon of vortex clustering are nonmonotonic vortex-vortex interactions [91]. It is shown that the sign of the surface energy, introduced in Section 1.1.3 to distinguish type-I and type-II superconductors, is not a good criterion for long-range vortex-vortex interactions in a multigap superconductor. For MgB₂, based on its microscopic values, it is found that short-range repulsion and long-range attraction coexist, which can lead to the behavior observed in Ref. 89.

Moreover, different approaches to the two-gap GL theory have shown that the coherence length of the weaker condensate diverges at its intrinsic T_{c2} (i.e., the T_c it would have in the absence of coupling to the other condensate) [92, 93], which has been called *hidden criticality* in Ref. 93. This phenomenon is particularly pronounced in case the interband coupling between the condensates is weak, and should then be observable in the vortex core size near the critical point T_{c2} .

Interband phase phenomena. Interesting new physics also emerges from the intrinsically complex order parameter of multigap superconductors. In 1966, inspired by transition metals, Leggett proposed that in a multiband

superconductor fluctuations of the relative phase and pair densities of the different condensates can occur [24]. The characteristic frequency of these *Leggett modes* is

$$\omega_0 = \sqrt{\frac{8J\Delta_1\Delta_2(\rho_1 + \rho_2)}{\rho_1\rho_2(UV - J^2)}}, \quad (1.46)$$

where parameters U , V and J are related to the coupling of the condensates as $\Delta_1 = V\psi_1 + J\psi_2$ and $\Delta_2 = J\psi_1 + U\psi_2$, and where $\rho_{1,2}$ are the densities of states in the normal states of the respective bands. It follows from this formula that the effect can be significant for two large gaps, with intermediate interband coupling J . Leggett showed that this frequency manifests itself, for example, in the specific heat as $C \propto \omega_0^4 \exp(-\beta\omega_0)$, on the condition that $\beta^{-1} = k_B T < \omega_0$.

An effect that is stronger than these phase fluctuations are interband phase difference solitons, called *i-solitons* [63, and references therein]. In this case the interband phase difference varies spatially from 0 to π . It can be induced in non-homogeneous superconducting systems, such as multilayer structures, rings made of two-band superconductors, can also be induced by local current injection, etc. [63, and references therein]. The energy cost for generating i-solitons is generally reduced in mesoscopic samples. In case an i-soliton coalesces with a vortex, the vortex can carry a *fractional flux quantum*, $\phi \neq 2\pi n$.

Furthermore, in three-gap systems and beyond it is not a priori evident what phases minimize the energy functional, especially when there are both attractive interactions between certain bands, e.g. mediated by phonons, and repulsive ones, e.g. mediated by spin fluctuation exchange. Between two condensates, attractive interactions lead to 0 phase difference as the ground state, while repulsive interactions favor a phase difference of π [94]. As before, we define $V_{ij} > 0$ as attractive and $V_{ij} < 0$ as repulsive.

Let us consider all possibilities for the interband coupling in a three-band superconductor. The condensate wave function components are $\psi_1 = \Delta_1$, $\psi_2 = \Delta_2 e^{i\phi_2}$ and $\psi_3 = \Delta_3 e^{i\phi_3}$. In case all interactions are attractive, $V_{12} = V_{23} = V_{13} > 0$, the situation is trivial: all components are aligned with $\phi_2 = \phi_3 = 0$. Similarly, in case of two repulsive interactions and one attractive interaction, e.g., $V_{12}, V_{13} < 0$ and $V_{23} > 0$, the situation is also easy: ψ_2 and

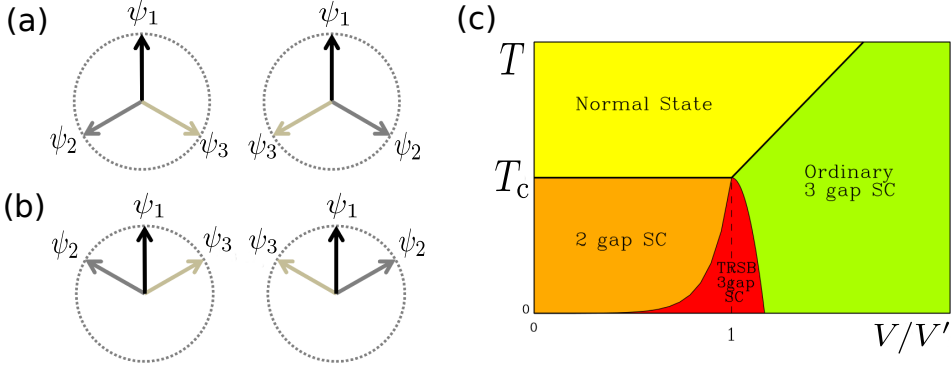


FIGURE 1.13: *Time-reversal symmetry breaking (TRSB) in three-band superconductors. (a) Chiral three-gap states, originating from repulsive interactions between all the bands [94]. (b) Chiral three gap states, this time with a repulsive interaction between bands 2 and 3. (c) The phase diagram of a three-band system with repulsive interaction between all the bands, namely $V_{12} = V_{13} = V < 0$ and $V_{23} = V' < 0$ [95].*

ψ_3 are diametrical to ψ_1 ($\phi_2 = \phi_3 = \pi$). However, in case $V_{12}V_{23}V_{13} < 0$, two chiral, degenerate solutions appear. When all interactions are repulsive, an interesting situation arises. None of the components can adopt a phase that completely minimizes the energy with respect to either of the other components. The phases can be both $\phi_2 = -\phi_3 = 2\pi/3$ and $\phi_2 = -\phi_3 = -2\pi/3$, as shown in Fig. 1.13 (a), so that there is a frustration between the chiral phase locking tendencies. Time-reversal symmetry is broken as $\Psi = (\psi_1, \psi_2, \psi_3)$ and Ψ^* cannot be related by a simple rotation. In other words, there is no phase θ such that $\Psi = e^{i\theta}\Psi^*$. $V_{11}, V_{13} > 0$ and $V_{23} < 0$ also yields two chiral solutions, with $\phi_2 = -\phi_3 = \pi/3$ and $\phi_2 = -\phi_3 = -\pi/3$, as shown in Fig. 1.13 (b). This case equally breaks time-reversal symmetry.

A more detailed illustration of this physics was given by Stanev and Tešanović [95]. Fig. 1.13(c) represents the case where all interband interactions are repulsive, specifically, $V_{12} = V_{13} = V < 0$ and $V_{23} = V' < 0$, and all intraband interactions are absent, $V_{11} = V_{22} = V_{33} = 0$. It is shown that three superconducting states can exist in this system: (i) ordinary three-gap superconductivity with a sign change of the order parameter between band 1 on the one hand and bands 2 and 3 on the other, (ii) two-gap superconductivity where only bands 2 and 3 are significantly gapped, and (iii) chiral three-gap superconductivity with TRSB as shown in Fig. 1.13(a) [95]. The latter is

expected to exhibit spontaneous currents and fields wherever translational symmetry is broken in the sample (e.g., at edges, impurities, domain walls), but has remained unobserved to date. Recent studies have also shown that the TRSB state supports chiral domain walls that can act as pinning centres for the fractional vortices discussed above [94]. For systems of four or five bands the situation is more complex, but is again generally frustrated if there is an uneven number of repulsive interactions between the bands.

1.2.2 Superconductivity in atomically thin materials

The realization of atomically thin materials. Dimensionality, ranging from 0D to 3D, is one of the prime characteristics of materials, and has seen a great resurgence of interest since the realization of two-dimensional (2D), one-atom thick *graphene* layers in 2004 [96]. These graphene layers consist of carbon atoms arranged in a planar honeycomb lattice, and form the basis for graphite when stacked together under the influence of van der Waals interactions. Two-dimensional systems were rather late to be realized compared with other low-dimensional systems, such as quasi-0D systems, e.g., quantum dots, and quasi-1D systems, e.g., nanotubes and nanowires. Since the discovery of graphene, many other 2D materials have been realized, both within the graphene family, e.g., hexagonal boron nitride (hBN) and fluorographene (graphene decorated with F adatoms), and in other families, e.g., the chalcogenides (binary compounds containing chalcogen atoms such as S and Se), phosphorene (a single layer of black phosphorus), etc.

The rapid progress in synthesis techniques for 2D materials, and in nanotechnology in general, lies at the base of recent advances in the field. Graphene was isolated for the first time using a technique called *mechanical exfoliation* [96]. It entails taking off part of a 3D sample with a sort of scotch tape, subsequently depositing a fraction of the layers from the tape onto a substrate. This technique is repeated on the new sample each time, so the number of deposited layers decreases and can produce monolayer films. To date mechanical exfoliation remains the preferred technique to make thin films of van der Waals materials with weak forces between the layers. It is a so-called *top-down* approach, where the 3D crystal is the starting point, which is thinned down to obtain atomically thin samples. On the other hand,

in *bottom-up* approaches the sample is grown from thin to thick, from monolayer to a specific number of layers if the growth is well controlled. In these growth methods, the substrate is crucial, as there is usually a strong interaction with the film. The optimal situation is when substrate and film have matching lattice parameters, or as little lattice mismatch as possible. Therefore, this growth mode is also called *epitaxy*. One of the main bottom-up growth techniques is molecular beam epitaxy (MBE), where effusion cells of specific atomic elements are heated, resulting in a beam of these elements directed at the substrate. MBE can be performed at a sufficiently slow rate, so that the thickness of the film can be controlled. Ultra-high vacuum growth conditions are needed for MBE. Another important method is chemical vapor deposition (CVD) which uses precursor gases to carry elements onto the substrate, where the desired compound forms due to chemical reactions. This method can be performed in all ranges of pressure conditions, from atmospheric pressure to high-vacuum. CVD is readily used nowadays to grow graphene and 2D transition metal dichalcogenides (TMDs).

Crucial in these advances of the growth methods of 2D systems are also *in situ monitoring* methods. The first category consists of electron diffraction methods. In *low-energy electron diffraction* (LEED) electrons with energy 20-200 eV are bombarded on the sample, where the diffracted electrons give information on the surface structure. Another set-up is *reflection high-energy electron diffraction* (RHEED), where the electrons reflect from the sample under a small angle. RHEED is particularly suited to monitor the growth of films by MBE. The intensity of the RHEED signal namely fluctuates with the number of layers of the film, that peaks each time a layer is completed. To characterize the samples after growth, many scanning techniques are available to date that provide local information, often with atomic resolution. A first way to perform such measurement uses electrons, and is therefore called *scanning transmission electron microscopy* (STEM), where – contrary to conventional transmission electron microscopy – the electron beam is focussed in a small spot. This is often combined in the same experimental set-up with spectroscopic techniques such as *energy dispersive X-ray* (EDX) and *electron energy loss spectroscopy* (EELS), that can be used to find out the local chemical composition of the sample, as well as the energy levels of the atoms. Another commonly used technique is based on quantum mechanical tunneling between a conducting tip and the sample, when a bias

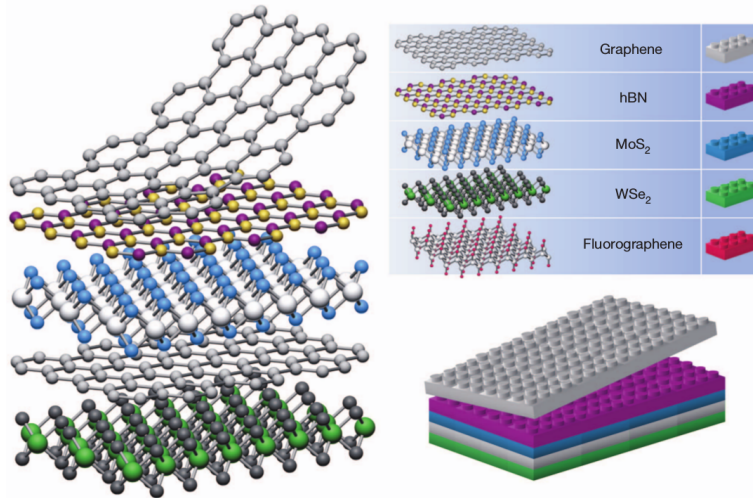


FIGURE 1.14: *Van der Waals stacking of different monolayer materials, from different 2D materials groups, from the graphene family (graphene, fluorographene, hexagonal BN) and from the chalcogenides (MoS₂, WSe₂). The analogy is made here with assembling lego blocks [97].*

voltage is applied. The resulting tunneling current gives information on the local density of states, and from this the structure of the sample can also be determined.

Currently, even heterostructures composed of monolayer materials, and held together by weak van der Waals interactions, are feasible [97]. This enables combining the properties of the different monolayer materials. An example is depicted in Fig. 1.14, where materials of the graphene family are combined with chalcogenide monolayers. The most recent advance is that in addition to these vertical heterostructures also lateral can be made, as realized, e.g., with the dichalcogenides MoS₂ and WS₂, by making use of different carrier gases in CVD in subsequent stages of the growth [98]. Moreover, atoms can be added to 2D materials, such as the above mentioned F in fluorographene. With advanced growth methods these adatoms can be locally controlled, so that 2D materials can be decorated to change the functional properties in different parts of the sample.

Superconductivity in two dimensions. This topic has emerged in recent years, following the advances in synthesis of atomically thin 2D materials, and has received considerable interest, with several review papers published already [99–101]. The now well-established fact that superconductivity can be realized in purely 2D systems is certainly not *a priori* evident. As we discussed above, the transition to the superconducting state is a phase transition accompanied by spontaneous symmetry breaking of a continuous symmetry. For such a transition, Mermin and Wagner formulated the following theorem in 1966 [102]¹⁰:

Continuous symmetries cannot be spontaneously broken at nonzero temperature in systems with sufficiently short-range interactions in dimensions equal to or smaller than two.

This implies that any attempt to introduce order in a low-dimensional system will suffer from long-range spatial and temporal fluctuations of the order parameter. If these are too strong, they can completely counteract the ordered state. This fundamental difference between normal 3D and low-dimensional systems is reflected in the different behavior of the correlation of the order parameter $\psi = \sqrt{n_s}e^{i\theta}$. In 3D, the correlation $\langle e^{i(\theta(\mathbf{r})-\theta(0))} \rangle$ of a condensed phase takes the form $e^{-c_1 T}$ (where c_1 is a constant), whereas in 2D it obeys the power law $c_2 \left(\frac{r}{L}\right)^{-\eta}$, where L is the system size and η is called the *critical exponent* [102]. This means that in the long-range limit, $r \rightarrow \infty$, 3D order has a constant, nonzero correlation, whereas 2D inevitably vanishes. This provides the mathematical formulation of the Mermin-Wagner theorem.

In ground breaking works (awarded with the 2016 Nobel prize in Physics) Berezinskii (1972) [103] and Kosterlitz and Thouless (1973) [104] have demonstrated that quasi-long range correlations that do not break any symmetry can occur in 2D systems. The eponymous name of these new and unexpected phase transitions is *Berezinskii-Kosterlitz-Thouless* (BKT) transitions. The most simple case of a BKT transition appears in the XY model, a 2D model of a spin lattice, characterized by Hamiltonian $H_{XY} = \frac{J}{2} \int d^2r (\nabla\theta(\mathbf{r}))^2$. So, the energy needed to create a vortex, with $\nabla\theta(\mathbf{r}) = 1/r$, amounts to $E_v = \frac{J}{2} \int_a^L d^2r r^{-2} = \pi J \ln\left(\frac{L}{a}\right)$, a being the size of the vortex core. On the other hand, the energy of a vortex-antivortex pair separated by distance r is

¹⁰It is interesting to note that the original work of Mermin and Wagner concerned (anti)ferromagnetic order in 1D and 2D within a Heisenberg model.

$E_{v-av} = 2\pi J \ln\left(\frac{r}{a}\right)$. Therefore, as $r \gg a$, such pairs are expected to be energetically preferred. To refine this argument, there is entropy (S) to be considered, as included in the free energy $F = E - TS$. The Boltzmann entropy of a vortex follows from the L^2/a^2 possible positions of the vortex (assuming for simplicity the sample and the vortex to both be square), so $S = 2k_B \ln\left(\frac{L}{a}\right)$. Therefore, we find that the free energy, $F = \pi J \ln\left(\frac{L}{a}\right) - 2Tk_B \ln\left(\frac{L}{a}\right)$ changes sign at $T_{\text{BKT}} = \pi J / (2k_B)$. So, for $T < T_{\text{BKT}}$, in 2D systems there are thermally excited, bound vortex-antivortex pairs related to quasi-long-range order (with critical exponent $\eta = T / (4T_{\text{BKT}})$), while for $T > T_{\text{BKT}}$ the excitations are unpaired (anti)vortices. This is the physical origin of the BKT transition that has been observed in several 2D superconducting systems [105, 106].

Nevertheless, many other 2D superconductors display superconductivity without a BKT mechanism. The reason is that long-range order at $r \rightarrow \infty$ is rather restrictive. If Cooper pair condensation with *sufficiently developed* correlation takes place, the system is effectively superconducting [100]. In other realizations of superconductivity in atomically thin materials, such as Pb and In monolayers on Si(111) substrates, the Mermin-Wagner theorem is circumvented by the $(2 + \delta)$ D nature of the system, since there is significant interaction with the substrate, characterized by the fractional dimensionality δ . However, as mentioned above, the superconducting state often remains fragile in the 2D limit. This shows, for instance, in the reaction to disorder. In a 3D material superconductivity is robust against disorder [107] (unless there are magnetic impurities), but in 2D disorder can induce a superconductor-insulator transition [100]. This effect was already seen in some of the first 2D superconductors. These were not atomically thin, but the main criterion for 2D superconductivity is that the thickness of the film $d \ll \xi$, in which case the pair wave function $\Psi(x, y)$ is uniform in the out-of-plane direction [4]. An interesting example is the material bismuth (Bi), which is not superconducting in bulk form at ambient pressure, but becomes superconducting in an amorphous 2D form, with T_c above 5 K [108]. However, thin samples become superconducting, due to increasing disorder inherent to the thin limit leading to pair-breaking scattering. This provides an example of a disorder-induced superconductor-insulator transition.

Material	Thickness	T_c (K)	Bulk T_c (K)	Reference
Pb/Si(111)	1 ML	1.5 – 1.8	7.2	[60]
In/Si(111)	1 ML	3.2	3.4	[60]
Ga/GaN	2 ML	5.4	1.1	[109]
LaAlO ₃ /SrTiO ₃	4 UC	0.2	0.3	[110]
La _{2-x} Sr _x CuO ₄ /LaCuO ₄	1 UC	40	40	[111]
Graphene/Re	1 ML	2.1	Re: 1.7	[112]
LiC ₆	1 ML	5.9	0.9	[113–115]
C ₆ CaC ₆	2 ML	3	11.5	[116]
Twisted BLG	2 ML	1.7	/	[117]
NbSe ₂	1 ML	3.1	7.2	[118, 119]
TaS ₂	1 ML	3.4	0.9	[120, 121]
MoS ₂	1 ML	10.8	7	[122, 123]
Mo ₂ C	~10 UC	2.6	3	[124]
FeSe/SrTiO ₃	1 ML	50 – 100	8	[54, 55]

TABLE 1.2: *Resume of the main atomically thin superconductors (non-exhaustive), their T_c , and a comparison with their bulk T_c . The thickness is expressed in monolayers (ML) and unit cells (UC). BLG denotes bilayer graphene.*

So, in summary, superconductivity in 2D is definitely possible, as recent experimental and theoretical advances have demonstrated, but there is always the challenge of optimally stabilizing the superconducting state, since it is vulnerable. We will now proceed to review the main atomically thin 2D superconductors that have been realized in the last decade. Table 1.2 gives an overview of the main 2D superconducting systems that have been discovered so far, and accompanies the discussion.

Atomically thin elemental metal films. Superconductivity in thin lead (Pb) films has been a long-standing endeavor, and has steadily converged to the monolayer limit. In 2006, superconductivity was realized in 7-monolayer thick crystalline films of Pb on Si(111) [126]. This limit was subsequently reduced to just 2 monolayers [127], followed by the experimental proof of superconductivity in just one-atom thick Pb and In [60, 125]. The advantage of this system is that Pb/In and Si do not alloy, so that the interface is atomically sharp. The structure of the films, grown epitaxially on the Si substrate, depends on the termination of the latter – which in

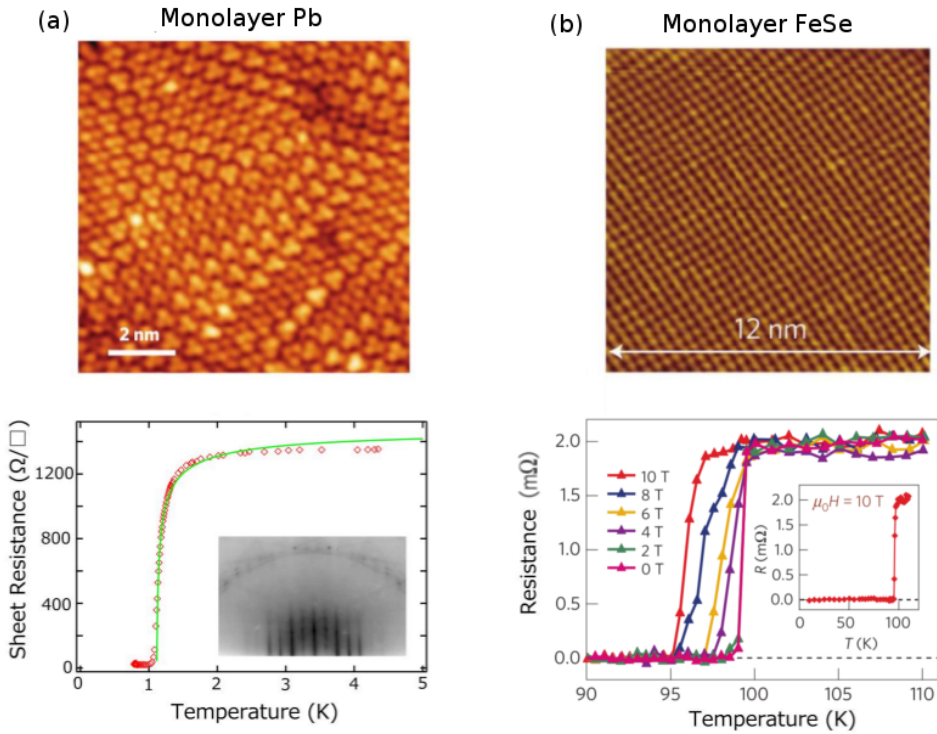


FIGURE 1.15: *Experimental realizations of superconductivity in monolayer materials.* (a) Atomic-resolution scanning tunneling microscopy (STM) image of monolayer lead in the striped incommensurate (SIC) phase on a Si(111) substrate [60], and the resistance of this system as a function of temperature, showing $T_c \simeq 1$ K [125]. (b) Atomic-resolution STM image of monolayer FeSe on a SrTiO₃ (STO) substrate, and resistance as a function of temperature and applied magnetic field, showing $T_c \simeq 100$ K in zero applied field [55].

turn varies according to the synthesis method. An unreconstructed bulk-terminated Si substrate has been shown to lead to a *striped incommensurate* (SIC) structure of the Pb monolayer, with 3 Si atoms per atomic layer and 4 Pb atoms in the unit cell [60, 125]. An atomic-resolution scanning tunneling microscopy (STM) image of monolayer Pb in this structure is shown in Fig. 1.15(a), along with a measurement of the resistance as a function of temperature, showing the emergence of the superconducting state around 1 K [125]. Here, first-principles calculations have revealed that the Si substrate plays an essential role in the superconducting properties, mainly through

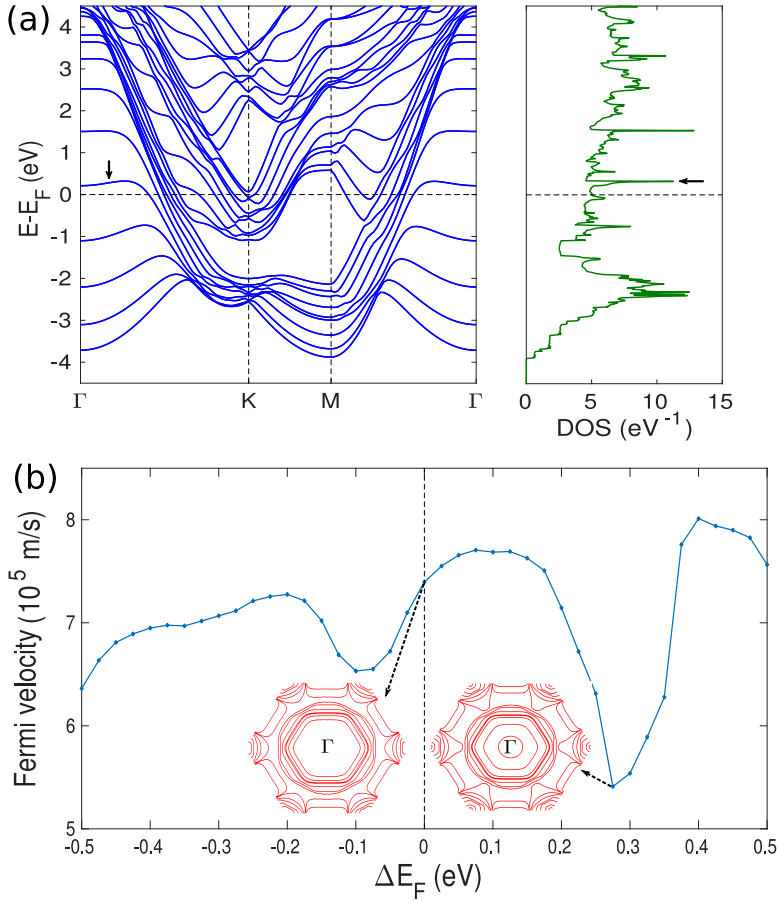


FIGURE 1.16: *Quantum well states (QWS) in 9-ML Pb (hcp structure), calculated from first-principles (own calculation). (a) The band structure and the DOS. The QWS closest to the Fermi level has been indicated with an arrow. (b) The average Fermi velocity as a function of the Fermi level (e.g. changed by electrostatic gating). The Fermi surface at the intrinsic Fermi level and the one resulting from the QWS are shown as insets.*

interface electronic bonds between substrate and film, but also through interface vibrational modes [128]. As a result, this system is not completely 2D, which helps to suppress the BKT transition, and thus fluctuations.

In these atomically thin metal films the quantum confinement in the perpendicular direction plays a crucial role. Owing to the resulting out-of-plane quantum well states (QWS), the density of states (DOS) oscillates, and this has a marked effect on the critical temperature of superconductivity in the

system. As $T_c \propto e^{-1/(N_F \tilde{V})}$, it also oscillates as a function of film thickness – also known as *shape resonances* – as witnessed both in theory [129] and in experiments on thin Pb films [130]. As an example of the strong influence of QWS, the electronic structure of 9-ML thick hcp Pb is shown in Fig. 1.16(a). There is a QWS at ~ 300 meV above the Fermi level, with little dispersion around Γ , and a resulting sharp peak in the DOS. In Fig. 1.16(b) I demonstrate how the average Fermi velocity (v_F), calculated from the band structure, changes with the Fermi level – which can be altered electrostatically. When the QWS is hit, this leads to a strong modification of the Fermi surface, and a significant lowering of v_F , with a considerable effect on the length scales $\xi \propto v_F$ and $\lambda_L \propto 1/v_F$.

Follow-up experiments have investigated different aspects of superconductivity in thin films, mainly the influence of nanostructuring. Several experiments on In [131, 132] and Pb [133, 134] have explored the effect of atomic step edges. It was found that these steps act as Josephson junctions where superconductivity is locally suppressed [131], and that they induce remarkable variations in the superconducting wave function on a scale significantly shorter than the coherence length [133]. Furthermore, nanoislands of Pb (12 – 14 MLs thick) have been found with STM measurements to be coupled – due to proximity effects – resulting in a weak link for superconductivity [135]. So, they form superconductor-normal-superconductor (SNS) *Josephson junctions*, wherein Josephson vortices were observed – where in the core the proximity-induced gap is suppressed. A third road to alter the properties of the elemental metal films is combining them with other chemical elements. In a monolayer compound of Pb and thallium (Tl), the spin-orbit coupling is increased, resulting in a Rashba-type split between the bands [136]. Recently, a monolayer of Pb was grown on islands of the magnetic element cobalt (Co) deposited on a Si substrate [137]. Due to the interplay with the magnetism, 2D topological superconductivity was observed, with an edge state in the gap. Moreover, it was predicted that there can be Majorana bound states in the vortex cores of this system.

Cuprate superconducting films. A single unit cell of the cuprate superconductor $\text{La}_{2-x}\text{Sr}_x\text{CuO}_4$ has been electrically tuned (by gating) to superconduct [111]. Different samples were made with different doping levels.

Some samples were already superconducting with low T_c in zero electric field, while other, underdoped samples were insulating. Both types of samples could reach $T_c \sim 40$ K with optimal gating. Notably, the transition from an insulating (“off”) to a superconducting (“on”) state by an applied electric field forms the basis for an atomically thin *superconducting field effect transistor* (FET). Interestingly, in this system a critical point was found with a resistance of exactly $R = h/Q^2$ with $Q = 2e$, which is the pair resistance quantum, suggestive of a quantum phase transition.

2D electron gas at insulator interfaces. The 2D electron gas at the interface between 2D perovskite oxide insulators, LaAlO_3 and SrTiO_3 , displays superconductivity [110] up to $T_c = 200$ mK, as well as ferromagnetism [138]. Direct imaging has indicated a nanoscale phase separation between both phases [139]. A similar result was obtained at the interface of the Mott insulator (i.e., insulating due to strong electronic correlation) LaTiO_3 and SrTiO_3 ($T_c = 300$ mK) [140].

Atomic sheets. Truly 2D superconductivity has been achieved in atomic sheets. This was first realized in graphite intercalation compounds (GICs), where the intercalants are alkali, alkaline earth metals or lanthanide elements. For instance, superconductivity has been established in Ca-intercalated graphite (CaC_6), with $T_c = 11.5$ K [83, 141], and in YbC_6 [141], with $T_c = 6.5$ K. The mechanism here is that the intercalants donate electrons to the unoccupied π^* band of graphite, resulting in Fermi level shifts and changes in the electron-phonon interaction [100]. In addition, an *interlayer state* emerges at the interface between the carbon planes and the intercalant planes.

From intercalated graphite on, the thickness of the material has systematically been reduced. Thin laminates (multilayer structures) of Ca-doped graphene were found to be superconducting [142], which was ultimately reduced to only bilayer graphene with Ca intercalation (C_6CaC_6) [116], albeit with a depleted T_c (3 K) with respect to the bulk value. Superconductivity in monolayer CaC_6 , on the other hand, has not been realized, and the reason behind this was revealed in a first-principles study [113]. Namely, the crucial interlayer state is almost completely absent at the Fermi level in monolayer CaC_6 , while in the bulk it is there. This work yielded another

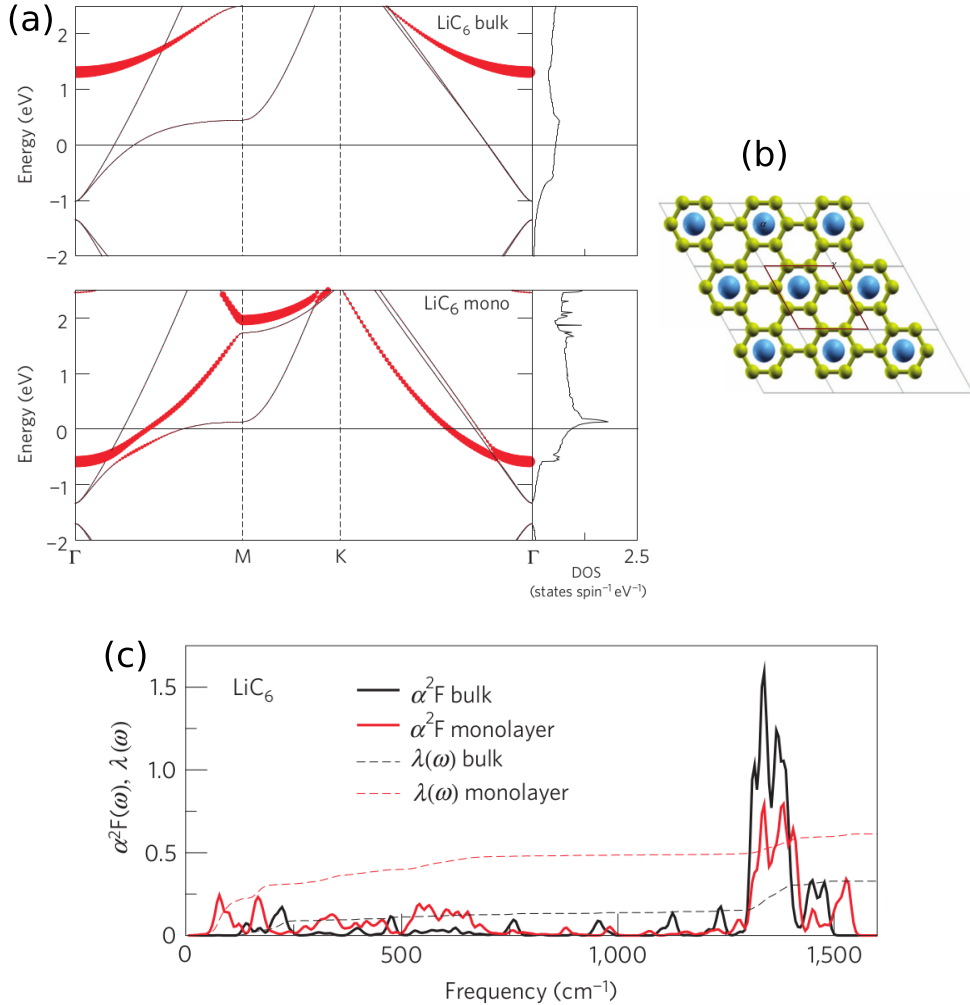


FIGURE 1.17: *First-principles theory of superconductivity in LiC_6 [113]. (a) Band structure of (top) bulk and (bottom) monolayer LiC_6 . The interlayer state is indicated in red. (b) Top view of the crystal structure of monolayer LiC_6 , where yellow spheres represent C atoms and blue spheres Li atoms. (c) The calculated Eliashberg function and electron-phonon coupling as a function of frequency for bulk and monolayer LiC_6 .*

interesting prediction, namely that in Li-intercalated graphene exactly the opposite is true, as shown in Fig. 1.17(a). This interlayer state results from specific positions of the Li atoms in LiC_6 in one out of every three honeycomb facets, as shown in Fig. 1.17(b). The effect of the interlayer state on the electron-phonon (e - ph) coupling becomes apparent in Fig. 1.17(c), where the Eliashberg functions, the spectral function of the e - ph coupling (to be

explained properly in Chapter 3), of bulk and monolayer LiC_6 are compared. It is found that the e - ph coupling, obtained from the Eliashberg function using $\lambda = 2 \int_0^\infty d\omega \omega^{-1} \alpha^2 F(\omega)$, of the monolayer ($\lambda = 0.61$) exceeds that of the bulk ($\lambda = 0.33$) by far [113]. The resulting T_c of monolayer LiC_6 amounted to 8 K, which is in good agreement with the experimental value of 6 K, obtained when this system was experimentally realized [115]. Later, anisotropic Eliashberg calculations have confirmed this estimate of T_c [82], so it can be concluded that the isotropic approximation used in Ref. 113 works well in the case of LiC_6 owing to its fairly isotropic Fermi surface. This is certainly not always the case, as calculations of ultrathin MgB_2 , presented in this thesis, have revealed.

Another pathway to establish superconductivity in graphene is depositing it on a superconducting substrate, $\text{Re}(0001)$, so that superconductivity is induced by a proximity effect [112]. Other atomic sheets that are superconducting in the monolayer limit are transition metal dichalcogenides (TMDs), such as NbSe_2 [118, 119], TaS_2 [120, 121] and (gated) MoS_2 [122, 123]. These materials exhibit very interesting and diverse quantum states. In addition to superconductivity they host spin textures due to the spin-orbit interaction, and charge density waves because of instabilities in the lattice at lower temperatures. We will expand on this in Chapter 8. A related material group are the MXenes, i.e., transition metal carbides and nitrides, like Mo_2C , where superconductivity is also approaching the atomically thin limit [124]. In bulk alkali-intercalated black phosphorus superconductivity has also been realized [143], therefore this system also holds promise for superconductivity in the thinnest limit. In the related compound alkali-intercalated blue phosphorous superconductivity above 20 K has been predicted using first-principles calculations [144].

The most recent, very unexpected discovery is that of superconductivity in bilayer graphene (BLG) twisted at a ‘magic’ angle, where the Fermi velocities vanish (the first one being 1.1°) [117]. Using transport measurements the corresponding electronic state was found to be a strongly correlated Mott insulating state. Upon electrostatic doping a superconducting state emerged below the T_c of 1.7 K. Such superconducting state adjacent to a Mott state is reminiscent of the unconventional cuprate superconductors. The T_c is remarkably high in view of the very low carrier density (10^{11} cm^{-2}), as

obtained from quantum oscillation measurements. Thus, it was concluded that the superconductivity in magic angle twisted bilayer graphene is unconventional and strongly coupled, lying in a regime close to the crossover between Bardeen-Cooper-Schrieffer pairing and Bose-Einstein condensation (BCS-BEC crossover).

Monolayer FeSe on a SrTiO₃ substrate. Very unexpectedly, superconductivity in monolayer FeSe on a SrTiO₃ (STO) substrate was found to be dramatically different compared with bulk FeSe [54, 55], as shown in Fig. 1.15(b). Not only does the monolayer have a much higher $T_c = 50 - 100$ K than the bulk $T_c = 8$ K under ambient conditions (boosted to 37 K under high pressure [145]), it also displays s-wave symmetry [146], as opposed to (probably) s_{\pm} -wave pairing symmetry in the bulk. These changes are accompanied with a drastic modification of the electronic structure. While bulk FeSe is a multiband superconductor with two or three hole pockets around Γ and two electron pockets around M (cf. Appendix B), in the monolayer only the electron pockets are left. So, the primary effect of the STO substrate is a change of the Fermi level due to electron doping, likely related to O vacancies – eliminating the hole bands. The importance of this effect is apparent in a different set-up where the electrons are provided by K doping on the surface of a 3-ML thick FeSe film, that acquired $T_c \sim 50$ K [147]. This indicates the importance of the doping effect, however, the T_c of the monolayer remains much higher. So, the general consensus now is that the change in Fermi level allows for $T_c \sim 50$ K, but that additional interface effects between substrate and film (which are strongest in case of a monolayer) boost it further to above 100 K. This extra effect is thought to stem from interface electron-phonon coupling, which a recent theoretical description has successfully linked to a high T_c , albeit with some simplifications, like a single dispersionless phonon mode and a lack of electron-electron interactions [148]. All by all this surprising system requires more experimental and theoretical investigations to be fully unraveled.

Superconducting strength as a function of thickness. As follows from the preceding discussions, the evolution of the superconducting properties with film thickness is central in this research field. Looking at Table 1.2 one observes that in almost all categories there exist materials for which

the T_c of a monolayer sample exceeds that of its bulk counterpart. The cases of CaC_6 and LiC_6 are extremely interesting, since the former is by far the stronger superconductor in bulk form, but completely the opposite is true for the monolayer form. This indicates clearly that the microscopic properties of the materials are extremely important for the superconducting behavior. This is the motivation for the thesis. In Chapter 5 we will study how the superconducting properties of MgB_2 change when adding layer by layer.

1.3 Applications

The unique properties of superconductors, namely dissipation-free electric conduction, extremely high current densities, high sensitiveness to and shielding from magnetic fields, rapid transfer of quantized flux (e.g., vortices), etc., allow for a very diverse range of applications. These can roughly be divided in two categories, namely the small and the large scale applications [29]¹¹. In the former there are electronic devices and sensors, while the latter consists of magnets and electric power and transport applications. In the following we will keep a focus on the category of small-scale applications since they are most closely related to this thesis.

1.3.1 Large-scale applications

This category of applications profits from the high current densities that superconductors can sustain. Since electric currents below the critical current are carried by a superconductor without resistance, *superconducting wires* are ideal for eliminating losses during electric transport. Currently, there are several electricity networks where this is put into practice. The first to be realized was the Holbrook Superconductor Project in the US, where superconducting power lines carry currents over a distance of 600 m. The material used there is the high- T_c cuprate superconductor $\text{Bi}_2\text{Sr}_2\text{CaCu}_2\text{O}_{8+x}$ (BSCCO), so that the cryostat surrounding the cables can rely on liquid nitrogen cooling. This is fairly inexpensive, so that the gain in efficiency

¹¹Another excellent reference is provided by the Coalition for the Commercial Application of Superconductors (CCAS) on http://www.ccas-web.org/pdf/CCAS_Brochure.pdf. For the large-scale applications this is the main reference used here.

outweighs the cooling cost. A similar project was realized in Germany, called the AmpaCity project, over a distance of 1 km between two power substations in the city of Essen.

The very high attainable current densities also allow to make much stronger electromagnets. These are now readily employed in several ways. The most widespread application is a medical one, Magnetic Resonance Imaging (MRI), where very strong magnetic fields (1.5 – 3 T) are needed to induce a significant resonant response from the nuclear spins. For the same reason superconductor-based magnets are used in Nuclear Magnetic Resonance (NMR) spectroscopy, a widespread method to probe the composition and the electronic structure of materials. Another application of these extremely strong magnets for scientific research is as accelerator magnets in high-energy physics, e.g., in the Large Hadron Collider in CERN. In transportation, superconducting magnets are already in use in superconducting magnetically levitated trains (SCMaglev), of which test lines have been built by the Central Japan Railway Company. In Brazil, superconductor-based magnets are in use in the MagLev Cobra system providing smaller vehicles for transportation in urban areas [149]. Among other future applications of superconductors in transportation magnetically assisted propulsion of spacecrafts has also been proposed. Finally, superconductor-based magnets will very likely play an important role in many future energy innovations. Nuclear fusion requires very strong magnetic fields to confine and to shape the hot plasmas in the reactor. Test projects like the International Thermonuclear Experimental Reactor (ITER) employ superconductor-based electromagnets for this purpose. Other possible applications in the domain of energy include rotors for wind turbines (that can be made much lighter than conventional electromagnets), high-voltage transformers cooled with liquid nitrogen (instead of the currently used, flammable oil-cooling), and flywheels with frictionless superconductor-based bearing for energy storage.

1.3.2 Small-scale applications

We will distinguish two major categories of small-scale applications, namely (i) in sensing and (ii) in communication and computation.

1.3.2.1 Sensors

The main sensing abilities superconductors rely on *Josephson junctions*, where a weak link between two superconductors – S – with a phase difference $\Delta\phi$ (e.g., a thin insulating barrier – I, a normal metal – N, or a constriction weakening the superconductivity – s) enables a constant supercurrent $I_s = I_c \sin(\Delta\phi)$ in the absence of any applied bias voltage or magnetic field (*DC Josephson effect*), and an alternating supercurrent $I_s = I_c \sin(\Delta\phi + QVt/\hbar)$ under applied bias voltage V (*AC Josephson effect*) [29]. The Josephson frequency resulting from the AC Josephson effect, $\omega_J = QV/\hbar$, thus allows for a highly accurate conversion between frequency and voltage, resulting in the *Josephson voltage standard* in metrology.

A particularly interesting type of Josephson junction in view of applications is a *SIS junction*, also called a *superconducting tunnel junction*. Here, the supercurrent passes the insulating layer through quantum tunneling of Cooper pairs. This type of tunneling is completely without dissipation, so there is no voltage drop over the junction. If a bias voltage $|V| > 2\Delta/e$ is applied, there is a current of quasiparticles (electrons from broken Cooper pairs) with an Ohmic, linear $I - V$ relation. This principle can be applied for *single-photon detection*. To this end a bias voltage $V < 2\Delta/e$ is applied to the junction. Photon absorption creates broken Cooper pairs, and the tunneling current due to the resulting quasiparticles is proportional to the energy of the incident photon. Thus, single-photon detection can replace CCDs in spectroscopic and astronomical instruments. Another route for single-photon detection is based on superconducting nanowires. Incident photons locally break Cooper pairs, creating a region with nonzero resistance in a part of the wire, which produces a voltage pulse and enables fast photon counting.

When two Josephson junctions are put in a parallel circuit they form a *Superconducting Quantum Interference Device* (SQUID). In an applied magnetic field with flux Φ through the circuit, the critical current in the SQUID resulting from Aharonov-Bohm-like quantum interference is $I_c = 2i_c |\cos(\pi\Phi/\Phi_0)|$, where i_c is the critical current of the individual Josephson junctions. Thus, SQUIDs provide the most accurate measurement tool for even the slightest magnetic fields. There are many important medical applications for SQUIDs.

First of all, helmets containing arrays of SQUIDS can scan the magnetic response of the brain with a method called *magnetoencephalography* (MEG). MEG provides information on the functioning of the brain and on possible diseases. Analogously, magnetocardiography (MCG) can probe electromagnetic signals from the nerves controlling the heart.

1.3.2.2 Communication and computing

Superconductors are also ideally suited for applications in communication technology, since they can handle AC signals with ultra-low dissipation and distortion, and since they possess intrinsic quantum efficiency. Superconductor-based tools for communication that are already put to practice are filters installed in cellular base stations reducing the interference of radiofrequency signals. This is an analog application, however, in future an increasing number of digital applications are expected.

The power consumption of modern large-scale supercomputers, based almost fully on semiconductors, poses an ever increasing power consumption problem [150]. Losses here are twofold, namely energy is dissipated in the form of heat, and this heat needs to be removed to prevent damage. Maintenance costs haven now risen to a level exceeding the expected cost of cryogenic cooling of superconducting devices. Downsizing electronic devices brings along additional challenges, such as gate leakage and reduced mobilities due to quantum confinement [151]. Slowly but steadily the limit of making smaller, higher performance integrated circuits is coming in sight, so that innovative technologies are called for. Zero resistance, thus zero dissipation make superconductors an ideal candidate for faster and extremely low-power electronic devices. The ultimate goal of the efforts to produce microelectronic devices based on superconductors is the development of more powerful, less consuming supercomputers. Therefore, very concrete actions are currently being undertaken for the development of superconductor-based computing, for instance by the US agency ‘Intelligence Advanced Research Projects Activity’ (IARPA).

In its Cryogenic Computing Complexity program¹² IARPA has provided conceptual estimates for a large-scale computer based on superconductors. In

¹²See <http://www.iarpa.gov/index.php/research-programs/c3/baa>.

2012 the most powerful supercomputer worldwide was Titan at the Oak Ridge National Laboratory, with a computing capacity of ~ 20 PFLOPS and a power consumption of ~ 8 MW¹³. IARPA predicts that a superconductor-based supercomputer with the same computational power would only consume 1% of Titan's power consumption, including the cooling needed for the superconducting state¹⁴. This can help to advance the development of *exaflop* supercomputing and beyond that would consume several hundreds of MWs if based on conventional semiconductor technology. The impact on society of more powerful and efficient supercomputers cannot be overestimated. It can enable simulations of outstanding complexity, ever gaining accuracy, reliability and the possibility to make long-term predictions. Applications range from high-throughput studies (e.g., in materials science), over real-scale neurological simulations, to meteorological and geological simulations.

Very promising systems for both communication and computing applications are the *Rapid Single Flux Quantum* (RSFQ) logic circuits. These are Josephson junctions in which a single flux quantum can be stored in the form of a vortex. RSFQ devices switch when current above the critical one is applied, causing them to output a single flux quantum voltage pulse. These devices have ultrafast operation speeds with switching times of the order of 1 ps, and dissipate extremely little energy ($\sim 10^{-19}$ J, which is thousands of times smaller than in a semiconductor-based device). Together they can be assembled into superconductor-based integrated circuits (IC).

Thus, RSFQ devices are ideally suited to construct superconducting transistors, but they also provide a way for superconducting *Random Access Memory* (RAM) or *cryogenic RAM*. In this type of RAM, individual Abrikosov vortices (AV), quantized amounts of flux in the superconductor, make up an information bit, which is why this emerging technology is also dubbed AVRAM [152, 154]. The size of the vortex cores is described by the superconducting coherence length which can be down to 10 nm. This means they can be very densely packed, so that a lot of information can be stored in a small space. Read and write operations are performed by injecting local current pulses, as shown in Fig. 1.18(a) [152, 155]. Components based on RSFQ effects can be combined with, e.g., the (ultrathin) superconducting

¹³For comparison, the whole of Belgium currently has an average power consumption of ~ 20 GW.

¹⁴See http://www.ccas-web.org/pdf/CCAS_Brochure.pdf.

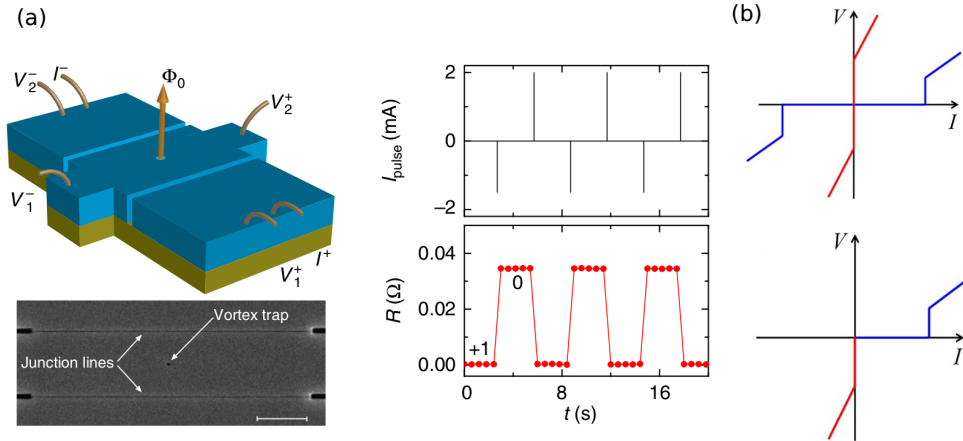


FIGURE 1.18: (a) Realization of an AVRAM device [152]. On the left a scheme of the AVRAM, consisting of a vortex trap in between two Josephson junctions is shown, as well as a SEM image. On the right current pulses applied to the device are shown, which induce write and erase operations. (b) I-V characteristics of an insulator (top, red), a superconductor (top, blue) and a superconducting diode (bottom) that can be made with a junction of a 2DEG and a metallic nanofilm [153].

Field Effect Transistors (FET) [111] described in Sec. 1.2.2 to establish a diverse set of functionalities.

A promising route to tailor and to enhance superconducting devices entails *hybrid systems*. A famous, long-standing example are *superconductor-ferromagnet* (S/F) systems, where the demagnetization fields of both components influence each other [156]. In recent years, other hybrid systems have been built. By bringing the 2D electron gas (2DEG) in AlGaAs/GaAs in proximity to an Al nanofilm, both components are in electronic contact [153]. When a positive voltage is applied to the Al film, the potential of the film lies above that of the 2DEG, resulting in electrical screening that reduces disorder in the latter. Therefore, when $V > 0$, superconductivity is enhanced, while the opposite is true for $V < 0$, whereby the 2DEG turns insulating. This causes the I-V characteristic of this system to lose its usual antisymmetry, as depicted in Fig. 1.18(b). For $V < 0$ the behavior is insulating, whereas for $V > 0$ it is superconducting, so the system functions as a *prototype superconducting diode* [153]. Finally, hybrid structures of superconductors and quantum dots have also been built, enabling a combination

of large numbers of condensed electrons in the former with control of single electrons in the latter [157]. Interesting behavior is observed as a function of coupling strength between a superconducting source and drain and a quantum dot gate. In case of strong coupling, Cooper pairs tunnel from source to drain via the quantum dot, whereas for weak coupling single electron tunneling is the preferred channel. The intermediate regime is arguably the most interesting one, since there is a strong competition between the coupling of the superconductors and the electron trapping of the quantum dot. This can give an extra phase to the tunneling wave function able to reverse the supercurrent across this device [157].

Superconducting devices provide moreover a route to *quantum computing*, where the superposition nature of quantum states enables operations beyond the binary level [158]. The elementary component of such a system, the *superconducting Qubit*, can be constructed in several ways. There are three archetypical systems, based on phase, flux and charge degrees of freedom [158]. A phase Qubit makes use of the phase difference between condensates in a Josephson junction, while SQUIDs form the base for a flux Qubit, operating with magnetic flux quanta. Finally, charge Qubits make use of the number of Cooper pairs within superconducting islands. These three Qubit prototypes can be combined into hybrid systems, to establish improved performances.

1.3.2.3 The prospect of atomically thin superconducting devices

It should be noted that the majority of the devices discussed above make use of superconductors with bulk-like thicknesses or at least films with $d > \xi$, so that they are not in the 2D regime. A highly notable exception is the FET based on a single UC of $\text{La}_{2-x}\text{Sr}_x\text{CuO}_4$ [111]. Nevertheless, ultra-thin superconductors are very promising for application in superconducting devices. Atomically thin films can be patterned by electron-beam lithography to create nanoscale circuitry. The resulting devices will be very compact, due to their 2D character, and ultralight-weight. As such, the size of superconductor-based supercomputers can be much reduced. Other applications where weight matters a lot – e.g., for the inclusion as sensors in satellite and other applications in outer space – can profit from the ultra-low weight of

the films, which together with ultra-low power consumption yields unrivalled properties.

1.4 Motivation and organization of the thesis

The introduction has shown that superconductivity research has seen many surprises in the last ten to twenty years. First, multigap superconductivity was discovered in bulk MgB_2 , leading to revived interest in various multi-component superconducting systems, where the condensate wave function has an increased number of degrees of freedom, which can be multiple bands, spins, competing interactions, topological effects, etc. Moreover, superconductivity down to the monolayer limit has been realized in diverse systems, holding promise for ultra-efficient small-scale applications. With all the successes that have been realized, still many pieces of the puzzle have remained missing. The main reason for this is the lack of atomic-scale descriptions of multicomponent superconductivity.

To accommodate this, the present thesis is devoted to constructing a coherent *ab initio* description of multicomponent superconductivity, originating from various different mechanisms. The overawing advantage of such *ab initio* (or equivalently, first-principles) description, that starts from the basic quantum many-body problem, is that no tunable parameters, phenomenological models, or other assumptions are employed. Thus, *ab initio* calculations of the electronic and vibrational states, and their mutual coupling, provide insight in how the superconducting pairing emerges, and how it is influenced by quantum confinement, by strain, etc. The *ab initio* description of the normal state properties of multicomponent superconductors is combined in this thesis with accurate calculations of the superconducting pairing based on statistical field theory, using the *ab initio* results as input. This provides unprecedented access to novel phenomena in multicomponent superconductors. The central question of this thesis can thus be summarized as:

How does multicomponent superconductivity originate and evolve under the influence of atom-scale interactions, and how does this change in the atomically thin limit?

To address this central question, the thesis is organized as follows.

In Chapter 2 the foundations of *ab initio electronic structure theory* are elaborated. Starting from the many-body problem various approximations are elucidated. A strong emphasis lies on *density functional theory*, starting from the underpinning Hohenberg-Kohn theorems, towards practical calculations.

In Chapter 3 the *ab initio* framework is extended to the calculation of phonons, electron-phonon interaction and superconducting pairing. First, it is explained how phonons are treated as perturbations in the *density functional perturbation theory*, starting from the underpinning theory, towards practical calculations. In the second part of this chapter the statistical field theory for superconducting pairing, *Migdal-Eliashberg theory*, is presented.

In Chapter 4 *multiband superconductivity* in the bulk boride superconductor osmium diboride (OsB_2) is investigated. To this end, we combine *ab initio* calculations, quantum oscillations and anisotropic Eliashberg theory. The main question addressed here is: **Why is superconducting OsB_2 fundamentally different from MgB_2 , and what causes its anomalous superconducting behavior under the influence of temperature and applied field?**

In Chapter 5 superconductivity under the influence of coexisting *lattice vibrations* and *ferromagnetic spin fluctuations* is investigated. For this purpose a *new, advanced Eliashberg framework* is developed. It is applied to the recently discovered iron-based multiband boride superconductor, iron tetraboride (FeB_4). The main question that is answered is: **What is the resulting superconducting pairing when lattice vibrations and spin fluctuations both contribute?**

In Chapter 6 superconductivity in atomically thin MgB_2 is investigated by a combination of *ab initio* calculations and Eliashberg theory. The theoretical results are compared to angle-resolved photoemission measurements. The central question is: **How does multigap superconductivity behave in the monolayer limit, and how does this evolve with every added monolayer?**

In Chapter 7 nanoscale manipulations of atomically thin superconductors are considered. The influence of *strain* and of *adatoms* is investigated

in atomically thin MgB_2 . The main question asked is: **Can superconductivity in atomically thin materials be enhanced by nanoscale manipulations?**

In Chapter 8 superconductivity in conjunction with *novel quantum states*, resulting from structural and spin degrees of freedom, is studied. The material class where such quantum states – the *Ising state* and *charge density wave state* – occur are the *atomically thin transition metal dichalcogenides*. To this end, a fully *ab initio* description of these novel states is developed. The question that will be addressed is: **How does the interplay between superconductivity and novel quantum states behave in atomically thin materials?**

Finally, in Chapter 9 a summary of the thesis and an outlook are provided, followed by a Dutch translation in Chapter 10.

Chapter 2

Electronic structure theory

2.1 Introduction

In this chapter, we explain the foundations of *Density Functional Theory* (DFT), a quantum mechanical method for the solution of many-body problems. The charge density is the central variable in DFT, since the energy is expressed as a functional (function with a function as variable) of the density. DFT is a so-called *first-principles* or *ab initio* method, as it is based only on the fundamental laws and constants of quantum mechanics and not on empirical input. To start with, the general many-body problem will be introduced. Approximations to the many-problem, such as the *Born-Oppenheimer* and *Hartree-Fock approximations* will also be studied. Subsequently, the theoretical backbone of DFT, the *Hohenberg-Kohn theorems* and the *Kohn-Sham equations* will be reviewed. Several functionals will be introduced, among which the Perdew-Burke-Ernzerhof (PBE) functional mainly used in this work. In a further section practical methods for DFT are summed up. This includes the Bloch theorem, the basis set, the electronic wave vector k-point grid, pseudopotentials and PAW pseudopotentials. Finally, we briefly discuss the *ABINIT* package and the *Vienna Ab initio Software Package* (VASP), that have been employed in the research presented in this thesis.

References used throughout the whole chapter are Refs. 159–163, while alternative references are listed explicitly.

2.2 The many-body problem in solids

The quantum mechanical many-body problem in a solid is described by the time-independent Schrödinger equation,

$$\hat{H}\Psi(\mathbf{r}_1, \sigma_1, \mathbf{r}_2, \sigma_2, \dots, \mathbf{R}_1, \mathbf{R}_2, \dots) = E\Psi(\mathbf{r}_1, \sigma_1, \mathbf{r}_2, \sigma_2, \dots, \mathbf{R}_1, \mathbf{R}_2, \dots) \quad (2.1)$$

where Ψ is the many-body wave function, dependent on the positions and spin of the electrons, \mathbf{r}_i, σ_i and the positions of the nuclei, \mathbf{R}_i . In principle, the wave function also depends on the spins of the nuclei, but this will be neglected. The reason is that we can treat the nuclei in a solid as classical particles within the Born-Oppenheimer approximation (discussed in the next section). The Hamiltonian \hat{H} of the system of electrons and nuclei reads

$$\begin{aligned} \hat{H} = & - \sum_i \frac{\hbar^2}{2m_e} \nabla_i^2 - \sum_I \frac{\hbar^2}{2M_I} \nabla_I^2 - \frac{1}{4\pi\epsilon_0} \sum_{i,I} \frac{Z_I e^2}{|\mathbf{r}_i - \mathbf{R}_I|} \\ & + \frac{1}{2} \frac{1}{4\pi\epsilon_0} \sum_{i \neq j} \frac{e^2}{|\mathbf{r}_i - \mathbf{r}_j|} + \frac{1}{2} \frac{1}{4\pi\epsilon_0} \sum_{I \neq J} \frac{Z_I Z_J e^2}{|\mathbf{R}_I - \mathbf{R}_J|} \end{aligned} \quad (2.2)$$

where m_e and M_I are the masses of electrons and nuclei, Z_I are the atomic numbers of the nuclei and ϵ_0 is the vacuum permittivity. The five terms of the Hamiltonian can be denoted as

$$\hat{H} = \hat{T}_e + \hat{T}_n + \hat{V}_{\text{ext}} + \hat{V}_{\text{int}} + \hat{V}_n \quad (2.3)$$

In this Hamiltonian, \hat{T}_e and \hat{T}_n are the kinetic energy operators of the electrons and nuclei respectively. \hat{V}_{ext} , \hat{V}_{int} and \hat{V}_n represent the electron-nucleus, electron-electron and nucleus-nucleus Coulomb interactions. To simplify the notation, we proceed with atomic units, i.e., $\hbar = e = m_e = 4\pi\epsilon_0 = 1$.

2.2.1 Born-Oppenheimer approximation

The many-body problem cannot be solved in an analytically exact way for any system beyond the dihydrogen cation (H_2^+) and thus approximations have to be made. A first one is the *Born-Oppenheimer approximation* (BO), where the electrons are considered to move in the field of fixed nuclei. The justification of the BO approximation is the fact that the nuclei are much

heavier than the electrons, the ratio of their masses being ~ 1800 even for the lightest chemical element, H. Within the BO approximation, the operators \hat{T}_n and \hat{V}_n are reduced to classical energies T_n and V_n . The direct consequence of the BO approximation is the decomposition of the many-body wave function into an electronic wave function ψ and a nuclear wave function χ , namely

$$\begin{aligned} \Psi(\mathbf{r}_1, \sigma_1, \mathbf{r}_2, \sigma_2, \dots, \mathbf{R}_1, \mathbf{R}_2, \dots) &= \psi(\mathbf{r}_1, \sigma_1, \mathbf{r}_2, \sigma_2, \dots; \mathbf{R}_1, \mathbf{R}_2, \dots) \\ &\quad \times \chi(\mathbf{R}_1, \mathbf{R}_2, \dots) . \end{aligned} \quad (2.4)$$

The electronic wave function depends on the nuclear positions as parameters and not as variables, since the electrons rearrange immediately as the nuclear positions are altered. In relation to the Pauli exclusion principle for fermions, the electronic wave function is antisymmetric under the interchange of two electrons. Filling in wave function 2.4 into the Schrödinger equation 2.1, the following electronic eigenvalue equation is obtained,

$$\begin{aligned} \hat{H}_{\text{BO}}\psi(\mathbf{r}_1, \sigma_1, \mathbf{r}_2, \sigma_2, \dots; \mathbf{R}_1, \mathbf{R}_2, \dots) &= E_e(\mathbf{R}_1, \mathbf{R}_2, \dots) \cdot \psi(\mathbf{r}_1, \sigma_1, \mathbf{r}_2, \sigma_2, \dots \\ &\quad ; \mathbf{R}_1, \mathbf{R}_2, \dots) . \end{aligned} \quad (2.5)$$

The BO Hamiltonian contains only those terms of the general Hamiltonian 2.3 involving electrons:

$$\hat{H}_{\text{BO}} = \hat{T}_e + \hat{V}_{\text{ext}} + \hat{V}_{\text{int}} , \quad (2.6)$$

and the associated energy $E_e(\mathbf{R}_1, \mathbf{R}_2, \dots)$ thus only depends on the nuclear coordinates and not on the electronic coordinates. The total energy of the many-body system in the BO approximation is

$$E_{\text{tot}} = E_e + T_n + E_n , \quad (2.7)$$

where the last two terms represent the classical kinetic energy and the classical electrostatic energy of the nuclei. The BO approximation is implied in the rest of the chapter.

2.2.2 Hartree-Fock approximation

A second approximation that can be applied, is the *Hartree-Fock approximation* (HF). In the HF approximation the electronic wave function ψ , introduced in the BO approximation, is rewritten as an antisymmetric product of one-particle wave functions $\phi_i(\mathbf{r}_i, \sigma_i)$,

$$\psi(\mathbf{r}_1, \sigma_2, \mathbf{r}_2, \sigma_2, \dots) = \frac{1}{\sqrt{N!}} \sum_p^{N!} (-1)^p \hat{P} [\phi_1(\mathbf{r}_1, \sigma_1) \cdot \phi_2(\mathbf{r}_2, \sigma_2) \dots \times \phi_N(\mathbf{r}_N, \sigma_N)] , \quad (2.8)$$

where N is the number of electrons and \hat{P} is the permutation operator yielding $N!$ permutations. Each of these is characterized by a number of elementary permutations of two electrons, p . As such, the wave function can be rewritten as a determinant, the so-called *Slater determinant*:

$$\begin{aligned} \psi(\mathbf{r}_1, \sigma_2, \mathbf{r}_2, \sigma_2, \dots) &= \frac{1}{\sqrt{N!}} \begin{vmatrix} \phi_1(\mathbf{r}_1, \sigma_1) & \phi_2(\mathbf{r}_1, \sigma_1) & \dots & \phi_N(\mathbf{r}_1, \sigma_1) \\ \phi_1(\mathbf{r}_2, \sigma_2) & \phi_2(\mathbf{r}_2, \sigma_2) & \dots & \phi_N(\mathbf{r}_2, \sigma_2) \\ \cdot & \cdot & \cdot & \cdot \\ \cdot & \cdot & \cdot & \cdot \\ \phi_1(\mathbf{r}_N, \sigma_N) & \phi_2(\mathbf{r}_N, \sigma_N) & \dots & \phi_N(\mathbf{r}_N, \sigma_N) \end{vmatrix} \\ &\equiv \frac{1}{\sqrt{N!}} |\phi_1, \phi_2, \dots, \phi_N| . \end{aligned} \quad (2.9)$$

An equation for the one-particle orbitals ϕ_i can be derived by making use of the *variational principle* of quantum mechanics. It states that the energy corresponding with a variational wave function $\tilde{\psi}$ always exceeds the ground state energy E_0 ,

$$E_0 \leq \frac{\langle \tilde{\psi} | \hat{H} | \tilde{\psi} \rangle}{\langle \tilde{\psi} | \tilde{\psi} \rangle} . \quad (2.10)$$

Orthonormalization of the one-electron orbitals, $\langle \phi_i | \phi_j \rangle = \delta_{ij}$, is imposed by using Lagrange multipliers. Since the derivation of the HF equation is lengthy, it will not be presented here¹.

¹It can be found in i.a. Ref. 159.

The result of the HF approximation is the HF equation for the one-electron orbitals $\phi_i(\mathbf{r}_1)$. The Hamiltonian consists of a one-electron operator, \hat{h}_1 and two two-electron operators, \hat{J} and \hat{K} ,

$$\left[\hat{h}_1 + \hat{J} - \hat{K} \right] \phi_i(\mathbf{r}_1) = \varepsilon_i \phi_i(\mathbf{r}_1) . \quad (2.11)$$

The one-electron operator is

$$\hat{h}_1 = -\frac{1}{2} \nabla_1^2 - \sum_I \frac{Z_I}{r_{1I}} , \quad (2.12)$$

where $r_{1I} = |\mathbf{r}_1 - \mathbf{R}_I|$. The first term represents the kinetic energy of the electrons and the second term is the operator of the Coulomb interaction between electrons and nuclei. The first two-electron operator, \hat{J} , is the *direct* operator. It is given by

$$\hat{J} = \sum_j \int \phi_j^*(\mathbf{r}_2) \frac{1}{r_{12}} \phi_j(\mathbf{r}_2) d\mathbf{r}_2 , \quad (2.13)$$

with $r_{12} = |\mathbf{r}_1 - \mathbf{r}_2|$. The second two-electron operator, \hat{K} , is the *exchange* operator:

$$\hat{K} = \sum_{j||i} \int \frac{\phi_i^*(\mathbf{r}_1) \phi_j^*(\mathbf{r}_2) (1/r_{12}) \phi_j(\mathbf{r}_1) \phi_i(\mathbf{r}_2)}{\phi_i^*(\mathbf{r}_1) \phi_i(\mathbf{r}_1)} d\mathbf{r}_2 . \quad (2.14)$$

The summation over $j || i$ runs over all electrons with spin parallel to the spin of particle i .

From this some important conclusions can be drawn about the HF approximation. First, an exchange density is subtracted and accordingly electrons with spin parallel to that of electron i are located outside a region around i . This region is called the *Fermi exchange hole*. Moreover, the self-interaction of the electrons cancels in the HF approximation due to the presence of the exchange operator. In the historical predecessor of the HF approximation, the Hartree approximation, the antisymmetrization of the wave function is not carried out. As a result, there is no exchange term within the Hartree approximation. Therefore, it suffers from self-interaction. We have mentioned that the HF equation is derived using the variational principle. This is why the corresponding energy E_{HF} is always an upper bound of the true

ground state energy E_0 . The energy difference is called the *correlation energy*, $E_C = E_{\text{HF}} - E_0$. The second consequence is that one can systematically improve the accuracy of the approximation in post-HF methods. One of these post-HF methods is the *configuration interaction method* using a linear combination of Slater determinants. The HF equation can be solved in practice by expanding the orbitals in a basis set, e.g., a plane wave basis. The plane wave basis is a complete basis set, yet for practical calculations, a finite number of basis functions, M , is selected. The computational cost of the integral evaluation scales as M^4 in the HF method.

2.3 The fundamentals of Density Functional Theory

In Density Functional Theory (DFT) the electron density $n(\mathbf{r})$ is the principal quantity. The aim of DFT is to reformulate the quantum mechanical theory in terms of the density instead of the wave function. As such, the historical predecessor of DFT is the Thomas-Fermi approach dating back to 1927. The electron density $n(\mathbf{r})$ can be calculated from the electron wave function using

$$n(\mathbf{r}) = \sum_{i=1}^N \int \dots \int \psi^*(\mathbf{r}_1, \dots, \mathbf{r}_N) \delta(\mathbf{r} - \mathbf{r}_i) \psi(\mathbf{r}_1, \dots, \mathbf{r}_N) d\mathbf{r}_1 \dots d\mathbf{r}_N, \quad (2.15)$$

where N is the number of electrons.

A *functional* is a function with another function as a variable, and is denoted $F[f]$. In DFT, the energy is written as a functional of the density, $E[n]$. The *functional derivative* is defined as

$$\frac{\delta}{\delta f(x)} F[f] = \lim_{\epsilon \rightarrow 0} \frac{F[f(x) + \epsilon \delta(x - x')] - F[f(x)]}{\epsilon}. \quad (2.16)$$

Important properties of functional derivation include

$$\frac{\delta}{\delta f(x)} \left(\int F[f] dx \right) = \frac{\partial F[f]}{\partial f(x)}, \quad (2.17)$$

$$\frac{\delta}{\delta f(x)} \left(\int F[f] f(x) dx \right) = \frac{\partial F[f]}{\partial f(x)} f(x) + F[f(x)], \quad (2.18)$$

$$\frac{\delta}{\delta f(x)} \left(\frac{1}{2} \iint g(x, x') f(x) f(x') dx dx' \right) = \int g(x, x') f(x') dx' . \quad (2.19)$$

2.3.1 The Hohenberg-Kohn theorems

The Hohenberg-Kohn theorems (HK), have been formulated in 1964 by P. Hohenberg and W. Kohn [164]. The HK theorems form the foundation of DFT. The **first HK theorem** reads:

For any system of interacting particles in an external potential $V_{\text{ext}}(\mathbf{r})$, this potential is determined uniquely – except for a constant – by the ground state density $n_0(\mathbf{r})$.

This can be proven by a *reductio ad absurdum*. Suppose two different Hamiltonians exist,

$$\begin{cases} \hat{H}_1 = -\frac{1}{2} \sum_{i=1}^N \nabla_i^2 + \hat{V}_{\text{int}} + \hat{V}_{\text{ext}}^{(1)} , \\ \hat{H}_2 = -\frac{1}{2} \sum_{i=1}^N \nabla_i^2 + \hat{V}_{\text{int}} + \hat{V}_{\text{ext}}^{(2)} , \end{cases} \quad (2.20)$$

with $\hat{V}_{\text{ext}}^{(1)}$ and $\hat{V}_{\text{ext}}^{(2)}$ differing by more than a constant. This is combined with the following set of Schrödinger equations:

$$\begin{cases} \hat{H}_1 \Psi_1 = E_1 \Psi_1 , \\ \hat{H}_2 \Psi_2 = E_2 \Psi_2 . \end{cases} \quad (2.21)$$

In this expression $\Psi_1 \neq \Psi_2$. To prove this lemma, suppose that $\Psi_1 = \Psi_2 = \Psi$, then subtracting the equations in Eq. 2.21 produces

$$\left(\hat{V}_{\text{ext}}^{(1)} - \hat{V}_{\text{ext}}^{(2)} \right) \Psi = (E_1 - E_2) \Psi . \quad (2.22)$$

The energy difference $E_1 - E_2$ is a constant shift and so $\hat{V}_{\text{ext}}^{(1)}$ and $\hat{V}_{\text{ext}}^{(2)}$ also differ by merely a constant. This contradicts our previous assumption and thus $\Psi_1 \neq \Psi_2$. However, both wave functions lead to the same electron density. Returning to the main proof, one uses the variational principle yielding

$$E_1 < \langle \Psi_2 | \hat{H}_1 | \Psi_2 \rangle = \langle \Psi_2 | \hat{H}_1 - \hat{H}_2 + \hat{H}_2 | \Psi_2 \rangle . \quad (2.23)$$

Using Eqs. 2.20 and 2.21 results in

$$\begin{aligned} \langle \Psi_2 | \hat{H}_1 - \hat{H}_2 + \hat{H}_2 | \Psi_2 \rangle &= \langle \Psi_2 | \hat{V}_{\text{ext}}^{(1)} - \hat{V}_{\text{ext}}^{(2)} | \Psi_2 \rangle + E_2 \\ &= \int n_0(\mathbf{r}) \left(V_{\text{ext}}^{(1)}(\mathbf{r}) - V_{\text{ext}}^{(2)}(\mathbf{r}) \right) d\mathbf{r} + E_2 , \end{aligned} \quad (2.24)$$

and combining Eqs. 2.23 and 2.24 gives

$$E_1 - E_2 < \int n_0(\mathbf{r}) \left(V_{\text{ext}}^{(1)}(\mathbf{r}) - V_{\text{ext}}^{(2)}(\mathbf{r}) \right) d\mathbf{r} . \quad (2.25)$$

An analogous derivation starting from

$$E_2 < \langle \Psi_1 | \hat{H}_2 | \Psi_1 \rangle \quad (2.26)$$

produces

$$E_1 - E_2 > \int n_0(\mathbf{r}) \left(V_{\text{ext}}^{(1)}(\mathbf{r}) - V_{\text{ext}}^{(2)}(\mathbf{r}) \right) d\mathbf{r} . \quad (2.27)$$

Since the inequalities are strict, Eqs. 2.25 and 2.27 cannot both be true and therefore the assumption that the external potentials differ by more than a constant does not hold. This proves the first HK theorem.

The **second HK theorem** reads:

A universal functional for the energy $E[n]$ in terms of the density $n(\mathbf{r})$ can be defined, valid for any external potential $V_{\text{ext}}(\mathbf{r})$. The exact ground state energy of the system is the global minimum of this functional and the density that minimizes the functional is the exact ground state density $n_0(\mathbf{r})$.

The first part of this theorem follows immediately from the first HK theorem, upon fixing the possible constant shift in the potential. The functional $E[n]$ takes the form

$$E[n] = T[n] + E_{\text{int}}[n] + E_{\text{ext}}[n] , \quad (2.28)$$

determined uniquely by the density. The second part of the theorem provides a method to determine the ground state density.

The proof follows directly from the variational principle. The ground state energy is

$$E_0 = \langle \Psi_0 | \hat{H} | \Psi_0 \rangle , \quad (2.29)$$

Ψ_0 being the true ground state wave function. The variational principle can then be stated as

$$E = \min_{\Psi} \langle \Psi | \hat{H} | \Psi \rangle . \quad (2.30)$$

This minimization over Ψ produces the correct ground state density n_0 , since $n \neq n_0$ corresponds to a wave function different from Ψ_0 . Therefore, the ground state density minimizes the energy functional, leading to the ground state energy

$$E_0 = E[n_0] = \min_{\Psi \rightarrow n_0} \langle \Psi | \hat{H} | \Psi \rangle . \quad (2.31)$$

This proves the second HK theorem.

In the proofs of the HK theorems we have used that two different wave functions cannot both minimize the expectation value of the Hamiltonian. This means that non-degenerate states are implied. The HK theorems can be extended to include degenerate states, in the Levy-Lieb formulation.

2.3.2 The Kohn-Sham equations

2.3.2.1 Derivation

The HK theorems provide a formal framework to find the ground state density and the ground state energy of a many-body system. Yet, so far, we do not have a method to simplify the many-body problem within DFT. The most widely method for this purpose has been established by W. Kohn and L. J. Sham [165]. The essence of the *Kohn-Sham approach* (KS) is rewriting the many-body problem as an auxiliary system of non-interacting electrons moving in an effective potential. The constraint is that this auxiliary system should lead to the same electron density as the real system (i.e. n must be ‘V-representable’). The functional of the real system is

$$E[n] = T[n] + E_{\text{int}}[n] + E_{\text{ext}}[n] . \quad (2.32)$$

We can rewrite $E_{\text{int}}[n]$ as

$$\begin{aligned} E_{\text{int}}[n] &= \frac{1}{2} \iint \frac{n(\mathbf{r}) n(\mathbf{r}')}{|\mathbf{r} - \mathbf{r}'|} d\mathbf{r} d\mathbf{r}' + E'_{\text{XC}} \\ &= E_{\text{H}} + E'_{\text{XC}} , \end{aligned} \quad (2.33)$$

where the first term is the *Hartree energy*, the classical Coulomb interaction energy in the electron gas, while E'_{XC} is the correction due to quantum mechanical *exchange and correlation* (XC). According to the second HK theorem the energy functional is minimal for the true ground state density. Therefore, functional derivation with respect to n , using Eqs. 2.17 and 2.19, yields

$$\frac{\delta E [n]}{\delta n} = \frac{\delta T}{\delta n} + V_{\text{H}}(\mathbf{r}) + \frac{\delta E'_{\text{XC}}}{\delta n} + V_{\text{ext}}(\mathbf{r}) = \mu . \quad (2.34)$$

In this expression

$$V_{\text{H}}(\mathbf{r}) = \int \frac{n(\mathbf{r}')}{|\mathbf{r} - \mathbf{r}'|} d\mathbf{r}' \quad (2.35)$$

is the the Hartree potential and μ is the chemical potential, fixing the number of electrons in the system. The functional of the auxiliary system of non-interacting electrons contains an effective potential $V_{\text{KS}}(\mathbf{r})$ replacing the interaction. The functional reads

$$E [n] = T_0 [n] + \int V_{\text{KS}}(\mathbf{r}) n(\mathbf{r}) d\mathbf{r} , \quad (2.36)$$

where $T_0 [n]$ is the kinetic energy of the fictitious non-interacting electrons. Functional derivation using Eq. 2.17 leads to:

$$\frac{\delta E [n]}{\delta n} = \frac{\delta T_0}{\delta n} + V_{\text{KS}}(\mathbf{r}) = \mu . \quad (2.37)$$

From the equality the chemical potential in Eqs. 2.34 and 2.37, the effective KS potential can be specified as

$$V_{\text{KS}}(\mathbf{r}) = \frac{\delta T}{\delta n} - \frac{\delta T_0}{\delta n} + \frac{\delta E'_{\text{XC}}}{\delta n} + V_{\text{H}}(\mathbf{r}) + V_{\text{ext}}(\mathbf{r}) . \quad (2.38)$$

Here, the first three terms can be combined to give

$$\frac{\delta T}{\delta n} - \frac{\delta T_0}{\delta n} + \frac{\delta E'_{\text{XC}}}{\delta n} = \frac{\delta E_{\text{XC}}}{\delta n} = V_{\text{XC}} , \quad (2.39)$$

an XC-type potential. As such, the KS potential is

$$V_{\text{KS}}(\mathbf{r}) = V_{\text{XC}}(\mathbf{r}) + V_{\text{H}}(\mathbf{r}) + V_{\text{ext}}(\mathbf{r}) . \quad (2.40)$$

The corresponding Hamiltonian of the non-interacting system is

$$\hat{H} = \sum_{i=1}^N \left(-\frac{1}{2} \nabla_i^2 + V_{\text{KS}}(\mathbf{r}_i) \right) = \sum_{i=1}^N \hat{h}_{\text{KS}}(i) . \quad (2.41)$$

The solution of the Schrödinger equation $\hat{H}\Psi = E\Psi$ is – since there are no interactions – a Slater determinant, $\Psi = |\phi_1, \phi_2, \dots, \phi_N|$, leading to the KS equations

$$\hat{h}_{\text{KS}}(i)\phi_i(\mathbf{r}) = \varepsilon_i\phi_i(\mathbf{r}) . \quad (2.42)$$

Here, $\phi_i(\mathbf{r})$ are the KS orbitals and ε_i are the KS eigenvalues. The ground state density is related to the KS orbitals by

$$n_0(\mathbf{r}) = \sum_{i=1}^N |\phi_i(\mathbf{r})|^2 , \quad (2.43)$$

the sum running over the N orbitals with the lowest eigenvalues. The challenge in the KS approach is to find suitable approximations for the XC functional,

$$E_{\text{XC}}[n] = T[n] - T_0[n] + E_{\text{int}}[n] - E_{\text{H}}[n] . \quad (2.44)$$

This will be the subject of the next section, in which several functionals will be discussed. In the Hartree energy $E_{\text{H}}[n]$, the electron in the KS orbital under study is included in $n(\mathbf{r})$. Consequently, when the XC energy is approximated, the self-interaction does not fully cancel anymore. The generalization of the KS approach to allow for spin-polarization is fairly straightforward. KS equations for both spin components can be established.

2.3.2.2 Total electronic energy

We will now derive an expression for the total electronic energy in the KS method. The total energy functional reads, using Eq. 2.44,

$$E[n] = T_0[n] + E_{\text{H}}[n] + E_{\text{XC}}[n] + E_{\text{ext}}[n] . \quad (2.45)$$

We can rewrite $T_0[n]$, making use of the KS equations,

$$T_0[n] = \sum_{i=1}^N \varepsilon_i - \int V_{\text{KS}}(\mathbf{r}) n(\mathbf{r}) d\mathbf{r} , \quad (2.46)$$

and fill in $V_{\text{KS}}(\mathbf{r})$ as given in Eq. 2.40, obtaining

$$T_0[n] = \sum_{i=1}^N \varepsilon_i - \int V_{\text{XC}} n(\mathbf{r}) \, d\mathbf{r} - 2E_{\text{H}}[n] - E_{\text{ext}}[n] . \quad (2.47)$$

Combining this with Eq. 2.45 produces

$$E[n] = \sum_{i=1}^N \varepsilon_i - E_{\text{H}}[n] + E_{\text{XC}}[n] - \int V_{\text{XC}} n(\mathbf{r}) \, d\mathbf{r} . \quad (2.48)$$

It is thus found that the total electronic energy is not simply a summation of the KS eigenvalues ε_i . The functional $E_{\text{XC}}[n]$ can be written as

$$E_{\text{XC}}[n] = \int \varepsilon_{\text{XC}}[n(\mathbf{r})] n(\mathbf{r}) \, d\mathbf{r} . \quad (2.49)$$

From Eq. 2.18 for functional derivation it follows that

$$V_{\text{XC}}[n] = \frac{\delta E_{\text{XC}}[n]}{\delta n(\mathbf{r})} = \varepsilon_{\text{XC}}[n(\mathbf{r})] + \frac{\partial \varepsilon_{\text{XC}}[n]}{\partial n(\mathbf{r})} n(\mathbf{r}) . \quad (2.50)$$

Therefore, the total energy of the electrons (E_e in Eq. 2.7) reads

$$E[n] = \sum_{i=1}^N \varepsilon_i - E_{\text{H}}[n] - \int \frac{\partial \varepsilon_{\text{XC}}[n]}{\partial n(\mathbf{r})} n(\mathbf{r}) \, d\mathbf{r} . \quad (2.51)$$

Contrary to the HF method, the total energy in the Kohn-Sham DFT approach is not necessarily an upper bound of the true total energy, when the XC energy is approximated.

The KS equations can be solved *self-consistently*. This is shown schematically in Fig. 2.1. The iteration starts with an initial (trial) value for the electron density $n(\mathbf{r})$. Given an XC functional, the KS potential $V_{\text{KS}}(\mathbf{r})$ follows from the initial density. Now the KS equations can be solved, yielding the KS orbitals $\phi_i(\mathbf{r})$. They lead to a new electron density $n(\mathbf{r})$ and a total energy. The density is fed as input to the iteration and this is repeated until self-consistency is reached. In practice, this self-consistency is assessed in terms of the convergence of the total energy. If subsequent values of the total energy differ less than the convergence criterion that has been selected, the total energy, forces, stresses, etc., can be output.

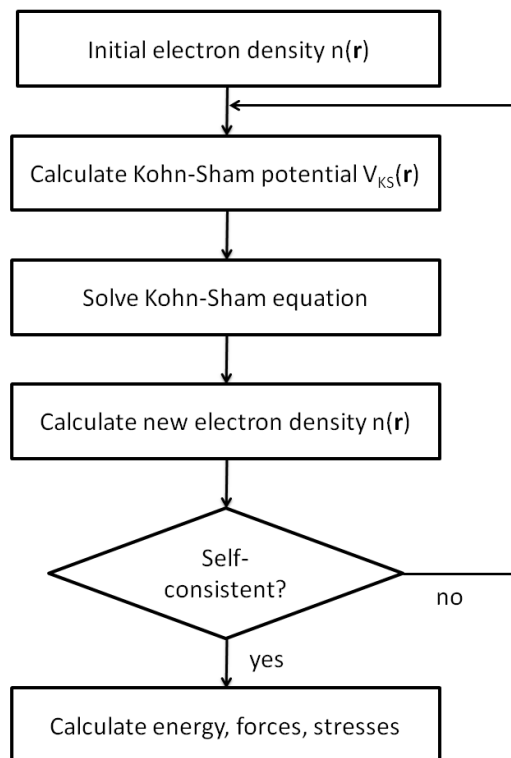


FIGURE 2.1: *Scheme of the self-consistent solution of the Kohn-Sham equations.*

2.4 Exchange-correlation functionals

We will review the most widely used exchange-correlation (XC) approximations, LDA, GGA, and (briefly) hybrid functionals.

2.4.1 Local density approximation

The *local density approximation* (LDA) is the most simple XC functional, defined as

$$E_{XC}^{LDA}[n] = \int \varepsilon_{XC}^{UEG}(n(\mathbf{r})) n(\mathbf{r}) d\mathbf{r}, \quad (2.52)$$

where $\varepsilon_{XC}^{UEG}(n(\mathbf{r}))$ is the XC energy of an electron in a uniform electron gas (UEG) of density $n(\mathbf{r})$. It depends solely on the local density at point \mathbf{r} . The

XC energy per electron can be split into the X and the C contribution:

$$\varepsilon_{\text{XC}}^{\text{UEG}}[n] = \varepsilon_{\text{X}}^{\text{UEG}}[n] + \varepsilon_{\text{C}}^{\text{UEG}}[n] . \quad (2.53)$$

The X energy of an electron in a uniform electron gas has the following analytic form:

$$\varepsilon_{\text{X}}^{\text{UEG}}[n] = -\frac{3}{4\pi} (3\pi^2 n(\mathbf{r}))^{1/3} , \quad (2.54)$$

which in the LDA functional is to be evaluated point-wise. There are, on the other hand, no exact analytic expressions available for $\varepsilon_{\text{C}}^{\text{UEG}}[n]$ (except in the high- and low-density limit). Approximations can be obtained from quantum Monte-Carlo simulations, as introduced by Ceperley and Alder [166].

2.4.2 Generalized gradient approximation

The LDA approximation can be improved on, taking into account the spatial change in the local density by including (powers of) the gradient in the XC functional. This approach is called the *generalized gradient approximation* (GGA). It is important to note that the GGA is still a semi-local approximation, since only the gradient at the same coordinate is taken into account. The XC functional thus takes the form

$$E_{\text{XC}}^{\text{GGA}}[n] = \int \varepsilon_{\text{XC}}(n(\mathbf{r}), |\nabla n(\mathbf{r})|, \nabla^2 n(\mathbf{r}), \dots) n(\mathbf{r}) \, d\mathbf{r} , \quad (2.55)$$

A commonly used GGA functional is the *Perdew-Burke-Ernzerhof* (PBE) functional [167].

2.4.3 Limitations of the local approximations

LDA and GGA functionals are meritorious in predicting lattice parameters and atomic positions within 1–5% of the experimental values. Also, the electronic structure of metals is reasonably well described. It is however important to realize that the KS eigenvalues do not necessarily agree with the real energy spectrum. In the derivation of the KS equations, we have only imposed that the density of the KS system coincides with the real density. Accordingly, the excitation energies are not accurately described by DFT in local approximations like LDA and DFT. As a consequence, the band gaps of insulators

and semiconductors are systematically underestimated – which is known as the *DFT band gap problem*. This can be understood by carefully studying the KS spectrum. The KS band gap is determined in terms of the N -electron eigenvalues,

$$E_g^{\text{KS}} = \varepsilon_{N+1}(N) - \varepsilon_N(N) , \quad (2.56)$$

while the real band gap is given by

$$E_g = \varepsilon_{N+1}(N+1) - \varepsilon_N(N) . \quad (2.57)$$

The deviation between both band gaps corresponds to a difference of XC potentials [168]:

$$\begin{aligned} E_g - E_g^{\text{KS}} &\equiv \Delta_{\text{XC}} = \varepsilon_{N+1}(N+1) - \varepsilon_{N+1}(N) \\ &= \lim_{\eta \rightarrow 0} \left[\left(\frac{\delta E_{\text{XC}}[n]}{\delta n(\mathbf{r})} \right)_{N+\eta} - \left(\frac{\delta E_{\text{XC}}[n]}{\delta n(\mathbf{r})} \right)_{N-\eta} \right] , \end{aligned} \quad (2.58)$$

where η is a fractional number of electrons. Δ_{XC} describes the discontinuity of the functional derivative of $E_{\text{XC}}[n]$ around N . This discontinuity is not captured by the local functionals and consequently, in LDA and GGA, $\Delta_{\text{XC}} = 0$. The resulting band gap is the pure KS band gap, leading to a consistent underestimation of the band gap. This is illustrated in Fig. 2.2 for a wide range of semiconductor and insulator materials [169]. The LDA band gaps are compared to the band gaps in the GW approximation (GWA) and the experimental gaps.

One of the most recent and best solutions to the DFT band gap problem is the *hybrid functional method*, where exact (Hartree) exchange is mixed into the functional, at the short range [170, 171]. Hybrid functional calculations are very computationally intensive. The HF method, on which hybrid functionals are based, uses the wave functions instead of the density, which have less symmetry, as a result of the Bloch theorem that will review in Sec. 2.6.1. The main computational challenge in this thesis is dealing with the gigantic task of performing all perturbation calculations needed to describe the phonons and electron-phonon coupling from first principles, as we will review in Chapter 3. This computational load is therefore currently not compatible with hybrid functionals because of limitations in the computing capacity. Therefore, almost all calculations in this thesis have been carried

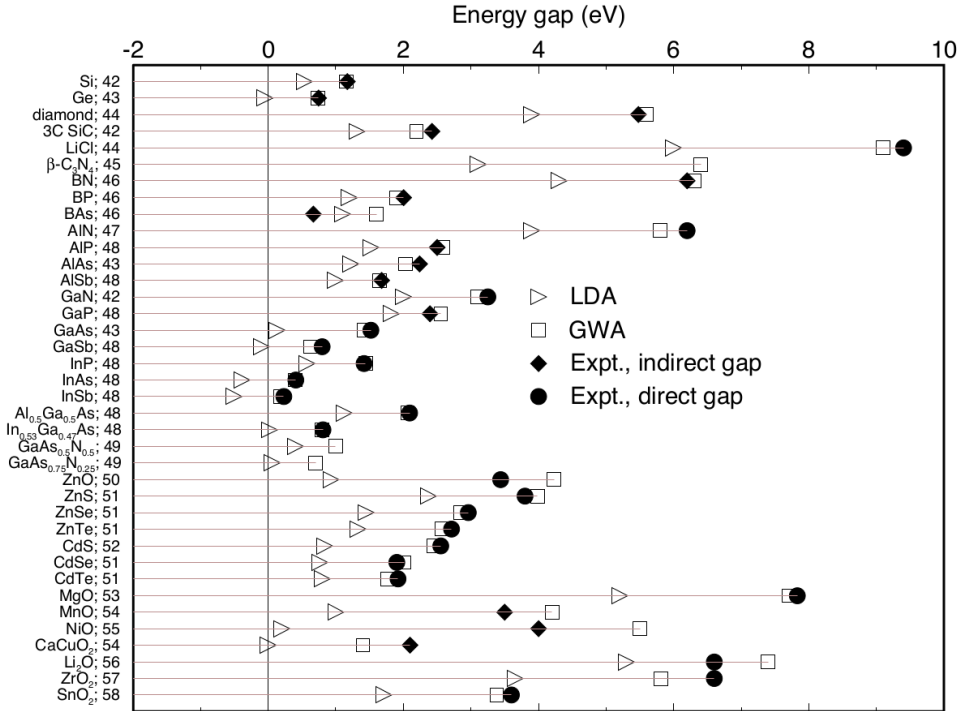


FIGURE 2.2: *Comparison of LDA, GWA and experimental band gaps of insulator and semiconductor materials [169]. It is apparent that LDA consistently leads to an underestimation of the band gap.*

out with GGA functionals, specifically the PBE functional. This is justified since we deal mainly with metallic and superconducting systems, that do not suffer from the band gap problem.

2.5 Geometry optimization using the Hellmann-Feynman theorem

The forces acting on the nuclei are obtained as the derivative of the total energy with respect to the atomic positions. In equilibrium, all forces are zero, i.e.,

$$\mathbf{F}_I = -\frac{\partial E}{\partial \mathbf{R}_I} = 0 . \quad (2.59)$$

The derivative can be evaluated using the *Hellmann-Feynman theorem*. It is valid for an eigenvalue $E(\lambda)$ of the Hamiltonian \hat{H} , λ being a parameter, the

derivative with respect to λ is obtained from

$$\frac{\partial E}{\partial \lambda} = \langle \psi | \frac{\partial \hat{H}}{\partial \lambda} | \psi \rangle, \quad (2.60)$$

where $|\psi\rangle$ is an eigenstate of the Hamiltonian. The proof of the Hellmann-Feynman theorem requires a simple application of the product rule of derivation. In our case, the Hamiltonian is given by

$$\hat{H} = \hat{T} + \hat{V}_{\text{int}} + \hat{V}_{\text{ext}} + \hat{H}_{\text{n}}. \quad (2.61)$$

Following the Born-Oppenheimer approximation the nuclear Hamiltonian \hat{H}_{n} can be evaluated classically. Application of the Hellmann-Feynman theorem yields

$$\begin{aligned} \mathbf{F}_I &= -\langle \psi_0 | \frac{\partial \hat{H}}{\partial \mathbf{R}_I} | \psi_0 \rangle \\ &= -\underbrace{\left\langle \frac{\partial \hat{T}}{\partial \mathbf{R}_I} \right\rangle}_{=0} - \underbrace{\left\langle \frac{\partial \hat{V}_{\text{int}}}{\partial \mathbf{R}_I} \right\rangle}_{=0} - \left\langle \frac{\partial \hat{V}_{\text{ext}}}{\partial \mathbf{R}_I} \right\rangle - \frac{\partial E_{\text{n}}}{\partial \mathbf{R}_I}. \end{aligned} \quad (2.62)$$

The first two terms vanish, since \hat{T} and \hat{V}_{int} do not depend explicitly on $\{\mathbf{R}_I\}$. We obtain that the forces can be calculated as

$$\mathbf{F}_I = - \int \frac{\partial V_{\text{ext}}(\mathbf{r})}{\partial \mathbf{R}_I} n_0(\mathbf{r}) d\mathbf{r} - \frac{\partial E_{\text{n}}}{\partial \mathbf{R}_I}. \quad (2.63)$$

Practical schemes for the variation of the atomic positions to approximate the equilibrium structure will be discussed in a Sec. 2.7.

2.6 Practical calculations

Previously, we have laid the foundation for DFT (the Hohenberg-Kohn theorems) and we have derived a set of equations that simplifies the many-body problem (the Kohn-Sham equations), studying also the crucial exchange-correlation energy. Now, we will investigate how DFT can be implemented practically, for numerical computation.

2.6.1 The Bloch theorem

The first requirement for a practical approach to DFT, is the use of the spatial periodicity of the crystal lattice. Accordingly, the KS potential is periodic for all lattice parameters \mathbf{R} of the lattice:

$$V_{\text{KS}}(\mathbf{R}) = V_{\text{KS}}(\mathbf{r} + \mathbf{R}) . \quad (2.64)$$

A periodic structure is defined by a unit cell, which is repeated in all spatial directions. This may be a supercell of the simple lattice of a material, to implement more complex structures, such as a slab, point defects, etc.

For the periodic lattice that has been introduced, the *Bloch theorem* holds:

The wave function of a particle in a periodic potential can be written as a product of a plane wave and a periodic function with the same periodicity as the lattice.

This wave function can be written as

$$\phi_{i\mathbf{k}} = e^{i\mathbf{k}\cdot\mathbf{r}} u_{i\mathbf{k}}(\mathbf{r}) \quad (2.65)$$

with

$$u_{i\mathbf{k}}(\mathbf{r}) = u_{i\mathbf{k}}(\mathbf{r} + \mathbf{R}) . \quad (2.66)$$

It follows easily that the energy spectrum is periodic with respect to the reciprocal lattice,

$$E_i(\mathbf{k}) = E_i(\mathbf{k} + \mathbf{G}) , \quad (2.67)$$

for all reciprocal lattice vectors \mathbf{G} . Therefore, the energy spectrum is fully represented within the *first Brillouin zone* (BZ), the primitive cell of the reciprocal lattice. This representation is called the *band structure*. It will continuously be used within this thesis to display the electronic structure.

2.6.2 Plane wave basis set

It is convenient to expand a periodic function such as $u_{n\mathbf{k}}(\mathbf{r})$ using a plane wave basis set,

$$u_{i\mathbf{k}}(\mathbf{r}) = \sum_{\mathbf{G}} c_{i\mathbf{k}}(\mathbf{G}) e^{i\mathbf{G}\cdot\mathbf{r}} , \quad (2.68)$$

where the summation runs over all reciprocal lattice vectors. The plane waves form a complete basis set and thus the expansion is a Fourier series. Herein lies one of the main advantages of a plane wave basis, namely, a fast Fourier transform (FFT) can be performed to switch between real and reciprocal space. Using the Bloch theorem, it follows that the electronic wave functions are

$$\phi_{i\mathbf{k}} = \sum_{\mathbf{G}} c_{i\mathbf{k}}(\mathbf{G}) e^{i(\mathbf{k}+\mathbf{G})\cdot\mathbf{r}} . \quad (2.69)$$

The kinetic energy related to plane waves in this expansion is $(\mathbf{k}+\mathbf{G})^2/2$. The summation over \mathbf{G} is infinite and thus for practical reasons an upper boundary should be set, the cutoff energy E_{cut} , so $\frac{(\mathbf{k}+\mathbf{G})^2}{2} < E_{\text{cut}}$ or, equivalently, $|\mathbf{G}| < G_{\text{max}}$. The cutoff energy can be understood in terms of a ‘resolution’: details in the wave function smaller than $2\pi/G_{\text{max}}$ are neglected. It results in the second important advantage of the plane wave basis set, namely the accuracy can be improved systematically by increasing E_{cut} .

2.6.3 Integration over the first Brillouin zone: the k-point grid

In DFT, all quantities are derived from the electron density,

$$n(\mathbf{r}) = \int_{\text{BZ}} d\mathbf{k} \sum_{i=1}^{N_{\mathbf{k}}} f_{i\mathbf{k}} |u_{i\mathbf{k}}(\mathbf{r})|^2 , \quad (2.70)$$

where the sum runs over all bands at point \mathbf{k} , $N_{\mathbf{k}}$, and $f_{i\mathbf{k}}$ is the occupancy of the band, either 1 – below the Fermi level – or 0². In order to facilitate the convergence of the integration with respect to the number of k-points, it is advantageous to replace the step function by a smooth function. This is a so-called *finite-temperature approach*, also known as *smearing*, since it mimics the effect of temperature [172]. Gaussian functions are frequently used to describe this smearing.

For an infinitely extended real space lattice, \mathbf{k} is a continuous variable, restricted to the first BZ owing to periodicity. In a numerical calculation,

²The occupancy is in principle either 1 or 0, but can be 2, 1 or 0 in case spin-orbit coupling is omitted. In the absence of spin-orbit coupling a fully occupied band contains 2 electrons.

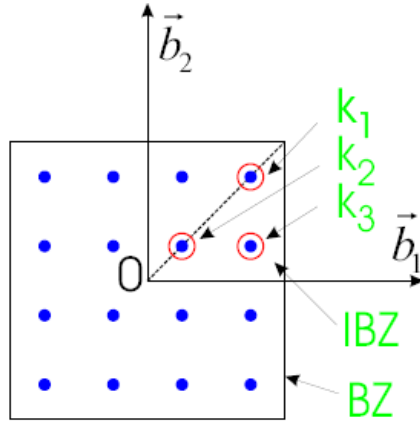


FIGURE 2.3: *The IBZ of a simple square reciprocal lattice in 2D. The IBZ contains the wave vectors $\mathbf{k}_1 = (\frac{3}{8}, \frac{3}{8})$ with weight $w_{\mathbf{k}_1} = \frac{1}{4}$, $\mathbf{k}_2 = (\frac{1}{8}, \frac{1}{8})$ with weight $w_{\mathbf{k}_2} = \frac{1}{4}$ and $\mathbf{k}_3 = (\frac{3}{8}, \frac{1}{8})$ with weight $w_{\mathbf{k}_3} = \frac{1}{2}$.*

integration over a continuous variable is not attainable. Therefore, a *k-point grid* is constructed to sample the first BZ. Commonly, a Monkhorst-Pack grid, an equidistant grid, is selected [173]. Additionally, sampling of the *irreducible Brillouin zone* (IBZ), the reduction of the first BZ by the lattice symmetries, is sufficient for the calculation of the density. The normalized weight $w_{\mathbf{k}}$ has to be included, to take into account the multiplicity of each *k*-point. Consequently, the electron density becomes

$$n(\mathbf{r}) \cong \sum_{\mathbf{k} \in \text{IBZ}} w_{\mathbf{k}} \sum_{i=1}^{N_{\mathbf{k}}} f_{i\mathbf{k}} |u_{i\mathbf{k}}(\mathbf{r})|^2 . \quad (2.71)$$

As an example, the IBZ of a simple square reciprocal lattice in 2D is depicted in Fig. 2.3.

2.6.4 Pseudopotentials

The electronic wave functions (orbitals) of the elements contained in the unit cell are fed as input to a practical DFT routine. The true orbitals may contain many nodes, leading to a huge basis set (a high E_{cut}). Moreover, for bonding, the core electrons are usually not relevant. The oscillations of the true (all-electron) valence electron orbitals near the core are due to the core electrons. The nodes - and thus the oscillations - arise from the

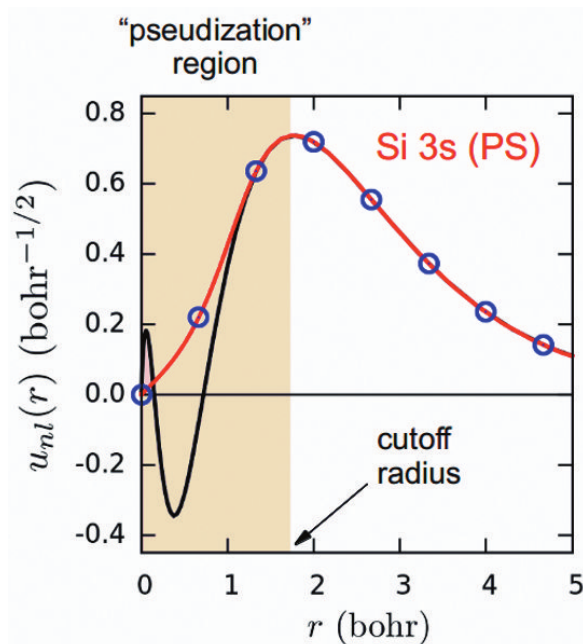


FIGURE 2.4: *The original (black curve) and smoothed (red curve) wave function for the Si 3s state [163].*

orthogonality of the orbitals to the core orbitals. In a *pseudopotential* (PP) method, the effect of the core electrons is removed from the true orbitals yielding a smoothed function. Let us consider an orbital ψ , resulting from a one-electron Schrödinger equation, e.g., the Kohn-Sham equation $\hat{h}\psi = \varepsilon\psi$.

Following the principle of the PP method, ψ can be written as:

$$\psi = \phi + \sum_c b_c \psi_c, \quad (2.72)$$

where ϕ is a smooth function, corresponding to the true wave function ψ outside of a cutoff radius r_c , in the region of chemical bonds. An example of a pseudopotential for Si is shown in Fig. 2.4, where the red curve is the smooth wave functions coinciding with the true wave function outside the cutoff radius r_c . The summation over c runs over all core orbitals and b_c are the coefficient of the linear combination. As such, we have split the true wave function into a smooth and an oscillating contribution. The constants b_c can be determined from the orthogonality of ψ to the core orbitals. We

select any of the core orbitals ψ_{c0} to obtain

$$\langle \psi_{c0} | \psi \rangle = \langle \psi_{c0} | \phi \rangle + b_{c0} . \quad (2.73)$$

Therefore $b_{c0} = -\langle \psi_{c0} | \phi \rangle$, which in combination with Eq. 2.74 results in

$$\psi = \phi - \sum_c \langle \psi_c | \phi \rangle \psi_c . \quad (2.74)$$

This formula is related to the Gram-Schmidt orthogonalization procedure. Then, using $\hat{h}\psi_c = \varepsilon_c\psi_c$, the one-electron eigenvalue equation Kohn-Sham becomes

$$\hat{h}\psi(\mathbf{r}) = \hat{h}\phi(\mathbf{r}) - \varepsilon_c \sum_c \int \psi_c^*(\mathbf{r}') \phi(\mathbf{r}') d\mathbf{r}' \psi_c(\mathbf{r}) . \quad (2.75)$$

Alternatively, we can write $\hat{h}\psi = \varepsilon\psi$ as

$$\hat{h}\psi(\mathbf{r}) = \varepsilon\phi(\mathbf{r}) - \varepsilon \sum_c \int \psi_c^*(\mathbf{r}') \phi(\mathbf{r}') d\mathbf{r}' \psi_c(\mathbf{r}) . \quad (2.76)$$

Combining Eqs. 2.75 and 2.76 gives a single-electron equation for the smooth wave function ϕ ,

$$\hat{h}\phi(\mathbf{r}) + \sum_c (\varepsilon - \varepsilon_c) \int \psi_c^*(\mathbf{r}') \phi(\mathbf{r}') d\mathbf{r}' \psi_c(\mathbf{r}) = \varepsilon\phi(\mathbf{r}) . \quad (2.77)$$

The left hand side consists of the one-particle Hamiltonian \hat{h} and a non-local operator, both acting on $\phi(\mathbf{r})$. Therefore, it can be rewritten by introducing the PP \hat{V}_{ps} ,

$$\left(-\frac{1}{2}\nabla^2 + \hat{V}_{\text{ps}} \right) \phi(\mathbf{r}) = \varepsilon\phi(\mathbf{r}) . \quad (2.78)$$

2.6.5 Projector augmented waves

Another method used to reduce the computational cost of electron-ion interaction in DFT, is the projector augmented wave (PAW) method, developed by Blöchl [174]. It is closely related to the PP method, since the aim is still to distinguish between the oscillating part of the orbitals close to the core and the smooth part of the orbitals further away. In contrast to the PP approach,

the all-electron character of the wave function is conserved. This is done as follows.

First, the true orbitals ψ_i of the isolated atom are obtained from an all-electron calculation. Then, as was the case for PP, the true wave functions are transformed into smoother wave functions ϕ_i , the so-called *partial waves*. Hereby the constraint is that the true and partial wave functions should coincide outside the core region (beyond the cutoff distance r_c). The inverse transformation is achieved by a linear transformation, $\psi_i = \hat{T}\phi_i$. The third step consists of expanding the smooth valence wave functions of the electrons, $\Phi_i = \sum_i c_i \phi_i$. The true wave function is obtained by the transformation with \hat{T} ,

$$\Psi_i = \hat{T} \left(\sum_i c_i \phi_i \right) = \sum_i c_i \psi_i . \quad (2.79)$$

The PAW method can furthermore be formulated using projectors p_i that operate only in the core region, within the radius r_c . With the definition of the projectors, $\langle p_i | \phi_j \rangle = \delta_{ij}$ the operator \hat{T} can be rewritten as

$$\hat{T} = 1 + \sum_j (|\psi_j\rangle - |\phi_j\rangle) \langle p_j| . \quad (2.80)$$

Thus we obtain

$$|\psi_i\rangle = \hat{T}|\phi_i\rangle = |\phi_i\rangle + \sum_j (|\psi_j\rangle - |\phi_j\rangle) \delta_{ij} , \quad (2.81)$$

which is consistent. Consequently, the true electron wavefunction in the system can be written as

$$|\Psi_i\rangle = \hat{T}|\Phi_i\rangle = |\Phi_i\rangle + \sum_j (|\psi_j\rangle - |\phi_j\rangle) \langle p_j | \Phi \rangle . \quad (2.82)$$

According to this expression, the all-electron wavefunction is reconstructed from the smooth pseudowavefunction by correcting for the differences between the true orbitals and the partial waves of the atoms. This is how the PAW method retains the all-electron character of the wavefunctions. As a result, the PAW method is generally more accurate than the PP method.

2.7 Implementations

We have seen that DFT can be used to reduce the many-body problem. Still, the KS equations are to be solved self-consistently and a sufficiently large basis set has to be selected, as well as an appropriate supercell to implement more complex systems. So, DFT is implemented numerically in a wide variety of software packages, such as ABINIT, Gaussian, Quantum ESPRESSO, SIESTA, VASP, WIEN2k etc. These differ in several aspects, i.a., the choice of the basis functions, the pseudopotentials, and the algorithms used for diagonalization of the KS Hamiltonian. All results presented in this thesis have been obtained using either ABINIT [175] or the Vienna *Ab initio* Simulation Package (VASP) [172, 176].

Both implementations have a lot in common. In both packages, several approaches to solve many-body problems are implemented, the main ones being Kohn-Sham DFT and the GW approximation (a method originating from many-body perturbation theory). Both also offer several XC functionals for the DFT, such as the LDA, the GGA, van der Waals functionals, hybrid functionals, etc. Wave functions and potentials are expanded in a plane wave basis set in both programs, and the electron-ion interactions can be treated either using PPs or PAW potentials. As we will see in more detail in Chapter 3, in addition in ABINIT *density functional perturbation theory* (DFPT) is implemented, which yield efficient calculations of phonons, and of the electron-phonon coupling. This is why the majority of the first-principles results in this thesis has been obtained in ABINIT. VASP is used in some cases, where it has very specific advantages; this will be pointed out explicitly where relevant. Computational details in the different systems that are studied will always be provided in the corresponding chapters.

In the self-consistent solution of the KS equations, several methods for the diagonalization of the KS Hamiltonian can be employed, such as the blocked Davidson algorithm, and the conjugate gradient algorithm (CGA). The efficiency of the self-consistency cycle can be improved by charge density mixing, i.e., taking a combination of previous output charge densities to create the input charge density for a new iteration step. Geometry optimization of the ionic structure is also executed in an iterative way. The geometry is considered optimized or relaxed if the forces on all ions are below the selected

convergence criterion. Within each step of the relaxation, the electronic structure has to be calculated in a self-consistency cycle. Subsequently, the forces can be calculated using the Hellmann-Feynman theorem, as we have explained in Sec. 2.5. One of the most reliable method for relaxations is based on a conjugate gradient algorithm. In the first step, the ionic positions are altered in the direction of the forces acting on them. This is a so-called line minimization. Similarly, the cell shape is changed in the direction of the calculated stress. The forces, stress tensor and total energy are recalculated, which concludes the trial step. For the corrector step, a third-order interpolation is performed to further approximate the minimum in total energy. Again, the forces on the ions are calculated. In case any force on an ion in the system exceeds the convergence criterion, the procedure is repeated. The new search direction are conjugated to the previous search directions.

To meet the computational demands, ABINIT and VASP support parallel computing, i.e., subtasks are divided over multiple central processing units (CPUs). Parallelization can be achieved over energy bands, k-points or a combination of both. For this thesis, dealing with metallic systems, very dense k-point grids were necessary to accurately describe the Fermi surface. Therefore, usually parallelization over the k-points was the preferred method.

Chapter 3

Phonons, electron-phonon interaction and Migdal-Eliashberg theory

3.1 Introduction

As we have reviewed in Chapter 1, phonons and electron-phonon coupling play a central role in the superconducting pairing of conventional superconductors. In Chapter 2 we saw how the electronic properties of materials can be calculated with *ab initio* methods. Since the aim of this thesis is developing a complete *ab initio* method to study the superconducting properties of multicomponent and atomically thin superconductors, we need to extend this framework to include the dynamical properties. To that end, we will start this chapter by briefly reviewing phonons in 3D and in 2D materials. Then, we will introduce the many-body description of electron-phonon interaction. With the acquired fundamental insight into this system, we will be able to subsequently extend DFT with the inclusion of lattice perturbations. This leads to adapted Kohn-Sham equations that form the base of *density functional perturbation theory* (DFPT), which is the workhorse tool for the *ab initio* study in this thesis. For an accurate description of the superconducting properties, we will explain how the *ab initio* results can be employed in a field theoretical description of superconductivity that is an extension of the BCS theory, reviewed in Chapter 1, namely *Migdal-Eliashberg theory*.

We will investigate the assumptions used to arrive at this theory, and the resulting strengths and weaknesses.

3.2 Phonons

Phonons are quantized lattice vibrations, with quantized energy levels at any particular wave vectors \mathbf{q} . Just like electrons in a solid, the energy of phonons depends on this wave vector, leading to the dispersion relation $\omega(\mathbf{q})$. These energies are the phonon eigenvalues, and the corresponding eigenvectors are the lattice displacements. Two main types of phonons exist, namely *acoustic* (A) and *optical* (O) phonons. In the former, the atom displacements are mutually in phase, while in the latter they are out of phase. This distinction already arises in the quantum-mechanical description of linear chains of atoms, with at least two atoms per unit cell [177, 178]. It can be proven that a material with N atoms in the unit cell has 3 acoustic phonon modes and $3N - 3$ optical modes, with a total of $3N$ phonon modes. These modes will be numbered as ω_ν with $\nu = 1, \dots, 3N$. Therefore, a material with a unit cell consisting of a single atom only has acoustic modes – which is exactly what justifies the use of the Debye model for many elementary superconductors as we did in Chapter 1. Within these categories one distinguishes, as always in the case of wave phenomena, longitudinal (L) and transverse (T) modes. In the longitudinal case, the phonon eigenmodes, $\mathbf{e}_{\kappa\nu}(\mathbf{q})$ where κ indicates a specific nucleus, are parallel to the propagation direction of the wave, characterized by wave vector \mathbf{q} , while in the transverse case it is perpendicular. Thus, phonons can be divided in 4 categories: LA, TA, LO and TO. Of the 3 acoustic modes in a bulk material 1 is LA and 2 are TA, and of the $3N - 3$ optical modes $N - 1$ are LO and $2N - 2$ are TO.

To a first approximation phonons are harmonic. In this limit they couple atoms in the way springs do, namely according to Hooke's law, where the reaction force is $\mathbf{F} = -k\mathbf{r}$, k being the spring constant. This leads to potential energy of the form $U = k|\mathbf{r}|^2/2$, as shown in Fig. 3.1. The springs in a solid are the electronic charge densities. Beyond the harmonic approximation, there can be anharmonic phonons, also shown in Fig. 3.1, which are not symmetric upon $\mathbf{r} \rightarrow -\mathbf{r}$. Phonon eigenvalues are generally positive real numbers, but not always. Imaginary phonon modes indicate that the structure is

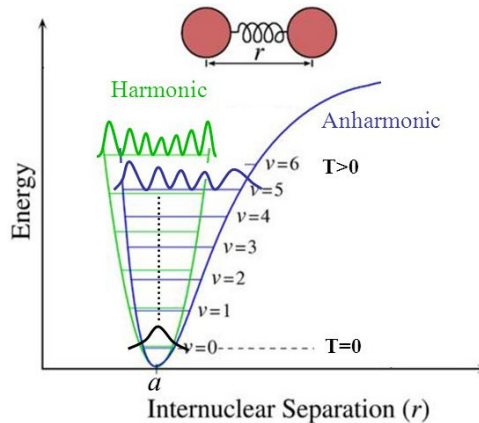


FIGURE 3.1: *Schematic representation of the potential energy as a function of internuclear separation, for an harmonic and an anharmonic case. Some phonon modes are shown as insets, the harmonic ones being symmetric with respect to the minimum, while the anharmonic ones are not.*

not stable¹. The resulting time evolution is $\exp(i\omega t) = \exp(-\text{Im}(\omega)t)$, which is a damped, evanescent oscillation. Fig. 3.1 also indicates that the lowest phonon mode is the ground state, the other modes being filled up according to the Bose-Einstein distribution at $T > 0$, since phonons are bosons.

3.2.1 Phonons in 2D materials

Phonons in 2D materials are substantially different from their bulk counterparts. In the direction perpendicular to the crystal plane there are no neighbors and therefore reduced reactive forces. This gives rise to different types of modes compared with 3D. The out-of-plane modes are indicated with Z (referring to the z-direction) [179]. Thus, 2D materials have 1 ZA mode, 1 TA mode and 1 LA mode, and $N - 1$ ZO modes, $N - 1$ TO modes and, finally, $N - 1$ LO modes. The LA and TA modes in 3D and 2D materials are linear with the wave vector in the vicinity of Γ ($\omega = v_s q$ with v_s the sound velocity in the material). Owing to rotational invariance in 2D materials, the first term of order q^2 vanishes in the expansion of ω^2 of the ZA mode, so that the leading order is q^4 [180]. Thus, it follows that the phonon dispersion

¹We wish to comment here already that often, in this thesis too, these imaginary phonon eigenvalues are mapped to negative real numbers, for graphical convenience.

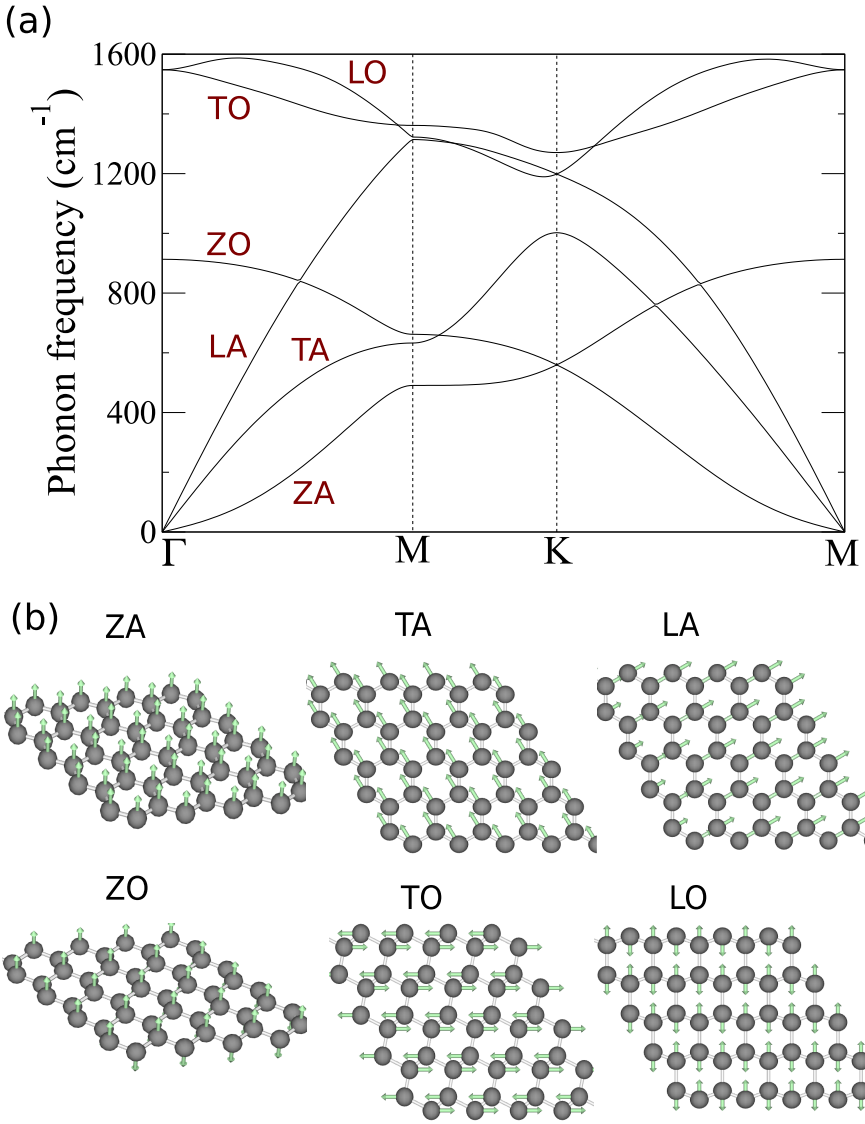


FIGURE 3.2: *Phonons in graphene calculated using density functional perturbation theory (implemented in ABINIT). (a) Phonon dispersion, where the character of the modes is indicated. (b) All 6 eigenmodes of graphene at wave vector Γ .*

of the ZA mode goes as $\omega = \alpha q^2$ in the vicinity of Γ . This mode is also called the *flexural* mode, since it corresponds to rippling of the 2D sheet in the out-of-plane direction (for $q \neq \Gamma$).

As an example, we will discuss the phonon modes of graphene. This is a very relevant example for this thesis, as the ultrathin MgB₂ sheets that we

will study in Chapters 6-7, as well as the ultrathin dichalcogenide sheets that will form the subject of Chapter 8 all have hexagonal symmetries like graphene. The result of a first-principles calculation of the phonon dispersion of graphene (performed in ABINIT using density functional perturbation theory – to be discussed further on in this chapter) is shown in Fig. 3.2(a). The quadratic dependence of the ZA mode is clearly visible here. It is instructive to study the eigenmodes at Γ . Since graphene has point group D_{6h} , the modes consist of four representations: E_{2g} , B_{2g} , E_{1u} and A_{2u} [181]. Here, g stands for *gerade* (German for even) and u stands for *ungerade* (German for odd). The gerade representations are symmetric under $\mathbf{r} \rightarrow -\mathbf{r}$, while the ungerade representations are antisymmetric under this transformation. The eigendisplacements of graphene at Γ are depicted in Fig. 3.2(b). At Γ the TO and LO phonon modes are part of the E_{2g} representation (doubly degenerate at Γ), the ZO mode of B_{2g} , the TA and LA modes of E_{1u} , and the ZA mode of A_{2u} [181]. In this figure one can nicely trace back everything we have introduced up to now regarding phonons. Notice, for example, that in the ZA, TA and LA modes the atoms move in-phase, while the atoms of the A and B sublattices move out-of-phase in the ZO, TO and LO modes.

Theoretically speaking only the E_{2g} mode is Raman active – it is also called the *G mode* in this context – however, the TO branch around K can become Raman active under the influence of disorder, hence the name *D mode*. The E_{2g} mode moreover has a strong interaction with electrons, that leads to cusps in the phonon dispersion, called *Kohn anomalies* [181]. These are absent in the phonon dispersion in Fig. 3.2(a) since it was calculated within the Born-Oppenheimer approximation, where the electrons see the lattice as static. The strong electron-phonon coupling of the E_{2g} mode will play an important role in Chapters 6-7, as we will prove that it is the main contribution to the phonon-mediated superconductivity in MgB_2 .

3.3 Electron-phonon interaction

The electron-phonon (*e-ph*) interaction plays a crucial role in various phenomena occurring in solids [182, 183]. In metals, the electrical resistivity depends on *e-ph* interaction, and in semiconductors the carrier mobility does so as well. In indirect semiconductors the optical transitions are enabled

by e - ph interaction. Even more generally, the e - ph coupling can distort the electronic band structure (in phenomena such as the Peierls distortion and charge density waves) as well as the phonon dispersion (leading, e.g., to the Kohn anomalies introduced in Sec. 3.2.1). By coupling lattice and spin degrees of freedom the e - ph interaction even plays a role in electrically active magnons (called electromagnons) which hold promise for spintronics [183]. Finally, it lies at the base of conventional pairing in superconductors – as we have already seen in Chapter 1 – which will be the focus of the discussion that follows.

The Hamiltonian describing the coupled electron-phonon system to first order is

$$\hat{H} = \sum_{\mathbf{k}i} \varepsilon_{i\mathbf{k}} \hat{c}_{i\mathbf{k}}^\dagger \hat{c}_{i\mathbf{k}} + \sum_{\mathbf{q}\nu} \hbar\omega_{\mathbf{q}\nu} \left(\hat{a}_{\mathbf{q}\nu}^\dagger \hat{a}_{\mathbf{q}\nu} + \frac{1}{2} \right) + N_p^{-\frac{1}{2}} \sum_{\mathbf{k}\mathbf{q}i j \nu} g_{\mathbf{k},\mathbf{k}+\mathbf{q},ij}^\nu \hat{c}_{j\mathbf{k}+\mathbf{q}}^\dagger \hat{c}_{i\mathbf{k}} \left(\hat{a}_{\mathbf{q}\nu} + \hat{a}_{-\mathbf{q}\nu}^\dagger \right), \quad (3.1)$$

where i, j are electronic band indices, the ν 's are phonon band indices and N_p is the number of unit cells in the system. The first two terms are the individual electron Hamiltonians (with creation/annihilation operators $\hat{c}_{i\mathbf{k}}^\dagger/\hat{c}_{i\mathbf{k}}$) and phonon Hamiltonians (with operators $\hat{a}_{\mathbf{q}\nu}^\dagger/\hat{a}_{\mathbf{q}\nu}$) in second quantization. The third term provides the coupling between these particles, where $g_{\mathbf{k},\mathbf{k}+\mathbf{q},ij}^\nu$ are the e - ph couplign matrix elements. The second order correction to Eq. 3.1 involves matrix elements of the form $\tilde{g}_{\mathbf{k},\mathbf{k}+\mathbf{q},\mathbf{k}+\mathbf{q}',ij}^{\nu\nu'}$ and depends on operator products $\left(\hat{a}_{\mathbf{q}\nu} + \hat{a}_{-\mathbf{q}\nu}^\dagger \right) \left(\hat{a}_{\mathbf{q}'\nu'} + \hat{a}_{-\mathbf{q}'\nu'}^\dagger \right)$, indicating the two-phonon nature of the second order [183]. In this thesis we will only consider the e - ph interaction to first order.

The main question to address is how to calculate the e - ph matrix elements. For scattering of electrons moving in an effective potential V_0 by acoustic phonons with wave vector \mathbf{q} one finds [183]

$$g_{\mathbf{k},\mathbf{k}+\mathbf{q},ij}^\nu = -i \sum_{\kappa} \left(\frac{\hbar}{2N_p M_\kappa \omega_{\mathbf{q}\nu}} \right)^{\frac{1}{2}} \mathbf{q} \cdot \mathbf{e}_{\kappa\nu} V_0. \quad (3.2)$$

Here, $\mathbf{e}_{\kappa\nu}$ is the eigenmode of the κ -th nucleus. This matrix element demonstrates that among the *acoustic* phonons only the longitudinal ones (with $\mathbf{e}_{\kappa\nu} \parallel \mathbf{q}$) can couple to electrons. Notice that there is no dependence on

the electronic band indices in this formula, so that it is only really valid for monovalent metals (with a single valence electron per atom). To extend this to systems with several different, interacting electron a more elaborate description that includes electronic screening is needed. This is the subject of the next section.

3.4 First-principles calculations

The majority of historical and present theoretical investigations of phenomena enabled by *e-ph* interaction rely on semi-empirical model Hamiltonians. However, it is possible to calculate the *e-ph* interaction completely from first principles, albeit with considerable computational complexity. The underpinning theory enabling these calculations is *density functional perturbation theory* (DFPT) [184–186].

3.4.1 Calculating phonons

The first step to compute phonon dispersions is to calculate how the total energy depends on atomic displacements. We will denote the position vectors of the nuclei as $\boldsymbol{\tau}_\kappa$, with components $\tau_{\kappa\alpha}$. Thus, the position of a nucleus in the p -th unit cell is $\boldsymbol{\tau}_{\kappa p} = \mathbf{R}_p + \boldsymbol{\tau}_\kappa$. To second order in the displacements, $\Delta\tau_{\kappa p\alpha}$, the expansion of the total energy of the electrons and the nuclei around the equilibrium value $E_{\text{tot}}^{(0)}$ is

$$E_{\text{tot}}(\{\boldsymbol{\tau}_{\kappa p}\}) = E_{\text{tot}}^{(0)} + \frac{1}{2} \sum_{\kappa\kappa'\alpha\alpha'pp'} \frac{\partial^2 E_{\text{tot}}(\{\boldsymbol{\tau}_{\kappa p}\})}{\partial\tau_{\kappa p\alpha}\partial\tau_{\kappa'p'\alpha'}} \Delta\tau_{\kappa p\alpha}\Delta\tau_{\kappa'p'\alpha'} . \quad (3.3)$$

This total energy can be calculated in DFT along the lines elaborated in Chapter 2, within the Born-Oppenheimer approximation. Thus, the *interatomic force constants* $C_{\kappa p\alpha,\kappa'p'\alpha'}$ emerge as an extension of the spring constant:

$$C_{\kappa p\alpha,\kappa'p'\alpha'} = \frac{\partial^2 E_{\text{tot}}(\{\boldsymbol{\tau}_{\kappa p}\})}{\partial\tau_{\kappa p\alpha}\partial\tau_{\kappa'p'\alpha'}} . \quad (3.4)$$

The Fourier transform of these interatomic force constants is the *dynamical matrix*,

$$\mathcal{D}_{\kappa\alpha,\kappa'\alpha'} = (M_\kappa M_{\kappa'})^{-\frac{1}{2}} \sum_p C_{\kappa 0\alpha,\kappa' p\alpha'} \exp(i\mathbf{q} \cdot \mathbf{R}_p) . \quad (3.5)$$

It is a Hermitian matrix, so with real eigenvalues,

$$\sum_{\kappa'\alpha'} \mathcal{D}_{\kappa\alpha,\kappa'\alpha'}(\mathbf{q}) e_{\kappa'\nu\alpha'}(\mathbf{q}) = \omega_{\mathbf{q}\nu}^2 e_{\kappa\nu\alpha}(\mathbf{q}) , \quad (3.6)$$

where $e_{\kappa\nu\alpha}$ is again the eigenmode of nucleus κ under the influence of phonon branch ν . From this eigenvalue equation the phonon dispersion $\omega_{\mathbf{q}\nu}$ and the eigenmodes can be determined.

3.4.2 Calculating the electron-phonon interaction

While the derivatives of the total energy suffice to calculate the phonon dispersions and eigenmodes, for the *e-ph* coupling the Kohn-Sham (KS) potentials – perturbed under the influence of the atomic displacements – are needed. We denote the variations in the KS potential under the influence of phonon mode ν and wave vector \mathbf{q} as $\Delta_{\mathbf{q}\nu} V^{\text{KS}}$. Then, the matrix elements arising in the third term of Eq. 3.1 are given by [183]

$$g_{\mathbf{k},\mathbf{k}+\mathbf{q},ij}^\nu = \langle \psi_{j\mathbf{k}+\mathbf{q}} | \Delta_{\mathbf{q}\nu} V_{\text{KS}} | \psi_{i\mathbf{k}} \rangle , \quad (3.7)$$

where the integral is carried out over the N_p unit cells we are considering.

3.4.3 Frozen-phonon method

The first approach to evaluate the variation of the KS potential in Eq. 3.7 is to expand it around the equilibrium position $\tau_{\kappa p}^0$ as

$$\Delta_{\mathbf{q}\nu} V_{\text{KS}} = \sum_{\kappa p} \left. \frac{\partial V_{\text{KS}}}{\partial \tau_{\kappa p\alpha}} \right|_{\tau_{\kappa p}^0} \Delta_{\mathbf{q}\nu} \tau_{\kappa p\alpha} , \quad (3.8)$$

and to approximate the derivative with finite differences b :

$$\left. \frac{\partial V_{\text{KS}}}{\partial \tau_{\kappa p \alpha}} \right|_{\tau_{\kappa p}^0} \simeq [V_{\text{KS}}(\mathbf{r}; \tau_{\kappa p \alpha}^0 + b) - V_{\text{KS}}(\mathbf{r}; \tau_{\kappa p \alpha}^0)] / b . \quad (3.9)$$

To this end, atom κ in cell p needs to be displaced along direction α . This means that in principle all atoms in the N_p unit cells need to be moved in all directions to obtain a complete description of the phonons. This supercell approach to calculating the e - ph coupling is also called the *frozen-phonon* method, as chosen vibrational eigenmodes are frozen in to evaluate Eq. 3.9. Clearly, this method comes with a great disadvantage, namely, that one needs to consider a set of N_p unit cells, not taking fully advantage of the periodic lattice symmetry. This leads to serious computational restrictions. Therefore, a more efficient approach is to include lattice periodicity, which forms the base of DFPT, discussed in the next section.

3.4.4 Density functional perturbation theory (DFPT)

3.4.4.1 Formalism

To fully take advantage of the lattice periodicity we define

$$\Delta_{\mathbf{q}\nu} v^{\text{KS}} = e^{-i\mathbf{q}\cdot\mathbf{r}} \Delta_{\mathbf{q}\nu} V^{\text{KS}} \quad (3.10)$$

as the lattice-periodic variation of the KS potential. It can be related to the *differential variation*, $\partial_{\kappa\alpha, \mathbf{q}} v_{\text{KS}}$, through

$$\Delta_{\mathbf{q}\nu} v_{\text{KS}} = \sum_{\kappa\alpha} \sqrt{\frac{\hbar}{2M_{\kappa}\omega_{\mathbf{q}\nu}}} e_{\kappa\nu\alpha} \partial_{\kappa\alpha, \mathbf{q}} v_{\text{KS}} . \quad (3.11)$$

The lattice-periodic differential variation can be explicitly calculated as

$$\partial_{\kappa\alpha, \mathbf{q}} v_{\text{KS}} = \sum_p e^{-i\mathbf{q}\cdot(\mathbf{r}-\mathbf{R}_p)} \left. \frac{\partial V_{\text{KS}}}{\partial \tau_{\kappa\alpha}} \right|_{\mathbf{r}-\mathbf{R}_p} . \quad (3.12)$$

Here $\tau_{\kappa} = \mathbf{r} - \mathbf{R}_p$ indicates that the whole system is indeed described by a single unit cell. From Eq. 3.10 it immediately follows that matrix element 3.7 can be stated in terms of the lattice-periodic factors $|u_{i\mathbf{k}}\rangle$ of the Bloch

wave function,

$$g_{\mathbf{k},\mathbf{k}+\mathbf{q},ij}^{\nu} = \langle u_{j\mathbf{k}+\mathbf{q}} | \Delta_{\mathbf{q}\nu} v_{\text{KS}} | u_{i\mathbf{k}} \rangle_{\text{uc}} , \quad (3.13)$$

‘uc’ indicating that the integral is restricted to a single unit cell.

Density functional perturbation theory (DFPT) can now be constructed analogously to DFT. The DFPT equivalent of the KS potential in Eq. 2.40 reads

$$\partial_{\kappa\alpha,\mathbf{q}} v_{\text{KS}} = \partial_{\kappa\alpha,\mathbf{q}} v_{\text{XC}} + \partial_{\kappa\alpha,\mathbf{q}} v_{\text{H}} + \partial_{\kappa\alpha,\mathbf{q}} v_{\text{ext}} . \quad (3.14)$$

The DFPT equivalents of the KS equations can be obtained from first-order perturbation theory. In terms of the KS Hamiltonian, $\hat{H}_{\text{KS},\mathbf{k}+\mathbf{q}} = e^{-i(\mathbf{k}+\mathbf{q})\cdot\mathbf{r}} \hat{H}_{\text{KS}} e^{i(\mathbf{k}+\mathbf{q})\cdot\mathbf{r}}$, and the wave function change, $\partial u_{i\mathbf{k},\mathbf{q}}$, the first-order variation of the KS equations takes the form of the *Sternheimer equations* [183]

$$\left(\hat{H}_{\text{KS},\mathbf{k}+\mathbf{q}} - \varepsilon_{v\mathbf{k}} \right) \partial u_{v\mathbf{k},\mathbf{q}} = -\partial_{\kappa\alpha,\mathbf{q}} v_{\text{KS}} u_{v\mathbf{k}} , \quad (3.15)$$

where v replacing electronic band index i indicates that only the occupied, *valence states* play a role here. Eq. 3.15 is restricted to $\mathbf{q} \neq 0$. At $\mathbf{q} = 0$ one obtains instead

$$\left(\hat{H}_{\text{KS},\mathbf{k}} - \varepsilon_{v\mathbf{k}} \right) \partial u_{v\mathbf{k},\mathbf{q}=0} = - \left[\partial_{\kappa\alpha,\mathbf{q}=0} v_{\text{KS}} + \langle u_{v\mathbf{k}} | \partial_{\kappa\alpha,\mathbf{q}=0} v_{\text{KS}} | u_{v\mathbf{k}} \rangle \right] u_{v\mathbf{k}} . \quad (3.16)$$

3.4.4.2 Computational approach and challenges

To step from the formalism elaborated in the preceding section to practical calculations, some additional considerations are required.

Projectors and iterations. In practice, evaluating Eqs. 3.15 and 3.16 yields problems in case of near-degeneracy $\varepsilon_{v'\mathbf{k}+\mathbf{q}} \simeq \varepsilon_{v\mathbf{k}}$, whereby the left-hand side of the Sternheimer equations becomes ill-conditioned. To resolve this issue, one defines the projector over occupied states with wave vector $\mathbf{k} + \mathbf{q}$ as $\hat{P}_{\mathbf{k}+\mathbf{q}}^{\text{occ}} = \sum_v |u_{v\mathbf{k}+\mathbf{q}}\rangle \langle u_{v\mathbf{k}+\mathbf{q}}|$. The resulting changes in the wave

functions can be denoted as

$$\partial\tilde{u}_{v\mathbf{k},\mathbf{q}} = \left(1 - \hat{P}_{\mathbf{k}+\mathbf{q}}^{\text{occ}}\right) \partial u_{v\mathbf{k},\mathbf{q}} , \quad (3.17)$$

so that this rewritten variation of the wave function involves *only unoccupied components* [187]. By projecting Eq. 3.15 onto $\left(1 - \hat{P}_{\mathbf{k}+\mathbf{q}}^{\text{occ}}\right)$ and by adding $\alpha\hat{P}_{\mathbf{k}+\mathbf{q}}^{\text{occ}}\partial\tilde{u}_{v\mathbf{k},\mathbf{q}}$ (α being a parameter larger than the valence bandwidth) – which is zero by construction – to the left-hand side, one obtains

$$\left(\hat{H}_{\text{KS},\mathbf{k}+\mathbf{q}} - \varepsilon_{v\mathbf{k}} + \alpha\hat{P}_{\mathbf{k}+\mathbf{q}}^{\text{occ}}\right) \partial\tilde{u}_{v\mathbf{k},\mathbf{q}} = -\left(1 - \hat{P}_{\mathbf{k}+\mathbf{q}}^{\text{occ}}\right) \partial_{\kappa\alpha,\mathbf{q}} v_{\text{KS}} u_{v\mathbf{k}} . \quad (3.18)$$

Now, the left-hand side is well-conditioned in case of (near-)degeneracies. The corresponding electronic density response is [183]

$$\partial n_{\mathbf{q}}(\mathbf{r}) = 2N_p^{-1} \sum_{v\mathbf{k}} u_{v\mathbf{k}}^* \partial\tilde{u}_{v\mathbf{k},\mathbf{q}} , \quad (3.19)$$

where the prefactor 2 stems from time-reversal symmetry.

Just like in the solution of the KS equations in DFT, in DFPT the Sternheimer equations are solved *iteratively*. First, an initial guess for the perturbation $\partial_{\kappa\alpha,\mathbf{q}} v_{\text{KS}} - \mathbf{q}$ being a specific wave vector under consideration – is chosen. Then, Eq. 3.18 is solved, yielding the density response $\partial n_{\mathbf{q}}(\mathbf{r})$. This density gives the updated KS potential. This procedure is repeated until the result is self-consistent, in other words, until the changes in $\partial n_{\mathbf{q}}(\mathbf{r})$ are converged within the chosen tolerance.

Acoustic sum rule. The perturbation $\partial_{\kappa\alpha,\mathbf{q}} v_{\text{KS}}$ is also the main ingredient for calculating the interatomic force constants. However, since finite \mathbf{k} grids are used in these calculations, numerical errors can introduce a violation of the invariance of the crystal energy under uniform translations. A major problem that arises is that in this case $\omega_{\nu}(\mathbf{q} \rightarrow 0) \not\rightarrow 0$ for the acoustic modes. To ensure that translational symmetries are obeyed, the force constants are corrected by imposing the constraint

$$\sum_{\kappa'} C_{\kappa\alpha,\kappa'\alpha'}(\mathbf{q} = 0) = 0 , \quad (3.20)$$

which is called the *acoustic sum rule* (ASR), that needs to be evaluated for all components α and α' .

Implementation in ABINIT. For this thesis DFPT as implemented in ABINIT was employed [185, 188–190]. In order to calculate the phonons, the first step is to carry out a ground state calculation that yields the wave functions needed to evaluate Eq. 3.18. In the next step, perturbations are carried out one by one, for each atom, each \mathbf{q} vector and for all Cartesian directions (x, y, z). The grid of \mathbf{q} -points needs to be a subgrid of the \mathbf{k} -point grid. E.g., when the latter is $24 \times 24 \times 1$ for a 2D material, a \mathbf{q} -point grid of $12 \times 12 \times 1$ can be selected. Finally, the *e-ph* matrix elements are evaluated as in Eq. 3.13.

Finally, the last steps of phonon and *e-ph* coupling calculations in ABINIT consist of constructing the dynamical matrices, and one can obtain isotropic estimates of superconducting properties, such as the isotropic Eliashberg function, α^2F , and the critical temperature, T_c .

Computational cost. From the preceding section one can see that DFPT calculations are computationally very challenging. In order to obtain accurate and well-converged results one needs to use a dense grid of phonon wave vectors, \mathbf{q} , and for each of the points of this grid one has to consider all atomic displacement, in all three Cartesian directions. So, per \mathbf{q} point, the number of perturbations that needs to be treated is $3N$, N being the number of atoms in the unit cell. Therefore, DFPT calculations bear the computational cost of $3N \cdot N_{\mathbf{q}}$ self-consistent field (SCF) calculations (where $N_{\mathbf{q}}$ is the number of phonon wave vectors). Moreover, each of these calculations also need very dense \mathbf{k} -point grids for the electronic wave vectors, in order to correctly describe the Fermi surfaces of the metals under consideration. The computational cost increases further with the number of atoms. Not only does $3N \cdot N_{\mathbf{q}}$ grow linearly, but the computational cost of each SCF calculation also increases as more electronic states have to be taken into account. Since DFT routines typically scale as N^3 , DFPT routines scale as N^4 with the system size. This leads to restrictions in feasible system sizes that can currently be investigated.

For some materials – those consisting of heavy nuclei – spin-orbit coupling (SOC) is considerable and needs to be taken into account. One example of such a system are the transition metal dichalcogenides (TMDs) in Chapter 8 of this thesis. The inclusion of SOC doubles the number of KS equations, since spin degeneracy is lifted. This increases the computational cost further. Fortunately, DFPT can be parallelized efficiently, as the Sternheimer equations can be solved independently for each \mathbf{k} -point (and each band, if necessary). Thus, large-scale \mathbf{k} -point parallelization on high-performance computational infrastructure has enabled the calculations needed for this thesis.

3.5 Migdal-Eliashberg theory

The aim of *Migdal-Eliashberg theory* is to describe the superconducting state in a more realistic way than BCS theory [191, 192]. In the BCS theory, the *e-ph* interaction is instantaneous and restricted to acoustic phonons. Eliashberg theory includes a more realistic description of the *e-ph* interaction, with *retardation effects* in the electronic states under the influence of the interaction with the phonon. Moreover, *Coulomb interactions* between the electrons are taken into account, leading to competition between phonon-mediated coupling and Coulomb repulsion. After this point, we will refer to the theory as *Eliashberg theory* in brief. As we will see, Migdal has provided the foundation for the theory, in the form of *Migdal's theorem*, but Eliashberg derived the central *Eliashberg equations* of the theory. Eliashberg theory is a *statistical field theory*, so we will use the concepts of field operators, propagators and Feynman diagrams [11].

3.5.1 Nambu spinor formulation

The electron-phonon coupling Hamiltonian of Eq. 3.1 can be restated in terms of the Nambu 2-component spinors, introduced in Chapter 1. The electronic field operators in Nambu form read,

$$\hat{\psi}_{\mathbf{k}} = \begin{pmatrix} \hat{c}_{\mathbf{k}\uparrow} \\ \hat{c}_{-\mathbf{k}\downarrow}^\dagger \end{pmatrix}; \quad \hat{\psi}_{\mathbf{k}}^\dagger = \left(\hat{c}_{\mathbf{k}\uparrow}^\dagger \quad \hat{c}_{-\mathbf{k}\downarrow} \right), \quad (3.21)$$

while the phonon field operators, $\hat{a}_{\mathbf{q}\nu}$ and $\hat{a}_{\mathbf{q}\nu}^\dagger$, remain unaltered, and their combination can be written as $\hat{\varphi}_{\mathbf{q}\nu} = \left(\hat{a}_{\mathbf{q}\nu} + \hat{a}_{-\mathbf{q}\nu}^\dagger\right)$. With this notation the *e-ph* coupled Hamiltonian introduced in Eq. 3.1 becomes²

$$\begin{aligned} \hat{H} = & \sum_{\mathbf{k}} \varepsilon_{\mathbf{k}} \hat{\psi}_{\mathbf{k}}^\dagger \hat{\tau}_3 \hat{\psi}_{\mathbf{k}} + \sum_{\mathbf{q}\nu} \hbar\omega_{\mathbf{q}\nu} \left(\hat{a}_{\mathbf{q}\nu}^\dagger \hat{a}_{\mathbf{q}\nu} + \frac{1}{2} \right) + \sum_{\mathbf{k}\mathbf{q}\nu} g_{\mathbf{k},\mathbf{k}+\mathbf{q}}^\nu \hat{\psi}_{\mathbf{k}+\mathbf{q}}^\dagger \hat{\tau}_3 \hat{\psi}_{\mathbf{k}} \hat{\varphi}_{\mathbf{q}\nu} \\ & + \frac{1}{2} \sum_{\mathbf{k}_1\mathbf{k}_2\mathbf{k}_3\mathbf{k}_4} \langle \mathbf{k}_3\mathbf{k}_4 | V_C | \mathbf{k}_1\mathbf{k}_2 \rangle \left(\hat{\psi}_{\mathbf{k}_3}^\dagger \hat{\tau}_3 \hat{\psi}_{\mathbf{k}_1} \right) \left(\hat{\psi}_{\mathbf{k}_4}^\dagger \hat{\tau}_3 \hat{\psi}_{\mathbf{k}_2} \right) , \end{aligned} \quad (3.22)$$

where the extra last term describes the Coulomb interaction, V_C being the Coulomb potential. Translational invariance dictates that $\mathbf{k}_1 + \mathbf{k}_2 - \mathbf{k}_3 - \mathbf{k}_4 = n\mathbf{G}$, where $n \in \mathbb{Z}$ and \mathbf{G} is a reciprocal lattice vector. We used here and will use throughout this chapter the following Pauli matrices (including the identity matrix), usually denoted $\hat{\tau}_i$ in Nambu space:

$$\hat{\tau}_0 = \begin{pmatrix} 1 & 0 \\ 0 & 1 \end{pmatrix}, \quad \hat{\tau}_1 = \begin{pmatrix} 0 & 1 \\ 1 & 0 \end{pmatrix}, \quad \hat{\tau}_2 = \begin{pmatrix} 0 & -i \\ i & 0 \end{pmatrix}, \quad \hat{\tau}_3 = \begin{pmatrix} 1 & 0 \\ 0 & -1 \end{pmatrix}. \quad (3.23)$$

In the Nambu formalism the electron and phonon Green's functions, in terms of imaginary time τ , become respectively [191]

$$\begin{aligned} \hat{G}(\mathbf{k}, \tau) &= -\langle \hat{\mathcal{T}} \{ \hat{\psi}_{\mathbf{k}}(\tau) \hat{\psi}_{\mathbf{k}}^\dagger(0) \} \rangle , \\ D_\nu(\mathbf{q}, \tau) &= -\langle \hat{\mathcal{T}} \{ \hat{\varphi}_{\mathbf{q}\nu}(\tau) \hat{\varphi}_{\mathbf{q}\nu}^\dagger(0) \} \rangle , \end{aligned} \quad (3.24)$$

where the average is over the grand canonical ensemble, i.e.,

$$\langle Q \rangle = \mathcal{Z}^{-1} \text{Tr} e^{-\beta \hat{H}} Q , \quad (3.25)$$

with $\mathcal{Z} = \text{Tr} e^{-\beta \hat{H}}$ and $\beta = T^{-1}$, and where $\hat{\mathcal{T}}$ is the time-ordering operator [11]. The electron Green's function is a 2×2 matrix here owing to the Nambu formulation. The diagonal elements are the conventional Green's functions, while the off-diagonal elements describe the pairing. We will calculate it explicitly in the following sections. Both Green's functions can be expanded

²For notational simplicity within the Nambu formulation we omit electronic band indices here. It is implied that there are different bands, so that the formalism derived here holds entirely in the multiband case. The matrix elements $g_{\mathbf{k},\mathbf{k}+\mathbf{q},ij}^\nu$ therefore also simplify to $g_{\mathbf{k},\mathbf{k}+\mathbf{q}}^\nu$.

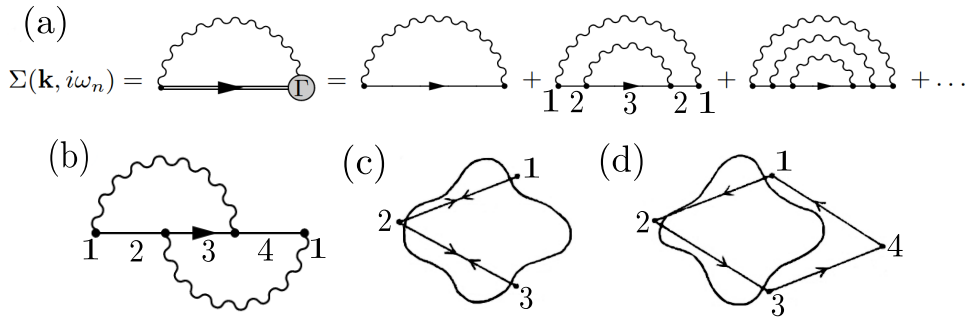


FIGURE 3.3: Feynman diagrams related to Migdal-Eliashberg theory. (a) The self-energy of the electron under the influence of electron-phonon interaction. The diagram on the left is a schematic representation of this system where the thick horizontal line is the interacting electron propagator, the wavy line interacting phonon propagator and Γ the vertex. On the right the Dyson series of this diagram is shown with increasingly higher orders of phonon exchange. (b) First-order vertex correction, which according to Migdal's theorem is negligible in most systems. (c) Fermi surface with second order phonon exchange depicted in (a). (d) Fermi surface corresponding to the vertex correction depicted in (b). Adapted from Ref. 191.

into Fourier series,

$$\hat{G}(\mathbf{k}, \tau) = \frac{1}{\beta} \sum_{n=-\infty}^{\infty} e^{-i\omega_n \tau} \hat{G}(\mathbf{k}, i\omega_n),$$

$$D_\nu(\mathbf{q}, \tau) = \frac{1}{\beta} \sum_{n=-\infty}^{\infty} e^{-i\tilde{\omega}_n \tau} D_\nu(\mathbf{q}, i\tilde{\omega}_n),$$
(3.26)

where $i\omega_n = i(2n+1)\pi/\beta$ are the fermionic Matsubara frequencies and $i\tilde{\omega}_n = i2n\pi/\beta$ are the bosonic Matsubara frequencies, with integer n .

3.5.2 Migdal's theorem

The starting point of Eliashberg theory is the Dyson summation of the electron-phonon interaction, shown as a Feynman diagram in Fig. 3.3(a). This also includes vertex corrections, like the one shown in Fig. 3.3(b). However, Migdal's theorem states that the vertex correction is smaller than the

leading terms in the Dyson summation by a factor $\omega_{\text{ph}/E_F} \sim \sqrt{m_e/M} \ll 1$, where m_e and M are electronic and nuclear masses respectively [193]³.

An intuitive picture of Migdal's theorem is provided in Figs. 3.3(c) and (d). These depict scattering between electronic states, where the solid line indicates the Fermi surface and the arrows indicate the scattering vectors [191]. Fig. 3.3(c) corresponds to the second-order phonon exchange shown in Fig. 3.3(a). The energy difference between two states, ϵ_{12} and ϵ_{23} , are small as all states, 1 to 3, are very near to the Fermi surface. These energy differences appear in the denominator of the self-energy due to the vertex correction, $\hat{\Sigma}_\Gamma$, so this contribution is important. This is why all orders are included in the Dyson summation of the e - ph interaction. Fig. 3.3(d) depicts the scattering of the Feynman diagram in Fig. 3.3(b). Here, ϵ_{14} is generally large, since state 4 does not lie near the Fermi level contrary to the other states, leading to a very small contribution to $\hat{\Sigma}_\Gamma$. This corresponds to Migdal's theorem.

Migdal's theorem does not necessarily hold in two cases, namely,

1. when either phonon has small $|\mathbf{q}|$,
2. when the Fermi surface has a 1D topology.

We can see this visually. In the first case, let us say that $|\mathbf{q}_{23}| \sim 0$, then the parallelogram describing the scattering in Fig. 3.3(d) becomes elongated and skinny, so that state 4 lies close to state 1. Thus, all energy differences are small, and $\hat{\Sigma}_\Gamma$ is large, so that Migdal's theorem does not necessarily hold in this case⁴. In the second case, the Fermi surface consists of parallel planes ($k_x = \pm k_F$). When the parallelogram has two sides parallel with these planes, states 2 and 3 will have the same k_x , hence the same energy, and the same for states 1 and 4. Clearly, Migdal's theorem also does not hold in this case.

³A modern version of the proof can be found in Ref. 182, pp. 115-116

⁴Nevertheless, recently Eliashberg theory within the Migdal approximation has been applied to superconductors with small- \mathbf{q} phonons, such as MgB₂, yielding results in qualitatively good agreement with the experiments [36, 38, 39]. Other cases exist where the vertex corrections are small despite the small- \mathbf{q} nature of the exchanged phonons [194]. This indicates that while the validity of Migdal's theorem is not guaranteed in the small- \mathbf{q} case, the vertex corrections can still be negligible. This justifies our treatment of atomically thin MgB₂ within the Migdal approximation in Chapters 6 and 7.

For 2D topologies, on the other hand, Migdal's theorem holds entirely, which is crucial for the study of atomically thin superconductors in this thesis.

In the case of multiband superconductors, with several different sheets at the Fermi level, Migdal's theorem also remains generally valid. Namely, the chance that the four vertices of parallelograms such as in Fig. 3.3(d) are all connected to points close to the Fermi level is not significantly higher than in the single-band case. Accidentally, two phonon wave vectors can exist such that point 4 lies near a second sheet (just like in the single-band case point 4 may accidentally lie near the sheet), but interband coupling according to a rainbow diagram as in Fig. 3.3(a) will generally outweigh this scenario by far, also in the multiband case.

So, owing to Migdal's theorem the vertex Γ in Fig. 3.3(a) can be set to the *bare (non-interacting) vertex* to a very good approximation, in other words, the diagram in Fig. 3.3(b) is disregarded in the Dyson summation. The electronic self-energy following from Fig. 3.3(a) within the Migdal approximation is [191]

$$\hat{\Sigma}(\mathbf{k}, i\omega_n) = -T \sum_{\mathbf{q}n'\nu} \hat{\tau}_3 \hat{G}(\mathbf{k} + \mathbf{q}, i\omega_{n'}) \hat{\tau}_3 \left[|g^\nu(\mathbf{q})|^2 D_\nu(\mathbf{q}, i\omega_n - i\omega_{n'}) + V_C(\mathbf{k}, \mathbf{k} + \mathbf{q}) \right], \quad (3.27)$$

where $D_\nu(\mathbf{q}, i\omega_n - i\omega_{n'})$ is the *dressed (interacting) phonon Green's function*,

$$D_\nu(\mathbf{q}, i\omega_n - i\omega_{n'}) = \frac{2\omega_{\mathbf{q}\nu}}{(\omega_n - \omega_{n'})^2 + \omega_{\mathbf{q}\nu}^2}. \quad (3.28)$$

3.5.3 Eliashberg equations

As stated in the previous section, we can determine the interacting electron Green's function by means of the Dyson equation,

$$\hat{G}^{-1}(\mathbf{k}, i\omega_n) = \hat{G}_0^{-1}(\mathbf{k}, i\omega_n) - \hat{\Sigma}(\mathbf{k}, i\omega_n), \quad (3.29)$$

where $\hat{G}_0(\mathbf{k}, i\omega_n)$ is the bare electron Green's function,

$$\hat{G}_0(\mathbf{k}, i\omega_n) = [i\omega_n \hat{\tau}_0 - \varepsilon_{\mathbf{k}} \hat{\tau}_3]^{-1}. \quad (3.30)$$

Owing to Migdal's theorem vertex contributions in the electronic self-energy $\hat{\Sigma}$ can be disregarded. In this we can use Eq. 3.27, which can be restated in the general form,

$$\hat{\Sigma}(\mathbf{k}, i\omega_n) = i\omega_n [1 - Z(\mathbf{k}, i\omega_n)] \hat{\tau}_0 + \chi(\mathbf{k}, i\omega_n) \hat{\tau}_3 + \phi(\mathbf{k}, i\omega_n) \hat{\tau}_1 + \bar{\phi}(\mathbf{k}, i\omega_n) \hat{\tau}_2, \quad (3.31)$$

where Z , χ , ϕ and $\bar{\phi}$ at this point are independent, arbitrary functions. By combining Eqs. 3.29, 3.30 and 3.31 we obtain

$$\hat{G}^{-1}(\mathbf{k}, i\omega_n) = i\omega_n Z \hat{\tau}_0 - (\varepsilon_{\mathbf{k}} + \chi) \hat{\tau}_3 - \phi \hat{\tau}_1 - \bar{\phi} \hat{\tau}_2, \quad (3.32)$$

and inverting yields

$$\begin{aligned} \hat{G}(\mathbf{k}, i\omega_n) &= \frac{1}{\det \hat{G}^{-1}} [i\omega_n Z \hat{\tau}_0 + (\varepsilon_{\mathbf{k}} + \chi) \hat{\tau}_3 + \phi \hat{\tau}_1 + \bar{\phi} \hat{\tau}_2] \\ &= \frac{1}{\det \hat{G}^{-1}} \begin{pmatrix} i\omega_n Z + (\varepsilon_{\mathbf{k}} + \chi) & \phi - i\bar{\phi} \\ \phi + i\bar{\phi} & i\omega_n Z - (\varepsilon_{\mathbf{k}} + \chi) \end{pmatrix}, \end{aligned} \quad (3.33)$$

with $\det \hat{G}^{-1} = (i\omega_n Z)^2 - (\varepsilon_{\mathbf{k}} + \chi)^2 - \phi^2 - \bar{\phi}^2$. The *poles* of the Green's function matrix – which are the *quasiparticle excitation energies* – occur when $\det \hat{G}^{-1} = 0$, yielding

$$E_{\mathbf{k}} = \frac{1}{Z} \sqrt{(\varepsilon_{\mathbf{k}} + \chi)^2 + \phi^2 + \bar{\phi}^2}. \quad (3.34)$$

By defining the *gap function* $\Delta(\mathbf{k}, i\omega_n) = (\phi - i\bar{\phi})/Z$ we obtain

$$E_{\mathbf{k}} = \sqrt{\frac{(\varepsilon_{\mathbf{k}} + \chi)^2}{Z^2} + |\Delta|^2}. \quad (3.35)$$

This corresponds to the *Bogoliubov spectrum*, introduced in Chapter 1, albeit with extra contributions χ and Z . Naturally, the diagonal Green's functions, with $\phi = \bar{\phi} = 0$ corresponds to the normal state. We can also interpret χ and Z from Eq. 3.35. The function χ shifts the electronic energies, while Z is a *renormalization function*. More specifically, it introduces a renormalization of the electron mass, hence the name *mass renormalization function*. It can be understood intuitively as the phonons slowing the electron down. To a first approximation, the Fermi velocity is renormalized by the average *e-ph* coupling constant λ as $v_{\mathbf{F}}^* = v_{\mathbf{F}}/(1 + \lambda)$ [182]. This can be described

alternatively as an increase in the electron mass, $m_e^* = m_e(1 + \lambda)$.

In order to fully characterize the quasiparticle spectrum, a recipe to calculate χ , Δ and Z needs to be provided. We will proceed immediately to the central result, the *anisotropic Eliashberg equations* [195, 196]⁵. Under ‘anisotropic’ we understand that the spatial dependence (in reciprocal space, \mathbf{k}) of the functions Δ and Z is fully accounted for. This is crucial to study anisotropic, multiband and multigap superconductors.

The resulting anisotropic Eliashberg equations are the following two coupled equations:

$$Z(\mathbf{k}, i\omega_n) = 1 + \frac{\pi T}{\omega_n} \sum_{\mathbf{k}'n'} \frac{\delta(\varepsilon_{\mathbf{k}'})}{N_F} \lambda(\mathbf{k}\mathbf{k}', i\omega_n - i\omega_{n'}) \times \frac{\omega_{n'}}{\sqrt{\omega_{n'}^2 + \Delta^2(\mathbf{k}', i\omega_{n'})}} \quad (3.36)$$

$$\Delta(\mathbf{k}, i\omega_n) Z(\mathbf{k}, i\omega_n) = \pi T \sum_{\mathbf{k}'n'} \frac{\delta(\varepsilon_{\mathbf{k}'})}{N_F} [\lambda(\mathbf{k}\mathbf{k}', i\omega_n - i\omega_{n'}) - N_F V_C(\mathbf{k}, \mathbf{k}')] \times \frac{\Delta(\mathbf{k}', i\omega_{n'})}{\sqrt{\omega_{n'}^2 + \Delta^2(\mathbf{k}', i\omega_{n'})}} . \quad (3.37)$$

Here, the *anisotropic e-ph coupling* is

$$\lambda(\mathbf{k}\mathbf{k}', i\omega_n - i\omega_{n'}) = \int_0^\infty d\omega \alpha^2 F(\mathbf{k}\mathbf{k}', \omega) \frac{2\omega}{(\omega_n - \omega_{n'})^2 + \omega^2} , \quad (3.38)$$

where we can clearly distinguish the phonon Green’s function (cf. Eq. 3.28), and where $\alpha^2 F(\mathbf{k}\mathbf{k}', \omega)$ is the *anisotropic Eliashberg function* defined as

$$\alpha^2 F(\mathbf{k}\mathbf{k}', \omega) = N_F \sum_{\nu} |g_{\mathbf{k}\mathbf{k}'}^{\nu}|^2 \delta(\omega - \omega_{\mathbf{q}\nu}) , \quad (3.39)$$

where $\mathbf{q} = \mathbf{k}' - \mathbf{k}$ and where $g_{\mathbf{k}\mathbf{k}'}^{\nu}$ and $\omega_{\mathbf{q}\nu}$ are the phonon branch-resolved *e-ph* scattering matrix elements and phonon frequencies, respectively. This function can be viewed as the phonon DOS renormalized by the *e-ph* coupling. Function χ has vanished from the Eliashberg equations within the approximation that the electronic DOS is constant in the vicinity of the Fermi level,

⁵The derivation of the Eliashberg equations is rather lengthy, therefore we do not show it here. It can be found in Ref. 191, pp. 41-45.

resulting to $\chi \equiv 0$. In the more general case two extra equations for χ needs to be taken into account [192].

The Eliashberg equations are to be solved *self-consistently*. Furthermore, the solution yields $\Delta(\mathbf{k}, i\omega_n)$ and $Z(\mathbf{k}, i\omega_n)$. Of course, we are interested in the real-frequency dependence of these functions. To that end, an *analytic continuation* needs to be carried out. We will briefly explain a practical scheme to do so in Sec. 3.5.7.2.

In Chapter 5 we will present an extension of the anisotropic Eliashberg equations that includes the interaction with ferromagnetic spin fluctuations.

3.5.4 Coulomb repulsion

The Coulomb repulsion $V_C(\mathbf{k}, \mathbf{k}')$ in Eq. 3.37 is hard to evaluate. In full, it reads $V_C(\mathbf{k}, \mathbf{k}') = \langle \mathbf{k}', -\mathbf{k}' | W | \mathbf{k}, -\mathbf{k} \rangle$, where W signifies the *screened Coulomb interaction*. The *e-ph* interaction acts on a long, thus low-frequency time-scale, ω_{ph} . This can be identified with the largest phonon frequency of the system, $\omega_{\text{ph,max}}$. On the other hand, the electron-electron interaction happens on a much larger energy scale, that of the Fermi energy, E_F ⁶. It is typically two orders of magnitude larger than $\hbar\omega_{\text{ph}}$. Thus, $V_C(\mathbf{k}, \mathbf{k}')$ cannot be treated with the same Matsubara frequency cutoff as the *e-ph* interaction.

A solution was provided by Morel and Anderson [197]. First one performs a double Fermi surface average of the Coulomb repulsion, $\mu = \langle \langle V_C(\mathbf{k}, \mathbf{k}') \rangle_{\mathbf{k}'_{\text{F}}} \rangle_{\mathbf{k}_{\text{F}}}$, defined as $\langle \dots \rangle_{\mathbf{k}_{\text{F}}} = \frac{1}{N_{\text{F}}} \sum_{\mathbf{k}} \delta(\varepsilon_{\mathbf{k}}) (\dots)$. To address the difference in the two time scales μ is renormalized as

$$\mu^* = \frac{\mu}{1 + \mu \log \left(\frac{E_{\text{F}}}{\hbar\omega_{\text{ph}}} \right)}. \quad (3.40)$$

This μ^* is called the *Morel-Anderson pseudopotential*. Empirically, the values have been found to be rather uniform for different materials. For the elemental metals the values are in the range 0.1 – 0.13, where the lower values are usually found for simple metals and the higher values for transition metals [182]. In more complex compound superconductors μ^* is in the range

⁶Alternatively the electron plasma frequency is sometimes considered [182].

0.1 – 0.25. It is common practice to fit it to the experimental critical temperature. Fortunately, the superconducting gap spectrum does not change qualitatively with an isotropic μ^* . From Eq. 3.37 we can see that an isotropic repulsion term merely introduces a rigid decrease of the e - ph interaction, so the distribution of the gap remains principally unaltered as μ^* is varied.

3.5.5 Isotropic approximations

Often isotropic solutions to the Eliashberg equations are employed, that disregard the dependence on \mathbf{k} and \mathbf{k}' entirely. In this case the isotropic Eliashberg function is obtained from

$$\alpha^2 F(\omega) = \langle \langle \alpha^2 F(\mathbf{k} \mathbf{k}', \omega) \rangle_{\mathbf{k}'_{\text{F}}} \rangle_{\mathbf{k}_{\text{F}}} , \quad (3.41)$$

with the double Fermi surface average defined in the previous section. From Eq. 3.38 we see that the isotropic e - ph coupling function is the first inverse moment of the isotropic Eliashberg function,

$$\lambda(\omega) = 2 \int_0^\omega d\omega' \omega'^{-1} \alpha^2 F(\omega') . \quad (3.42)$$

The electron-phonon coupling constant is $\lambda_{\text{tot}} = \lambda(\omega_{\text{max}})$, where ω_{max} is the maximum phonon frequency.

As an isotropic solution to the Eliashberg equations, McMillan derived a formula for T_c , valid up to $\lambda_{\text{tot}} \sim 1.5$ [198]. This formula was later refined by Allen and Dynes [199]. The McMillan-Allen-Dynes formula is

$$T_c = \frac{\hbar \omega_{\text{log}}}{1.2 k_{\text{B}}} \exp \left(- \frac{1.04(1 + \lambda_{\text{tot}})}{\lambda_{\text{tot}} - \mu^*(1 + 0.62\lambda_{\text{tot}})} \right) , \quad (3.43)$$

where

$$\omega_{\text{log}} = \exp \left(\frac{2}{\lambda_{\text{tot}}} \int_0^\infty d\omega \omega^{-1} \ln(\omega) \alpha^2 F(\omega) \right) . \quad (3.44)$$

In this thesis, we solve the fully anisotropic Eliashberg equations, however, sometimes we make the comparison to isotropic approximations, to characterize the importance of anisotropy.

3.5.6 Quasiparticle DOS in the superconducting state.

The Eliashberg framework also provides a way to calculate the quasiparticle DOS in the superconducting state, that can be probed by single-particle tunneling measurements, such as scanning tunneling spectroscopy (STS). It can be calculated as [39, 200]

$$N_S(\Omega) \propto \sum_{\mathbf{k}} A(\mathbf{k}, \Omega) \approx N_F \left\langle \int_{-\infty}^{\infty} d\xi A_{\mathbf{k}}(\xi, \Omega) \right\rangle_{\mathbf{k}_F}, \quad (3.45)$$

with the spectral function,

$$A(\mathbf{k}, \Omega) = -\frac{1}{\pi} \text{Im} \left[\hat{G}(\mathbf{k}, \Omega) \right]_{11}, \quad (3.46)$$

where $\left[\hat{G}(\mathbf{k}, \Omega) \right]_{11}$ is the (11) element of the interacting Green's function matrix obtained after analytic continuation of the Green's function in Eq. 3.33.

3.5.7 Uppsala superconductivity code (UppSC)

The aim of this thesis is combining accurate *ab initio* input of the electronic structure, the phonons and the *e-ph* interaction with fully anisotropic Eliashberg theory, to discover new properties of superconductors. The Uppsala Superconductivity Code (UppSC) uses this *ab initio* input to solve the anisotropic Eliashberg equations [39, 73, 148, 200–202]. Moreover, it is compatible with ABINIT, which we used for the DFPT calculations in this thesis. Here, we will discuss some practical considerations, needed to obtain accurate solutions to the Eliashberg equations.

3.5.7.1 Interpolation of the electron-phonon coupling

As stated above, carrying out the perturbations to obtain the *e-ph* matrix elements is a formidable task. The resulting amount of phonon wave vectors is therefore limited. To achieve good accuracy the matrix elements obtained from ABINIT are interpolated by the UppSC code used in this thesis [39, 73, 148, 200–202]. The main difference between the UppSC code and the Electron-Phonon Wannier (EPW) code distributed by the university

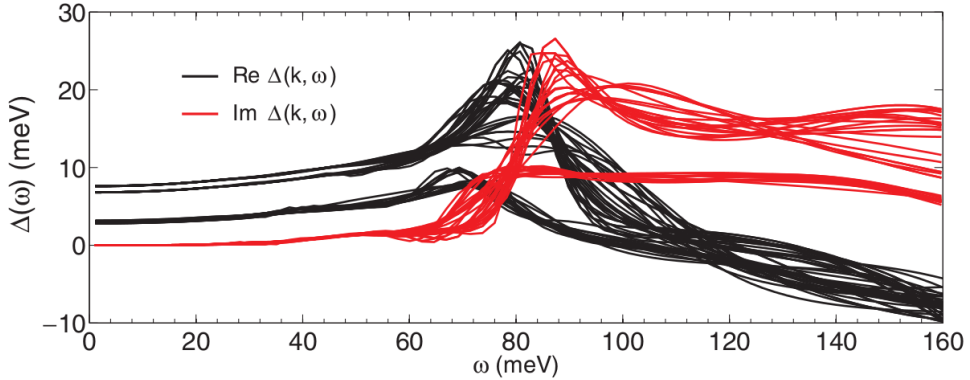


FIGURE 3.4: *The frequency dependence of the superconducting gap of bulk MgB₂ obtained from solving the anisotropic Eliashberg equations for different points of the Fermi surface ($T = 4.2$ K) within the UppSC code [39].*

of Oxford is that the former does not employ maximally-localized *Wannier functions* [38, 183].

3.5.7.2 Numerical treatment

In the UppSC code, the coupled equations 3.36–3.37, supplemented by the *ab initio* electron and phonon band structure and the electron-phonon coupling, are solved self-consistently in Matsubara space and the converged solutions are analytically continued to real frequencies. The analytic continuation is performed numerically by employing the high-accuracy Padé scheme [39, 203].

The Eliashberg equations need to be solved for a range of temperatures, to investigate the temperature-evolution of the superconducting state. The critical temperature, T_c , is obtained as the lowest T for which the solution $\Delta = 0$ is found. The superconducting gap can be expressed by means of the *gap edge*, defined as $\text{Re}(\Delta(\mathbf{k}, \omega)) = \omega$ [39]. An example of the frequency-dependence of the gap function of bulk MgB₂ is shown in Fig. 3.4. Near zero frequency (specifically where $\text{Re}(\Delta(\mathbf{k}, \omega)) = \omega$) the superconducting gaps of bulk MgB₂ are retrieved. There is a clear split between the σ states with $\Delta(0) \sim 7$ meV and the π states with $\Delta(0) \sim 3$ meV, as discussed in Chapter 1.

3.5.8 Density functional theory for superconductors (SCDFT)

A different approach to treating *e-ph*-based superconductivity from first principles was elaborated by Gross and coworkers, and was named DFT for superconductors (SCDFT) [76–78]. The starting point is an extension of the Hohenberg-Kohn theorems underpinning DFT, to include three densities instead of one density. These are (i) the usual electronic density, n , (ii) the nuclear density matrix, and (iii) the superconducting anomalous density $\chi(\mathbf{r}, \mathbf{r}') = \langle \hat{\psi}_\uparrow(\mathbf{r})\hat{\psi}_\downarrow(\mathbf{r}') \rangle$. Just like in DFT, in SCDFT the interacting system is mapped to effective Kohn-Sham equations, that take the form of Bogoliubov-de Gennes equations. The main advantage of SCDFT is that the *e-ph* interaction and the Coulomb repulsion are treated on the same footing, which eliminates the need for an adjustable parameter μ^* like in Eliashberg theory. However, recent advances in the development of the anisotropic Eliashberg theory are also starting to enable *ab initio* calculations of the full $V_C(\mathbf{k}, \mathbf{k}')$ based on the random phase approximation [84].

3.5.9 Nuclear quantum effects and phonon anharmonicity

In some special cases two of the approximations made in this chapter may not be justifiable. These approximations are the Born-Oppenheimer (BO) – or adiabatic – approximation, i.e., that nuclei can be described classically because they move on much longer time scales than electrons, and the harmonic approximation (cf. Fig. 3.1). Both approximations are not generally valid for the lightest nuclei, such as hydrogen (H) and deuterium (D). Based on path-integral molecular dynamics it was shown that *nuclear quantum effects* beyond the BO approximation strongly affect the bond stability in liquid H under high pressure [204]. Moreover, non-local electronic interactions such as van der Waals interactions are also shown to be important in this system. For H₂S and D₂S it was demonstrated that phonon anharmonicity leads to a reduction of the *e-ph* coupling by 30% [205]. Finally, for H₃S and D₃S it was equally shown that the stabilities of certain bonds are strongly influenced by phonon anharmonicity, leading to a strong reduction of the critical pressure for phase transitions [206].

Chapter 4

Anomalous multiband superconductivity in osmium diboride

*A microscopic study of superconductivity in osmium diboride (OsB_2) is presented, with a discussion of the origin and characteristic length scales of the superconducting state. From first-principles I show that OsB_2 is characterized by three different Fermi sheets, and prove that this fermiology complies with recent quantum-oscillation experiments. Using the found microscopic properties, and experimental data from the literature, I employ Ginzburg-Landau relations to reveal that OsB_2 is a distinctly type-I superconductor with very low Ginzburg-Landau parameter κ – a rare property among compound materials. I show that the found coherence length and penetration depth corroborate the measured thermodynamic critical field. Moreover, the calculation of the superconducting gap structure using anisotropic Eliashberg theory and *ab initio* calculated electron-phonon interaction as input reveals a single but anisotropic gap. The calculated gap spectrum is shown to give an excellent account for the unconventional behavior of the superfluid density of OsB_2 measured in experiments as a function of temperature. This reveals that gap anisotropy can explain such behavior, observed in several compounds, which was previously attributed solely to a two-gap nature of superconductivity.*

4.1 Introduction

The question of particular types of superconductivity emerged in the early years of the Ginzburg-Landau (GL) theory [5, 8]. In type-I superconductors under applied magnetic field, an interface between normal (N) and superconducting (S) domains is energetically costly, causing normal domains to merge, whereas type-II superconductors minimize the normal domains to single vortices (which repel and organize in an Abrikosov lattice [8]). Type-I superconductivity mainly occurs in elemental metals (Pb, Sn, In, Al, etc.), but is very rare in compounds. The fact that virtually all superconducting compounds discovered since the early 1960s are type-II superconductors [9] (with a few notable exceptions such as YbSb_2 , TaSi_2 , etc. [207, 208, and references therein.]) reduced the interest in type-I superconductors, until modern experimental and numerical techniques enabled more careful investigations of their rich intermediate state due to demagnetization effects in applied magnetic field: topological hysteresis of tubular/laminar domains depending on sample shape [209–211], the ‘suprafroth’ ground-state [212], mesoscopic effects [213, 214], intricate dynamics of normal domains under applied current [215], etc. Moreover, a transitional regime between standard types I and II exists, that has been noted in both experiment [216, 217] and microscopic theory [218–220]. Its rich physics can become accessible by adding a controlled rate of non-magnetic impurities in a type-I superconductor [217, 221].

One recently studied superconducting compound of which the length scales remained elusive is osmium diboride (OsB_2). Its rather low critical temperature (2.1 K) and the recently measured magnetization and heat-capacity of single-crystal samples [222] pointed at possible type-I superconducting behavior, but that was not corroborated by simplified estimates of the superconducting length scales and the Ginzburg-Landau parameter $\kappa \sim 1-3 \gg 1/\sqrt{2}$. OsB_2 displayed additional unconventional properties, notably the temperature dependence of the superfluid density that deviates from the Bardeen-Cooper-Schrieffer (BCS) result. In order to explain this observation, a two-gap model was proposed for superconductivity in OsB_2 [222].

Here, an extensive theoretical study that clarifies all of the anomalous properties of OsB_2 outlined above is presented. Based on a combination of first-principles calculations and mean-field theory, I provide proof of deeply type-I

behavior in OsB₂. Detailed knowledge of microscopic parameters and superconducting length scales obtained in this study enabled us to perform a very accurate analysis of the experimental data of Ref. 222, notably the critical magnetic field, supporting this conclusion. Furthermore, I reveal, based on Eliashberg calculations, that the superconducting gap spectrum of OsB₂ is anisotropic rather than multigap as previously proposed [222]. These revisions of both the superconducting spectra and the length scales of OsB₂, starting from first principles, make an exemplary case for the interaction between experiment and theory in the description of superconductivity on the nanoscale.

This chapter is organized as follows: first, the crystal structure and ground state electronic structure of OsB₂ are discussed in Secs. 4.2 and 4.3, followed by a thorough comparison to available experimental data such as Shubnikov-de Haas measurements in Sec. 4.4. I proceed by presenting the phonon structure and the electron-phonon coupling in Sec. 4.5. In Sec. 4.6 the superconducting gap spectrum is discussed, where I show an excellent comparison with superfluid density measurements. Finally, in Sec. 4.7 the length scales of OsB₂ are derived from the calculated microscopic properties using Ginzburg-Landau relations, and the resulting interaction with applied magnetic fields. Throughout, I make the comparison between the OsB₂ and MgB₂, the archetypical two-gap superconductor, pointing out both similarities and differences. Ultimately, Sec. 4.8 summarizes the findings.

4.2 Crystal structure

OsB₂ adopts the orthorhombic space group $Pm\bar{m}n$ (No. 59) [223], depicted in Fig. 4.1(a). One should note a very good agreement between calculated and experimental [222] lattice parameters, displayed in Table 4.1, with relative deviations below 1%. Os occupies Wyckoff position $2a$ depending on one internal parameter z_{Os} and B Wyckoff position $4f$ depending on internal parameters x_{B} and z_{B} , giving a total of 6 atoms in the OsB₂ unit cell. The internal parameters compare equally well with experimental values (added between parentheses): $z_{\text{Os}} = 0.155$ (0.153), $x_{\text{B}} = 0.056$ (0.049) and

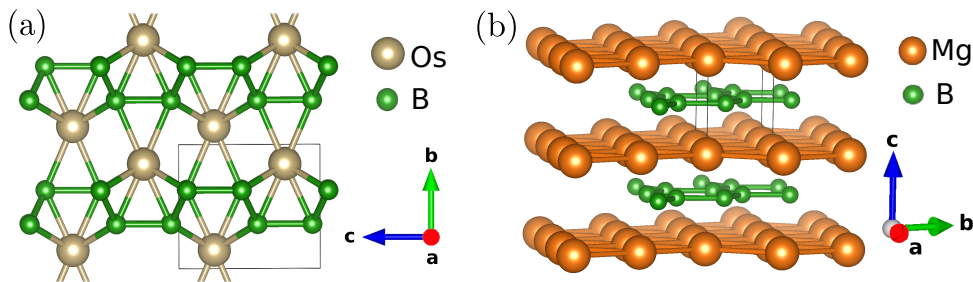


FIGURE 4.1: (a) The orthorhombic crystal structure of OsB_2 . (b) The hexagonal crystal structure of MgB_2 . In both cases, the unit cells are indicated by grey boxes.

$z_{\text{B}} = 0.638$ (0.641). For comparison, we show in Fig. 4.1(b) the crystal structure of MgB_2 (hexagonal space group $\text{P6}/\text{mmm}$), that is clearly layered in consecutive planes of Mg and B, as opposed to the structure of OsB_2 .

4.3 Electronic properties

We start from a first-principles study of the electronic structure of OsB_2 based on density functional theory (DFT), implemented in VASP [172, 176]. In this study – for which computational details can be found in Appendix A – we take into account spin-orbit coupling, in view of the high atomic number of Os. The band structure according to orbital character, shown in Fig. 4.2(a), reveals predominant Os-d character of the bands crossing the Fermi level (E_{F}). A fraction of B-p states also contributes to the band we denote M because of this mixed character. A total of three bands is present at E_{F} , so the resulting Fermi surface, depicted in Fig. 4.2(b), consists of three sheets. First, there are two nested quasi-ellipsoidal sheets with pure Os-d character, centered around X, the inner one denoted E_1 and the outer

Parameter	Calc. (Å)	Exp. (Å) [222]	relative dev. (%)
a	2.893	2.870	+0.8
b	4.098	4.079	+0.5
c	4.705	4.673	+0.7

TABLE 4.1: Lattice parameters of OsB_2 : a comparison between calculations and experiment [222], including the relative deviation between them.

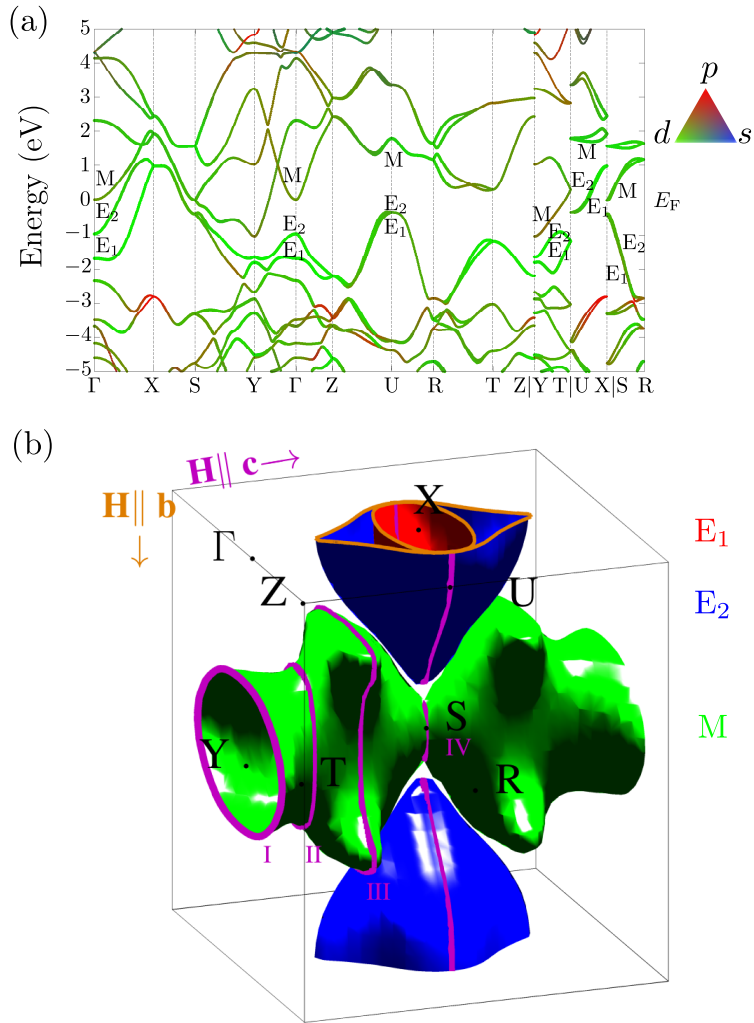


FIGURE 4.2: (a) The calculated band structure of OsB_2 around the Fermi level E_F . The color code denotes the character of the band (s , p or d), while the line thickness denotes the band character varying between pure Os (thickest) and pure B (thinnest). (b) The Fermi surface, consisting of 3 sheets: two quasi-ellipsoidal sheets E_1 (red) and E_2 (blue) and an anisotropic sheet M (green). Shubnikov-de Haas orbits in applied magnetic fields $\mathbf{H} \parallel \mathbf{b}$ and $\mathbf{H} \parallel \mathbf{c}$ are also indicated, \mathbf{b} and \mathbf{c} being the unit cell vectors.

one E_2 . The third sheet M , with central axis along direction Y - S , is more anisotropic.

4.4 Shubnikov-de Haas oscillations

4.4.1 Theory behind Shubnikov-de Haas oscillations

One of the most successful experimental techniques to probe Fermi surfaces is the one of quantum oscillations, utilizing the Shubnikov-de Haas (SdH) effect. In this effect, the conductivity of a metal shows oscillations with frequencies proportional to the areas of extremal orbits of the Fermi surface, $A(E_F)$, perpendicular to the applied magnetic field [10]:

$$F = \frac{\hbar}{2\pi e} A(E_F) , \quad (4.1)$$

where F is expressed in units of Tesla. The amplitude of the SdH oscillations depends on the cyclotron mass of the electrons, m_c . To find m_c we can start from the definition of the *cyclotron frequency*, ω_c (in SI units):

$$\frac{2\pi}{\omega_c} = \frac{\hbar}{eH} \oint \frac{dk}{v_{\perp}} , \quad (4.2)$$

where H is the magnitude of the applied field and v_{\perp} is the velocity perpendicular to the orbit. This cyclotron frequency is $\omega_c = eH/m_c$, so m_c of an electron in a Fermi surface orbit is given by

$$m_c = \frac{\hbar}{2\pi} \oint \frac{dk}{v_{\perp}} . \quad (4.3)$$

The perpendicular velocity can be expressed by

$$v_{\perp} = \frac{1}{\hbar} \frac{dE}{dk_{\perp}} , \quad (4.4)$$

where $dk \times dk_{\perp} = dA$, i.e., an infinitesimal area in reciprocal space. Therefore, the contour integral integrates to

$$m_c = \frac{\hbar^2}{2\pi} \left. \frac{\partial A}{\partial E} \right|_{E=E_F} . \quad (4.5)$$

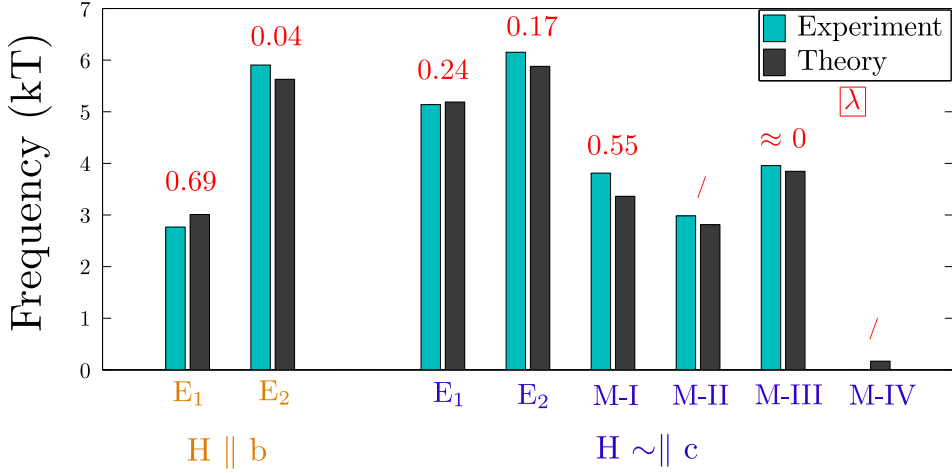


FIGURE 4.3: A comparison between the calculated Shubnikov-de Haas frequencies (in units of kilotesla – kT) and the experimental values from Ref. 222. The resulting electron-phonon coupling values λ are added in red. Slashes indicate that the experimental cyclotron masses were not available.

Numerically, this derivative with respect to E can be approximated by the central difference approximation,

$$\left. \frac{\partial A}{\partial E} \right|_{E=E_F} \approx \frac{A(E_F + \epsilon) - A(E_F - \epsilon)}{2\epsilon}. \quad (4.6)$$

In experimental measurements, where the electrons are ‘dressed’ with phonon interactions, the cyclotron masses are enhanced to m_c^* (analogously to the enhancement of the *band mass*, discussed in Sec. 3.5.3). Therefore, an estimate of the e - ph coupling constant λ can be calculated from the mass enhancement using

$$m_c^* = (1 + \lambda)m_c. \quad (4.7)$$

This gives access to the e - ph coupling in different Fermi sheets, averaged over *specific orbits*.

4.4.2 Shubnikov-de Haas oscillations in OsB₂

The extremal orbits contributing to SdH oscillations in the case of OsB₂ are indicated in Fig. 4.2(b) for two different magnetic fields. From the Fermi

surface I calculated the SdH frequencies f and the bare cyclotron masses m_c (i.e., *without* phonon dressing)¹.

The agreement between theoretical and experimental SdH frequencies, displayed in Fig. 4.3, is excellent, validating the electronic structure of OsB₂ presented in Figs. 4.2(a) and (b). The e - ph coupling λ in specific orbits, also shown in Fig. 4.3, is obtained from the cyclotron mass renormalization.

This analysis reveals that the e - ph coupling in E₁ and E₂ is strongly anisotropic. The coupling is strong in E₁ in the orbit perpendicular to \mathbf{b} , while it is very small in E₂. The orbits of E₁ and E₂ perpendicular to \mathbf{c} show similar, moderate e - ph coupling. Band M has no closed orbits perpendicular to \mathbf{b} , but the e - ph coupling in the other direction ranges from almost zero to quite strong, depending on the orbit. The most important conclusion from this analysis is that *all* bands contribute to the e - ph coupling. The question of how the superconducting gap is distributed over the bands is treated in the following sections.

Extension to iron selenide. Having established SdH oscillations as a powerful tool to probe the Fermi surface of metals, I extended this study to bulk iron selenide (FeSe). As explained in Sec. 1.1.4.3 of this thesis, FeSe is an unconventional Fe-based superconductor akin to the pnictides. Therefore, it is of great interest to gain more insight into its microscopic properties, first and foremost the electronic behavior. Two independent experimental SdH studies available in the literature give similar values [224, 225]. In a comparison of these experimental SdH frequencies to values calculated from the Fermi surface topology – analogously to what I did for OsB₂ – a large discrepancy is found. The predicted cross sectional areas are about 5 – 10 larger than the experimental values. Details of this study are given in Appendix B, including figures showing the FeSe band structure and Fermi surface. In this band structure, it becomes clear that the bands crossing the Fermi level have dominant Fe-d character. Such d-bands are not always well-described by DFT. There is growing evidence of strong correlations in bulk FeSe [226, 227] leading to a renormalization of the electronic structure

¹Here, I accounted for the fact that the applied field was not exactly parallel to unit cell vector \mathbf{c} in the corresponding experiment (noted in Ref. 222). I found that calculations performed for field angle 23° with respect to \mathbf{c} in the \mathbf{ac} plane yield the best fit to the experimental values.

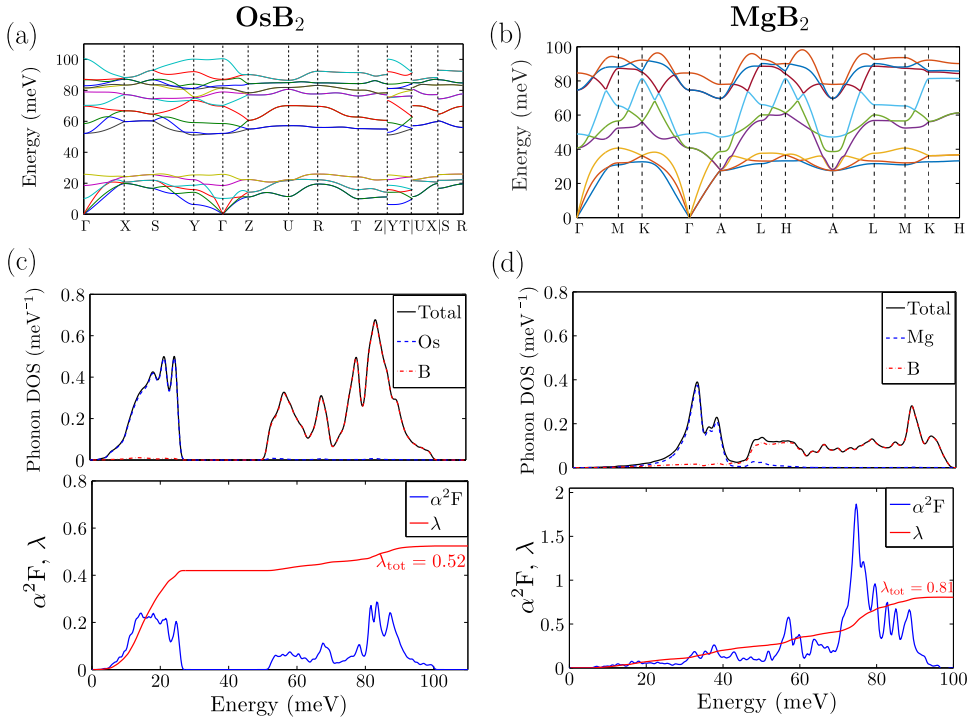


FIGURE 4.4: (a) and (b) The phonon band structure calculated using density-functional perturbation theory, for OsB_2 and MgB_2 respectively. (c) and (d) Top panel: The phonon DOS of OsB_2 and MgB_2 respectively, split into contributions of Os/Mg and B. Bottom panel: The Eliashberg function α^2F describing the energy-dependent electron-phonon coupling, and the resulting isotropic electron-phonon coupling constant λ_{tot} .

as shown here. This electronic structure could be treated by methods beyond DFT, such as dynamical mean field theory (DMFT).

4.5 Phonons and electron-phonon interaction

In order to analyze the mechanism leading to superconductivity in OsB_2 , I carried out a first-principles calculation of the e - ph interaction. To this end we used Eliashberg theory combined with density functional perturbation theory (DFPT), as implemented in ABINIT [175, 185, 188–190], and details on which are specified in Appendix A. The phonon band structure, shown in Fig. 4.4(a), is characterized by a distinct gap of ~ 25 meV. The characteristic

Debye temperature is obtained from the speed of sound v_s in the material as

$$\Theta_D = \frac{hv_s}{2k_B} \sqrt[3]{\frac{6}{\pi} N(E_F)}, \quad (4.8)$$

where $N(E_F)$ is the total density of states at the Fermi level. The effective speed of sound is calculated as the following average of the values due to the transversal and longitudinal acoustic modes, v_t and v_l (the slope of the phonon dispersions near Γ) [228]:

$$v_s = \sqrt[3]{3} \left(\frac{2}{v_t^3} + \frac{1}{v_l^3} \right)^{-\frac{1}{3}}. \quad (4.9)$$

This yields $\Theta_D = 471$ K, in good accordance with the experimental value of 539 K [222]. The origin of the gap in the phonon band structure becomes clear in the phonon density of states (PHDOS) shown in Fig. 4.4(c). Owing to the high mass of Os, its phonons are low-energy ones, in contrast with B-related phonons extending up to energies of ~ 100 meV. The Eliashberg function and e - ph coupling shown in Fig. 4.4(c) indicate the dominance of Os-related phonons in the coupling constant. Therefore, both the fermionic and the phononic features of superconductivity in OsB₂ are driven by Os. The total isotropic coupling amounts to $\lambda_{\text{tot}} = 0.52$. Using the McMillan-Allen-Dynes formula [199], the critical temperature $T_c = 2.1$ K is found (taking as Coulomb pseudopotential $\mu^* = 0.13$).

A comparison of the e - ph interaction in OsB₂ to the case of the well-known two-gap superconductor MgB₂ is instructive. As shown in Fig. 4.4(b), the contributions of Mg and B to the phonon DOS are again quite distinguishable, due to the mass difference, similar to the case of OsB₂. In the latter, the Os modes are even lower in energy because of the high atomic number of Os. From the Eliashberg function, shown in Fig. 4.4(d), coupling constant $\lambda_{\text{tot}} = 0.81$ is obtained for MgB₂, compared to $\lambda_{\text{tot}} = 0.52$ for OsB₂. This yields $T_c = 24$ K for MgB₂, significantly higher than for OsB₂. The main contribution to this strong coupling in MgB₂ is the pronounced peak in the Eliashberg function around ~ 75 meV, stemming from B-related phonon modes, in contrast with the findings for OsB₂. $T_c = 24$ K is still an underestimation of the experimental $T_c = 39$ K for bulk MgB₂, due to the limitations of the isotropic Eliashberg theory. In reality, the electron-phonon coupling in bulk MgB₂ is very anisotropic and this anisotropy has a pronounced effect on

T_c [229]. This fact has been established by combined anisotropic Eliashberg theory and DFT calculations that have been very successful in explaining superconductivity in this material [36, 38, 39] and also made predictions for further experiments [39].

The anisotropic electron-phonon coupling and the particular Fermi surface of MgB_2 result in two distinct superconducting gaps over different Fermi surface sheets in this material. Therefore, it is possible to obtain an effective isotropic two band model that captures the essential characteristics of two-gap superconductivity in MgB_2 [230]. In this case, the coupling is described by a 2×2 matrix of coupling constants. For MgB_2 , it has been measured to be [74]

$$\Lambda = \begin{pmatrix} 0.84 & 0.19 \\ 0.19 & 0.39 \end{pmatrix}, \quad (4.10)$$

with the largest eigenvalue of this matrix playing the role of an effective coupling constant in the multigap case [231]: $\lambda_{\text{eff}} = 0.91$. In this approach, the multigap effect accounts for a higher $T_c = 37$ K (using $\mu^* = 0.1$). In the next section I show that the application of a similar effective two-gap model to OsB_2 leads to incorrect conclusions about the nature of the superconducting state of the material.

In MgB_2 , the dominant phonon mode in the e - ph coupling is the in-plane hexagon deformation mode E_{2g} of the B atoms [36]. In OsB_2 , on the other hand, 80% of all e - ph coupling is contributed by Os-related modes. The strongest coupling resides in the three optical modes of Os, with energy values between 9 and 26 meV, cf. Fig. 4.4. Although spread over \mathbf{q} -space², the coupling in these modes is strongest at $\mathbf{q} = (0, 0, 0) = \Gamma$, thus promoting intraband coupling. In its turn, it bears important consequences for the superconducting gap spectrum, as will be shown in the next section. The atomic displacements corresponding to the different optical modes of Os (with mode numbers $n = 4, 5, 6$) at Γ are shown in Fig. 4.5. The displacements are directed along the three crystal axes, along \mathbf{c} , \mathbf{a} and \mathbf{b} for $n = 4, 5, 6$ respectively. The mode with the lowest energy (the softest mode), $n = 4$, carries the strongest e - ph coupling $\lambda_{\mathbf{q}=\Gamma, n=4} = 0.69$, compared to $\lambda_{\mathbf{q}=\Gamma, n=5} = 0.19$ and $\lambda_{\mathbf{q}=\Gamma, n=6} = 0.21$ for the other two modes. The residual 20% of the

²For the choice of the \mathbf{q} -point grid, see Appendix A.

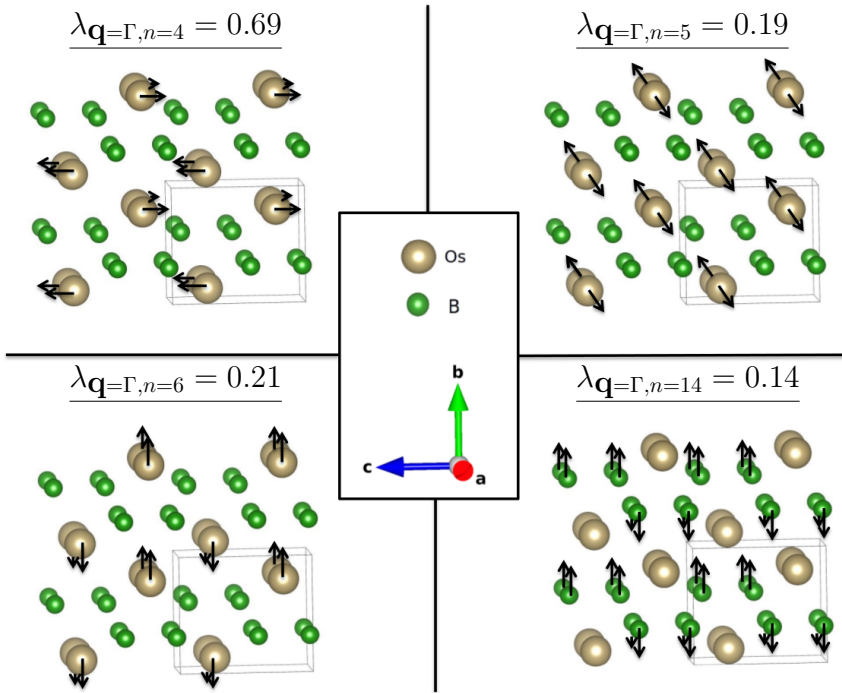


FIGURE 4.5: *Atomic displacements of phonon modes that couple strongly to electrons in OsB_2 . In each case $\lambda_{\mathbf{q},n}$ is given. Modes $n = 4, 5, 6$ are optical modes of Os, along the three crystal axes. Mode $n = 14$, with displacements along axis \mathbf{b} , is the optical B-mode with strongest coupling to electrons. The inset shows the legend for the atom types and the crystal axes.*

total e - ph coupling is contributed by B-related optical modes. It is strongest in mode $n = 14$, at Γ , and corresponds to a displacement of the B-atoms along \mathbf{b} , as shown in Fig. 4.5, and leads to the peak in α^2F at 81 meV.

4.6 Anisotropic superconducting gap and anomalous superfluid density

Starting from the electron-phonon interaction obtained in the previous section, the superconducting gap spectrum was calculated using fully anisotropic Eliashberg theory. Technical aspects of this calculation can be found in Appendix A. The resulting superconducting gap spectrum $\Delta(\mathbf{k})$ of OsB_2 , at an

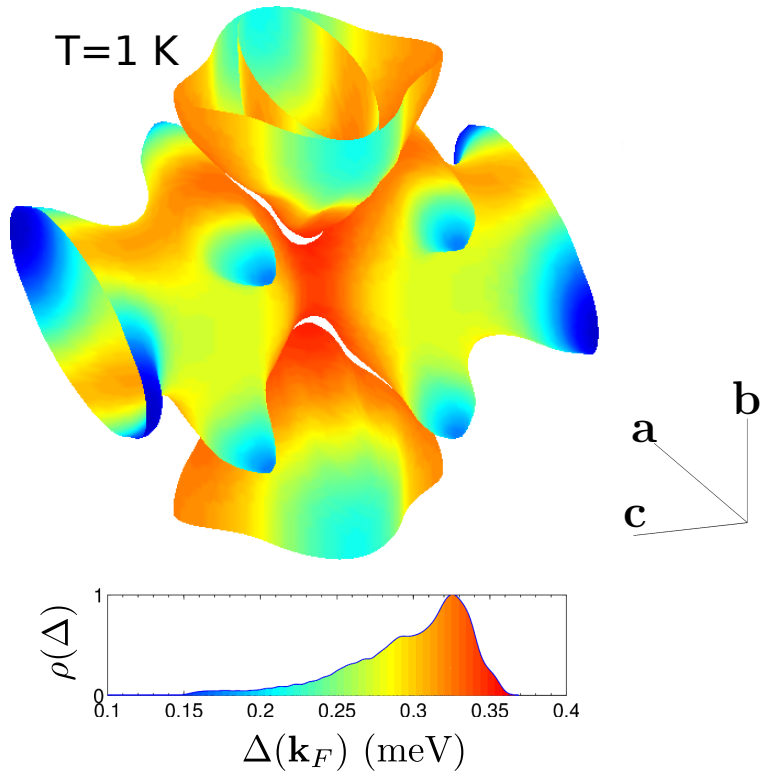


FIGURE 4.6: *The superconducting gap spectrum of OsB_2 on the Fermi surface, calculated using fully anisotropic Eliashberg theory at $T = 1$ K, using the electron-phonon coupling obtained from first-principles as input. $\rho(\Delta)$ is the distribution of the gap, thus showing a single anisotropic gap.*

intermediate temperature of $T = 1$ K, is displayed in Fig. 4.6. The distribution $\rho(\Delta)$ shows that the gap varies continuously over all Fermi sheets. Therefore, OsB_2 is identified as an *anisotropic*, due to the spread of the gap spectrum, but *single-gap superconductor*. It is apparent that the gap spectrum is entirely symmetric within the **bc**-planes, but has a strong evolution along the **a**-axis. A rather strong electron-electron interaction is found to be at play between the condensed electrons, since an elevated Coulomb pseudopotential, $\mu^* = 0.215$, is needed to obtain the correct T_c in the Eliashberg calculations. As a result of this and the moderate electron-phonon coupling, the gap values are on the low side, ranging between 0.15 and 0.37 meV at 1 K.

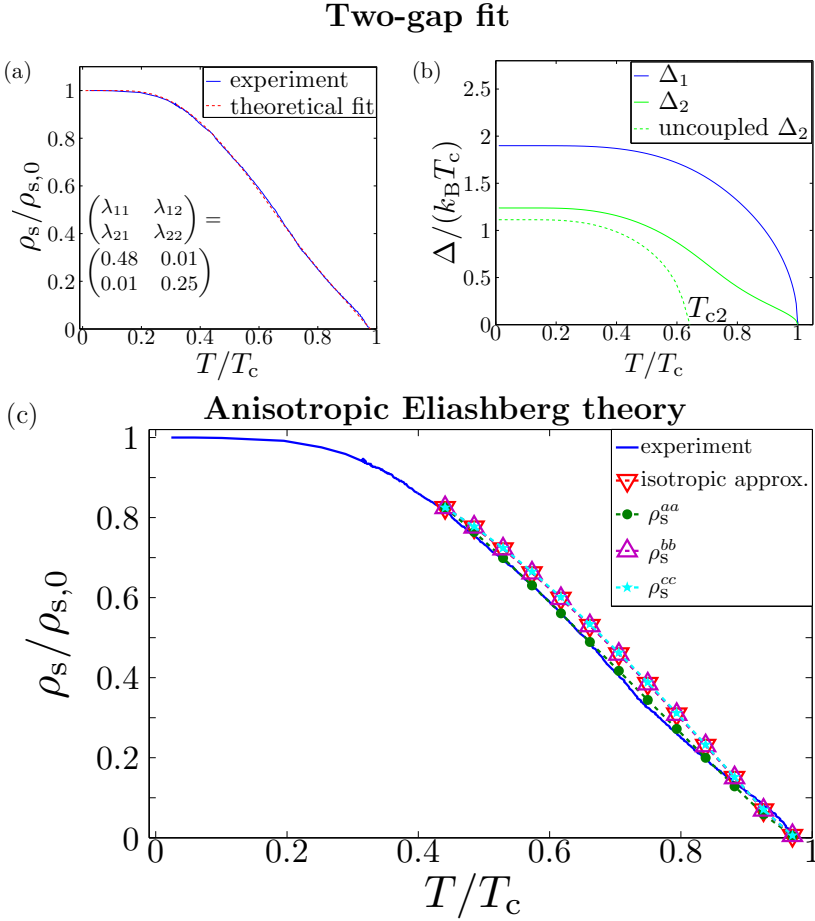


FIGURE 4.7: (a) The two-gap γ fit of the superfluid density ρ_s from Ref. 222 (normalized with the superfluid density at zero temperature $\rho_{s,0}$), using the microscopic parameters calculated here from first-principles. The matrix of coupling constants obtained from the fit is shown as inset. (b) The gap profiles as a function of temperature, obtained by solving the BCS gap equations for two coupled condensates. Dashed line shows the weaker gap (Δ_2) in the absence of interband coupling, with $T_{c2} = 1.35$ K. (c) The superfluid density calculated from anisotropic Eliashberg theory, both isotropic and along specific directions. Component ρ_s^{aa} matches the experimental data extremely well.

This result of a single, anisotropic gap in OsB₂ seems to contradict the findings in Ref. 222 at first sight, where two-gap superconductivity in OsB₂ was suggested based on a successful fit of the two-gap γ model [232]. In Fig. 4.7 an updated version of this fit is shown, using the calculated density

of states per band. The obtained coupling constant matrix, shown as inset in Fig. 4.7(a), was subsequently used in the Bardeen-Cooper-Schrieffer (BCS) gap equations to calculate the evolution of both gaps with temperature, displayed in Fig. 4.7(b). The obtained values of the gaps at zero temperature are $\Delta_1(0) = 0.36$ meV and $\Delta_2(0) = 0.24$ meV.

It follows thus that a two-gap superconductivity model is *sufficient* to fit the superfluid density measurements, but is it *necessary*? To answer this question, the superfluid density was calculated within anisotropic Eliashberg theory. The normalized superfluid density tensor is given by

$$\frac{\rho_s^{\alpha\beta}(T)}{\rho_s^{\alpha\beta}(0)} = T \sum_n \left\langle (\nabla_\alpha E_{\mathbf{k}} \nabla_\beta E_{\mathbf{k}}) \frac{\Delta^2(\mathbf{k}, i\omega_n)}{Z(\mathbf{k}, i\omega_n) [\omega_n^2 + \Delta^2(\mathbf{k}, i\omega_n)]^{\frac{3}{2}}} \right\rangle_{\mathbf{k}_F}, \quad (4.11)$$

where ω_n are the Matsubara frequencies, $E_{\mathbf{k}}$ signifies the normal-state electronic spectrum, $Z(\mathbf{k}, i\omega_n)$ is the mass renormalization and $\langle \dots \rangle_{\mathbf{k}_F}$ denotes the Fermi surface average.

We plot the evolution of the different elements of the superfluid density tensor as a function of temperature in Fig. 4.7(c). For OsB₂, all off-diagonal terms of the superfluid density tensor are zero. In the isotropic approximation, $\nabla_\alpha E_{\mathbf{k}} \nabla_\beta E_{\mathbf{k}}$ (product of Fermi velocity components) is pulled out of the Fermi surface average in Eq. 4.11. Within this approximation, the superfluid density matches $\rho_S^{bb} = \rho_S^{cc}$. Along the **b** and **c** directions, the superfluid density is the same, due to the **bc**-symmetry of the superconducting gap spectrum that we pointed out earlier. The superfluid density along the **a** direction, however, is significantly different and matches the experimental measurement extremely well.

Importantly, in the case of OsB₂, the convex shape of ρ_S^{aa} is *not* a result of the *multigap* character [65], but follows naturally from the temperature evolution of the *anisotropic* condensate. This comparison of Eliashberg theory to the experiment provides a clear example of an anomalous superfluid density of a *single gap* superconductor, and hence an *important caveat* for future identifications of multigap superconductors.

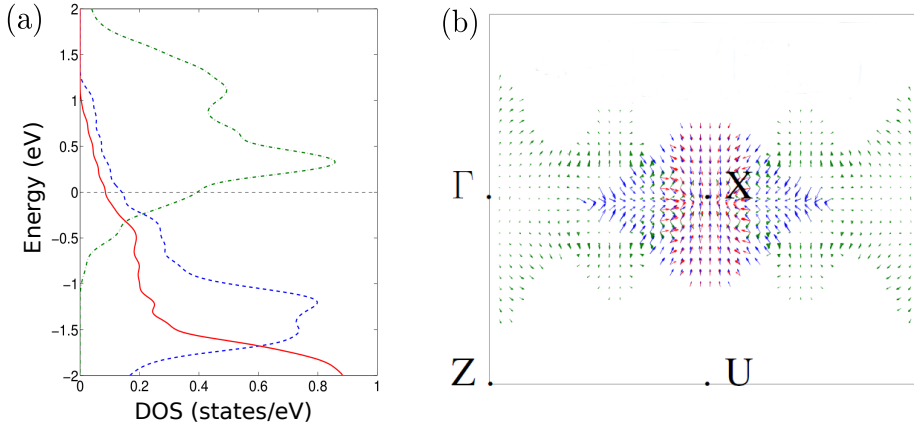


FIGURE 4.8: (a) The density of states per band of OsB_2 , where the line colors indicate the bands according to Fig. 4.2(b), i.e., red corresponds to E_1 , blue to E_2 and green to M . (b) The Fermi velocity field calculated from the DFT band structure projected onto the ac plane.

4.7 Superconducting length scales and type-I behavior

To further understand the superconducting behavior of OsB_2 , particularly under applied magnetic field, I calculate the characteristic length scales of superconductivity, i.e., the coherence length at $T = 0$ [72]

$$\xi(0) = \frac{\hbar v_F}{4\pi T_c} \sqrt{\frac{7\zeta(3)}{3}}, \quad (4.12)$$

and the London penetration depth at $T = 0$

$$\lambda_L(0) = \sqrt{\frac{3c^2}{16\pi e^2 v_F^2 N(E_F)}}. \quad (4.13)$$

The microscopic parameters coming into play here are the Fermi velocity, v_F , and the density of states, $N(E_F)$. The components of the Fermi velocity are defined as

$$v_{F,i} = \frac{1}{\hbar} \left. \frac{\partial E}{\partial k_i} \right|_{E=E_F}, \quad (4.14)$$

Sheet name	N_F (states/eV/f.u.)	$v_{F,x}$ ($10^5 \frac{\text{m}}{\text{s}}$)	$v_{F,y}$ ($10^5 \frac{\text{m}}{\text{s}}$)	$v_{F,z}$ ($10^5 \frac{\text{m}}{\text{s}}$)	v_F ($10^5 \frac{\text{m}}{\text{s}}$)
E ₁	0.086	4.31	2.63	3.80	6.32
E ₂	0.141	3.01	3.23	4.98	6.65
M	0.395	1.79	2.21	2.39	3.71

TABLE 4.2: *Density of states at E_F (states/eV/f.u., f.u. being the formula unit OsB₂), per band. The total DOS, 0.6209 states/eV/f.u., is in good agreement with the experimental value obtained from heat capacity measurements (0.55 states/eV per formula unit) [222].*

where in an orthorhombic structure such as OsB₄ one can choose i to be x, y, z , so the total Fermi velocity follows as

$$v_F = \sqrt{\sum_i v_{F,i}^2}. \quad (4.15)$$

The band-resolved density of states (DOS), $D_i(E)$, is obtained from the DFT-calculated eigenvalues $E_{n,\mathbf{k}}$ using

$$D_i(E) = \sum_{\mathbf{k} \in \text{IBZ}} w_{\mathbf{k}} \delta(E - E_{i\mathbf{k}}), \quad (4.16)$$

where $w_{\mathbf{k}}$ is the weight of the \mathbf{k} -point in the irreducible Brillouin zone (IBZ). To obtain a smooth DOS the Dirac delta function is to be replaced by its Gaussian approximant (where we use $\sigma = 0.05$ eV):

$$D_i(E) = \sum_{\mathbf{k} \in \text{IBZ}} \frac{w_{\mathbf{k}}}{\sqrt{\pi}\sigma} \exp\left(-\frac{(E - E_{i\mathbf{k}})^2}{\sigma^2}\right). \quad (4.17)$$

The band-resolved DOS around E_F is depicted in Fig. 4.8(a) and the Fermi velocity field in Fig. 4.8(b). The values are also specified in Table 4.2. There are significant differences between the quasi-ellipsoids and sheet M with regard to the microscopic parameters. The former account for a density of states of 0.23 states/eV per formula unit, whereas the latter occupies 0.39 states/eV per formula unit. On the other hand, the quasi-ellipsoidal sheets are more highly curved than sheet M, with respective average Fermi velocities of $6.5 \cdot 10^5$ m/s and $3.7 \cdot 10^5$ m/s.

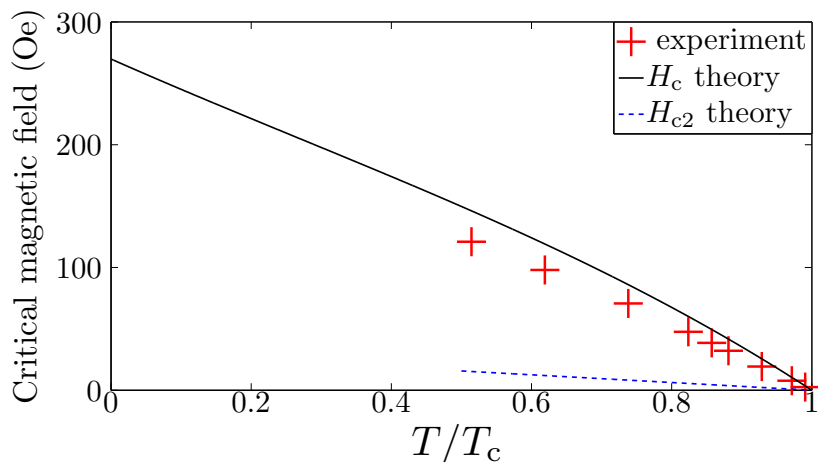


FIGURE 4.9: *The thermodynamic critical magnetic field H_c calculated using the extended Ginzburg-Landau formalism [75], compared to experimental data from Ref. 222. To further illustrate the strong type-I character of OsB_2 we include the calculated upper critical field H_{c2} to visualize that $H_{c2} \ll H_c$.*

Nevertheless, since a single condensate in OsB_2 was found in the previous section, I perform a weighted average over the whole Fermi surface within mean-field theory. This leads to $N(E_F) = 0.62$ states/eV per formula unit and $v_F = 4.7 \cdot 10^5$ m/s. The resulting length scales are $\lambda_L(0) = 27$ nm and $\xi(0) = 229$ nm. The GL parameter $\kappa = \lambda_L/\xi = 0.12$ is therefore far below $\kappa = 1/\sqrt{2}$, the value separating type-I from type-II superconductors [8], indicating that OsB_2 is deeply in the type-I regime. The small penetration depth and large coherence length in OsB_2 occur due to the large v_F , comparable to the high Fermi velocities in elemental metals, and due to the rather low T_c .

To further corroborate our findings, I will show the compliance of our conclusions with the available experimental data. Specifically, we can look at the experimental critical magnetic fields [222], to determine whether they correspond to the thermodynamic critical field H_c or the upper critical field H_{c2} . Experimentally, it is not trivial to distinguish between both critical fields, since samples of a type-I superconductor can equally show an intermediate state between the superconducting and normal states (where normal and superconducting domains coexist) as a result of demagnetization, as discussed in the Introduction. To calculate H_c , I use the expression from the recently developed Extended Ginzburg-Landau (EGL) theory, stated in Sec. 1.2.1.2 of

this thesis. EGL was demonstrated to be in very good accordance with BCS results even quite far from T_c [71, 75]. The hereby obtained H_c of OsB₂ is presented in Fig. 4.9 – revealing a very good agreement with the experimental values, in a broad temperature range. The non-linearity of H_c away from T_c is captured by the EGL theory. As expected for a pure type-I superconductor, the calculated upper critical field $H_{c2} = \frac{\Phi_0}{4\pi\xi^2(0)}\tau$, where $\tau = 1 - \frac{T}{T_c}$, is much lower, since $H_{c2}/H_c \propto \kappa$. The fact that EGL theory, in combination with the calculated microscopic parameters, predicts H_c so well, yields another proof of the type-I behavior of OsB₂, be it indirect. For direct experimental proof, imaging of the intermediate state of OsB₂ can be performed, which may show the large normal domains characteristic of type-I materials, but may also reveal surprises related to the anisotropy of the gap spectrum.

Recently, the superconducting properties of RuB₂, a compound isostructural to OsB₂ with a very similar Fermi surface, were studied experimentally in applied magnetic field [233]. The GL parameter in this material was estimated to be below $1/\sqrt{2}$, corroborating the type-I behavior expected for RuB₂, owing to the similarity to OsB₂.

4.8 Conclusions

In summary, I presented solid and multiscale proofs for anisotropic type-I superconductivity in OsB₂, combining first-principles calculations, mean field theory and recent experimental data. The Fermi surface of OsB₂ consists of two nested quasi-ellipsoidal Fermi sheets with Os-d character and a third sheet with mixed band character. From a first-principles calculation of the electron-phonon coupling, I found that OsB₂ has very moderate coupling amounting to the isotropic value $\lambda = 0.52$. The main contribution to this value (80%) stems from the low-energy Os-related modes. This is a very different situation from the coupling in MgB₂, due to the entirely different crystal structure of the two compounds, where a particular optical vibration of B-atoms couples strongly with the electrons. From the electron-phonon coupling the superconducting gap spectrum was calculated using fully anisotropic Eliashberg theory. The result is a single, anisotropic gap at odds with the available two-gap fit of the superfluid density in Ref. 222. To settle this issue, the superfluid density was calculated within Eliashberg

theory, taking into account the anisotropy in the Fermi surface. This calculation shows that the superfluid density along the shortest lattice axis (\mathbf{a} in Fig. 4.5) matches the experimental data with excellent accuracy. Thus, OsB_2 provides an instructive example of an anomalous temperature dependence of the superfluid density due to a single, anisotropic gap, that cannot be fitted within the simplest BCS model.

The relatively high Fermi velocities in OsB_2 combined with its rather low T_c result in a very low Ginzburg-Landau parameter – setting OsB_2 deeply in the type-I superconducting regime. Moreover, I showed that this complies with the available measurements of the critical magnetic field. The here revealed characteristics of OsB_2 provide a general recipe for other type-I superconducting compounds to be discovered, combining moderate electron-phonon coupling (thus low T_c , and long coherence lengths), and a highly curved Fermi surface (thus high Fermi velocities, diminishing κ with a squared dependence). Such materials will in turn provide more direct access to the scarcely studied regimes of superconductivity away from the standard type-II, especially interesting in multigap superconductors and superconductors with an anisotropic gap.

Publication

J. Bekaert, S. Vercauteren, A. Aperis, L. Komendóva, R. Prozorov, B. Partoens, and M. V. Milošević, *Anisotropic type-I superconductivity and anomalous superfluid density in OsB_2* , Phys. Rev. B **94**, 144506 (2016).

Chapter 5

Coexisting lattice vibrations and spin fluctuations, with application to iron tetraboride

*An advanced method to study spin fluctuations in superconductors quantitatively, and entirely from first principles is presented. This method can be generally applied to materials where electron-phonon coupling and spin fluctuations coexist. I employ it here to examine the recently synthesized superconductor iron tetraboride (FeB_4) with experimental $T_c \sim 2.4 \text{ K}$ [H. Gou et al., Phys. Rev. Lett. **111**, 157002 (2013)]. I prove that FeB_4 is particularly prone to ferromagnetic spin fluctuations due to the presence of iron, resulting in a large Stoner interaction strength, $I = 1.5 \text{ eV}$, as calculated from first principles. The other important factor is its Fermi surface that consists of three separate sheets, among which two nested ellipsoids. The resulting susceptibility has a ferromagnetic peak around $\mathbf{q} = 0$, from which the repulsive interaction between Cooper pair electrons is calculated using the random phase approximation. Subsequently, the electron-phonon interaction calculated from first principles is combined with the spin fluctuation interaction in fully anisotropic Eliashberg theory calculations. I show that the resulting superconducting gap spectrum is conventional, yet very strongly depleted due*

to coupling to the spin fluctuations. The critical temperature decreases from $T_c = 41$ K, if they are disregarded, to $T_c = 1.7$ K, in good agreement with the experimental value.

5.1 Introduction

Spin fluctuations are magnetic excitations in materials without long-range magnetic order. Ferromagnetic spin fluctuations (FSFs), or paramagnons, specifically arise in materials which are close to ferromagnetic instabilities, as described by Stoner theory [234]. In the case of spin singlet Cooper pairing, the interaction between electrons mediated via FSFs is repulsive, and therefore competing with Cooper pairing, in addition to the Coulomb interaction between electrons [235]. On the other hand, the opposite is true for spin triplet pairing, where paramagnons are considered as the primary mediators [235], although not the only ones [236].

Competition between attractive electron-phonon interaction and the repulsive interaction mediated by FSFs forms a long standing problem that emerged less than a decade after the theory of Bardeen-Cooper-Schrieffer (BCS) [237]. Among the earliest attempts for a quantitative analysis, Riblet introduced the coupling to FSFs in the isotropic McMillan formula for the critical temperature (T_c) [182, 238]. Similar attempts have also been made for anti-ferromagnetic spin fluctuations [239]. Dolgov *et al.* subsequently derived an improved McMillan formula for T_c [240]. The latter can be combined with first-principles calculations as was done for, e.g., hole-doped CuBiSO, where pairing to spin fluctuations was found to be very strong and able to induce spin triplet superconductivity under certain doping conditions [241]. Another notable example where spin triplet superconductivity is rather well established and where FSFs have been proposed to play a role is Sr₂RuO₄ ($T_c = 1.5$ K) [56], although the microscopic pairing mechanism is still not completely understood (see Refs. 57 and 58 for reviews on this topic).

I revisit here the question of spin fluctuations, with a new and advanced computational method. It consists of first calculating the microscopic pairing mechanisms, i.e., electron-phonon coupling and coupling of electrons to

FSFs. The electron-phonon interaction is calculated using density functional perturbation theory (DFPT) [242], similar to what is done in, e.g., Refs. 39, 73, 200, 201. Spin fluctuations are treated by means of the random phase approximation (RPA), afterwards building it into the anisotropic Eliashberg equations. Specifically, the susceptibility is calculated from the electronic band structure, and so is the interaction strength, in this case the Stoner interaction strength. Subsequently, the multiband anisotropic Eliashberg equations are solved self-consistently using the full *ab initio* calculated input [36, 38, 39, 73, 73, 200, 201].

Here, this technique is applied successfully to the recently discovered superconductor iron tetraboride (FeB_4). A famous example of first-principles materials design, superconductivity in FeB_4 was first predicted *in silico* by Kolmogorov *et al.* in 2010 [243], after which the material was synthesized and measured to be superconducting with $T_c \sim 2.4$ K by Gou *et al.* in 2013 [244]. The crystal structure of FeB_4 is orthorhombic – shown in Fig. 5.1 – and consists of FeB_{12} polyhedra stacked in columns along the \mathbf{a} -direction (where we defined $a < b < c$). A more detailed description of the crystal structure is given in Sec. 5.3.1. This crystal structure, and in particular the presence of the light element boron, gives FeB_4 a very high mechanical hardness [244–247].

The motivation to study FeB_4 in more depth stems from several aspects. First of all, its T_c was severely overestimated (by an order of magnitude) in the theory of Ref. 243 with respect to the experimental value [244]. The prediction was based on the isotropic McMillan-Allen-Dynes formula where only electron-phonon interaction and usual Coulomb repulsion was taken into account. I recognized this as a smoking gun for unconventional interactions in FeB_4 , which I will prove to be FSFs in this chapter. Secondly, superconductors containing Fe have attracted much interest recently, since the discovery of superconductivity in the iron-oxypnictides (e.g., F-doped LaFeAsO [248]), the iron-arsenides (e.g., $\text{Ba}_{1-x}\text{K}_x\text{Fe}_2\text{As}_2$ [249], and LiFeAs [250]), and the iron-chalcogenides (e.g., FeSe [251, 252]). In this respect, the analysis in this chapter contributes to the understanding of the microscopic mechanisms at work in the Fe-based superconductors. I must stress, however, that the properties of spin fluctuations in FeB_4 are fundamentally different from those of other Fe-based superconductors, e.g., the iron pnictides. F-doped LaFeAsO ,

for instance, shows a susceptibility peak at nonzero $\mathbf{q} = (\frac{\pi}{a}, \frac{\pi}{a})$, as discovered by Mazin *et al.* [52], and thus a tendency for antiferromagnetic spin fluctuations. As such, the study presented in this chapter establishes Fe-based superconductors as a diverse family, in which various different types of spin fluctuations occur. Thirdly, the multiband and multigap superconductivity in borides such as MgB_2 [28, 35–39, 200, 201], OsB_2 [73, 222], and ZrB_{12} [253, 254] is known to be very rich, and consequently possible relations to superconductivity in FeB_4 are worthy of further exploration.

This chapter is organized as follows. First, in Sec. 5.2, I elaborate on the methodology developed in this work, building FSFs calculated from first-principles into the anisotropic Eliashberg equations. In Sec. 5.3.1 the crystal structure of FeB_4 is discussed, followed by the multiband electronic structure of FeB_4 in Sec. 5.3.2 (showing its Fermi surface, not available in the literature to date) and the electron-phonon (e - ph) interaction in Sec. 5.3.3. I proceed by discussing first-principles calculations of the FSFs and their coupling to the electrons in FeB_4 in Sec. 5.3.4. This is followed by a discussion of the superconducting properties of FeB_4 , the gap spectrum and the very good agreement between the theoretical and experimental T_c , in Sec. 5.3.5. Finally, a summary is provided in Sec. 5.4.

5.2 Methodology

The idea is to build FSFs into the anisotropic Eliashberg equations within the random phase approximation (RPA). The tendency for spin fluctuations is mainly determined by the susceptibility, and in particular its behavior at the Fermi level (E_F). The bare (i.e., noninteracting) susceptibility at E_F (known as the Lindhard function), is given by the following function of momentum (\mathbf{q}) and Matsubara frequencies (ω_n):

$$\chi^0(\mathbf{q}, i\omega_n) = \sum_{jj'} \chi_{jj'}^0(\mathbf{q}, i\omega_n) = \sum_{jj'} \sum_{\mathbf{k}} \frac{n_F(\xi_{\mathbf{k},j}) - n_F(\xi_{\mathbf{k}+\mathbf{q},j'})}{\xi_{\mathbf{k},j} - \xi_{\mathbf{k}+\mathbf{q},j'} + i\omega_n} \delta(\xi_{\mathbf{k},j}) \delta(\xi_{\mathbf{k}+\mathbf{q},j'}) , \quad (5.1)$$

where $n_F(\xi_{\mathbf{k},j})$ is the Fermi-Dirac distribution, $\xi_{\mathbf{k},j} = E_{\mathbf{k},j} - E_F$ is the electronic band structure relative to E_F , and where we sum over the electronic band indices j and j' . To arrive at this expression, the constant matrix element approximation (CMEA) has been employed [255], as explained in Appendix C. The Dirac δ -functions are introduced in order to restrict the susceptibilities to the Fermi surface contributions. For practical calculations in this chapter $\delta(\xi_{\mathbf{k},j})$ is evaluated numerically as $\delta(\xi_{\mathbf{k},j}) = \frac{1}{\sqrt{\pi}\sigma} \exp\left(-\left(\frac{\xi_{\mathbf{k},j}}{\sigma}\right)^2\right)$ with broadening $\sigma = 0.01$ Ha.

In compounds with more than one atomic species one needs to take into account that not necessarily all the electronic states are involved in the FSFs. This is only the case for the states belonging to the element(s) with a ferromagnetic tendency. To take the example of FeB_4 , as I will show in Sec. 5.3.4, Fe lies at the origin of the fluctuations. This means that the susceptibility to FSFs needs to be normalized with the ratio of Fe-electronic states (N_{Fe}) to the total intraband susceptibility in the limit $\mathbf{q} \rightarrow 0$, $\omega \rightarrow 0$, i.e., $\sum_j \chi_{jj}^0(0,0)$. I will denote this fraction as $\mathcal{F}_{\text{Fe}} = N_{\text{Fe}} / \sum_j \chi_{jj}^0(0,0)$. Thus, for the total susceptibility the following RPA expression can be used,

$$\chi^{\text{RPA}}(\mathbf{q}, i\omega_n) = \frac{\mathcal{F}_{\text{Fe}} \chi^0(\mathbf{q}, i\omega_n)}{1 - I \mathcal{F}_{\text{Fe}} \chi^0(\mathbf{q}, i\omega_n)}, \quad (5.2)$$

where I is the ferromagnetic interaction strength. I will expand on how the latter can be calculated from first-principles in Sec. 5.3.4. Then, based on the RPA susceptibility, the coupling of electrons to FSFs can be calculated as

$$\lambda_{\text{sf}}(\mathbf{q}, i\omega_n) = \frac{3}{2} N_{\text{Fe}} I^2 \chi^{\text{RPA}}(\mathbf{q}, i\omega_n). \quad (5.3)$$

Finally, we can include FSFs in the anisotropic Eliashberg equations [39, 73, 200, 201] within spin singlet pairing by means of two pairing kernels, one expressing mass enhancement of the electrons (K^+), the other expressing the net coupling strength (K^-). As the electron mass is enhanced by both e - ph interaction, $\lambda_{\text{ep}}(\mathbf{q}, i\omega_n)$, and by FSFs, the kernel is given by

$$K^+(\mathbf{q}, i\omega_n) = \lambda_{\text{ep}}(\mathbf{q}, i\omega_n) + \lambda_{\text{sf}}(\mathbf{q}, i\omega_n). \quad (5.4)$$

On the other hand, the coupling strength in the spin singlet case is depleted, as expressed by

$$K^-(\mathbf{q}, i\omega_n) = \lambda_{\text{ep}}(\mathbf{q}, i\omega_n) - \lambda_{\text{sf}}(\mathbf{q}, i\omega_n) . \quad (5.5)$$

The momentum-dependent e - ph coupling, $\lambda_{\text{ep}}(\mathbf{q}, i\omega_n)$, can be calculated within density functional perturbation theory (DFPT) [242].

As we saw in Chapter 3, for spin singlet superconductivity the coupled anisotropic Eliashberg equations assume the generic form,

$$Z(\mathbf{k}, i\omega_n) = 1 + \frac{\pi T}{\omega_n} \sum_{n'} \left\langle K^+(\mathbf{k}\mathbf{k}', i\omega_n, i\omega_{n'}) \right. \\ \left. \times \frac{\omega_{n'}}{\sqrt{\omega_{n'}^2 + \Delta^2(\mathbf{k}', i\omega_{n'})}} \right\rangle_{\mathbf{k}'_{\text{F}}} \quad (5.6)$$

$$\Delta(\mathbf{k}, i\omega_n) Z(\mathbf{k}, i\omega_n) = \pi T \sum_{n'} \left\langle [K^-(\mathbf{k}\mathbf{k}', i\omega_n, i\omega_{n'}) - \mu^*(\omega_c)] \right. \\ \left. \times \frac{\Delta(\mathbf{k}', i\omega_{n'})}{\sqrt{\omega_{n'}^2 + \Delta^2(\mathbf{k}', i\omega_{n'})}} \right\rangle_{\mathbf{k}'_{\text{F}}} , \quad (5.7)$$

where $\langle \dots \rangle_{\mathbf{k}'_{\text{F}}} = \sum_{\mathbf{k}'_{\text{F}}} \frac{\delta(\xi_{\mathbf{k}'})}{N_{\text{F}}} (\dots)$ denotes a Fermi surface average, $\xi_{\mathbf{k}}$ are the electron energy dispersions relative to the Fermi level, N_{F} is the density of states at the Fermi level, T is temperature and $\omega_n = \pi T(2n + 1)$ are the fermionic Matsubara frequencies. The momentum and frequency dependent functions $Z(\mathbf{k}, i\omega_n)$ and $\Delta(\mathbf{k}, i\omega_n)$ describe electron mass renormalization and even-frequency spin singlet superconductivity, respectively, and $\mu^*(\omega_c)$ is the Anderson-Morel Coulomb pseudopotential which comes with a cut-off ω_c , as explained in Sec. 3.5.4. The e - ph coupling is treated in the way described in Chapters 3 and 4. Similar equations as for the e - ph coupling apply for the electron-spin fluctuation coupling,

$$\lambda_{\text{sf}}(\mathbf{q}, i\omega_m) = \frac{3N_{\text{Fe}}}{2\pi} \int_0^\infty d\omega I^2 \chi''(\mathbf{q}, \omega) \frac{2\omega}{\omega_m^2 + \omega^2} , \quad (5.8)$$

where $\chi''(\mathbf{q}, \omega)$ is the imaginary part of the RPA susceptibility and $\omega_m = \omega_n - \omega_{n'}$.

To study spin-triplet pairing, one needs to adapt the Eliashberg kernels. The mass enhancement remains unaffected ($K^+ = \lambda_{\text{ep}} + \lambda_{\text{sf}}$), while, on the other hand, FSFs become attractive in the spin triplet channel. Moreover, only longitudinal spin fluctuations contribute to spin triplet pairing [235] (hence a factor $1/3$), so that the coupling kernel in the spin triplet channel (substituting K^- in Eq. 5.7) amounts to

$$K_t(\mathbf{k}\mathbf{k}', i\omega_n, i\omega_{n'}) = \lambda_{\text{ep}}(\mathbf{k}\mathbf{k}', i\omega_n, i\omega_{n'}) + \frac{1}{3}\lambda_{\text{sf}}(\mathbf{k}\mathbf{k}', i\omega_n, i\omega_{n'}) . \quad (5.9)$$

It is worth noting that even in the presence of spin-orbit coupling, inversion and time-reversal symmetries and the combination thereof, still guarantee Kramers degeneracy throughout the whole Brillouin zone, so that one can work in a pseudospin space where labelling the superconducting state as singlet or triplet is possible. Moreover, due to spatial inversion symmetry, singlet and triplet superconducting components cannot mix, so that we can look for different solutions (singlet or triplet) of the Eliashberg equations separately.

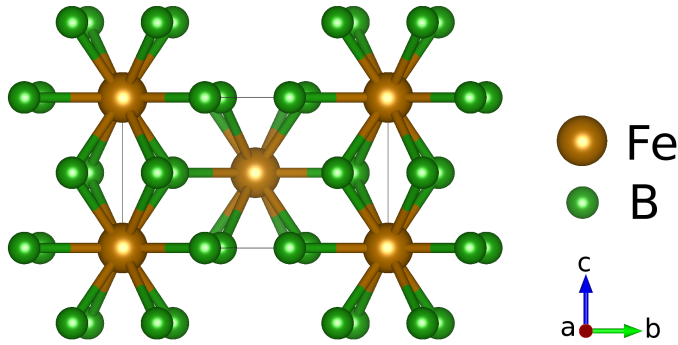
5.3 Application to FeB₄

Here, the approach described in Sec. 5.2 is applied to FeB₄, in order to demonstrate that quantitative results can be obtained.

5.3.1 Crystal structure

The FeB₄ crystal structure is depicted in Fig. 5.1. Its oP10 phase (where o stands for orthorhombic, P for primitive and 10 for the number of atoms in the unit cell) consists of the primitive orthorhombic space group Pnmm (No. 58). As can be found in the supplementary information of Ref. 244, Fe occupies Wyckoff position $2a$, i.e., $(0, 0, 0)$ and $(\frac{1}{2}, \frac{1}{2}, \frac{1}{2})$, and B Wyckoff position $4g$, i.e., $(\pm x, \pm y, 0)$ and $(\pm x + \frac{1}{2}, \mp y + \frac{1}{2}, \frac{1}{2})$, where x and y are internal parameters.

The results of our calculations are listed in Table 5.1, and compared to the experimental values. It is observed that the deviations from the experimental

FIGURE 5.1: *Crystal structure of FeB_4 .*

values are all well below 1%. This very good agreement on the structural level propagates a high level of accuracy to all further calculations, of the electronic structure, phonons, spin fluctuations, and ultimately of the superconducting properties.

5.3.2 Electronic structure

This investigation starts from the electronic structure of FeB_4 , near E_F , calculated using density functional theory (DFT) as implemented in ABINIT [175]. More detailed information on the first-principles calculations is given in Appendix A. The band structure of FeB_4 around E_F is shown in Fig. 5.2(a). Three bands are observed to cross E_F , as indicated with three different colors (red, blue and green). The corresponding Fermi surface is displayed in Fig. 5.2(b), where the same colors are used. Around point R, the center of the

Experimental	Calculated
$a = 2.999 \text{ \AA}$	$3.023 \text{ \AA} (+ 0.8\%)$
$a = 4.579 \text{ \AA}$	$4.552 \text{ \AA} (-0.6\%)$
$b = 5.298 \text{ \AA}$	$5.309 \text{ \AA} (+0.2\%)$
$x = 0.249$	$0.247 (-0.8\%)$
$y = 0.312$	$0.312 (+0.0\%)$

TABLE 5.1: *Comparison between experimental [244] (from room-temperature, single-crystal x-ray diffraction) and calculated structural parameters of FeB_4 , obtained using the PBE exchange-correlation functional. The relative deviations of the calculated parameters from the experimental ones are added between parentheses.*

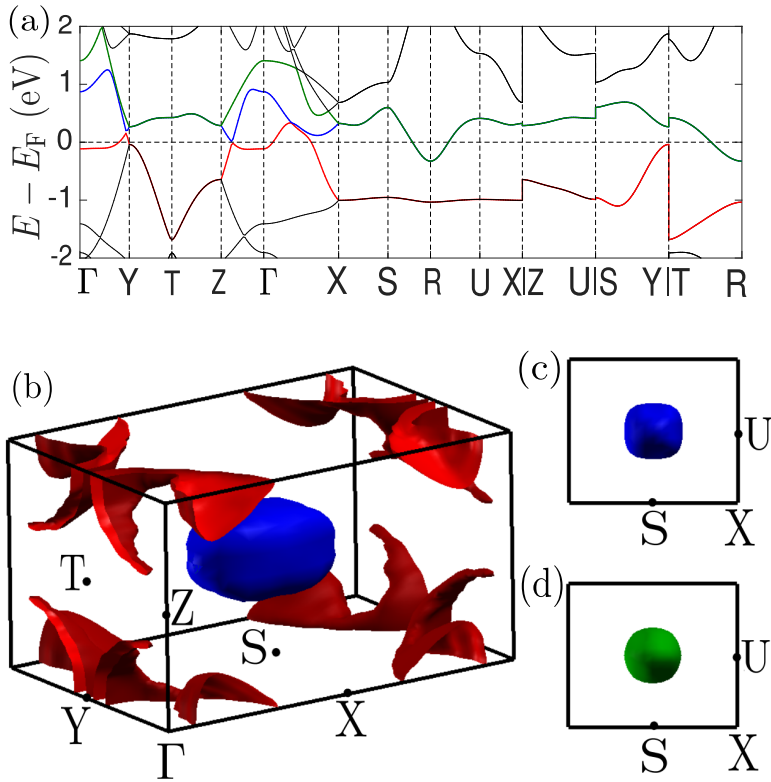


FIGURE 5.2: *The electronic structure of FeB_4 , calculated using DFT. (a) The band structure around the Fermi level (E_F), where three bands are seen to cross E_F . (b) The calculated Fermi surface of FeB_4 , where the colors correspond to those of (a). It consists of two nested ellipsoids around high-symmetry point R (blue and green), as well as a third, anisotropic sheet (red). (c) and (d) The two nested ellipsoids pictured individually in frontal view.*

cell, there are two nested ellipsoidal sheets (blue and green), while the third sheet (red) is more anisotropic. In Figs. 5.2(c) and (d) the nested ellipsoids are depicted individually, so that also the inner ellipsoid (green) becomes visible. The ellipsoids touch along all principal directions in the BZ (S-R, T-R and U-R). Due to their nesting, $\xi_{\mathbf{k},j} - \xi_{\mathbf{k}+\mathbf{q},j'} \sim 0$ in the denominator of Eq. 5.1, which contributes to the peak around Γ in the susceptibility, and thus to the enhancement of FSFs.

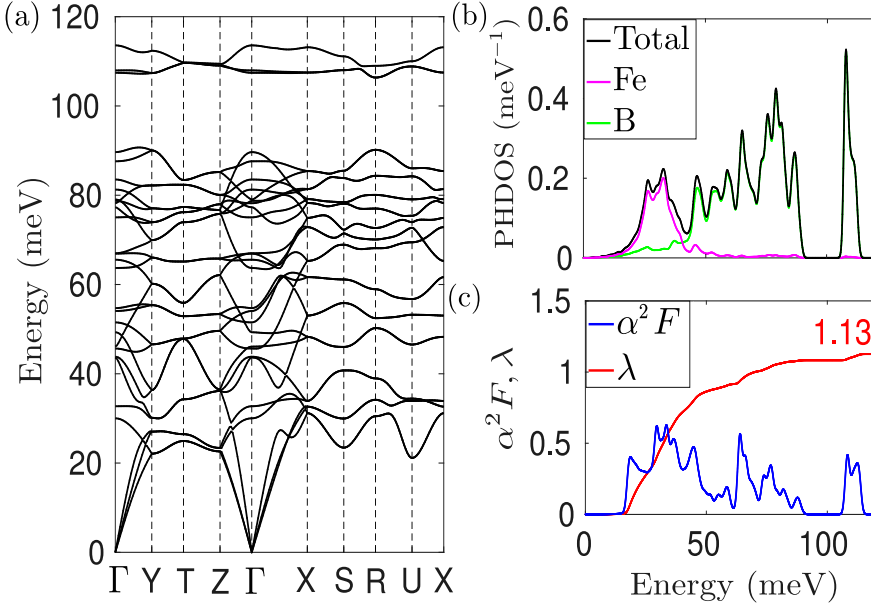


FIGURE 5.3: *Phonons and electron-phonon coupling, calculated within DFPT. (a) The phonon dispersion, extending as high as ~ 115 meV. (b) The phonon density of states (PHDOS), including the contributions of Fe (purple) and B (green). (c) The isotropic Eliashberg function, obtained as $\alpha^2 F(\omega) = \langle \langle \alpha^2 F(\mathbf{k}\mathbf{k}', \omega) \rangle_{\mathbf{k}'_F} \rangle_{\mathbf{k}_F}$ (i.e., the double Fermi surface average of the full Eliashberg function), and the corresponding total e - ph coupling.*

5.3.3 Electron-phonon interaction

Subsequently, I calculated the phonon dispersion and the e - ph coupling in FeB_4 using DFPT. The phonon dispersion is shown in Fig. 5.3(a). The highest phonon frequencies reach almost 120 meV, a considerably high value, due to the very light B atoms. This maximum frequency is even higher for FeB_4 than for other borides such as MgB_2 [200, 201] and OsB_2 [73]. It corroborates its extreme hardness, also mentioned in the introduction. Moreover, the difference in mass between Fe and B explains why their respective vibrational modes are well separated, as shown in the phonon density of states (PHDOS) in Fig. 5.3(b). In Fig. 5.3(c), the isotropic Eliashberg function is displayed, obtained from the full Eliashberg function as the double Fermi surface average $\alpha^2 F(\omega) = \langle \langle \alpha^2 F(\mathbf{k}\mathbf{k}', \omega) \rangle_{\mathbf{k}'_F} \rangle_{\mathbf{k}_F}$, and the resulting isotropic e - ph coupling $\lambda(\omega) = 2 \int_0^\omega d\omega' \omega'^{-1} \alpha^2 F(\omega')$. The contributions of the two atomic species to

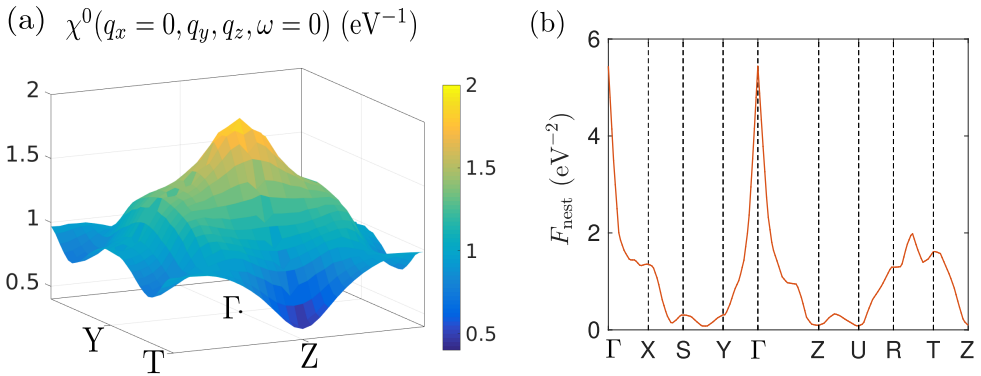


FIGURE 5.4: (a) The bare susceptibility of FeB_4 , $\chi^0(\mathbf{q}, \omega)$, for $q_x = 0$ and $\omega = 0$ (static), calculated from the band structure at $T = 1.5$ K. It shows a strong peak around the Γ point, corresponding to FSFs. (b) The nesting function of FeB_4 on a path along the first Brillouin zone.

the e - ph coupling are comparable, in contrast to, e.g., MgB_2 (where B dominates) [36, 200, 201] and OsB_2 (where Os dominates) [73]. The e - ph coupling amounts in total to a very high value, $\lambda = 1.13$ ¹, much too high to corroborate the experimental $T_c \sim 2.4$ K. This is the motivation for the following section, where we address FSFs in FeB_4 .

5.3.4 Ferromagnetic spin fluctuations and their coupling to electrons

5.3.4.1 Susceptibility

In this section I demonstrate the occurrence of FSFs in FeB_4 from first principles, and calculate their coupling to the electronic states. First, the bare susceptibility of FeB_4 at E_F was calculated, from the band structure shown in Fig. 5.2, using Eq. 5.1. The result is shown in Fig. 5.4 (a), in the static limit, and for $q_x = 0$. The peak in χ^0 around Γ indicates FSFs. It can be traced back to small- \mathbf{q} intraband transitions, as well as to interband contributions of the nested ellipsoidal Fermi sheets, as discussed in the previous section.

¹It was found that a high degree of interpolation of the *ab initio* electron-phonon coupling was necessary to obtain a well-converged result. With a lesser degree of interpolation isotropic e - ph coupling values similar to those of Ref. 243 are obtained, but with sufficient interpolation the e - ph coupling increases to $\lambda_{ep} = 1.13$.

To investigate further the influence of nesting, I also calculated the nesting function,

$$F_{\text{nest}} = \sum_{\mathbf{k}ij} \delta(E_{\mathbf{k},i} - E_{\mathbf{F}}) \delta(E_{\mathbf{k},i} - E_{\mathbf{k}+\mathbf{q},j}) , \quad (5.10)$$

where i and j are band indices. This function peaks at $|\mathbf{q}|$ if the conditions described by the δ -functions are fulfilled by many \mathbf{q} 's, called nesting vectors. This happens in case of parallel Fermi sheets, hence the term *nesting*. The nesting function corresponds to $\lim_{\omega \rightarrow 0} \{\chi''^0(\mathbf{q}, \omega)/\omega\}$, where χ''^0 is the imaginary part of the bare susceptibility, as proven in Appendix C. Thus, the peak of F_{nest} around Γ corroborates the peak in the susceptibility originating from band nesting.

For small, though nonzero q , there are strong interband contributions to the peak, which ultimately vanish for $q \rightarrow 0$. The value of $\chi^0(0, 0)$ therefore reduces in principle to the electronic DOS at $E_{\mathbf{F}}$. The numerical evaluation of Eq. 5.1 depends, however, also on the broadening factor σ . A significant broadening of $\sigma = 0.01$ Ha was needed for a well-converged susceptibility. As such, $\chi^0(0, 0)$ is artificially enhanced beyond the DOS at $E_{\mathbf{F}}$ [$N(E_{\mathbf{F}}) = 0.70$ states/(eV spin)]. The definition of \mathcal{F}_{Fe} in Sec. 5.2, entering in Eq. 5.2, nevertheless ensures that this enhancement cancels out completely in the RPA susceptibility.

5.3.4.2 Stoner interaction strength

The susceptibility peaking at Γ is a necessary condition for FSFs, but is not sufficient for a significant effect of these FSFs on superconductivity. The important other factor is the interaction strength, which is given by the Stoner parameter in the ferromagnetic case. I obtained the Stoner parameter by introducing nonzero magnetization into the material within a fixed spin moment (FSM) calculation, resulting in an energy shift between majority and minority spin states. The results of this calculation are depicted in Fig. 5.5(a), where the electronic density of states (DOS) in different states of magnetization is shown. In the case where $m = 0$ (m being the magnetization per Fe atom) the contributions of different atomic states are also depicted. This DOS corresponds to the electronic structure shown in Fig. 5.2. The states at and near $E_{\mathbf{F}}$ are dominated by Fe-d and B-p character. $N_{\text{Fe}}(E_{\mathbf{F}}) =$

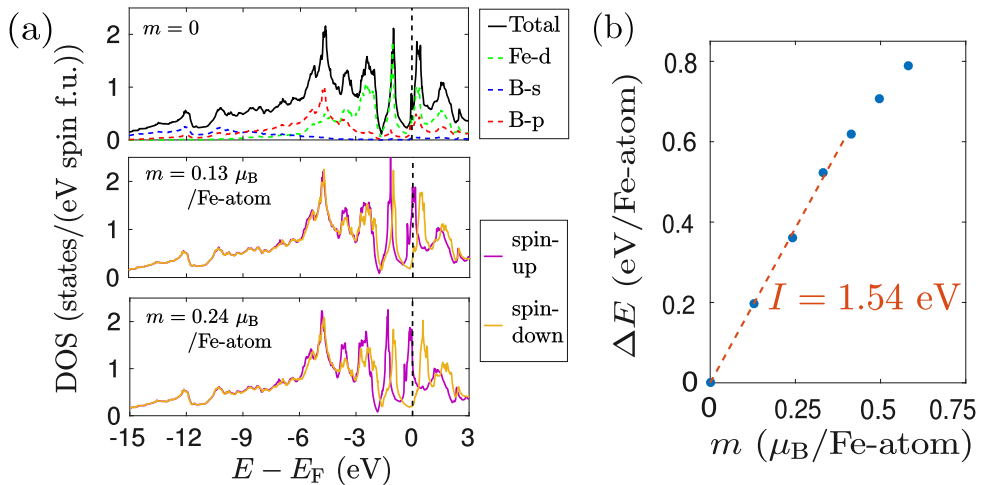


FIGURE 5.5: (a) The electronic density of states (DOS) per formula unit (f.u.) of FeB_4 for different levels of magnetization of the Fe atoms: the paramagnetic case with $m = 0$ (top panel), $m = 0.13 \mu_B/\text{Fe-atom}$ (middle panel), and $m = 0.24 \mu_B/\text{Fe-atom}$ (lower panel), where in the latter two cases an energy shift between spin-up and spin-down states is apparent. In the top panel, the contributions of Fe-d, B-s and B-p states are also shown. (b) The corresponding energy shift, which obeys $\Delta E = Im/\mu_B$ for small m (dashed line), from which the Stoner parameter is obtained. For FeB_4 , the result is $I = 1.54 \text{ eV}$.

0.29 states/(eV spin) was obtained, compared to the total $N(E_F) = 0.70$ states/(eV spin). For nonzero m , the energy shift between spin-up and spin-down bands can be clearly observed, and can be seen to increase with m in Fig. 5.5(a).

Extracting the shifts near E_F from Fig. 5.5(a), for different values of m , I obtained Fig. 5.5(b). Within Stoner theory, this shift due to the magnetization obeys the linear relation $\Delta E = Im/\mu_B$. For low values of m , the linear relation is indeed obeyed, as shown in Fig. 5.5(b), whereby a fit yields $I = 1.54 \text{ eV}$. For higher values of m , the increase in ΔE weakens, as expected. Since we obtain that $N_{\text{Fe}}(E_F)I = 0.45 < 1$ (the Stoner criterion), FeB_4 indeed does not have a ferromagnetic ground state. On the other hand, the Stoner parameter is certainly high enough to induce considerable FSFs.

It is interesting to note the importance of restricting the interaction strength to the Fe states, mentioned already in Sec. 5.2. If the total DOS were

used instead, FeB_4 would come out as marginally ferromagnetic according to $N(E_F)I = 1.08 > 1$. This may be related to the tendency of DFT in local spin density approximation (LSDA) or generalized gradient approximation (GGA) to overestimate static magnetism [241]. However, I found the magnetic moments to be completely localized on the Fe atoms, in the FSM calculations. This provides me with the physical rationale for limiting the Stoner-type interaction to Fe states only. Thus, by avoiding to treat I as a free parameter – as in, e.g., Ref. 241 – I have remained close to a fully *ab initio* approach.

5.3.4.3 Coupling of electrons to ferromagnetic spin fluctuations

The interaction strength plays a crucial role in the coupling of FSFs to electrons, according to Eqs. 5.2 and 5.3. Here, $\lambda_{\text{sf}}(\mathbf{k}_F, \omega)$ is evaluated for FeB_4 using these equations, where the dependence on \mathbf{k}_F is obtained by convolution with the Fermi surface. The result in the static limit, $\omega \rightarrow 0$, in particular λ_{sf} in the Γ -Y-T-Z plane ($k_x = 0$), is shown in Fig. 5.6(a). It is observed that there is strong coupling to FSFs in the direction Γ -Y, since in this direction small \mathbf{q} 's connect parts of the anisotropic Fermi sheet (red), evident from Fig. 5.2(b). In the other directions λ_{sf} drops significantly. In Fig. 5.6(b) I show λ_{sf} in the X-S-R-U plane ($k_x = \frac{\pi}{a}$), that cuts through the center of the nested ellipsoidal Fermi sheets. Here, the coupling λ_{sf} shows a broad peak around R, due to nesting of these sheets with small \mathbf{q} . It diminishes accordingly in all other directions. The total static coupling of FSFs to electrons, calculated as the Fermi surface average, amounts to $\lambda_{\text{sf}} = \langle \lambda_{\text{sf}}(\mathbf{k}_F, \omega = 0) \rangle_{\mathbf{k}_F} = 0.55$.

5.3.5 Superconducting properties

Having established the e - ph coupling and the coupling of electrons to FSFs in Secs. 5.3.3 and 5.3.4.3, we can now study the competition between these interactions in relation to superconductivity. To this end, the anisotropic Eliashberg equations are solved including both the e - ph coupling and the coupling to FSFs in the interaction kernel of the spin singlet channel. Here, the full momentum and frequency dependence of the coupling are retained.

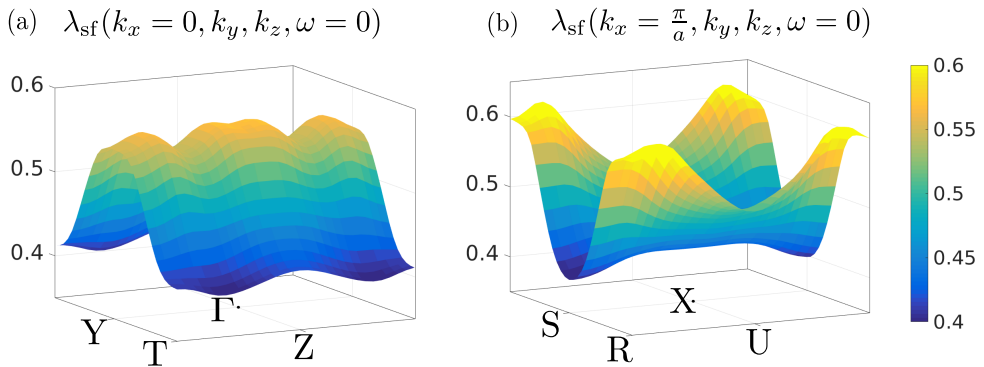


FIGURE 5.6: *The coupling between electrons and FSFs in FeB_4 , $\lambda_{sf}(\mathbf{k}_F, \omega_n)$, in the static limit ($\omega = 0$), calculated using Eq. 5.3, and convoluted with the Fermi surface to obtain the dependence on \mathbf{k}_F . (a) The coupling for $k_x = 0$, (b) The coupling for $k_x = \frac{\pi}{a}$. The average over the whole Fermi surface is $\lambda_{sf} = \langle \lambda_{sf}(\mathbf{k}_F, \omega = 0) \rangle_{\mathbf{k}_F} = 0.55$.*

More information on how the anisotropic Eliashberg equations are solved numerically is provided in Appendix A.

We started by solving the anisotropic Eliashberg equations, taking into account just the e - ph coupling, not yet the interaction with FSFs. The resulting superconducting gap spectrum $\Delta(\mathbf{k}_F, T)$ at low temperature ($T = 0.5$ K) is shown on the Fermi surface in Fig. 5.7(a). The gap spectrum consists of a single, anisotropic gap with large values for Δ , ranging from 5 to 8 meV (again at $T = 0.5$ K). The corresponding critical temperature obtained from solving the anisotropic Eliashberg equations for a range of temperatures is $T_c = 41$ K (using the standard value for the Coulomb pseudopotential, $\mu^* = 0.1$). This value exceeds the experimental value ($T_c \sim 2.4$ K) by more than an order of magnitude.

When including the effect of FSFs, this changes drastically. In this case, the superconducting gap spectrum at low temperature ($T = 0.5$ K) is shown in Fig. 5.7(b). $\Delta(\mathbf{k}_F, T)$ presents again a single, anisotropic gap, but now in the range $\Delta(\mathbf{k}_F, T) \sim 0.1 - 0.3$ meV. With such anisotropic, single-gap, FeB_4 is more similar to OsB_2 (an orthorhombic material, like FeB_4 , also with three bands at E_F , cf. Chapter 4) [73] than to MgB_2 (a layered hexagonal material, cf. Chapters 6 and 7), which is a well-established two-gap boride superconductor [28, 36–39]. As the superconducting gap depletes rather uniformly

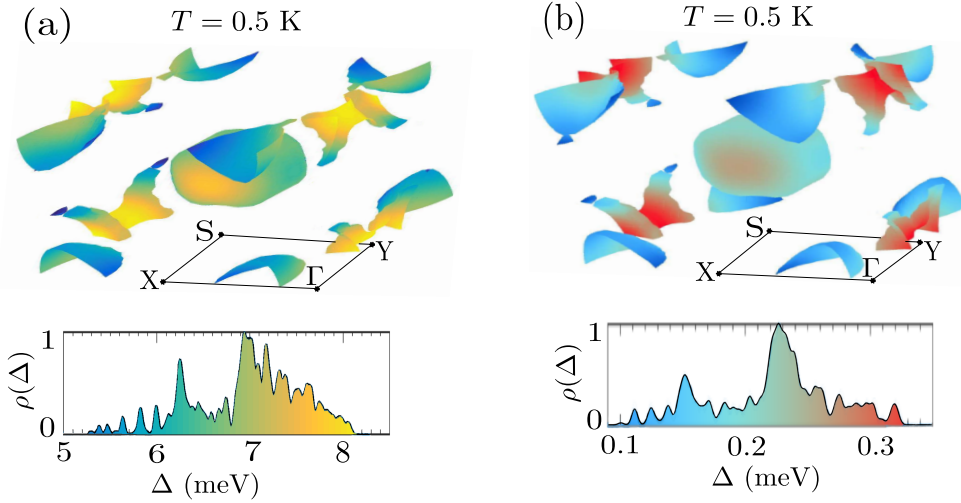


FIGURE 5.7: *The superconducting gap spectrum, $\Delta(\mathbf{k}_F, T)$, of FeB_4 on the Fermi surface at $T = 0.5$ K, calculated using anisotropic Eliashberg theory with *ab initio* input (and using $\mu^* = 0.1$). (a) Gap spectrum obtained when only *e-ph* coupling is taken into account. (b) Gap spectrum obtained when both *e-ph* coupling and interaction with FSFs are taken into account. $\rho(\Delta)$ represents the distribution of the gap, showing a single, yet anisotropic gap in both cases. However, the superconducting gap is strongly depleted from the range 5–8 meV to the range 0.1 – 0.3 meV, under the influence of the FSFs.*

under the influence of FSFs, as seen in Fig. 5.7, we can conclude that the effect of FSFs is fairly isotropic in FeB_4 .

Subsequently, we again solved the anisotropic Eliashberg equations for a range of different temperatures, now taking into account both the *e-ph* coupling and coupling to FSFs (using $\mu^* = 0.1$ for the Coulomb pseudopotential). The resulting gap spectrum as a function of temperature is displayed in Fig. 5.8. The critical temperature obtained here is $T_c = 1.65$ K, in very good agreement with the experimental value $T_c \sim 2.4$ K². FeB_4 is thus a superconductor with very strong *e-ph* coupling, that in itself would lead to $T_c = 41$ K, which is however depleted to $T_c \sim 2$ K due to FSFs. The very good agreement with the experimental value demonstrates that FSFs can be

²In Ref. 244, in Fig. 2 specifically, critical temperatures are obtained for FeB_4 with two different B isotopes. For ^{10}B , $T_c \sim 2.7$ K is obtained, while for ^{11}B , $T_c \sim 2.4$ K. In my calculations a weighted average of these isotopes was used (mass of 10.81 atomic units), based on the natural occurrences of these isotopes. The resulting mass is closest to that of the heavier isotope, therefore our result can be compared to the experimental value $T_c \sim 2.4$ K.

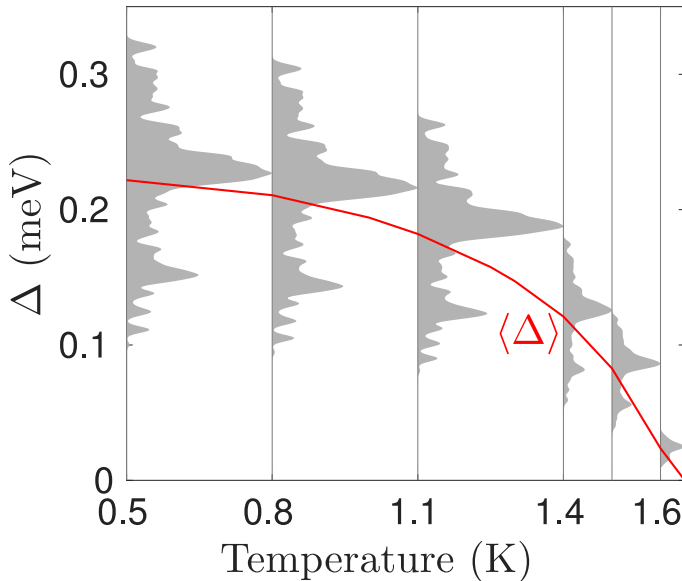


FIGURE 5.8: *The superconducting gap distribution as a function of temperature, calculated using anisotropic Eliashberg theory with *ab initio* input, including FSFs. The critical temperature can be seen to be $T_c = 1.65$ K. The red line represents the average value of the gap weighted with the distribution.*

included in the anisotropic Eliashberg equations, to obtain a quantitatively accurate superconducting gap spectrum. To the best of my knowledge, the analysis provided here is the first to report on this.

In addition, the tendency for spin triplet pairing in FeB_4 due to FSFs was investigated. Solving the anisotropic Eliashberg equations with the kernels outlined in Sec. 5.2, we did not obtain a gap function with symmetry $\Delta(\mathbf{k}_F) \rightarrow -\Delta(-\mathbf{k}_F)$, i.e., with an odd (ungerade) momentum dependence. Therefore, within the theoretical framework established here we can exclude the possibility of spin triplet pairing in FeB_4 .

5.4 Conclusions

In summary, I have presented an advanced approach to treat both lattice vibrations and ferromagnetic spin fluctuations in superconductors, entirely from first principles. Specifically, I extended the framework where the *ab initio* calculated electron-phonon coupling (λ_{ep}) is used to solve to anisotropic

Eliashberg equations for the gap spectrum (which has been done for materials like MgB_2 [36, 38, 39, 200, 201] and OsB_2 [73]). The first step is to calculate the bare susceptibility of the material from the electronic structure (in this work also calculated from first principles), specifically that near the Fermi level [cf. Eq. 5.1]. The next step is calculating the interaction strength of the ferromagnetic spin fluctuations. This can be achieved by means of the energy shift between minority and majority bands in the competing, ferromagnetic phase, which obeys $\Delta E = Im/\mu_B$, where the Stoner parameter I yields the interaction strength. Then, the RPA susceptibility can be calculated, yielding directly the coupling of ferromagnetic spin fluctuations with electrons λ_{sf} [using Eqs. 5.2 and 5.3]. For the spin singlet superconducting channel, the resulting total coupling is $\lambda_{\text{ep}} - \lambda_{\text{sf}}$, while for the spin triplet channel it amounts to $\lambda_{\text{ep}} + \frac{\lambda_{\text{sf}}}{3}$ [256].

I have applied this new approach to the recently discovered Fe-based superconductor iron tetraboride (FeB_4) [244], to resolve the large discrepancy between the predicted [243] and measured [244] critical temperature, and to learn more about its superconducting gap structure. I showed first that the Fermi surface has contributions from three different bands, resulting in two nested ellipsoids and an anisotropic sheet. This nesting at small \mathbf{q} is the main contribution to the peak in the calculated susceptibility of FeB_4 , for small wavevectors, corresponding to ferromagnetic spin fluctuations. The Stoner parameter in FeB_4 is considerably high (~ 1.5 eV) – though not high enough for a ferromagnetic ground state. Accordingly, a strong coupling of the spin fluctuations to the electronic states was found, in particular to the nested ellipsoids, with an average of $\langle \lambda_{\text{sf}} \rangle_{\mathbf{k}_F} = 0.55$ over the Fermi surface. This mediates a repulsive interaction between the electrons that is in direct competition with the strong, attractive interaction mediated by phonons (with Fermi surface average $\lambda_{\text{ep}} = 1.13$). By solving the anisotropic Eliashberg equations, it was revealed that the spin fluctuations are able to reduce the critical temperature from a very high $T_c = 41$ K to $T_c = 1.7$ K, in very good agreement with the experimental value ($T_c = 2.4$ K [244]). In spite of this drastic effect on T_c , I found that the distribution of the gap spectrum on the Fermi surface, namely a single anisotropic gap (similar to, e.g., OsB_2 [73]), is largely unaltered.

The excellent agreement between the results obtained with this new method

and the corresponding experiment demonstrates the potential of an *ab initio* approach to anisotropic Eliashberg theory in describing interactions that coexist and compete with the electron-phonon interaction. Although ferromagnetic spin fluctuations showed a primarily detrimental effect on superconductivity in FeB_4 , I expect that the approach will lead to the detection and quantification of spin fluctuations in other materials with coexisting conventional and unconventional pairing mechanisms, resulting in nontrivial contributions to the superconducting gap spectrum and to the superconducting properties in general.

Publication

J. Bekaert, A. Aperis, B. Partoens, P. M. Oppeneer, and M. V. Milošević, *Advanced first-principles theory of superconductivity including both lattice vibrations and spin fluctuations: The case of FeB_4* , Phys. Rev. B **97**, 014503 (2018).

Chapter 6

Multigap superconductivity in the atomically thin limit: magnesium diboride

*Two-dimensional materials are known to harbor properties very different from those of their bulk counterparts. Recent years have seen the rise of atomically-thin superconductors, with a caveat that superconductivity is strongly depleted unless enhanced by specific substrates, intercalants or adatoms. Surprisingly, the role in superconductivity of electronic states originating from simple free surfaces of two-dimensional materials has remained elusive to date. Starting from first principles, I show the formation and evolution of superconducting gaps in MgB_2 at its ultrathin limit. Atomically thin MgB_2 is distinctly different from bulk MgB_2 in that surface states become comparable in electronic density to the bulk-like σ and π bands. Combining the *ab initio* electron-phonon coupling with the anisotropic Eliashberg equations, I show that monolayer MgB_2 develops three distinct superconducting gaps, on completely separate parts of the Fermi surface due to the emergent surface contribution. These gaps hybridize nontrivially with every extra monolayer added to the film, owing to the opening of additional coupling channels. Furthermore, I reveal that the three-gap superconductivity in monolayer MgB_2 is robust over the entire temperature range that stretches*

up to a considerably high critical temperature of 20 K. Subsequently, an experimental validation by means of angle-resolved photoemission spectroscopy (ARPES) of the predicted emerging surface state and the resulting superconducting gap is provided in this chapter. These findings establish free surfaces as an unavoidable ingredient in understanding and further tailoring of superconductivity in atomically thin materials.

6.1 Introduction

As explained in Sec. 1.2.1, competition and coupling between the multiple condensates in a multigap superconductor can lead to rich new physics [64]. In that sense, one expects superconductors with three or more gaps to be far more exciting than the two-gap ones, due to additional competing effects and possible quantum frustration between the condensates [95]. However, a major roadblock is the lack of distinctly multi-gap (beyond two-gap) superconductors. In recent years two such materials were proposed theoretically by Gross and coworkers, using density functional theory for superconductors [83]. One is molecular hydrogen, which under very high pressure develops three superconducting gaps on different Fermi sheets [42]. However, due to anisotropy two of the gaps strongly overlap. The other material is CaBeSi, a MgB₂-like compound in which splitting of the π -bands was predicted to give rise to three-gap superconductivity [79], but with impractically low $T_c \cong 0.4$ K.

Here, we follow a different route, namely that of atomically-thin instead of bulk superconductors. Recently, owing to immense experimental progress [100, 101], superconductivity was realized down to monolayer thickness in several materials, as discussed in Sec. 1.2.2. It is well known that quantum confinement in the vertical direction generally separates subbands in ultrathin films, innating multiband and thereby potentially multigap superconductivity [129]. We note here an additional, natural connection between two-dimensional and multigap superconductors, much less explored to date: *surface states* can equally host new superconducting gaps without equivalent in the bulk material.

Hints of additional superconducting gaps opening in 2D materials have been suggested in recent works, for materials such as two-dimensional Ga and FeSe [257]. They are deduced from fitting of the measured temperature dependence of, e.g., the London penetration depth, which unfortunately does not provide much insight into the origin of the proposed additional gaps. The fitting technique is moreover not fully waterproof, as the measurements can equally result from just anisotropy of the superconducting gap, and no additional gap opening, as shown in Chapter 4.

A particularly interesting candidate to examine the effect of thinning on superconductivity is hexagonal magnesium diboride (MgB_2), owing to its conveniently layered, graphene-related structure as well as to its high critical temperature of 39 K in bulk form. MgB_2 consists of alternating Mg- and B-planes, with stronger in-plane (σ) than out-of-plane (π) electronic bonds. As such, its anisotropic layered crystal structure gives rise to innate multigap superconductivity, while also enabling growing the material at atomic thickness, layer by layer. In bulk MgB_2 , superconductivity is fully governed by B-atoms [36, 231, 258, 259], since both the σ and π gaps originate from electrons in B-planes that couple to lattice vibrations of the B-atoms. In the thinnest limit, however, the relative importance of the free Mg surface increases, which may influence the role Mg plays in the superconducting properties¹. It is therefore of particular interest to understand how superconductivity would change in the thinnest limit.

Using a combination of first-principles calculations and anisotropic Eliashberg theory, we reveal the major influence of an emerging surface state on superconductivity in ultrathin MgB_2 . This contribution hybridizes with those of the σ and π bands in a highly nontrivial manner, changing the multigap physics with every additional monolayer. This finally leads to pure three-gap superconductivity in one-monolayer MgB_2 , retained up to a high critical temperature of 20 K. This is to date the highest T_c among monolayer superconductors without coupling to a substrate.

¹This goes beyond a previous study of few-monolayer MgB_2 , based on the tight-binding formalism, in which surface states (electronic as well as vibrational) were completely omitted [260].

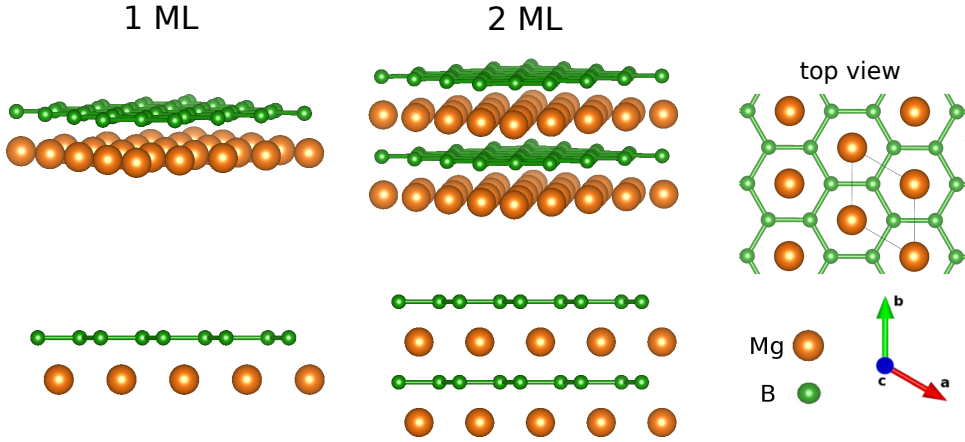


FIGURE 6.1: *Crystal structure of one-monolayer (1 ML) and two-monolayer (2 ML) MgB₂, both depicted under an angle as well as in side view. On the right a top view of MgB₂ is given, showing the honeycomb structure of the boron atoms. The lattice vectors **a**, **b** and **c** are also shown in this case.*

Finally, in collaboration with several experimental groups, 1 – 8 monolayers (MLs) of MgB₂ were realized using molecular beam epitaxy, and using in-situ room- and low-temperature angle-resolved photoemission spectroscopy (ARPES) the theoretical predictions for the surface state were validated (where I performed the theoretical interpretation of the results). By comparing the *ab initio* anisotropic Eliashberg theory results and the measured superconducting gap for six MLs MgB₂, we can fully assess the surprisingly distinct and influential contribution of the surface states to the superconducting gap spectrum and tunneling properties of few-layer MgB₂.

6.2 Crystal structure

Bulk MgB₂ consists of hexagonal Mg layers intercalated with B layers in a honeycomb lattice. It thus adopts the hexagonal space group P6/mmm (No. 191) [223]. Mg occupies Wyckoff position 1*a*, i.e., (0, 0, 0), while B occupies Wyckoff position 2*d*, i.e., $(\frac{1}{3}, \frac{2}{3}, \frac{1}{2})$ and $(\frac{2}{3}, \frac{1}{3}, \frac{1}{2})$.

Albeit not being the thermodynamic ground state, MgB₂ with this structure thinned down to the atomic limit has been predicted to be mechanically stable and to be realizable owing to kinetic barriers [261]. Magnesium is crucial in

forming ultrathin MgB_2 , and in its absence a monolayer of boron organizes in a more intricate way, known as borophene [262]. As such, few-monolayer MgB_2 has already been synthesized experimentally, on a Mg substrate [263]. Here, we first consider *freestanding* MgB_2 films, but in Sec. 6.5 we investigate the influence of attaching the film onto a Mg substrate.

One monolayer (1-ML) of MgB_2 consists of one magnesium and one boron layer, the latter in a honeycomb lattice, and thus structurally similar to doped graphene. Magnesium is positioned above the center of the boron honeycomb tiles, and thus forms an hexagonal close packed (hcp) structure. The in-plane lattice vectors of the hexagonal lattice of MgB_2 , shown as \mathbf{a} and \mathbf{b} in Fig. 6.1, thus have an angle of 120° between them. The in-plane lattice vectors are thus given by

$$\mathbf{a} = \frac{a}{2}\hat{x} - \frac{\sqrt{3}a}{2}\hat{y}, \quad \mathbf{b} = \frac{a}{2}\hat{x} + \frac{\sqrt{3}a}{2}\hat{y}, \quad (6.1)$$

where a is the in-plane lattice parameter and \hat{x} and \hat{y} are the Cartesian unit vectors. Atomic-scale structures of one-monolayer and two-monolayer (or bilayer) MgB_2 are depicted in Fig. 6.1. Here, the space group is $P6mm$ (No. 183), where Mg still occupies Wyckoff position $1a$, while B now occupies position $2b$, i.e., $(\frac{1}{3}, \frac{2}{3}, z)$ and $(\frac{2}{3}, \frac{1}{3}, z)$, where z is the distance from the Mg plane. These Wyckoff positions correspond to the two *sublattices* of the honeycomb structure (usually called A and B). The DFT calculations yielded for ML MgB_2 that the equilibrium values are $a = 3.04 \text{ \AA}$ as the lattice parameter and $z = 1.65 \text{ \AA}$ as as the distance between the B and Mg planes.

I modeled these structures using DFT (using ABINIT [175], details given in Appendix A) by constructing slabs, where a sufficient amount of vacuum is implemented by means of an elongated lattice vector perpendicular to the 2D crystal plane. No tendency to break the in-plane lattice symmetry (no buckling, etc.) was found.

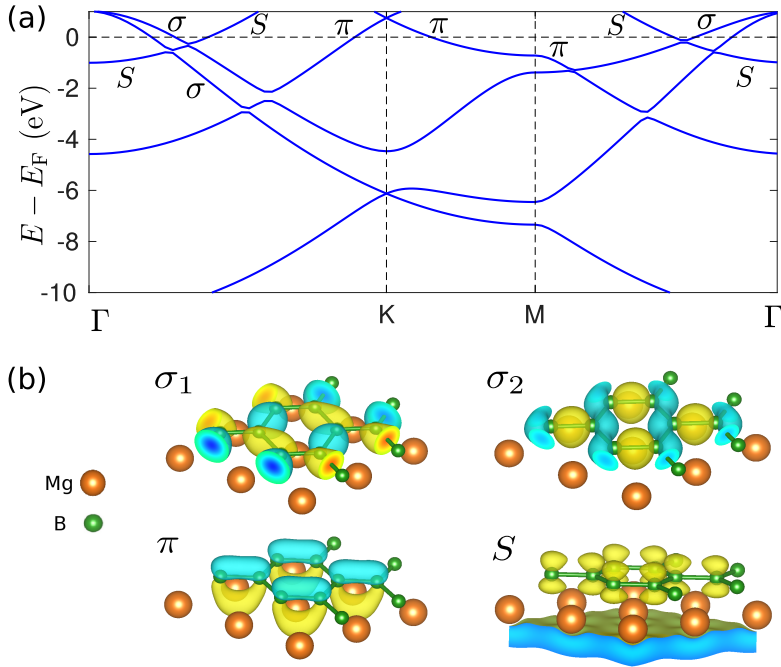


FIGURE 6.2: *Electronic properties of 1-monolayer MgB₂. (a) The band structure obtained from DFT, where the three different states near the Fermi level (σ , π and S) are indicated. (b) Wave functions of the states at the Fermi level. σ_1 and σ_2 indicate the wave functions of respectively the inner and outer σ band (the inner band cuts E_F closer to Γ). For σ_1 , σ_2 , and π the real part of the wave function is shown (obtained along Γ - K), the color change between blue and green indicating a change of sign. For S the norm of the wave function is shown (obtained along Γ - M), giving a better representation because there is a large imbalance between the magnitudes of the real and imaginary parts.*

6.3 Properties of the monolayer

6.3.1 Electronic structure

The electronic structure lies at the base of the superconducting properties. I performed DFT calculations (again in ABINIT) to characterize the electronic properties of 1-ML MgB₂. The result is shown in Fig. 6.2(a). Three distinctly different types of bands are seen to cross E_F , namely σ , π and S . These are the σ bands – two of them (around Γ), the π band (around K), and the surface band S . The character of these bands can be studied from the corresponding

wave functions, shown in Fig. 6.2(b). The σ wave functions originate from σ bonds between the boron atoms. These are made up of p_x and p_y orbitals (mutually hybridized to accommodate the hexagonal structure), that overlap with their axes aligned along the interatomic axis. The fact that there are two σ bands originates from the two boron atoms in the unit cells (occupying different sublattice sites). The π wave function, on the other hand, stems from π bonds between the boron p_z orbitals, with their axes perpendicular to the interatomic axis. The overlap thus creates a nodal plane with zero electronic density, in this case the boron plane.

So far, the σ and π bands are essentially the same as in bulk MgB_2 . However, the surface band, S , is a distinct feature of two-dimensional forms of MgB_2 , and is thus not present in the bulk. As can be deduced from its wave function shown in Fig. 6.2(b) it originates directly from the Mg atoms that face vacuum, in other words the free Mg surface. As such, it possesses predominant Mg-p character, as opposed to the B-p character of the other bands. It can be observed in Fig. 6.2(b) to contain a fraction of B- p_z character in addition. So, there is increased hybridization between B and Mg state in the atomically thin limit. The S state is very delocalized, thus, archetypically metallic-like. The corresponding Fermi surface is depicted in Fig. 6.5(a) – the colors corresponding to the superconducting gap, we will get back to that in the next sections.

6.3.2 Electron-phonon interaction

To find out if 1-ML MgB_2 can develop superconductivity I calculated the electron-phonon ($e-ph$) coupling from first principles, employing density functional perturbation theory (DFPT), introduced in Chapter 3. The resulting phonon band structure, phonon DOS and Eliashberg function are shown in Fig. 6.3. The flexural ZA mode (cf. Sec. 3.2.1) displays the expected quadratic dispersion prominently. As in bulk, discussed in Sec. 4.5, the phonon energies reach quite high values of almost 100 meV. As for the phonon density of states (DOS), Mg-related modes are still at lower energies than B-related modes, due to their mass difference. However, there is more hybridization for energies 30 – 50 meV, due to increased interaction between the layers, manifesting also in the hybridization of the electronic states discussed above.

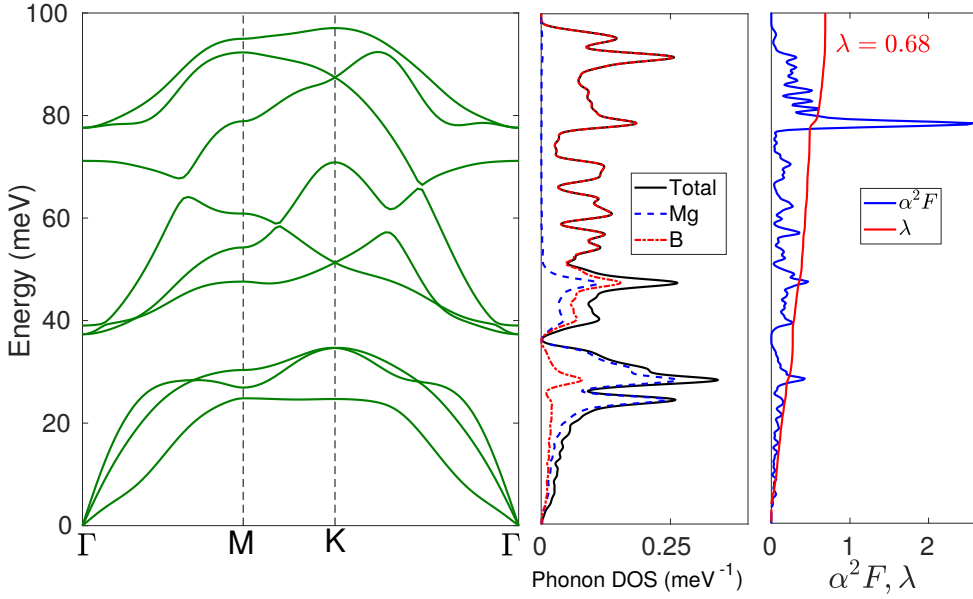


FIGURE 6.3: *The phonon dispersion, phonon density of states (DOS) and the isotropic Eliashberg function of 1-ML MgB₂, calculated using DFPT. The isotropic Eliashberg function is defined as $\alpha^2 F(\omega) = \langle \langle \alpha^2 F(\mathbf{k}\mathbf{k}', \omega) \rangle_{\mathbf{k}'_{\text{F}}} \rangle_{\mathbf{k}_{\text{F}}}$ (i.e., the double Fermi surface average). The resulting isotropic electron-phonon coupling, λ , is also shown.*

The isotropic Eliashberg function, $\alpha^2 F$, of 1-ML MgB₂ shows similarities with that of bulk MgB₂, discussed in Sec. 4.5. The strongest peak in $\alpha^2 F$ occurs slightly below 80 meV in the monolayer and around 75 meV in the bulk. This mode is an optical B-mode, specifically the doubly degenerate E_{2g} mode². The eigendisplacements are along the armchair direction of the honeycomb lattice, as depicted in Fig. 6.4, in the LO case. In this mode, B atoms of the two sublattices move out-of-phase (as required for an optical mode), so that the honeycomb tiles are deformed. The TO mode is also part of the doubly degenerate E_{2g} . In this case the phonons move similarly, yet along the zigzag direction. The TO and LO modes by symmetry host the same electron-phonon coupling, so that the total coupling is double.

The main difference between bulk and monolayer MgB₂ is that in the latter the E_{2g} is narrower and more sharply peaked. Therefore, it contributes less to the total e - ph coupling in the monolayer compared with the bulk. As a

²The E_{2g} mode is generally present in honeycomb lattices, and thus also in graphene, as we saw in Sec. 3.2.1.

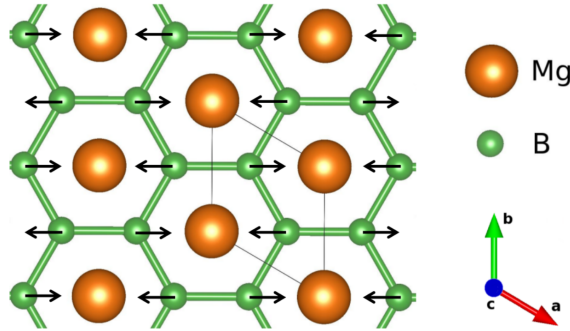


FIGURE 6.4: *The E_{2g} phonon mode of the B atoms giving the dominant contribution to the electron-phonon coupling in 1-ML MgB_2 .*

result, the total e - ph coupling is mildly depleted in the monolayer ($\lambda = 0.68$) compared with the bulk ($\lambda = 0.81$). In Chapter 7 I will offer several pathways to increase the e - ph coupling in monolayer MgB_2 .

6.3.3 Superconducting properties

With the *ab initio* e - ph coupling as input, the anisotropic Eliashberg equations were subsequently solved self-consistently (more details are provided in Appendix A). The Coulomb repulsion is described by $\mu^* = 0.13$, yielding correct T_c for bulk MgB_2 . This value is also in line with previously established values [36, 264]. The Coulomb pseudopotential is not expected to change drastically in the 2D limit, owing to the layered structure of MgB_2 . Namely, superconductivity of the dominant σ -bands is quasi-two-dimensional even in bulk MgB_2 , so the same is expected for the screening.

In Fig. 6.5(a) the resulting superconducting gap spectrum on the Fermi surface, $\Delta(\mathbf{k}_F, T)$, at $T = 1$ K, is shown as well as the distribution of the gap, $\rho(\Delta)$. This result shows that 1-ML MgB_2 is a distinctly three-gap superconductor, with separate gaps opening on the σ , π and S bands. The gap amplitudes are about half of those of bulk MgB_2 , with Fermi surface averages at zero temperature of $\langle \Delta_\sigma(0) \rangle = 3.3$ meV, $\langle \Delta_S(0) \rangle = 2.7$ meV and $\langle \Delta_\pi(0) \rangle = 1.4$ meV. The critical temperature of $T_c = 20$ K, compared to the bulk $T_c \cong 39$ K [28, 36–39], follows the same trend.

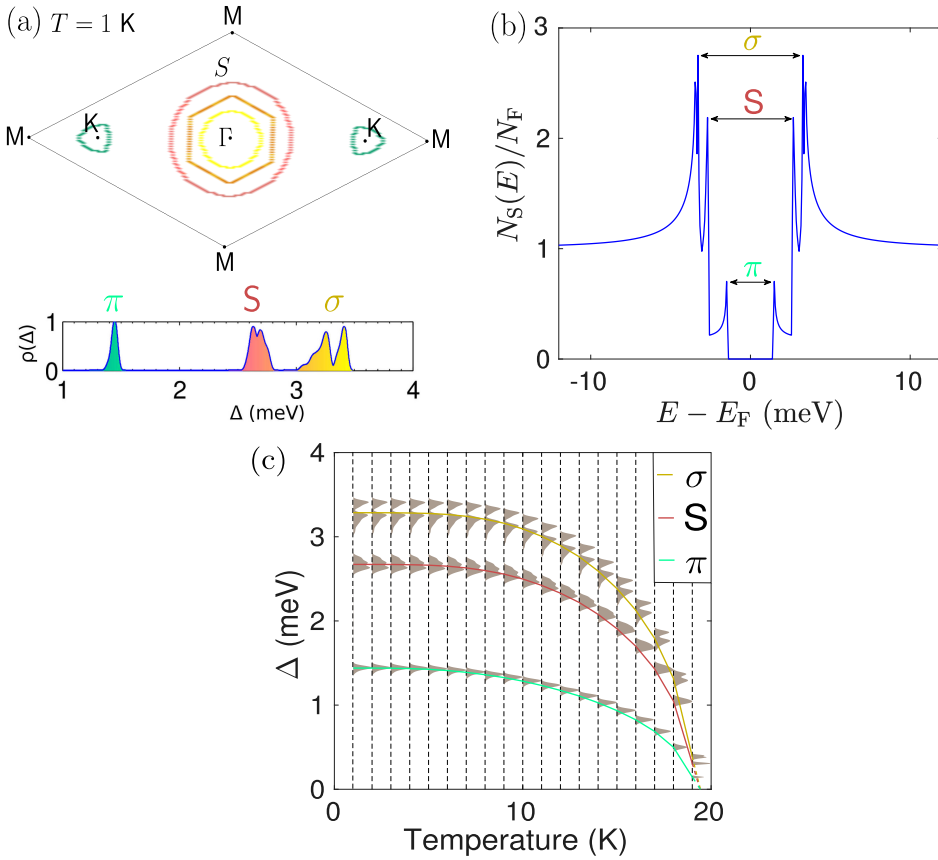


FIGURE 6.5: *The superconducting spectrum of 1-ML MgB₂, calculated by anisotropic Eliashberg theory with ab initio input. (a) The distribution of the three superconducting gaps $\Delta(\mathbf{k}_F, T)$ on the Fermi surface: π , S (for surface) and σ , at $T = 1$ K. (b) The density of states in the superconducting state at $T = 1$ K, showing three distinct peaks corresponding to the three gaps. (c) The evolution of the gap spectrum with temperature, including the gap averages. The calculation shows that 1-ML MgB₂ has $T_c \cong 20$ K.*

One should note that the McMillan-Allen-Dynes formula using the isotropic e - ph coupling, $\lambda = 0.68$, produces merely $T_c = 11$ K, which is a severe underestimation compared with the proper value $T_c = 20$ K. This demonstrates the importance of multiband effects in MgB₂, which makes that isotropic approximations do not suffice at all.

To corroborate further the predicted three-gap superconductivity in 1-ML MgB₂, we calculated the density of states (DOS) in the superconducting state N_S , using the Eliashberg expression given in Sec. 3.5.6. The result displayed

in Fig. 6.5(b) shows that N_S for 1-ML MgB₂ consists of three distinct and narrow peaks, corresponding to the three superconducting gaps. On the other hand, in bulk MgB₂ the DOS in the superconducting state consists of only two peaks, corresponding to the σ and π gaps (as shown both in theory [39] and in scanning-tunneling spectroscopy experiments [27, 28, 62, 265]). As such, the tunneling properties undergo equally radical changes going from bulk to ML MgB₂. Since N_S determines the superconducting tunneling properties, the predicted three-gap superconductivity in ML MgB₂ can be verified with low-temperature scanning tunneling spectroscopy [28].

Last but not least, I want to note that three-gap superconductivity in 1-ML MgB₂ is very robust with temperature. Fig. 6.5(c) displays the calculated temperature evolution of the superconducting gap spectrum, proving that the three superconducting gaps are well separated up to 18 K, very close to $T_c = 20$ K.

6.4 Evolution with added monolayers

6.4.1 Evolution of the superconducting gap spectrum

To provide a deeper understanding of the origin of three-gap superconductivity in 1-ML MgB₂, we will study what changes when adding monolayers to the system, by considering in particular 2-ML and 4-ML thick MgB₂. The superconducting gap spectra, again obtained using anisotropic Eliashberg theory, are displayed in Fig. 6.6(a) and (b). One observes in Fig. 6.6(a) that a hexagonal band lying between the S band and the σ bands develops an additional gap in 2-ML MgB₂. This band is a split-off band of the σ -bands (with B-p character), indicated with S' as it originates from a surface state of the *free B surface*. The superconducting gap opening on band S' is weakly linked to the gaps opening on the π and S bands, but (barely) separate from the gap on the σ bands, making 2-ML MgB₂ an *anisotropic two-gap* (nearly single-gap) superconductor. In 4-ML MgB₂ we see a higher degree of hybridization between the π , S and S' condensates, forming an anisotropic gap clearly separated from the σ gap.

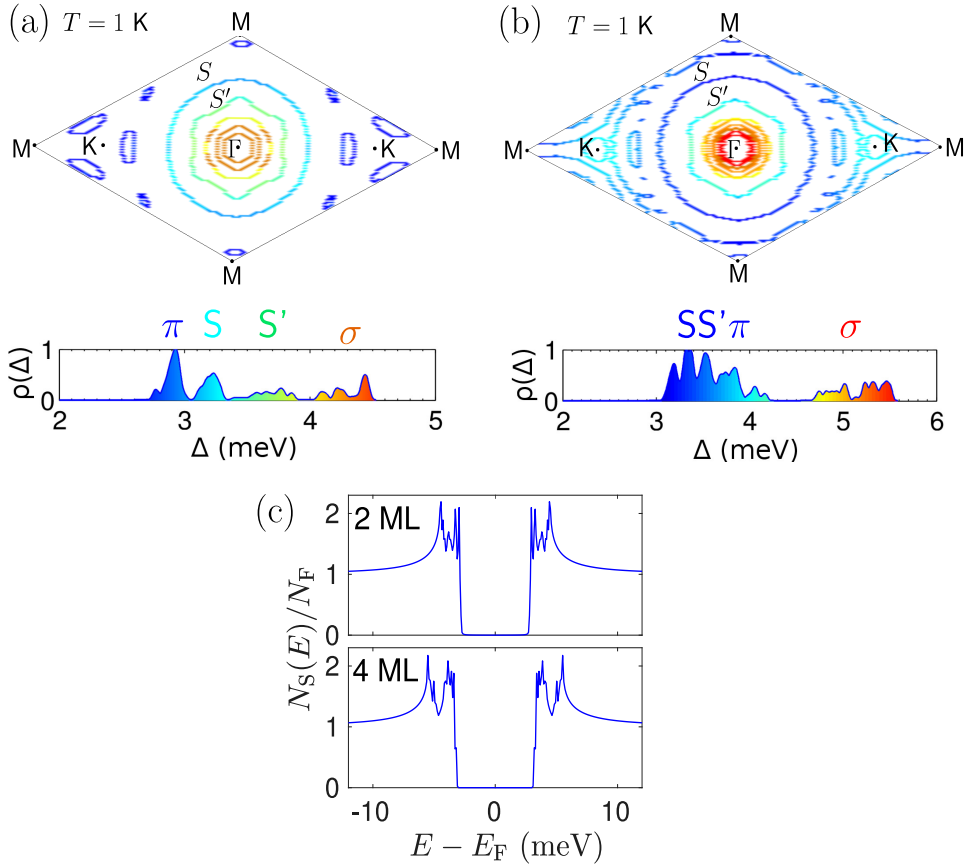


FIGURE 6.6: (a) and (b) The distribution of the superconducting gap spectrum on the Fermi surface of 2-ML and 4-ML MgB₂, respectively calculated from anisotropic Eliashberg theory with *ab initio* input. Both are anisotropic two-gap superconductors, with surface condensates S and S' hybridized with the π condensate. (c) The density of states in the superconducting state for 2 and 4 MLs, calculated at $T = 1$ K, showing the overall two gap-nature as well as the anisotropy of the gap spectrum. The critical temperatures found for 2 and 4 MLs MgB₂ are 23 K and 27 K respectively.

In Fig. 6.6(c) the corresponding quasiparticle DOS in the superconducting state is shown. For 2-ML MgB₂, N_S clearly reflects the anisotropy of the gap spectrum, while for 4-ML MgB₂ N_S consists of two broader peaks, resulting from the strong hybridization between the condensates. The critical temperatures we obtained from the solution of the anisotropic Eliashberg equations are larger than that of 1-ML MgB₂, namely 23 K and 27 K for 2-ML and

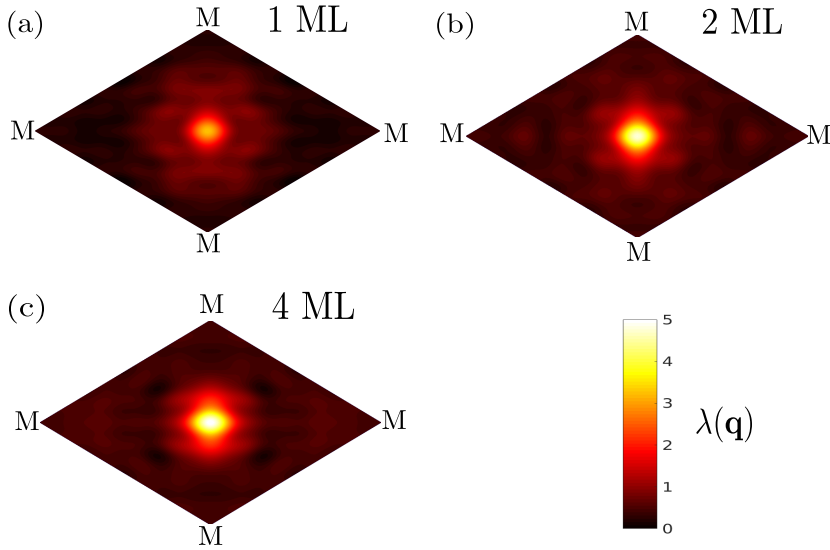


FIGURE 6.7: The overall e - ph coupling $\lambda(\mathbf{q}) = \sum_{\nu} \lambda_{\nu}(\mathbf{q})$ (i.e., summed over all phonon nodes) as a function of phonon wave vectors \mathbf{q} for (a) 1-ML, (b) 2-ML and (c) 4-ML MgB_2 .

4-ML MgB_2 respectively (still well below the bulk value of 39 K³).

The transition from three-gap superconductivity in ML MgB_2 to anisotropic two-gap superconductivity and 2-ML and 4-ML MgB_2 can be explained by means of the e - ph coupling field shown in Fig. 6.7. In all cases, the e - ph coupling peaks for phonon wave vectors $\mathbf{q} \simeq 0$ (i.e., Γ), which promotes intraband coupling, giving rise to separate condensates on different sheets. However, in Fig. 6.7 one observes also a clear evolution towards stronger coupling at non-zero wave vectors going from a ML to thicker structures. These emerging coupling channels enable scattering between different sheets, notably between the close-lying S , S' and π bands. This leads to the hybridization between the corresponding condensates shown in Fig. 6.6.

These results show thus a drastic change from the distinctly three-gap superconductivity in single ML MgB_2 to very anisotropic two-gap superconductivity by addition of even a single monolayer. Bearing in mind that the superconducting gap opening on the surface band in very thick MgB_2 films

³We note here that this result is different from that obtained in Ref. 266 for 2-ML MgB_2 , where T_c was found to exceed the bulk value. The difference can be traced back to the unreasonably low Coulomb pseudopotential used in this work, to compensate the lack of multi-band effects in their isotropic Eliashberg approach.

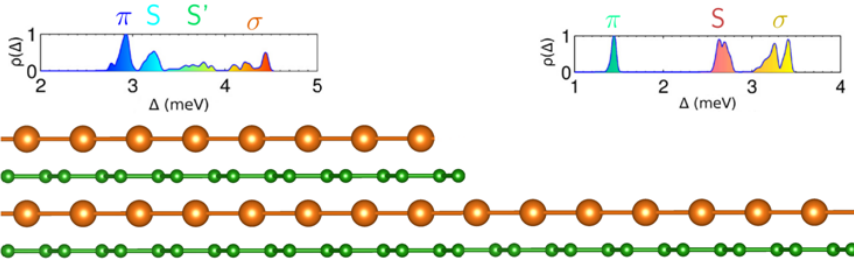


FIGURE 6.8: *Prototype nano-engineered superconducting junction of 1-ML and 2-ML MgB₂.*

was found experimentally to be nearly degenerate with the gap on the σ band [68], further rich behavior of the gap spectrum is to be expected as the MgB₂ film is made progressively thicker beyond 4 MLs. Besides accompanying fundamental physics, this strong variation of the gap structure with the number of MLs opens perspectives for nano-engineered superconducting junctions using one single material with spatially varied thickness on the atomic scale. Such local control of thickness is readily available for, e.g., Pb films [100, 101]. In Fig. 6.8 I show such prototype junction of 1-ML and 2-ML MgB₂, along with their superconducting gap spectra.

6.4.2 Evolution of the superconducting length scales

To characterize further the evolution of the condensates with the number of layers of the films, I calculated the nominal characteristic length scales of superconductivity using Ginzburg-Landau (GL) relations. The coherence length at temperature zero is given by

$$\xi_i(0) = \frac{\hbar v_{F,i}}{4\pi T_c} \sqrt{\frac{7\zeta(3)}{3}}, \quad (6.2)$$

and the London penetration depth by

$$\lambda_{L,i}(0) = \sqrt{\frac{3c^2}{16\pi e^2 v_{F,i}^2 N_i(E_F)}}, \quad (6.3)$$

where the index i runs over the different band condensates, and $v_{F,i}$ and $N_i(E_F)$ are the Fermi velocity and density of states at the Fermi level [72]. Here, $v_{F,i}$ is restricted to the in-plane values, hence we are describing only

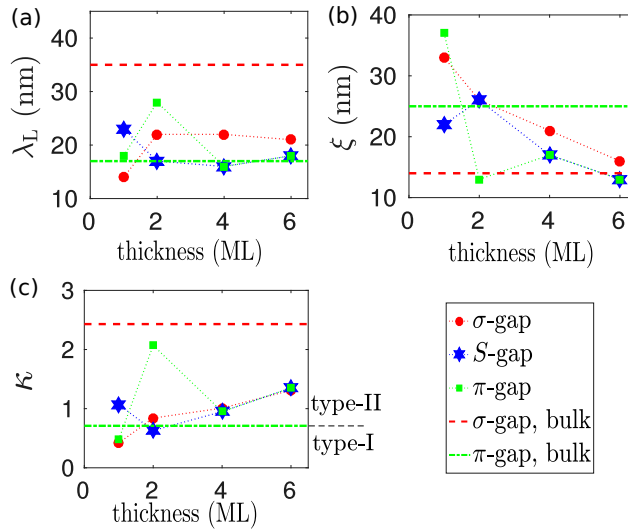


FIGURE 6.9: *The evolution of the superconducting length scales with added monolayers. (a) The London penetration depths (λ_L). (b) The coherence lengths (ξ). (c) The Ginzburg-Landau parameters (κ). The lines serve as a guide for the eye.*

the effect of in-plane supercurrents shielding out-of-plane applied magnetic fields, and the in-plane component of ξ_i only.

The GL parameter $\kappa_i = \lambda_{L,i}/\xi_i$ indicates whether the band condensate displays type-I ($\kappa_i < 1/\sqrt{2}$) or type-II ($\kappa_i > 1/\sqrt{2}$) behavior under applied magnetic field, as we saw in Chapters 1 and 4. In bulk MgB_2 , a disparity between the length scales of the σ and π condensates was found experimentally (the former having a much larger GL κ than the latter), proposed to give rise to unusual vortex matter [89].

The results for 1 – 6 MLs are displayed in Fig. 6.9. The length scales change quite strongly with each added ML. In a single ML, the coherence lengths are generally larger than their bulk counterparts. The coherence lengths decrease strongly upon addition of a second ML, because of lower Fermi velocities, especially of the π condensate⁴.

⁴The length scales in the 2D case do not exactly converge to the bulk values. The reason is that the perpendicular direction is omitted so that some features of the bulk Fermi surface are not recovered even for a quite large number of layers.

Thus, the length scales of atomically thin MgB_2 , and the associated behavior in applied magnetic field, are intrinsically different from their bulk counterparts. Moreover, by layer addition the length scales can be adapted, from large coherence lengths in the single ML limit (and associated low κ 's lying around the critical value $\kappa_c = 1/\sqrt{2}$) to smaller coherence lengths (whereby $\kappa > \kappa_c$, i.e., type-II behavior).

6.5 Influence of a magnesium substrate

6.5.1 Structural properties

It is interesting to consider what the influence would be if the atomically thin MgB_2 is deposited on a magnesium substrate, which is readily done experimentally [263], and will be the approach in the experiments described in Sec. 6.6. The substrate we will consider is specifically hexagonal $\text{Mg}(0001)$, terminated by a hcp Mg plane.

The crystal structure of one ML of MgB_2 on a Mg-substrate is depicted in Fig. 6.10(a). The calculated in-plane lattice parameter of the Mg substrate is slightly larger than that of a freestanding ML of MgB_2 (3.16 Å compared with 3.09 Å⁵), resulting in an advantageous, small lattice mismatch (below 3%) in case the ML is grown on this substrate. The calculated interlayer distance evolves from 3.34 Å for one ML to 3.49 Å for eight MLs, steadily converging towards the bulk value 3.52 Å. Few-layer MgB_2 on a substrate can adopt two different forms, namely with B or Mg termination.

To find out which termination is energetically favored, I calculated the heat of formation of both possible structures. The heat of formation per atom, $H_f(\text{Mg}_x\text{B}_y)$, of the binary structures with stoichiometry Mg_xB_y , including the Mg substrate, is calculated as

$$H_f(\text{Mg}_x\text{B}_y) = \frac{1}{x+y} \left[E_{\text{tot}}(\text{Mg}_x\text{B}_y) - x \frac{E_{\text{tot}}(\text{elem. Mg}_2)}{2} - y \frac{E_{\text{tot}}(\text{elem. B}_{12})}{12} \right]. \quad (6.4)$$

⁵These values have been obtained using VASP. As mentioned above, the value of the in-plane lattice parameter in ABINIT is 3.04 Å for freestanding ML MgB_2 .

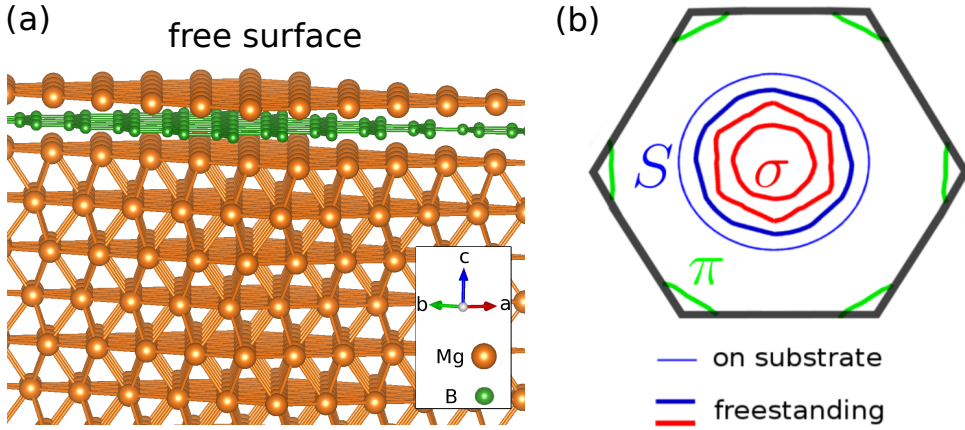


FIGURE 6.10: (a) Atomistic picture of a single Mg-terminated monolayer MgB_2 on a $\text{Mg}(0001)$ substrate. The inset shows the crystal axes and the atomic species. (b) The Fermi surface of ML MgB_2 with and without substrate, depicted in the first hexagonal Brillouin zone (solid black line).

Here, the total energies are calculated using DFT. The total energy of elemental metallic Mg_2 was calculated in its hexagonal form (identical to the substrate), while for B_{12} the trigonal α -phase was selected. The results are listed in Table 6.1. Mg terminated structures consistently have a lower heat of formation compared with B-terminated structures for more than one ML, the difference being in the order of a few tens of meV per atom. For one ML, the difference in heat of formation of both terminations is small. Therefore we find that Mg-termination is preferred in few-layer MgB_2 . Thus, the surface band, S , can be expected to play a crucial role in the electronic and superconducting properties of this structure.

Number of MLs	B-terminated	Mg-terminated	Difference
1	0.1211	0.1260	-0.0049
2	0.0761	-0.0114	0.0875
4	0.0030	-0.0542	0.0572
6	-0.0354	-0.0781	0.0427
8	-0.0593	-0.0935	0.0342

TABLE 6.1: Heat of formation H_f , in units of eV/atom, as a function of the number of MLs for B- and Mg-termination, as well as the difference in heat of formation between B- and Mg-termination.

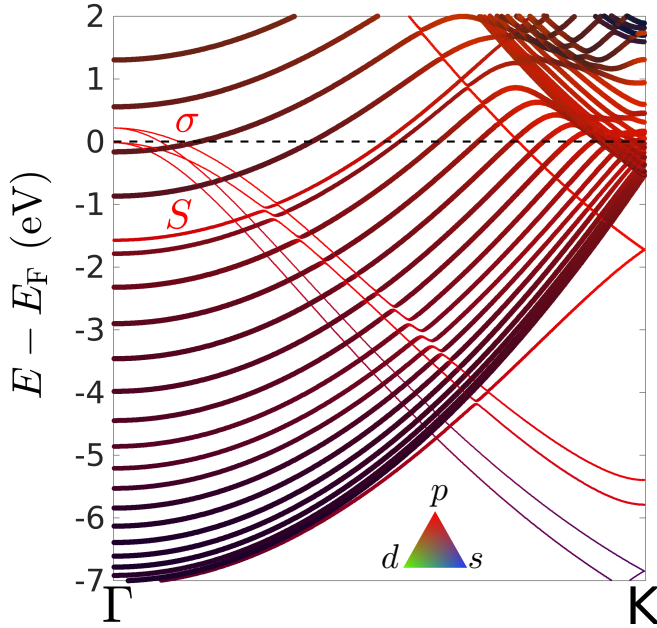


FIGURE 6.11: *Calculated band structure of two MgB_2 monolayers on the Mg substrate, where colors denote the band character (s, p, d), as shown in the inset, and line thickness denotes the atomic species it originates from (thin for B and thick for Mg).*

6.5.2 Electronic properties

In Fig. 6.10 the Fermi surface of ML MgB_2 with and without $Mg(0001)$ substrate (calculated using DFT) is displayed. The σ band is thus eliminated as part of the Fermi surface of one ML of MgB_2 on the Mg-substrate, as seen in Fig. 6.10(b). Band S , on the other hand, remains present as a very robust feature of ultrathin MgB_2 films.

In MgB_2 , the Mg atoms donate electrons to the B planes, hence, the inter-layer bond has an ionic character (this makes that MgB_2 cannot be exfoliated easily). For a better understanding of the origin of this large difference between freestanding and epitaxial films I carried out a Bader charge analysis. I found that in bulk MgB_2 Mg-atoms donate approximately 0.8 electrons per B atom. In a freestanding ML, Mg donates 0.7 electrons to each B-atom, hence the similarity of its Fermi contour to the bulk Fermi surface, less the presence of surface band S . However, in one ML on the $Mg(0001)$ substrate,

the single B layer is sandwiched between two Mg layers. As such, each atom in this B-layer receives 1.3 electrons from the two adjacent Mg-layers, in other words, it is *overdoped*. As a result, the σ band is pushed down, and thus eliminated from the Fermi surface.

For two MLs, the σ band reappears at the Fermi level, and the difference in electronic structure at E_F between freestanding and epitaxial structures vanishes. For four MLs and more, the σ band starts converging towards its bulk limit. In contrast, the Mg-based surface band S persists as a distinct and prominent feature. As in freestanding films, band S has Mg-p character, as shown in Fig. 6.11, where the DFT-calculated orbitals are projected onto atomic orbitals (for the example of 2-ML MgB_2). Owing to its p_z -character, the π band of few-monolayer MgB_2 hybridizes with Mg- p_z states of the substrate. This effect, due to Kronig-Penney-like interaction between Mg-layers in the substrate and the films, diminishes with an increasing number of layers, becoming weak in six MLs and more.

Finally, there is an interesting difference between the electronic states in freestanding MgB_2 films and those attached to the Mg(0001) substrate. The σ bands of epitaxial 2-ML-thick films (and more) deposited on the Mg(0001) substrate lie close together (cf. Fig. 6.11). As stated in Sec. 6.4.1, in freestanding form one band splits off from the σ bands. This is shown in Fig. 6.12, for 6 ML thickness (treated further in the next section regarding its superconducting properties). This split-off band, S' , has B- p_{xy} character and originates from a surface state of the free B surface, in the absence of the substrate.

6.6 ARPES experiments

I now present a series of angle-resolved photoemission spectroscopy (ARPES) experiments aimed to validate the predictions of this chapter. With room-temperature ARPES the normal-state electronic structure is probed, while with low-temperature ARPES the superconducting gap can be measured. The experiments were performed by the group of Prof. dr. Petra Rudolf at the Zernike Institute for Advanced Materials (University of Groningen, the Netherlands), the group of Dr. Cinzia Cepek at the ‘Istituto Officina dei Materiali’ (IOM) in Trieste (Italy), and the group of Dr. Andrea Goldoni at

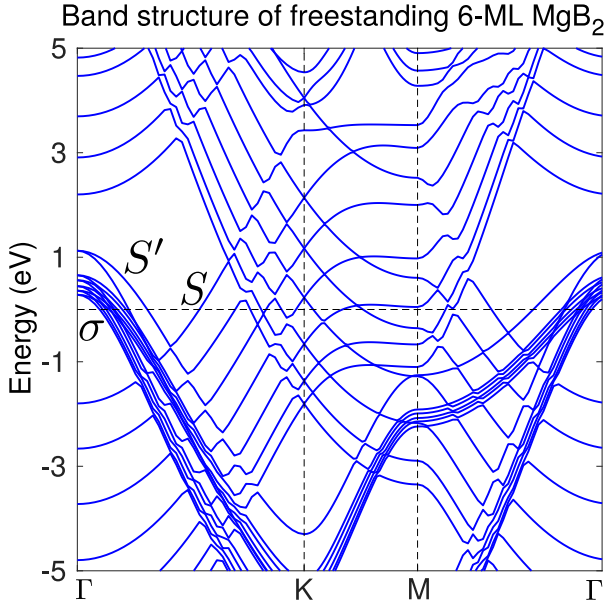


FIGURE 6.12: *The calculated band structure of freestanding 6-ML thick MgB₂. In addition to the surface band S , originating from the Mg-terminated site, the absence of the substrate opens an additional surface band, S' , as a split-off band from the σ bands. It arises from the B layer facing vacuum instead of facing the substrate, so contrary to band S , it has the same B-p character as the σ bands.*

the Elettra Sincrotrone Trieste, where the ARPES measurements have been performed. A list of all collaborators can be found in Ref. 201. I carried out the theoretical interpretation of the results.

6.6.1 Sample growth

MgB₂ films were grown on a Mg(0001) substrate using molecular beam epitaxy, using a technique developed for high-purity and high-quality films [263, 267]. The Mg(0001) substrate was selected because of the minimal lattice mismatch with few-layer MgB₂, as mentioned above. The thickness of the samples was monitored in situ by a combination of photoemission and calibrated evaporators, a technique explained in more detail in the resulting

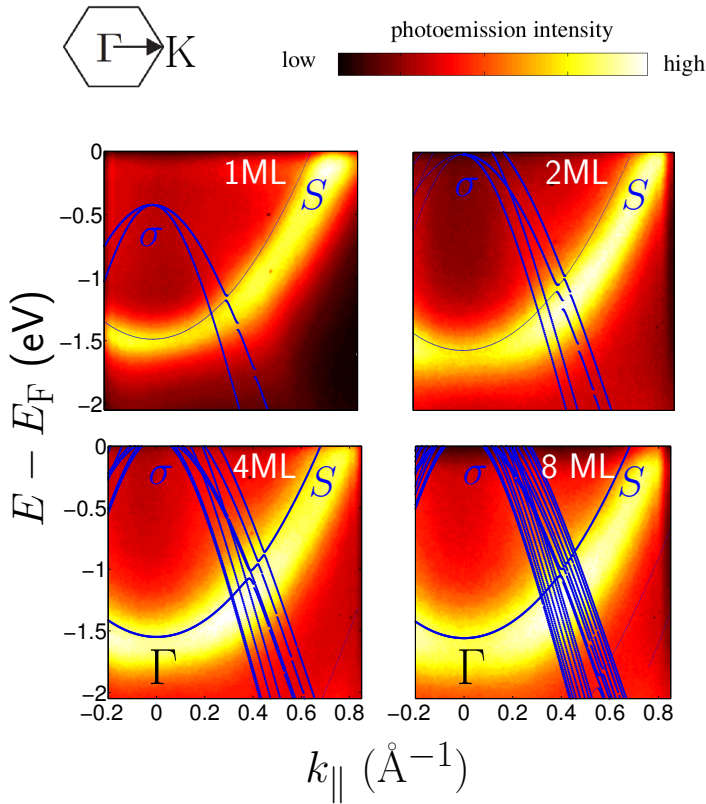


FIGURE 6.13: *Room-temperature ARPES measurements of ultrathin MgB₂. Data is shown for the valence bands of one, two, four, and eight MLs MgB₂, along Γ -K, with band structure calculations plotted on top. In the latter, thin lines indicate states originating for 75 to 90% from the layers adjacent to the Mg-vacuum interface, namely those states spatially localized within at most 2 nm from the top of the film – corresponding to the depth down to which ARPES can probe – while thick lines indicate states where this contribution exceeds 90%.*

publication (Ref. 201) and in Refs. 263, 267. All measurements were performed in situ, under ultra-high vacuum conditions, to avoid contamination of the samples.

6.6.2 Normal-state electronic properties

To verify the appearance of the surface band near E_F in few-monolayer MgB₂, room-temperature ARPES measurements were performed, shown in Fig. 6.13

together with the σ and S bands obtained from DFT. The latter becomes increasingly localized near the surface for thicker films, explaining the increase in intensity of the ARPES signal. The ARPES signal from the σ bands is significantly weaker than that of the S band, especially in the one-ML case. The lack of intensity at Γ for MgB_2 layers thicker than 1 ML indicates that the σ band is shifted towards lower binding energies in the 1-ML case, as predicted by the calculations in Sec. 6.5.2.

6.6.3 Superconducting properties

To study superconductivity stemming from the surface band in few-layer MgB_2 , low-temperature ARPES measurements were performed, down to 20 K. Given the very strong ARPES signal on band S (cf. Fig. 6.13), the superconducting gap opening on this band can be determined very accurately. Therefore, the experiment focusses on superconductivity in band S , unique to ultrathin MgB_2 . The spectral edge of 6-ML and 8-ML samples was observed shift towards lower energies, indicating a vanishing density of states at the Fermi level and therefore the opening of a superconducting gap [268]. For samples thinner than six MLs no superconducting gap is observed in the temperature range attainable with our experimental set-up.

For six MLs, measurements were performed at several temperatures in the range 20 – 30 K, shown in Fig. 6.14(a). The gap width, Δ , was obtained by fitting the valence band spectra with a BCS spectral function multiplied by a Fermi-Dirac distribution and convoluted with the experimental Gaussian broadening. The measurement enables us to fit the superconducting gap as a function of temperature according to $\Delta(T) = \Delta(0) (1 - (T/T_c)^p)^{1/2}$, from which $p = 2.4$, $\Delta(0) = 3.6$ meV, and a critical temperature of this gap, $T_{c,S} = 31$ K were obtained.

6.6.4 Theoretical interpretation

To unravel the origin of the measured superconductivity in the surface band of 6-ML MgB_2 , and its relation to the other gaps, anisotropic Eliashberg calculations were carried out on a freestanding 6-ML film, using the electron-phonon coupling coefficients obtained from first-principles as input. The

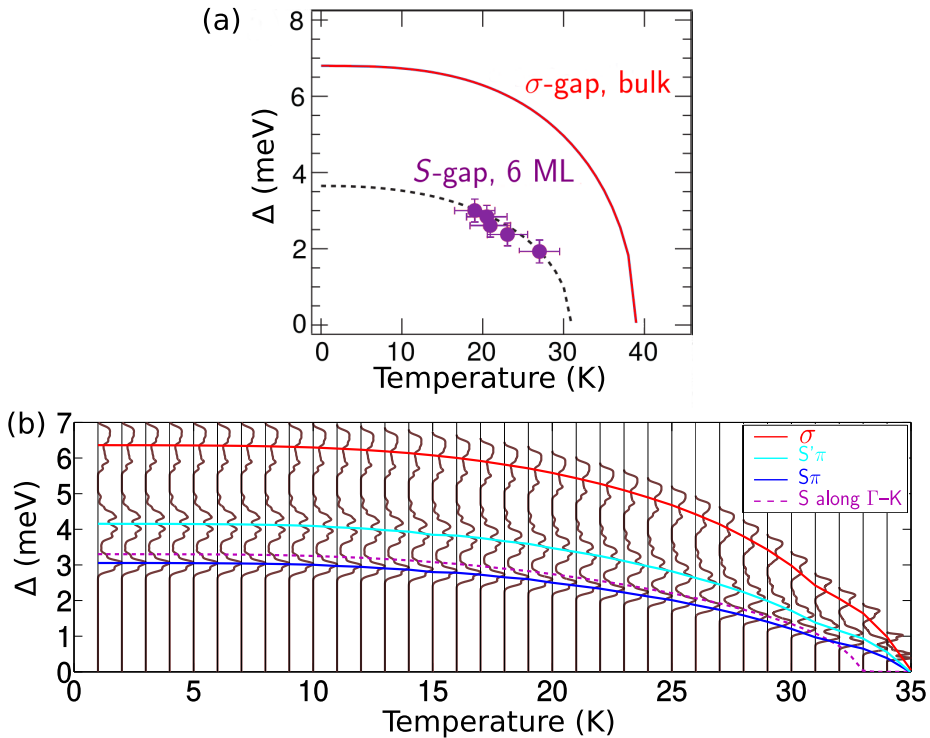


FIGURE 6.14: (a) The evolution of the gap on the surface band with temperature, as measured using low-temperature ARPES. A fit of the profile yields $\Delta_S(0) = 3.6$ meV and $T_{c,S} \sim 31$ K, the critical temperature of superconductivity stemming from the surface band. The σ gap profile of bulk MgB₂ is added for comparison. (b) The temperature dependence of the superconducting gap spectrum, Δ , of six MLs of MgB₂ calculated using Eliashberg theory. The spectrum consists of three distinct contributions (domes), $S\pi$, $S'\pi$ and σ . The dome averages are also indicated, as well as the gap specifically opening on the S band along $\Gamma - K$, for direct comparison to the experimental result. The theoretical critical temperature $T_{c,S} = 33$ K of this band and the strength of the gap are in excellent agreement with the experiment.

calculated distribution of the gap opening specifically on band S as a function of temperature is shown in Fig. 6.14(b) (dashed line). It is observed that this S gap closes at $T_{c,S} = 33$ K – in excellent agreement with the experimental value ($T_{c,S} = 31$ K). The overall T_c of 6-ML MgB₂ is found to be 35 K, thus it has almost reached the bulk value of 39 K. There is also a very good agreement for the characteristic exponent p of the temperature dependence of the gap opening on S , obtained as $p = 2.2$ in the theory (vs. $p = 2.4$ in

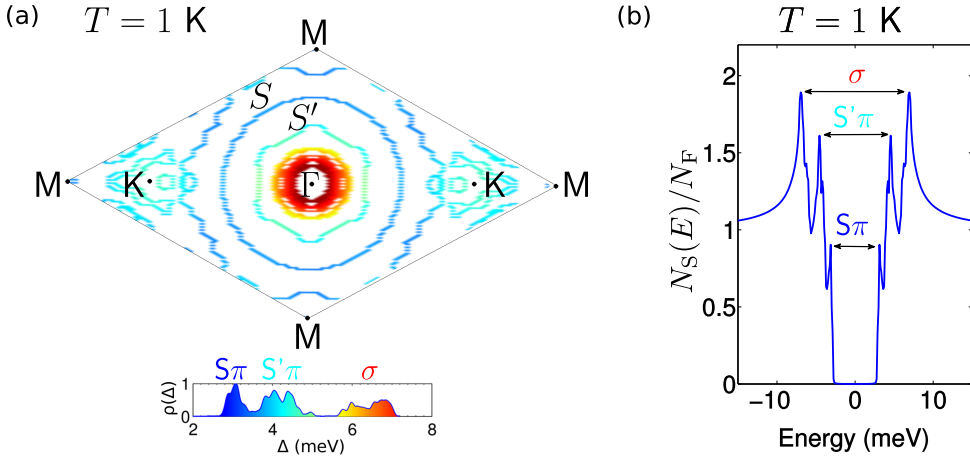


FIGURE 6.15: (a) The calculated superconducting gap spectrum of six-ML MgB_2 at temperature $T = 1$ K, obtained using Eliashberg theory, plotted on the Fermi surface. The inset shows the distribution of the gap, $\rho(\Delta)$, whereby the three distinct domes are indicated, showing their origin from the bands of the Fermi surface. (b) The density of states in the superconducting state at 1 K, with three distinct peaks related to the three domes in the superconducting gap spectrum.

the experiment). The calculated gap on S , $\Delta_S(0) = 3.3$ meV is also in very good accordance with ARPES result ($\Delta_S(0) = 3.6$ meV). In the anisotropic Eliashberg calculation we employed the standard value $\mu^* = 0.13$. From the close agreement between our theoretical predictions and experimental data it can be concluded that the screening modeled by μ^* does not change in the ultrathin limit in the case of MgB_2 , as opposed to, e.g., ultrathin TaS_2 where it was proposed that a renormalization of this repulsion lies at the base of the increase in critical temperature in thinner samples [269].

The gap spectrum displayed in Fig. 6.14(b) consists of three domes. The corresponding distribution of the gap on the Fermi surface, $\rho(\Delta)$ at 1 K, is shown in Fig. 6.15(a). The Mg-based band S contributes to the first dome by hybridizing with the π gap (denoted $S\pi$ dome), similar to the case of 2-ML and 4-ML MgB_2 . The gap on band S' is in the range 4–5 meV and is also mixed with the π -gap, forming the central dome of $\rho(\Delta)$ denoted $S'\pi$. Compared with 2-ML and 4-ML we see that the gaps are steadily increasing towards the bulk values. The gap opening on S evolves more slowly than those of σ and π (that have already reached their bulk values in the 6-ML case). This difference in evolution between surface and π states is closely linked to the

hybridization between both. The effect of the surface contributions on the DOS in the superconducting state N_S , displayed in Fig. 6.15(b), is also very pronounced. N_S exhibits three sharply resolved peaks, corresponding to the three domes in $\rho(\Delta)$.

As bands S and S' stem from the free surfaces of opposite sides of the film, they are to a large extent mutually independent. Therefore, separate control of the contributions of these two surface states to the gap spectrum can be achieved by means of chemical functionalization of one or either of these free surfaces. In Chapter 7 it will be demonstrated that the surface bands can be eliminated from the Fermi surface by means of adatoms on either side.

6.6.5 Path to experimental realization of superconductivity in the thinnest limit

Further measurements below 20 K are needed to explore possible superconductivity in the thinnest structures of MgB_2 – in line with theoretical predictions presented in this chapter. In that limit, our results indicate a considerable role of the substrate owing to several *proximity effects*. Firstly, there is the purely *electronic proximity effect* for one ML MgB_2 (cf. Figs. 6.10(b) and 6.13), where charge transfer from the substrate to the film eliminates the σ bands from the Fermi surface. The second kind of proximity effect stems from a *transfer of Cooper pairs* from the superconducting film to the metallic substrate, which also depletes superconductivity.

Since purely from theory there is no reason why there would be no superconductivity in the thinner films, it is very likely that the second kind of proximity effect inhibits superconductivity in films thinner than six MLs. Using non-metallic substrates would exclude the possibility of Cooper-pairs escaping and would thus make the superconducting state more robust. On a related note, recent experimental advances enable non-epitaxial fabrication of not only weakly bound layered materials, e.g., NbSe_2 [270], but also of ultrathin compounds with ionic interlayer bonds, like MgB_2 [271]. It is thus envisioned that the full potential of superconductivity from free surfaces can be explored using the already available technology.

6.7 Conclusions

In summary, I presented the formation and evolution of three-gap superconductivity in few-monolayer MgB_2 , by solving the anisotropic Eliashberg equations with full *ab initio* input. I showed that the electronic surface band, originating from the free Mg-surface, plays a major role in ultrathin MgB_2 , and hosts a third superconducting gap that coexists with the bulk-like π and σ gaps. The impact of free surfaces on superconductivity is inherent to atomically thin materials, but also susceptible to further chemical functionalization and nanoscale engineering. The gaps in one-monolayer MgB_2 are distinctly separate, so the resulting three pronounced peaks in the superconducting tunneling spectrum provide a clear signature for further experimental validation of our prediction. The shown three-gap superconductivity is moreover very robust with temperature, persisting even close to the critical temperature of 20 K. As more monolayers are added to the film, different condensates hybridize, changing the multi-gap spectrum drastically with every added monolayer. Our investigation therefore establishes atomically thin MgB_2 as a unique system to explore tunability of high- T_c , multi-gap superconductivity, and its possible applications in ultrathin cryogenic electronics engineered by atomically controlled thickness.

In the second half of this chapter, I presented a combined theoretical and experimental study of few-monolayer MgB_2 , grown on a hexagonal Mg(0001) substrate. The predicted surface band originating from the free Mg surface was indeed observed very clearly in ARPES measurements. Superconductivity was observed by means of a vanishing density of states in low-temperature ARPES measurements. A comparison of the measured and calculated gap spectra of six-ML MgB_2 shows a very good agreement between both regarding the evolution of the amplitude of the gap opening on the surface band with temperature and the T_c . I showed furthermore that also for 6 MLs the condensate originating from the surface state hybridizes with the π condensate. This is entirely different from bulk-sized MgB_2 where ARPES experiments indicate near-degeneracy of a surface state gap with the σ gap, without any clear influence on the measured two-gap superconductivity [68]. Superconductivity in samples thinner than 6 MLs was not observed, which can be traced back to proximity effects due to the metallic Mg substrate. Therefore, I finished with prospective ideas on how to realize superconductivity

in the thinnest limit, by using insulating substrates and by exploiting recent advances in non-epitaxial growth.

Publications

(1) **J. Bekaert**, A. Aperis, B. Partoens, P. M. Oppeneer, and M. V. Milošević, *Evolution of multigap superconductivity in the atomically thin limit: Strain-enhanced three-gap superconductivity in monolayer MgB_2* , Phys. Rev. B **96**, 094510 (2017).

(2) **J. Bekaert**, L. Bignardi, A. Aperis, P. van Abswoude, C. Mattevi, S. Gorovikov, L. Petaccia, A. Goldoni, B. Partoens, P. M. Oppeneer, F. M. Peeters, M. V. Milošević, P. Rudolf, and C. Cepek, *Free surfaces recast superconductivity in few-monolayer MgB_2 : Combined first-principles and ARPES demonstration*, Sci. Rep. **7**, 14458 (2017).

Chapter 7

Strain- and adatom-enhanced superconductivity in monolayer magnesium diboride

Here, we investigate how superconductivity in the atomically thin limit can be enhanced. There are several pathways to achieve this, all based on nano-engineering of the structural and electronic properties of the 2D materials. We will explore these specifically for monolayer magnesium diboride, in view of its interesting multigap characteristics. First, we explore biaxial strain, which is shown to boost the critical temperature above 50 K under the influence of limited biaxial tensile strain of $\sim 4\%$. This enhancement is stronger than in any other 2D superconductor known to date. We demonstrate that the principle behind this enhancement, namely phonon softening, is intrinsic to many 2D materials, thus opening a very general road for stronger superconductivity in the atomically thin limit. As a second option, we investigate the influence of adatoms, specifically hydrogen, which is abundantly present during and after synthesis of 2D materials. It is shown that hydrogen adatoms at the magnesium plane eliminate the characteristic surface band of monolayer magnesium diboride. Nevertheless, the electron-phonon coupling strongly increases due to hydrogenation, under the influence of an increased electronic density of states, and of adatom-host

hybridized states with strong coupling to phonons. Thus, the critical temperature is strongly enhanced above that of the pure monolayer. This can be enhanced even further by applying biaxial strain, reaching unexpectedly strong electron-phonon-based superconductivity.

7.1 Introduction

There is a long-standing tradition of investigating the influence of pressure and strain on superconductivity. They have been found to exert very diverse effects on the superconducting properties of both bulk and 2D materials. Historically, it was first discovered that the critical temperature (T_c) of elemental metallic superconductors (Al, Bi, Pb, Sn, etc.) decreases with compression [272, 273]. The main mechanism behind this decrease is a shift of the Eliashberg function to higher energies, leading to a decrease in the electron-phonon ($e-ph$) coupling λ , and thus in T_c according to the BCS relation $T_c \propto \omega_D \exp(-1/\lambda)$. This exponential effect dominates over the accompanying decrease of the Debye frequency ω_D , with a linear relation to T_c . To give an example, for Al, λ decreases from 0.45 to 0.42 under a pressure of 2 GPa [273].

However, many other conventional $e-ph$ -based superconductors exhibit a different behavior. Alkaline metals (Ba, Ca, Li, Sr, etc.) have increasing T_c with pressure (up to a certain point where the trend is reversed) [273]. What is more, they are even non-superconducting at ambient pressure. Transition metals display even more complicated trends. Some have increasing T_c with pressure (e.g., V and Zr), while others display the opposite trend (e.g., Nb) [273]. This indicates that in such metals changes in the electronic structure outweigh monotonous changes in the Eliashberg function. The most extreme example of such a system are the sulfur hydrides. Very high pressures (induced with a diamond anvil cell) are needed to create sufficient orbital overlap for superconductivity. T_c keeps on increasing with pressure, ultimately reaching values above 200 K [41]. A similar behavior has been predicted for metallic hydrogen under high pressure [42].

For MgB_2 some experiments on the effect of lattice deformation have been carried out. In bulk MgB_2 , T_c decreases under the influence of hydrostatic

pressure, following the trend in many elemental metallic superconductors [274]. An expansion of the MgB_2 lattice was equally realized, via strain induced in few-100 nm thick MgB_2 islands [275]. However, the largest increase in T_c that could be realized in this way was 5% [275], and the theoretical limit for bulk-sized MgB_2 was found to be 10% [276]. However, in the atomically thin limit, nothing was known yet on the response of MgB_2 to lattice deformations until the investigations presented in this chapter were carried out.

Generally, in 2D and atomically thin materials more options are available to adapt the structural properties externally. Not only compression but also stretching of the lattice can be applied. Both in electron- [277] and hole-doped [278, 279] graphene significant enhancements of the e - ph coupling and of T_c were found, albeit only at larger strain levels beyond 5%. Since T_c of unstrained monolayer Li-doped graphene is only about ~ 8 K, T_c does not exceed 30 K, even at 10% tensile strain [277]. Moreover, Li-doped graphene has been found to be an isotropic single-gap superconductor [82], as opposed to the distinct three-gap superconductivity in monolayer MgB_2 , revealed in Chapter 7. This opens possibilities in the latter to obtain stronger superconductivity, due to intrinsic enhancement in the multigap case (as explained in Sec. 1.2.1). Moreover, the preferred experimental growth method of atomically thin MgB_2 is epitaxial growth on a substrate, with ever-present lattice mismatch [263]. Therefore, it is very interesting to consider the effect of strain on atomically thin MgB_2 .

Here, I demonstrate that three-gap superconductivity in monolayer MgB_2 remains robust under strain, and that tensile strain of just $\sim 4\%$ boosts T_c to above 50 K. The general principle behind this enhancement will be unraveled in this chapter, based on Eliashberg theory. Considering that such amount of straining can be conveniently realized by growing the monolayer MgB_2 on substrates with a somewhat larger lattice constant (e.g., $\text{Si}_{1+x}\text{C}_{1-x}$ or $\text{Al}_x\text{Ga}_{1-x}\text{N}$ alloys, with a lattice constant tunable by x) [276], these results are expected to be of immediate experimental relevance.

The second option we will explore to modify and to enhance superconductivity in the atomically thin limit is motivated by a plethora of recent advances on functionalization of 2D materials. A particularly promising route is that of *adatoms* on their surface, i.e., dopants of a different atomic species from

those contained in the host material, arranged in a regular pattern. The motivation for this route is fairly straightforward. The surface band in monolayer MgB_2 originates from the interaction between the Mg layer and the vacuum. Therefore, it is easily accessible, and can be suppressed by the adatom layer. Specifically, I considered hydrogen as the adatom species. The reason is that with this element with the lowest atomic number charge transfer between the adatoms and the film can be limited. In this way, the σ and π states can remain largely unaltered. This provides for a unique (possibly local) control of the superconducting gap spectrum through easily accessible surfaces.

Very surprisingly, the calculations presented in this chapter have revealed that the hydrogenation not only suppressed the surface band, but that it also boosts the e - ph coupling and thus the T_c . At the origin of this enhancement are profound changes in the electronic and vibrational properties, characterized by hybridized states that form between hydrogen and boron. This finding demonstrates in general the potential of enhancing and tailoring 2D superconductivity.

7.2 Strain-enhanced superconductivity

7.2.1 The effect of strain on the electron-phonon interaction

In a strained material the lattice parameters are fixed to non-equilibrium values (by means of epitaxial growth on a substrate, by forces exerted on a suspended monolayer, etc.). Here, I concentrate on *biaxial strain* applied with respect to the in-plane cell parameter. Such biaxial straining of a 2D hexagonal material preserves the hexagonal symmetry, since biaxial refers to treating both lattice directions (viz., \mathbf{a} and \mathbf{b} in Fig. 7.1) on the same footing. Another type of strain where only one of the two directions is deformed, is called uniaxial strain. Here, symmetry breaking can lead to very drastic changes. However, I will show that biaxial strain also hosts surprises with regard to the superconducting properties. The experimental realization of biaxial strain is furthermore very convenient, when a hexagonal substrate with a lattice parameter different from that of MgB_2 is used, as mentioned in the introduction.

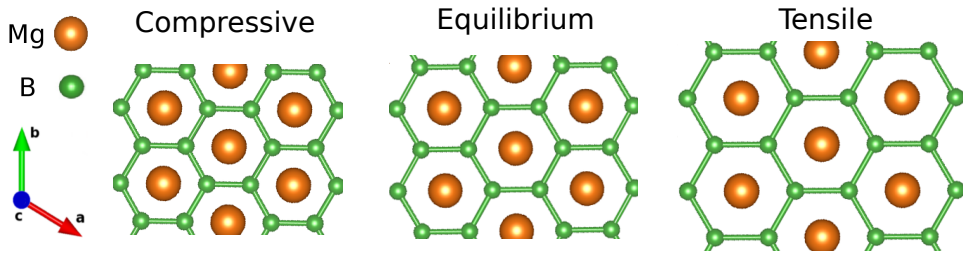


FIGURE 7.1: *Different monolayer MgB_2 lattices under the influence of biaxial strain. From left to right compressive strain, the equilibrium case, and tensile strain are depicted. The strain level used in this visualization is 10%, which is exaggerated for the sake of clarity with respect to what can realistically be realized in monolayer MgB_2 (up to $\sim 5\%$).*

In Fig. 7.1 I show the different types of lattice deformations in the biaxial case. When the lattice parameter is decreased with respect to the equilibrium value, this is called *compressive strain*. When on the other hand the lattice parameter is increased, this is called *tensile strain*. I will refer to strain levels relative to the equilibrium values. Supposing that a_0 is the equilibrium lattice parameter, strain is thus denoted as $(a - a_0)/a_0$. Therefore, compressive strain yields negative fractions and tensile strain positive ones.

In MgB_2 , the lattice parameter equals the Mg-Mg distance, with equilibrium value $a_0 = 3.04 \text{ \AA}$. The structural changes induced by strain have a profound effect on the lattice vibrations. In Fig. 7.2(a), the equilibrium phonon band structure of 1-ML MgB_2 (already presented in Chapter 6) is compared with the cases of -4.5% compressive strain and $+4.5\%$ tensile strain. One observes that the phonon frequencies increase with compressive strain and decrease with tensile strain. As such, the maximum phonon frequency – around 100 meV in the equilibrium case – increases to ~ 120 meV in the compressive case and decreases to ~ 80 meV in the tensile case.

The explanation for this trend starts from the interatomic charge densities. In the compressive case, they are enlarged as the distances between atoms decrease, while the total amount of charge is, of course, unaltered. In the tensile case, exactly the opposite occurs. The charge densities act as spring constants in the (simplified) description of lattice vibrations. Denser charge clouds act as stronger springs (in the compressive case), and less dense clouds

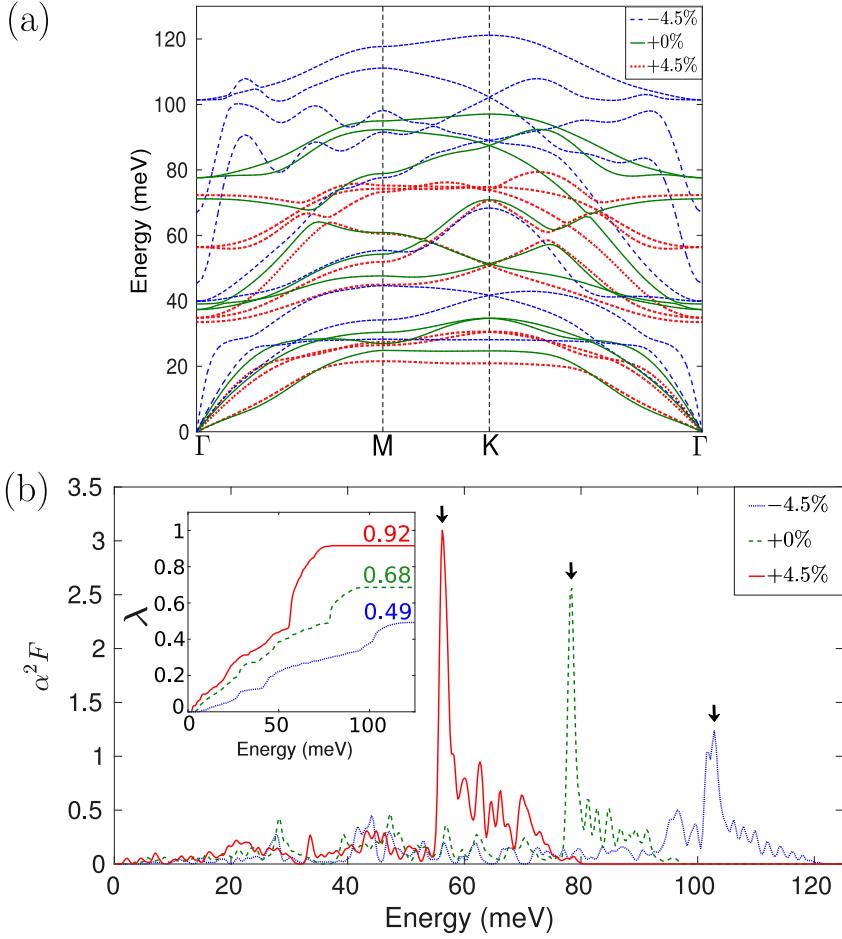


FIGURE 7.2: *Phonons and electron-phonon coupling of biaxially strained 1-ML MgB₂ calculated using DFPT. (a) The phonon dispersion for strains of -4.5% , $+0\%$ and $+4.5\%$. Increasing strain leads to lower phonon frequencies. (b) The isotropic Eliashberg function under different strains, $\alpha^2 F(\omega) = \langle \langle \alpha^2 F(\mathbf{k} \mathbf{k}', \omega) \rangle_{\mathbf{k}'_{\text{F}}} \rangle_{\mathbf{k}_{\text{F}}}$ (i.e., the double Fermi surface average). The peaks originating from the E_{2g} mode are indicated by arrows. The resulting electron-phonon coupling λ is shown as inset.*

as weaker ones (in the tensile case). Spring constants are related to frequencies as $\omega = \sqrt{k/m}$, so phonon frequencies indeed go up (down) in the compressive (tensile) case. A schematic description of this argument is provided in Fig. 7.3. Similarly, due to enlarged (depleted) charge densities in the inter-layer space, the Mg and B planes move further apart (come closer together) under the influence of compressive (tensile) strain, to partially compensate

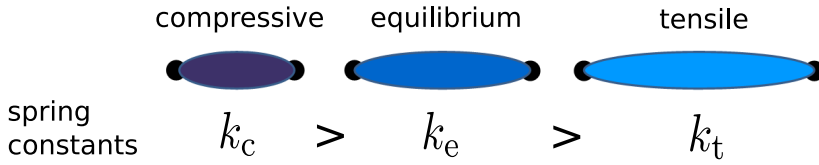


FIGURE 7.3: *Schematic description of how different types of strain influence the atomic bond between two atoms (black dots), and how this influences the spring constants resulting from the atomic bonds in each case. Darker colors represent higher electron densities. The general finding is that the compressive, equilibrium and tensile spring constant are related as $k_c > k_e > k_t$.*

the change in the bonding. In spite of this, the electron clouds effectively become less dense in the tensile case, leading to the phonon softening described above.

In Fig. 7.2(b) the corresponding Eliashberg functions, α^2F , are shown in isotropic form for $\pm 4.5\%$ strain and in the equilibrium case. The peaks in α^2F due to the E_{2g} mode (indicated by arrows), introduced in Chapter 6, remain prominent in case of applied strain. The peak even becomes stronger in the case of tensile strain. Its shift to lower energy (following the general trend for the phonons) and amplification due to tensile strain lead to a significant enhancement of the e - ph coupling, as shown in the inset of Fig. 7.2(b). This results in enhanced e - ph coupling, since the integrand of

$$\lambda = 2 \int_0^\infty d\omega \omega^{-1} \alpha^2 F(\omega) \quad (7.1)$$

is weighted by ω^{-1} within Eliashberg theory, as explained in Chapter 3 (where a more general expression is given in the anisotropic case, cf. Eq. 3.38). I must stress that this effect is particularly strong in 1-ML MgB_2 due to the occurrence of the E_{2g} phonon mode, which not only goes down in energy but also develops stronger intrinsic coupling to electrons, as follows from the evolution of the Eliashberg function shown in Fig. 7.2(b). A similar trend in the e - ph coupling under the influence of strain in both electron- and hole-doped graphene [277–279] was found to be much less pronounced at such limited straining levels, as explained in the introduction to this chapter.

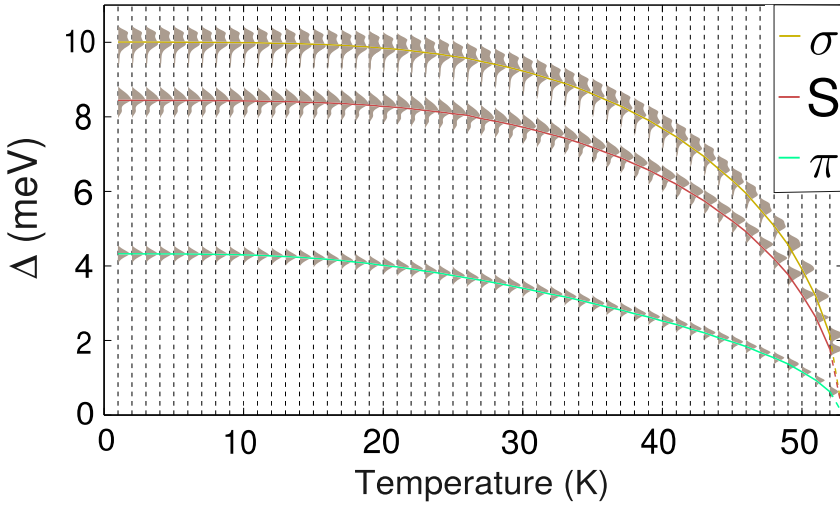


FIGURE 7.4: *The distribution of the superconducting gap for +4.5% tensile strain as a function of temperature, displaying the same three gaps (π , S and σ) as in the unstrained case (cf. Fig. 6.5). The calculation shows an enhancement of the critical temperature to $T_c = 53$ K.*

7.2.2 The effect of strain on the superconducting properties

With the first-principles results for strained 1-ML MgB₂ as input, the anisotropic Eliashberg equations were again solved. In the studied range of straining of -4.5% to $+4.5\%$, the Fermi surface of the strained structures is almost unaltered with respect to that of unstrained 1-ML MgB₂, shown in Fig. 6.5(a) of Chapter 6. This, in combination with the robust coupling to the E_{2g} mode, leads to a conservation of three-gap superconductivity in ML MgB₂ under all strains considered here¹.

In Fig. 7.4(a) the temperature evolution of the gap spectrum of 1-ML MgB₂ subject to tensile strain of $+4.5\%$ is shown, proving the robustness of its three-gap superconductivity even under a considerable amount of strain. Owing to the enhanced e - ph coupling [cf. Fig. 7.2(b)] the superconducting gaps are much larger than in the equilibrium case. For $+4.5\%$ strain, the average gaps amount to $\langle \Delta_\sigma(0) \rangle = 10.0$ meV, $\langle \Delta_S(0) \rangle = 8.4$ meV and $\langle \Delta_\pi(0) \rangle = 4.3$ meV,

¹Note that for compressive strains exceeding -1.5% σ and S gaps become hybridized, albeit that their contributions can still be distinguished. Their partial overlap is not due to new physics – it is provoked by a general depletion of the superconducting gap values, forcing the gaps closer together.

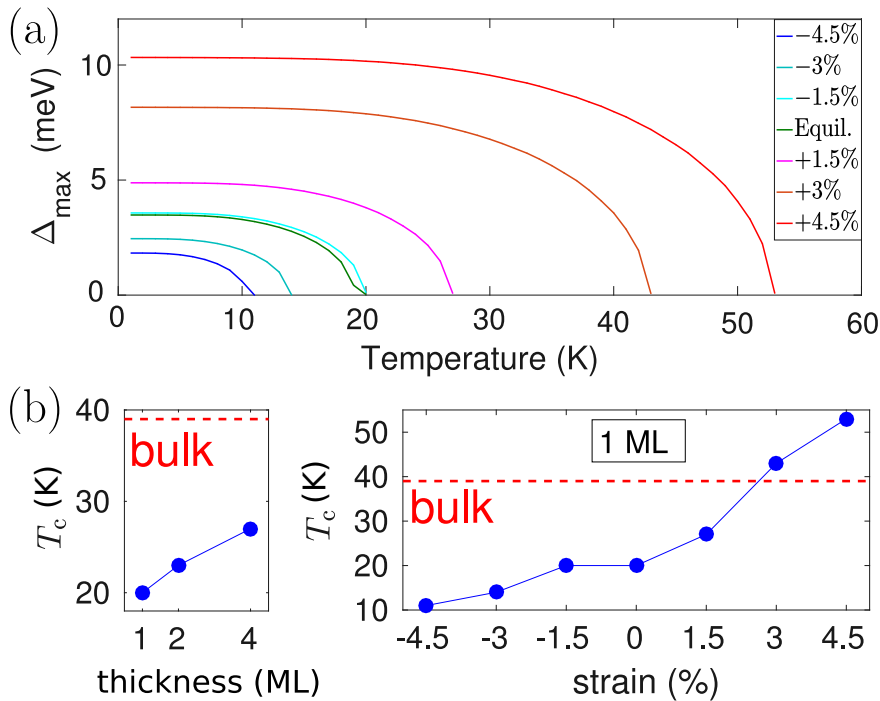


FIGURE 7.5: (a) The maximum value of the superconducting gap, Δ_{\max} , as a function of temperature and strain. Superconductivity is depleted upon compression and is strongly boosted with tensile strain. (b) T_c as a function of the film thickness (units of ML), and as a function of strain for 1-ML MgB_2 . The bulk value, $T_c = 39$ K, is shown for comparison.

with a corresponding critical temperature as high as $T_c = 53$ K, compared with 20 K for the equilibrium case. I must again stress the importance of anisotropy and multigap effects, since an isotropic approximation (using the McMillan-Allen-Dynes expression) severely underestimates T_c (yielding just 20 K).

In Fig. 7.5(a) the temperature evolution of the maximum (σ) gap value is displayed – effectively the edge of the σ gap – comparatively for different strains. This reveals that upon compression, superconductivity is greatly suppressed (T_c drops to 11 K for -4.5% strain), while it is strongly boosted when the ML is subject to tensile strain. The changes are particularly drastic for such limited amounts of strain, in comparison to, e.g., superconducting doped graphene [277–279]. In Fig. 7.5(b) the evolution of T_c with strain is shown, as well as the evolution with the number of monolayers (discussed

already in Chapter 6), for comparison. It is apparent that the effect of strain on superconductivity is stronger, with a ML strained at +3% already surpassing bulk MgB_2 as to its T_c . A major difference between layer addition and strain is that the latter preserves the three-gap superconductivity of monolayer MgB_2 , while increasing thickness strongly changes the gap spectrum with every added monolayer, as shown in Sec. 6.4.1.

7.3 Superconductivity enhanced by hydrogen adatoms

Here, we consider how the superconducting properties of monolayer MgB_2 change under the influence of adatoms, specifically focussing on hydrogen².

7.3.1 Structural properties

The main motivation for adding hydrogen adatoms was already provided in the introduction to this chapter, namely, to tweak the electronic properties of the surface state. We found that the result depends critically on the concentration of the hydrogen adatoms. Hydrogen donates electronic density to the MgB_2 layer. Therefore, if two hydrogen atoms per unit of MgB_2 are added, the DFT calculation shows that the Fermi level shifts up by so much that the π bands are eliminated from the Fermi surface, and the Fermi contours due to the σ bands become very small. Because a sufficient density of states at the Fermi level is required to achieve superconductivity, this is certainly no benign scenario.

Therefore, we restrict the adatoms to only one hydrogen atom per unit cell – on the Mg side – which we will refer to as H- MgB_2 in brief. For the preferred crystal structure two different options were explored. First, the structure where the H atom is positioned directly above the Mg atom was considered. A calculation of the phonons proved, however, that this structure is not dynamically stable. The second highly symmetric option is to place hydrogen

²This work was carried out together with Mikhail Petrov, who performed the calculations in the context of his Master thesis in the period 2017-2018. I acted as co-supervisor of his thesis, helped with the calculations and with the interpretation of the results, which I describe in my own words here.

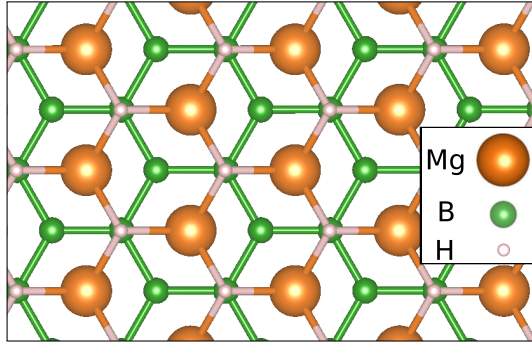


FIGURE 7.6: *Equilibrium structure of hydrogen adatoms on monolayer MgB_2 . The hydrogen atoms, one per unit cell, are positioned above one of the boron sublattices, on the side of the magnesium plane.*

above one of the two B sublattices, with a resulting trivalent coordination of the Mg atoms, as shown in Fig. 7.6. This structure was found to be dynamically stable (cf. the phonon dispersion in Fig. 7.8).

There are some remarkable changes in the lattice parameters of ML MgB_2 upon hydrogen addition. First of all the in-plane lattice parameter slightly shrinks to $a = 3.00 \text{ \AA}$, compared with $a = 3.04 \text{ \AA}$ for pure ML MgB_2 . So, there is an intrinsic compression of the lattice by $\sim 1\%$. In addition, the B layer becomes slightly *buckled*, with a distance of 0.04 \AA between the two sublattice planes. The reason for this emerging buckling is the position of H on one of the two sublattice sites, which breaks the sublattice symmetry. On the other hand, the distance between the Mg and the B layer increases, to $z = 1.80 \text{ \AA}$ (distance to the closest B plane), compared with $z = 1.65 \text{ \AA}$ for the pure ML. The distance between the Mg and the H layer is found to be 1.01 \AA .

7.3.2 Electronic properties

The resulting electronic band structure of H- MgB_2 is displayed in Fig. 7.7(a). The two σ bands around Γ are there, like they are for ML MgB_2 – cf. Fig. 6.2(a). However, the surface band of ML MgB_2 (band S) is eliminated. We observe in Fig. 7.7(a) that this is not just due to a rigid shift of E_F . On the contrary, there is no trace of band S even away from E_F . The main effect

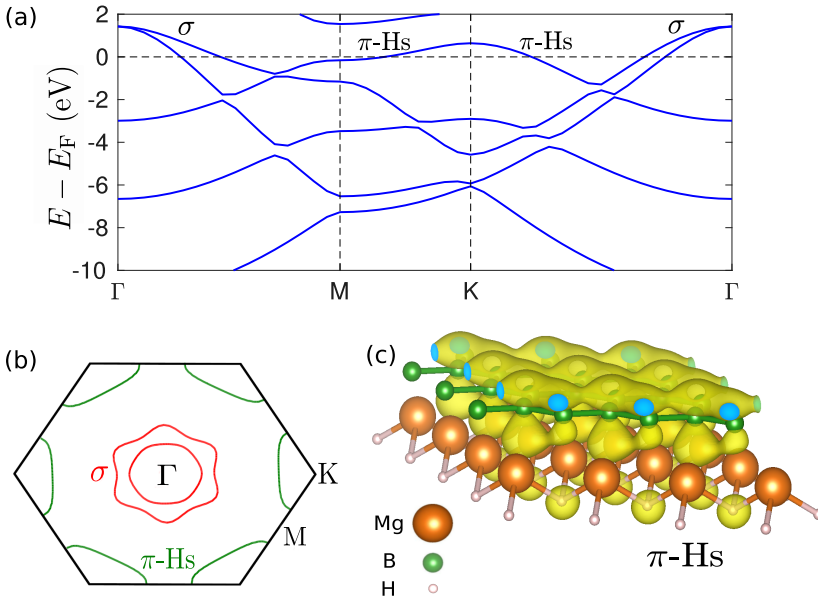


FIGURE 7.7: *The electronic structure of monolayer H-MgB₂. (a) The band structure obtained with DFT. Two bands cross E_F , the σ band and the hybrid band π -Hs. (b) The corresponding Fermi surface in the first Brillouin zone. (c) The norm of the wave function of the π -Hs state at E_F , obtained along the direction Γ -K.*

of the H adatoms is thus that they spatially isolate the Mg plane from the vacuum. Quite counterintuitively the H-s state forms a distant bond with the B- p_z states instead of with Mg states. This explains why the hydrogen atoms prefer to occupy a position with the same in-plane coordinate as one of the B sublattices. In Fig. 7.7(a) I have denoted this hybrid state of the boron- π bond and the hydrogen-s state as band π -Hs. The corresponding Fermi surface is shown in Fig. 7.7(b). It consists of the σ sheets around Γ and the π -Hs state centered at K. In Fig. 7.7(c) the wave function of the π -Hs state is depicted. There, it is clearly visible that this state is indeed comprised of a spherical s state, centered around the hydrogen atoms and of the boron- π bonds.

In spite of the elimination of band S from the Fermi surface the DOS at E_F is higher for ML H-MgB₂ compared with ML MgB₂. The ratio of the two DOS values is ~ 1.5 (1.41 states/eV for H-MgB₂ and 0.96 states/eV for MgB₂). This enhanced DOS plays an important role in the increase of the e - ph coupling which we will discuss in the next section.

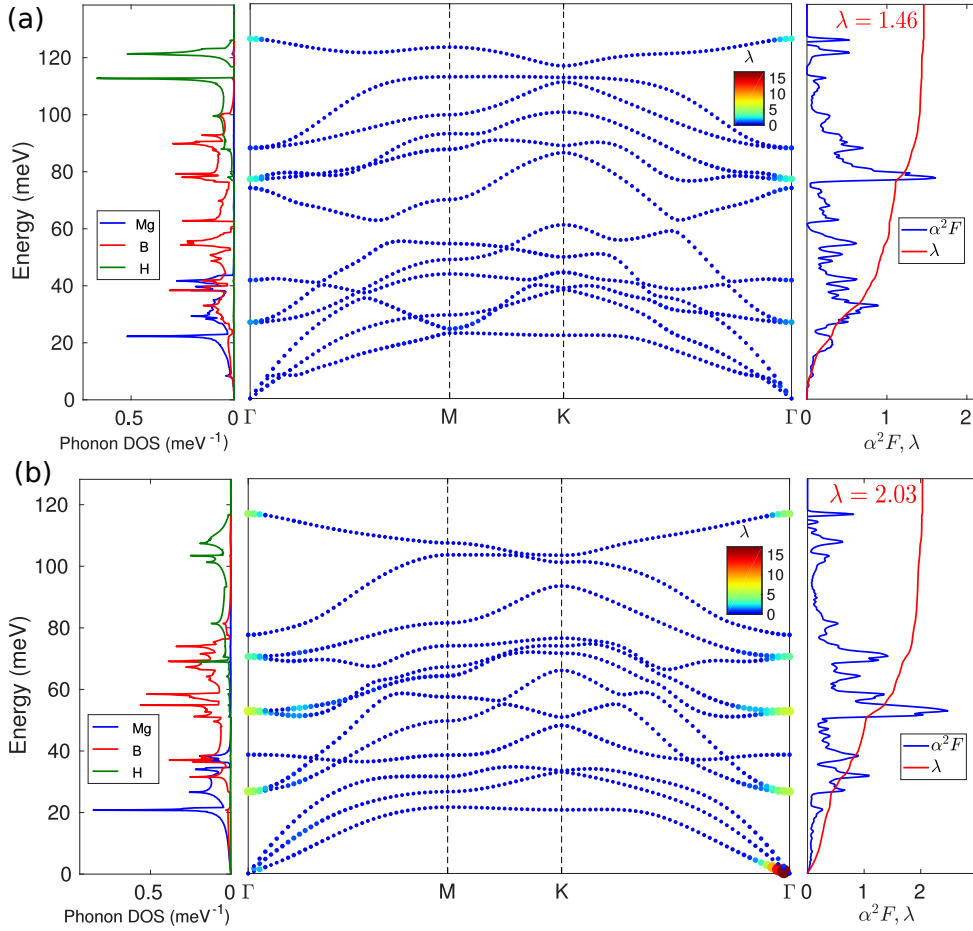


FIGURE 7.8: *The phonon dispersion, phonon DOS, Eliashberg function ($\alpha^2 F$) and electron-phonon coupling (λ) of H-MgB₂, calculated using DFPT. In the phonon dispersions the colors (see the color legend) as well as the size of the dots (larger means stronger coupling, with the radius of the dots directly proportional to the coupling) indicate the coupling strength phonon mode $\omega_{\mathbf{q}\nu}$ to the electrons, i.e., $\lambda_{\mathbf{q}\nu}$. (a) The unstrained, equilibrium case. (b) The case of +5% biaxial tensile strain.*

7.3.3 Electron-phonon interaction and superconducting properties

To study the e - ph interaction in ML H-MgB₂ we again employed DFPT as implemented in ABINIT (computational details provided in Appendix A). The result is shown in Fig. 7.8(a). As expected, the H-related phonon modes occur at the highest energies because of its very low mass. Therefore, H also

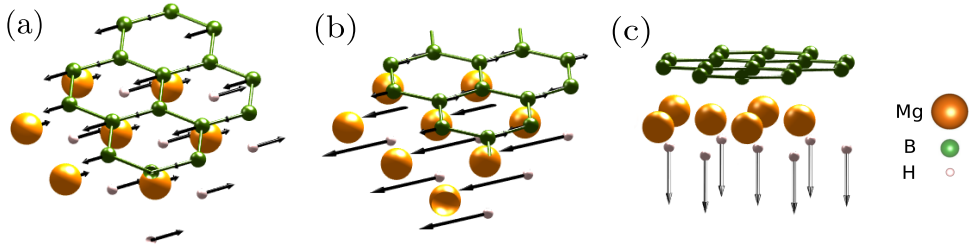


FIGURE 7.9: *The eigendisplacements corresponding to the three phonon modes of H-MgB₂ that couple most strongly to the electrons.*

enhances the maximal phonon frequency of the system to above 125 meV. The isotropic Eliashberg function α^2F and the resulting e - ph coupling constant λ shown in Fig. 7.8(a) reveal an enhancement of the e - ph coupling to $\lambda = 1.46$, compared with $\lambda = 0.68$ in pure ML MgB₂. This strong enhancement is caused by two factors. First of all, the *electronic DOS* at E_F of H-MgB₂ is about 1.5 times *higher* than that of MgB₂. As we saw in Chapter 3, $\lambda \propto N_F$, so this accounts for a part of the enhancement.

Secondly, due to the structural and electronic changes induced by the H adatoms, there are now several (three) *emerging strongly coupling channels* instead of the one dominant E_{2g} B mode in MgB₂. These three main modes can be observed in Fig. 7.8(a), where the band-resolved $\lambda_{\mathbf{q}\nu}$ values are plotted into the phonon band structure. In all cases the coupling is maximal at and around Γ , so there is a strong tendency for intraband coupling. Such small-momentum coupling was also present in MgB₂ (monolayer to bulk), and lies at the origin of the multigap behavior there. The first strongly coupling mode occurs at ~ 27 meV (degenerate phonon bands 4 and 5). As shown in Fig. 7.9(a), the Mg atoms and B atoms move out-of-phase with each other along the zigzag direction (the H atoms follow the Mg atoms to a lesser extent). The second strongly coupling mode, shown in Fig. 7.9(b), occurs at ~ 76 meV (degenerate bands 8 and 9), and is akin to the E_{2g} mode in MgB₂. However, here the H atoms also move, specifically out-of-phase (in-phase) with the B atoms of the same (other) sublattice. Finally, the mode at ~ 126 meV (band 12), depicted in Fig. 7.9(c), consists of Mg and H atoms moving out-of-phase in the out-of-plane direction. The details of these modes indicate that hydrogen plays a direct role in most of the strong e - ph coupling channels.

With $\lambda = 1.46$ – and using as before $\mu^* = 0.13$ – we obtain $T_c \simeq 45$ K from the *isotropic* McMillan-Allen-Dynes formula. This is a large enhancement with respect to ML MgB₂ (where anisotropic Eliashberg calculations yielded $T_c = 20$ K, and the isotropic approximation 11 K). Bearing in mind that the Fermi surface of H-MgB₂ consists of two distinctly different sheets (σ and π -Hs) and that the small-momentum e - ph coupling favors multigap superconductivity (likely two-gap in this case), I expect that this T_c may in fact be significantly larger. To investigate this, anisotropic Eliashberg calculations will be performed in the near future.

7.3.4 Additional enhancement with strain

In view of the results I obtained for the effect of biaxial strain on the superconducting properties of ML MgB₂, it is certainly of interest to also consider strain in ML H-MgB₂. The evolution of the e - ph coupling and of T_c with strain is listed in Table 7.1. The strains considered here are in the range -1% to $+5\%$. Larger compressive strain resulted in structural instabilities. H-MgB₂ is thus found to be much less compressible than ML MgB₂. We see again an enhancement of λ and of T_c with tensile strain, on top of the intrinsic enhancement due to the hydrogen atoms. The mechanisms at play in this additional enhancement are essentially the same as in ML MgB₂. First and foremost, there is a softening of the main coupling modes, which leads to the peaks in α^2F moving to lower energies, and thus contributing more to the e - ph coupling. This is shown in Fig. 7.8(b) for a tensile strain of $+5\%$ ³. In addition, the electronic DOS at E_F increases significantly with tensile strain (and decreases with compressive strain), by 45% for tensile strain of $+5\%$, compared with the equilibrium value.

These trends make that the e - ph coupling systematically increases with biaxial tensile strain. At $+5\%$ tensile strain, λ attains a very high value of 2.03, as shown in Fig. 7.8(b). This leads to a considerable enhancement of the T_c , to 53 K (cf. Table 7.1 for the complete data). Again, this result is obtained within the isotropic approximation, so it necessarily is an underestimation of the true T_c that can be obtained with anisotropic Eliashberg theory. Thus,

³One notices on the other hand that the upper phonon band does not change by much between 0% and $+5\%$ strain. The reason is that the atoms move in the out-of-plane direction here and are consequently less affected by in-plane strain.

Strain (%)	ω_{\log} (K)	λ	T_c (K)
-1	500.6	1.21	39.9
0	441.6	1.46	44.7
+1	483.9	1.41	47.2
+2	515.5	1.38	48.8
+3	457.8	1.62	51.4
+4	377.8	1.89	48.6
+5	393.4	2.03	53.4

TABLE 7.1: *The evolution of the isotropic electron-phonon coupling properties of H-MgB₂ with strain, specifically the logarithmic frequency ω_{\log} (Eq. 3.44), the electron-phonon coupling constant λ and the T_c obtained from the McMillan-Allen-Dynes formula (Eq. 3.43) using $\mu^* = 0.13$.*

we have found a new pathway to bring T_c of 2D superconductors to unprecedentedly high values. Here, only a single layer of H adatoms is needed, and not a substrate like in high- T_c ML FeSe [54, 55]. Moreover, in (strained) ML H-MgB₂ the coupling mechanism is completely conventional, but as yet unknown for ML FeSe.

7.4 Conclusions

In this chapter we have studied how superconductivity in a single-monolayer superconductor can be enhanced. Here, we specifically focussed on monolayer magnesium diboride (MgB₂), because of the promising properties emerging from its three-gap superconductivity.

The first route that was investigated is that of biaxial strain applied to monolayer MgB₂. First-principles indicate a strong phonon softening with tensile strain (i.e., expanding the lattice), as a result of depleted electron densities, thus weaker response to atomic displacements. Consequently, also the main coupling mode, the E_{2g} mode, is lowered in energy. This results in a shift of the main peak of the Eliashberg spectral function to lower energies, and thus an enhancement of the electron-phonon coupling. From anisotropic Eliashberg calculations it was found that with only $\sim 4\%$ tensile strain, the superconducting critical temperature is boosted to temperatures beyond 50

K (compared with 20 K in the unstrained case). Important for this enhancement is that it fully profits from multigap effects, since the three-gap superconductivity of ML MgB₂ is preserved under applied strain.

The second route that was explored here is that of adatoms on ML MgB₂, specifically hydrogen atoms. From *ab initio* calculations it was found that the equilibrium structure contains one hydrogen atom per MgB₂ unit, at the side of the magnesium plane and with an in-plane position identical to one the boron sublattice sites. The electronic structure of this resulting H-MgB₂ compound has two different electronic bands at the Fermi level, namely the σ bands and a novel state comprised of hybridized hydrogen s and boron π states. The surface band characteristic of atomically thin MgB₂ is eliminated by the hydrogen adatoms. From the *ab initio* calculations a considerable enhancement of the electron-phonon coupling in H-MgB₂ with respect to MgB₂ was found. This can be attributed to a higher density of states, especially due to the hybrid electronic state, as well as changes in the phonon modes mainly due to the hydrogen adatoms.

Finally, these two routes were combined in studying the effect of strain on ML H-MgB₂. It was found that there is an additional enhancement of the electron-phonon coupling, for which phonon softening just like in strained MgB₂, as well as a significant increase in the electronic density of states lie at the base. Within an isotropic approximation to Eliashberg theory a T_c above 50 K was obtained, which is expected to increase further when properly taking into account multiband effects (which will be performed at a later stage).

Both pathways explored in this chapter unequivocally prove the potential of boosting superconductivity in 2D materials on the nanoscale, by engineering the structural, electronic and vibrational properties with strain and adatoms.

Publication

J. Bekaert, A. Aperis, B. Partoens, P. M. Oppeneer, and M. V. Milošević, *Evolution of multigap superconductivity in the atomically thin limit: Strain-enhanced three-gap superconductivity in monolayer MgB_2* , Phys. Rev. B **96**, 094510 (2017).

Chapter 8

Interplay of superconductivity and novel quantum states in 2D transition metal dichalcogenides

Two-dimensional transition metal dichalcogenides (2D TMDs) are atomically thin materials at the forefront of research, owing to their special electronic and optical properties, their tunability by electric gating and mechanical strain, and easy heterostructuring. It is much less explored that they also exhibit a wealth of collective quantum phases, characterized by a collective behavior of electrons that is entirely different from their individual states. One such phase is a charge density wave, where the electrons form an ordered quantum fluid at lower temperatures that restructures the host material. Another low-temperature collective quantum phase emerging in 2D TMDs is superconductivity. Furthermore, the spins of the electrons add to the combinatorial possibilities for novel quantum states, forming Ising spin textures in monolayer TMDs that are wholly absent in the bulk. All these states are strongly intertwined, but the fundamentals of their interplay are not well understood. In this chapter, it is proven that superconductivity in 2D TMDs cannot be described adequately when disregarding the coexisting novel quantum states, such as the charge density wave and Ising states.

Subsequently, the basis is laid for studying this interplay by establishing adequate ab initio descriptions of the Ising and charge density wave states.

8.1 Introduction

Many ordered quantum phases in 2D materials are characterized by *collective behavior*, whereby the electrons collaborate in forming a new state that is fundamentally different from their single-particle states. Superconductivity in 2D materials, which we have been studying in Chapters 1, 6 and 7, is one of the the most prominent examples of a collective phase occurring in the 2D limit. Another notable example of collective behavior in some 2D metallic systems is an instability of the electron cloud, evoking a structural phase transition upon cooling, akin to the Peierls transition in 1D systems. As the phase transition results in a modulation of the electronic charge density, it is known as the *charge density wave* (CDW) phase [280].

Prime candidates to study collective phases in 2D materials are the *transition metal dichalcogenides* (TMDs), where both superconductivity and CDWs have been observed [280]. TMD monolayers consist of a transition metal layer in between two layers of chalcogen atoms. The coupling between such TMD monolayers is mediated by van der Waals (vdW) interaction, so that ultrathin samples can be mechanically exfoliated [118, 269, 270, 281], but also synthesized by controlled molecular beam epitaxy [119] and chemical vapor deposition [282]. Moreover, TMDs can be stacked in both vertical and lateral heterostructures, so that properties of different TMDs can be combined [97, 98].

The key ingredient in TMDs is the richness of their structural phases, the main two being the *H* phase (with ABA stacking) and the *T* phase (with ABC stacking) [280]. Depending on the structural phase and the atomic species, TMDs can have *highly versatile electronic properties* [280]. For instance, TMDs based on group V (Nb, Ta) and group VI (Mo, W) transition metal elements both adopt the *H* phase, but the former are metallic while the latter are semiconducting. The metallic TMDs are generally superconductors, and display an interesting behavior when their thickness decreases to the atomic

scale, namely a reduction of the critical temperature in NbSe₂ [118], opposed to an enhancement in TaS₂ [121, 269], hypothesized to be related to changes in the coexisting CDW state [121]. Superconducting TMDs exhibit moreover features indicating multiple and/or anisotropic gaps in the superconducting state [283]. Interestingly, 2D superconductivity can also be established in intrinsically semiconducting 2D TMDs by altering the Fermi level by gating [122, 123, 282, 284–286], doping [287] or high pressure [288, 289].

The other collective quantum state in TMDs, the CDWs, can also change drastically in the 2D limit, where enhancement [290, 291], depletion [121] and non-monotonic behavior [281] of the CDW phase have all been observed. Other nanoscale manipulations influencing the CDW order include interlayer twist [120], doping in the vdW gap [292–294] and gating [295]. Being both based on collective behavior of the electrons, and sharing several means of manipulation, it remains as an open question to date if CDWs and superconductivity actually compete, and if their *interplay* can be tuned to achieve novel hybrid phases.

A characteristic example of the richness in structural phases and collective behavior in 2D TMDs is TiSe₂ with controlled Cu intercalation in the vdW gap. Fig. 8.1(a) shows different CDW orders, depending on the Cu concentration. At higher concentrations, the CDW transition is suppressed and the system becomes superconducting [292]. Gating provides another route to suppress CDWs and to stimulate superconductivity in TiSe₂ [295]. CDWs are often thought to be in direct competition with superconductivity, as the Fermi surface can become fully or partially gapped due to CDW order [119, 296, 297]. However, the most recent experiments indicate that the relation between CDWs and superconductivity may be more intricate, and that the precise effect of the CDWs on the electronic properties should be considered [298].

Adding further to the richness of 2D TMDs, a splitting of the electronic bands and pinning of the electron spins perpendicular to the crystal plane takes place in films consisting of an odd number of monolayers, as a result of *strong spin-orbit coupling* (SOC) and a lack of a spatial inversion center. As depicted in Fig. 8.1(b), electrons in the same band with opposite momentum necessarily have opposite spin due to *spin-valley locking*. The same effect lies at the base of valleytronics in 2D semiconducting TMDs [299, 300]. The

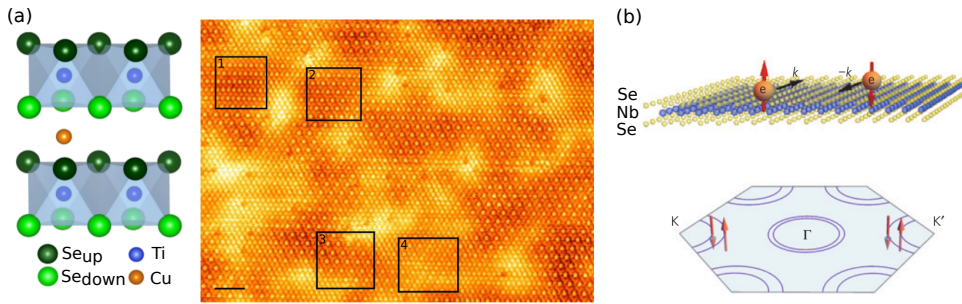


FIGURE 8.1: *Novel quantum states in 2D TMDs. (a) A structural model of Cu-intercalated 1T-TiSe₂, and a low-temperature, atomic-resolution STM image showing striped CDW order (panels 1 and 4) and a 2×2 CDW reconstruction (panels 2 and 3) [294]. (b) The Ising state in monolayer NbSe₂, both in real space and on the Fermi surface [118].*

resulting spin texture is known as the *Ising state*, and exerts a strong influence on the collective states. For instance, experiments have shown a strong enhancement of the in-plane critical magnetic field in superconducting monolayer NbSe₂ [118, 301], and in gated thin flakes of MoS₂ [123, 284]. This effect promises to be only the tip of the iceberg, as the Ising state can lie at the base of *unconventional and topological superconductivity* as well [302, 303].

Interesting physics is also achieved by coupling TMDs with *magnetic impurities*. For instance, Fe atoms on 2D NbSe₂ [304] give rise to long-range Yu-Shiba-Rusinov (YSR) bound states. It is convincingly shown that the long range of the state originates from the 2D nature of the sample. Chains of these impurities can yield topological superconductivity with Majorana quasiparticles at the extremities of the sample, applicable in quantum computing. The samples considered there are still thick compared with the monolayer limit, where the Ising state becomes of increasing importance. On a related note, it has been shown that magnetism can also be induced in 2D TMDs by applying strain [305], pressure [306], or by means of adatoms [305, 307, 308].

Altogether, 2D TMDs provide an unprecedented combination of controllable structural phase transitions, spin-valley coupling and (topological) superconductivity. This makes them a *unique 2D platform* to explore the interplay between collective quantum phases, prone to *tailoring* on the atomic scale by means of strain, gating and doping. The main objectives of this chapter

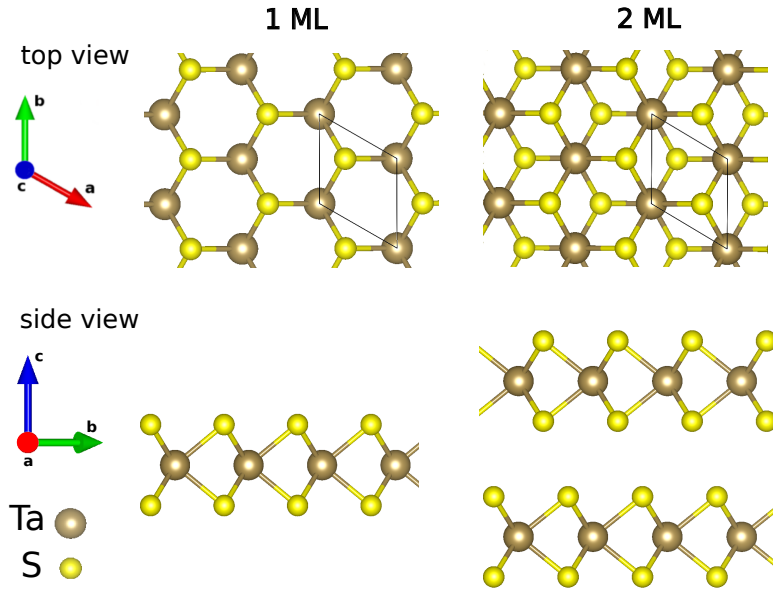


FIGURE 8.2: TaS_2 monolayer and bilayer in the H crystal structure, shown in a top and in a side view.

are (i) to provide further evidence from theory that the different components of 2D TMSs indeed exert a strong mutual influence, and (ii) to construct a proper *ab initio* description of the Ising state and the CDW state. Here, I will focus on intrinsically metallic TMDs such as $NbSe_2$ and TaS_2 .

8.2 Crystal structure

The intrinsically metallic TMDs like $NbSe_2$ and TaS_2 adopt the H crystal structure. As shown in Fig. 8.2 the monolayer is characterized by ABA stacking. The H structure is hexagonal (space group $P\bar{6}m2$, No. 187), and shows a honeycomb pattern in the top view, where one sublattice consists of the transition metal (Nb, Ta, etc.) and the other of the chalcogen atom (S, Se, etc.). The corresponding unit cell of the monolayer shown in Fig. 8.2 lacks an in-plane inversion center. This has important consequences for the spin parts of the electronic states, as I will discuss in more detail in Sec. 8.5. This lack of an inversion center is the case for all H-structured TMDs consisting of an odd number of monolayers. On the other hand, Fig. 8.2 also shows that 2 monolayers, and with them all structures consisting of an even number

of monolayers, do possess an in-plane inversion center, namely the center of the unit cell. In two monolayers the stacking is ABA in the first monolayer, followed by CBC in the second monolayer. The bulk has two monolayers in its unit cell, hence its structure is called the 2H structure, following space group $P6_3/mmc$ (No. 194) – which possesses an in-plane inversion center. The transition metals occupy the corresponding Wyckoff positions 2b, i.e., $(0, 0, \frac{1}{4})$ and $(0, 0, \frac{3}{4})$, and the chalcogen atoms the Wyckoff positions 4f, i.e., $(\frac{1}{3}, \frac{2}{3}, z)$, $(\frac{2}{3}, \frac{1}{3}, z + \frac{1}{2})$, $(\frac{2}{3}, \frac{1}{3}, -z)$ and $(\frac{1}{3}, \frac{2}{3}, -z + \frac{1}{2})$.

8.3 Electronic structure

The electronic structure of TMDs is strongly influenced by spin-orbit coupling (SOC), owing to their high atomic masses, e.g., $Z = 41$ for niobium (Nb) and $Z = 73$ for tantalum (Ta). Therefore, in all the calculations presented here SOC has been taken into account in a fully relativistic way (details on which can be found in Appendix A). The resulting electronic band structures of monolayer (ML) NbSe₂ and TaS₂ are shown in Fig. 8.3 (a) and (b). Two bands, stemming from one band split under the influence of SOC, cross the Fermi level (E_F).

With SOC, the wave functions take the spinor form

$$|\psi\rangle = \begin{pmatrix} |\psi^{(1)}\rangle \\ |\psi^{(2)}\rangle \end{pmatrix}. \quad (8.1)$$

Fig. 8.3 shows the leading spinor components of the lowest band crossing the Fermi level in ML NbSe₂ – which I will call the *inner* band (*i*) because it lies on the inside of the other, *outer* band (*o*) [cf. the Fermi surfaces in Figs. 8.1(b) and 8.5]. The leading component is each time an order of magnitude larger than the other one. Fig. 8.3(c) shows the leading component of the band *i* around Γ , viz., $\psi_{i\Gamma}^{(2)}$. The relation to the dominant component of band *o* is

$$\psi_{i\Gamma}^{(2)} \simeq -\psi_{o\Gamma}^{(1)}. \quad (8.2)$$

The wave function in Fig. 8.3(c) shows mixed Nb 4d and Se 4p character. Here, the wave function is a combination of atomic orbitals oriented in the out-of-plane directions, with respectively 4d_{z²} and 4p_z character.

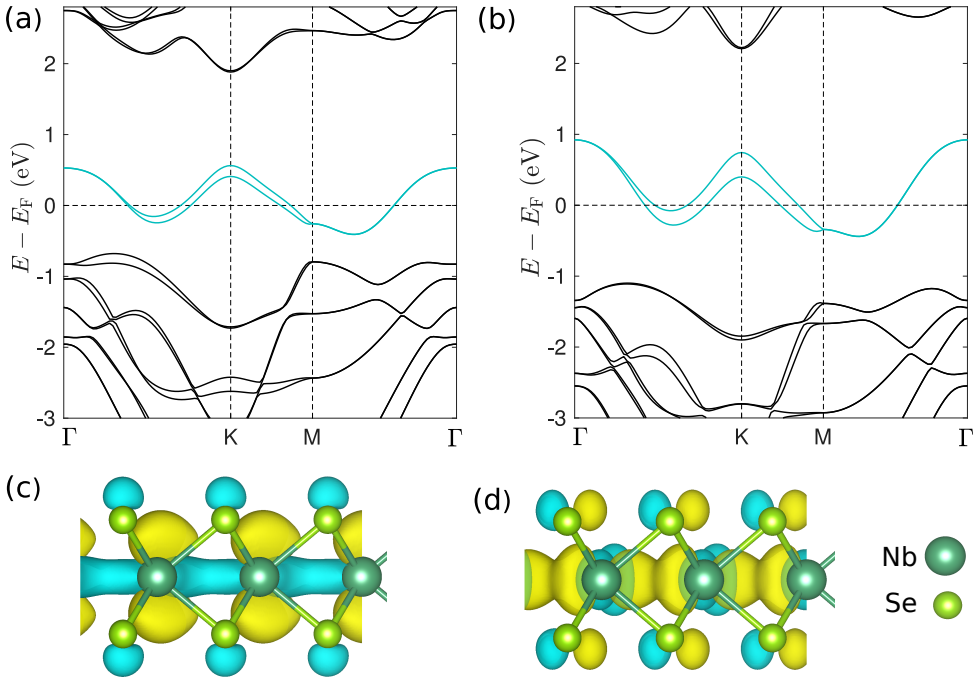


FIGURE 8.3: *The electronic structure of TMDs monolayers, specifically the band structure of (a) NbSe₂ and (b) TaS₂. The bands crossing E_F are plotted in cyan. (c) and (d) Wave functions obtained on the lower band crossing E_F (thus inner band in terms of the Fermi surface), around respectively (c) Γ and (d) K .*

Around point K , the wave function is a combination of in-plane atomic orbitals displaying Nb $4d_{x^2-y^2}$ and Se $4p_{x,y}$ character respectively, as shown in Fig. 8.3(d). The leading spinor components are related as

$$\psi_{iK}^{(2)} \simeq \psi_{oK}^{(1)}. \quad (8.3)$$

Here, the difference between the bands is larger than at Γ , as a result of the larger split between the bands around K , that can be evidenced in Fig. 8.3(a). Namely, band i shows slightly more overlap between the orbitals than band o .

The electronic structure and wave functions of TaS₂ are similar to those of NbSe₂. One major difference between the two is that the SOC split between the bands crossing E_F is larger in TaS₂ – as observed in Fig. 8.3(b) – because of the higher atomic number of Ta compared with Nb.

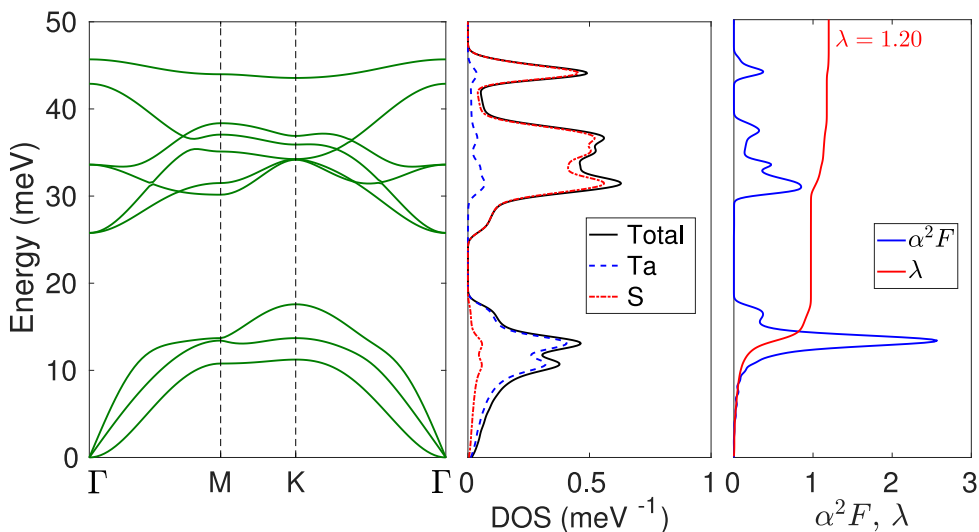


FIGURE 8.4: *Phonon band structure, phonon DOS, Eliashberg function ($\alpha^2 F$) and electron-phonon coupling constant (λ) of monolayer TaS₂, calculated using DFPT.*

8.4 Phonons, electron-phonon coupling and Eliashberg theory

Since we want to study superconductivity resulting from e - ph interaction, the phonons and e - ph coupling matrix elements were again calculated using DFPT. The resulting phonon band structure, phonon DOS and Eliashberg function ($\alpha^2 F$) of ML TaS₂ are depicted in Fig. 8.4. The phonon band structure shows a clear flexural ZA mode with quadratic dispersion. From the phonon DOS it follows that the lower, acoustic phonon modes have predominantly Ta character, owing to the higher mass of the Ta atoms. The e - ph coupling constant attains a high isotropic value of $\lambda = 1.20$ in ML TaS₂, with the main contribution at 13 meV stemming from the LA mode. This mode accounts for 81% of the total e - ph coupling.

8.4.1 Issue of the overestimated superconducting strength

The T_c resulting from the e - ph coupling shown in Fig. 8.4 is 13.7 K (using standard $\mu^* = 0.13$). As listed in Table 8.1 the experimental value is much lower, namely 3.4 K [121]. Such overestimations are generally observed in

Material	d (ML)	λ , calc.	T_c (K), calc.	T_c (K), exp.	Ref., exp.
NbSe ₂	1	1.00	9.8	3.0	[118]
	2	1.05	10.4	5.3	
	bulk	0.93	9.9	7.0	
TaS ₂	1	1.20	13.7	3.4	[121]
	2	1.26	14.4	2.8	
	bulk	1.26	10.3	0.8	

TABLE 8.1: *The evolution of the isotropic electron-phonon coupling properties of NbSe₂ and TaS₂ with thickness d , the calculated electron-phonon coupling constant λ and T_c obtained from the McMillan-Allen-Dynes formula (Eq. 3.43) using $\mu^* = 0.13$, compared to available experimental values.*

Table 8.1, albeit that in bulk NbSe₂ it is rather limited. The systematic overestimations are a smoking gun for a strong impact of CDWs on superconductivity in atomically thin TMDs. In Sec. 8.6 I will show that the mode with the strongest contribution to the e - ph coupling constant is exactly the one inducing the CDW instability. Therefore, this contribution to the e - ph coupling is invested in the structural transition and no longer in establishing superconductivity. This is a case of pure competition between the CDW state and the superconducting state, as discussed in the introduction to this chapter.

I envisage that the only truly unambiguous theoretical solution of this problem consists of reconstructing the crystal under the influence of the CDW, and re-evaluating the e - ph interaction of the resulting structure. Older, more approximative approaches to include the effect of the CDWs on superconductivity were based on the self-energy of the CDW state [309] and on the susceptibility resulting from the Fermi surface [310]. The clear benefit of calculating the reconstruction of the crystal structure within the *ab initio* approach is that the effect on the atomistic properties are taken into account self-consistently. I will present a proof of concept of this idea in Sec. 8.6. This case proves once more the power of *ab initio* calculated e - ph interactions to assess the main processes at the base of multicomponent superconductivity.

As we saw in the previous section, there are two different electronic contributions at E_F , namely pockets around Γ and K. To find out the effect of this multiband character of the superconductivity, anisotropic Eliashberg

calculations were carried out. The main result is that the multiband effect is much smaller in TMDs than in MgB₂ (cf. Chapters 6–7). The obtained gap spectrum shows a single, anisotropic gap, in all cases ranging from a single ML to the bulk limit. However, it should be noted that it is not a priori clear that this type of gap spectrum would be conserved upon the CDW-driven reconstruction of the crystal structure described above. The overestimation of T_c is confirmed in the anisotropic calculations. To give an example, to match the calculated T_c of bulk NbSe₂ with the experimental value of 7.0 K [118], an enhanced Anderson-Morel pseudopotential of $\mu^* = 0.23 - 0.24$ is required in the model. It is more likely that in reality the competition with the CDW state lowers T_c , as discussed above.

8.5 The Ising state

As discussed in Sec. 8.3, spin-orbit coupling (SOC) plays a crucial role in TMDs. We will review here how this affects the behavior of the electron spins, especially in stacks consisting of an odd number of monolayers that lack an in-plane inversion center. First, I will review how the behavior of the spins can be studied in a quantum-mechanical fashion, by calculating the *spin expectation values*, then I will present the crucial role of symmetries, and finally I will show how to couple this to *ab initio* calculations.

8.5.1 Spin expectation values

Spin expectation values are the matrix elements of the operators $\hat{S}_i = \frac{\hbar}{2}\hat{\sigma}_i$, where $i = x, y, z$ and where $\hat{\sigma}_i$ are the Pauli matrices¹. Here we need to bear in mind that the wave functions are spinors of the form given in Eq. 8.1. Thus, the spin expectation values are

$$\begin{cases} S_x = \frac{\hbar}{2}\langle\psi|\hat{\sigma}_x|\psi\rangle = \frac{\hbar}{2}(\langle\psi^{(1)}|\psi^{(2)}\rangle + \langle\psi^{(2)}|\psi^{(1)}\rangle) , \\ S_y = \frac{\hbar}{2}\langle\psi|\hat{\sigma}_y|\psi\rangle = \frac{\hbar}{2}i(\langle\psi^{(2)}|\psi^{(1)}\rangle - \langle\psi^{(1)}|\psi^{(2)}\rangle) , \\ S_z = \frac{\hbar}{2}\langle\psi|\hat{\sigma}_z|\psi\rangle = \frac{\hbar}{2}(\langle\psi^{(1)}|\psi^{(1)}\rangle - \langle\psi^{(2)}|\psi^{(2)}\rangle) , \end{cases} \quad (8.4)$$

¹The Pauli matrices read $\hat{\sigma}_x = \begin{pmatrix} 0 & 1 \\ 1 & 0 \end{pmatrix}$, $\hat{\sigma}_y = \begin{pmatrix} 0 & -i \\ i & 0 \end{pmatrix}$, and $\hat{\sigma}_z = \begin{pmatrix} 1 & 0 \\ 0 & -1 \end{pmatrix}$.

which are to be divided by the square of the norm, $\langle\psi^{(1)}|\psi^{(1)}\rangle + \langle\psi^{(2)}|\psi^{(2)}\rangle$, in case the spinors were not yet normalized. Note that all of these expectation values are real², as they should be in order to be correct physical observables.

8.5.2 The crucial role of symmetry

Spin expectation values in condensed matter are dictated by symmetry [311]. The two main symmetries at play here are *spatial inversion symmetry* and *time-reversal symmetry*. Spatial inversion symmetry means invariance under the transformation $\mathbf{r} \rightarrow -\mathbf{r}$. This immediately translates into the relation $E(\mathbf{k}, \uparrow) = E(-\mathbf{k}, \uparrow)$ for the energy spectrum of a solid with spatial inversion symmetry.

On the other hand, time-reversal symmetry (TRS) in solids describes the transformation of the wave function under the influence of the time reversal operator \hat{T} that transforms $|\mathbf{k}\rangle \rightarrow |-\mathbf{k}\rangle$ and $|\uparrow\rangle \rightarrow |\downarrow\rangle$, so that $\hat{T}\psi(\mathbf{k}, \uparrow) = \psi(-\mathbf{k}, \downarrow)$. This implies for the energy spectrum of the solid that $E(\mathbf{k}, \uparrow) = E(-\mathbf{k}, \downarrow)$. Thus, if both symmetries are combined – as is the case in centrosymmetric materials – the energy spectrum obeys $E(\mathbf{k}, \uparrow) = E(\mathbf{k}, \downarrow)$, so that two states with opposite spin are completely degenerate.

Time-reversal symmetry breaking (TRSB) can occur in relatively simple condensed matter systems, for instance in ferromagnetic materials. As a result, even though, e.g., ferromagnetic iron adopts the centrosymmetric space symmetry of group $\text{Im}\bar{3}\text{m}$ (No. 229), $E(\mathbf{k}, \uparrow) \neq E(\mathbf{k}, \downarrow)$. A traditional superconductor in a singlet state (electrons with opposite spin are paired up) and a simple Fermi surface, as described by Bardeen-Cooper-Schrieffer theory, obeys fully time-reversal symmetry. However, in some less conventional superconductors, such as three-gap superconductors with phase frustration and triplet superconductors, TRSB can occur, as discussed in Chapters 1 and 5.

² S_x is of the form $\int d\mathbf{r} \left(\psi^{(1)}(\mathbf{r})\psi^{(2)*}(\mathbf{r}) + \text{c.c.} \right)$, and is thus real and S_y is of the form $i \int d\mathbf{r} \left(\psi^{(1)}(\mathbf{r})\psi^{(2)*}(\mathbf{r}) - \text{c.c.} \right)$, which also proves it being real, while for S_z , it suffices to note that it is a sum of squared norms.

8.5.3 Rashba effect and spin-valley locking

A notable example of a spin texture phenomenon occurring in two-dimensional materials is the *Rashba effect* [311]. It originates from *spatial inversion symmetry breaking* in the *out-of-plane* direction. This can for instance be realized by an applied electric field perpendicular to the crystal plane. The resulting spin texture is characterized by in-plane spins with a momentum-dependence parametrized by a circle. Bulk, non-centrosymmetric crystals display related behavior, called the *Dresselhaus effect* [311].

In contrast to the in-plane spins emerging in the Rashba effect, odd-layered TMDs display a spin texture which we will denote as *spin-valley locking*, and the resulting quantum state as the *Ising state*. It results from the crystal structure of these materials – as discussed in Sec. 8.2 and depicted in Fig. 8.2 – combining out-of-plane mirror symmetry (for instance, in TaS₂ the mirror plane corresponds to the Ta plane), a lack of in-plane inversion symmetry and strong SOC.

Before going to the complete *ab initio* description, we will make full use of the symmetries to derive as much of the properties of the Ising state as possible. Due to the mirror plane, the crystal field originating from the SOC, ϵ , cannot have a gradient perpendicular to this plane. As such it is confined to the (x, y) -plane of the atoms, and therefore takes the form $\epsilon = (\epsilon_x, \epsilon_y, 0)$. Since the electron motion is also confined to the (x, y) -plane, $\mathbf{k} = (k_x, k_y, 0)$. As a consequence, the effective magnetic field due the SOC reads

$$\mathbf{H}_{\text{SO}} = \mathbf{k} \times \boldsymbol{\epsilon} = (\epsilon_y k_x - \epsilon_x k_y) \hat{z}, \quad (8.5)$$

and is therefore polarized completely in the z -direction. Under the influence of this SO magnetic field the spin expectation values also polarize in the z -direction.

This phenomenon is called *spin-valley locking*, as the spin polarization depends on the electronic valleys related to the two sublattices. Namely, owing to TRS, the spin expectation values are reversed in K' with respect to K , for the same band. The resulting state is called the *Ising state* in view of its likeness to the Ising model for ferromagnetism.

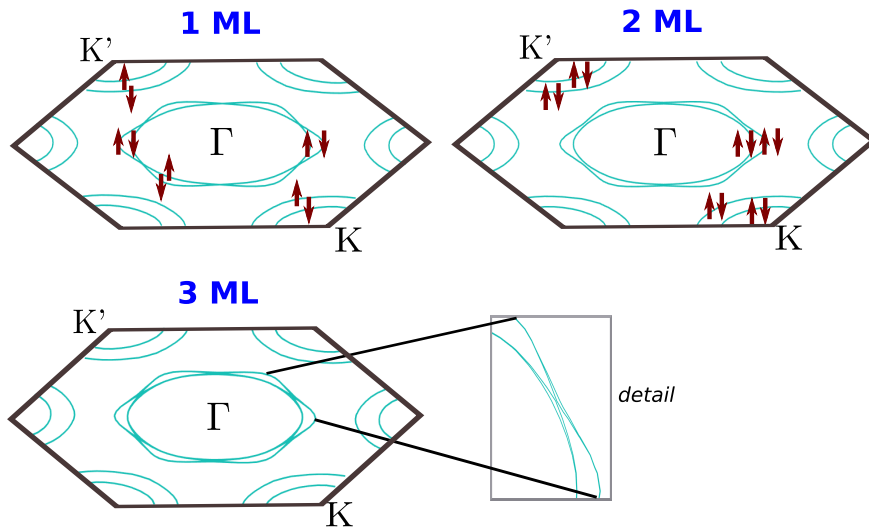


FIGURE 8.5: *Calculated Fermi surfaces of 1 – 3 ML TaS₂, including the calculated band- and momentum-dependent spin expectation values.*

It is instructive to consider the relation of spin-valley locking to magnetism. Locking of specific spin states to electronic bands is a property of the reciprocal space, and the bands result from hybridization between states from different atoms, so the spins cannot be mapped to a magnetic state. What is more, the net polarization of spins over the whole unit cell amounts to zero, since TRS is conserved – so there is no spontaneous magnetization.

8.5.4 *Ab initio* description

To a first approximation the spin expectation values are dictated by the spinor properties described in Sec. 8.3. These indicate first of all that since there is always a leading spinor component, an order of magnitude larger than the other one, cross terms containing both $\psi^{(1)}$ and $\psi^{(2)}$ are small. As such, according to Eq. 8.4 that S_x and S_y are negligible. Moreover, the specific relation between the leading spinor components of both bands, given by Eqs. 8.2 and 8.3, dictates that they have opposite sign.

A more detailed *ab initio* description of the spin texture can be obtained by explicitly carrying out the integrals contained in the spinor inner products of Eq. 8.4. Apart from very small numerical rounding errors, almost perfect

polarization of the spin expectation values in the z-direction is obtained. These are depicted in Fig. 8.5, plotted onto the Fermi surfaces of 1 – 3 ML TaS₂. The case of 1-ML TaS₂ is the one discussed earlier, namely the Ising state. Around K, there is an inner and an outer band, which have opposite spin expectation values polarized in the z-direction. Around K', the expectation values carry the opposite signs with respect to those around K, as a result of TRS. Around Γ , we see a different situation to that depicted in Fig. 8.1(b) – which I took from the existing literature – where no spin expectation values are depicted on those bands. In reality, the calculations show that the two bands around Γ display spin-valley locking too, touching in six points (nodes) to ensure TRS.

In the 2-ML case there are two spin states per band – stemming from the two layers – such that there is usual spin degeneracy of each band. Notice that the nodes around Γ have vanished, since they are not required to ensure TRS here. Therefore, this case does not have a special effect on superconductivity. In the 3-ML, there is a fine-structure consisting of four bands around both Γ and K. In this case, the Ising state re-emerges, albeit not explicitly shown here because of the required detail.

The relevance or strength of the Ising state depends on the split between the bands. So, especially the TMDs consisting of heavier transition metals hold promise for a maximal Ising state that might show unconventional and/or topological superconductivity.

8.6 *Ab initio* description of the charge density wave state

In addition to the Ising state, the CDW state is also crucial for a proper description of superconductivity in 2D TMDs, as already indicated in Sec. 8.4.1. In case of a CDW instability, the eigenvalues of the corresponding phonon mode turn imaginary, provided that the electronic smearing in the calculations (introduced in Sec. 2.6.3) is sufficiently small to resolve this effect [312, 313]. The electronic smearing can be linked to an effective temperature, since the electronic occupancies are distributed according to a Fermi-Dirac

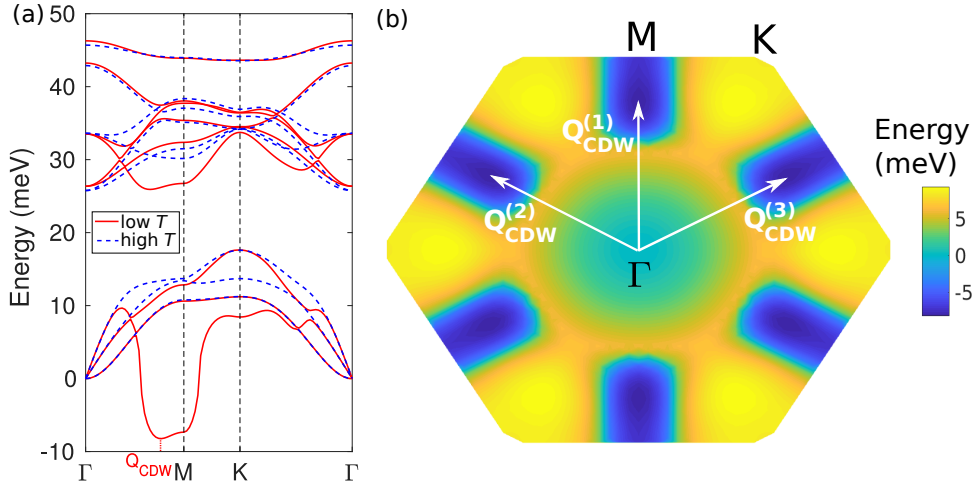


FIGURE 8.6: *First-principles approach to the CDW state. (a) Phonons of 1-ML TaS₂ calculated at high and at low temperature (T), the latter showing a CDW instability at Q_{CDW} . (b.) The LA phonon mode, showing the triple nature of the CDW, characterized by vectors $Q_{\text{CDW}}^{(1)}$, $Q_{\text{CDW}}^{(2)}$ and $Q_{\text{CDW}}^{(3)}$. These are given by $Q_{\text{CDW}}^{(1)} = \frac{3}{4}M = (\frac{3}{8}, 0, 0)$, and $Q_{\text{CDW}}^{(2)} = \frac{3}{4}M' = (0, \frac{3}{8}, 0)$, $Q_{\text{CDW}}^{(3)} = \frac{3}{4}M'' = (-\frac{3}{8}, \frac{3}{8}, 0)$.*

distribution,

$$f(E) = \frac{1}{e^{\frac{E-E_{\text{F}}}{\sigma}} + 1}, \quad (8.6)$$

where σ is the smearing factor. In the majority of the calculations presented in this thesis an electronic smearing amounting to $\sigma = 0.01$ Ha was used, but for resolving CDW instabilities I used $\sigma = 0.0025$ Ha. It should be stressed that the equivalent temperature of this smearing factor cannot be directly related to the transition temperature for the CDW phase. It merely corresponds to the numerical precision needed to resolve the CDW ground state. To determine the transition temperature a description of finite-temperature excitations beyond DFT would be required.

The main goal here is to determine the *atomic reconstruction* from the CDW vector describing the displacements of the atoms. The strength of the CDW can then be calculated by means of a structural relaxation (e.g., in ABINIT) of the reconstructed unit cell. Subsequently, the electronic and vibrational properties of this relaxed supercell, as well as the reconstructed e - ph coupling can be calculated.

As a proof of concept, I considered monolayer TaS₂. Fig. 8.6(a) shows two regimes in the phonon eigenvalues, namely the high temperature (T) regime (modeled with large electronic smearing) with stable phonon modes, and the low T one (modeled with lower electronic smearing). The latter shows an instability in the LA mode around the CDW, vector Q_{CDW} .

This is just the manifestation of the CDW in the *irreducible BZ*. In the full BZ, the CDW instability has a triple nature, with three fundamentally different minima, as shown in Fig. 8.6(b). The minima are given by $\mathbf{Q}_{\text{CDW}}^{(1)} = \frac{3}{4}\mathbf{M} = (\frac{3}{8}, 0, 0)$, $\mathbf{Q}_{\text{CDW}}^{(2)} = \frac{3}{4}\mathbf{M}' = (0, \frac{3}{8}, 0)$, and $\mathbf{Q}_{\text{CDW}}^{(3)} = \frac{3}{4}\mathbf{M}'' = (-\frac{3}{8}, \frac{3}{8}, 0)$ ³, with each time an angle of 60° in between. The reconstruction following from the eigendisplacements of the unstable mode is described a large unit cell of size $8 \times 8 \times 1$, containing 192 atoms.

The eigenvalue of the LA mode at M is only slightly larger than that at Q_{CDW} , as seen in Fig. 8.6, so the CDW reconstruction can be approximated by the one exactly at M. The advantage is that this instability corresponds to a smaller reconstructed unit cell of size $2 \times 2 \times 1$, thus containing 12 atoms – making it more feasible to be treated computationally. It is characterized by the formation of *trimers*, where the bond lengths between the Ta and the S atoms are shorter, as depicted in Fig. 8.7.

The variation in the overestimation of the calculated T_c 's for different cases, listed in Table 8.1, indicates that the CDW amplitudes (i.e., how large the changes in the crystal structure due to the CDW instability are) are influenced by dimensionality and material-specific characteristics. Interestingly, the T_c of TaS₂ increases as the thickness is reduced, while in NbSe₂ the opposite trend is observed. In the experimental study of Ref. 121 it is suggested that CDW transitions in TaS₂ are suppressed in the monolayer limit, leading to a higher T_c . This scenario is plausible, but not yet supported by calculations proving directly the effect of dimensionality on the CDW amplitudes.

³The different copies of point M in the full Brillouin zone are $\mathbf{M} = (\frac{1}{2}, 0, 0)$, $\mathbf{M}' = (0, \frac{1}{2}, 0)$, and $\mathbf{M}'' = (-\frac{1}{2}, \frac{1}{2}, 0)$

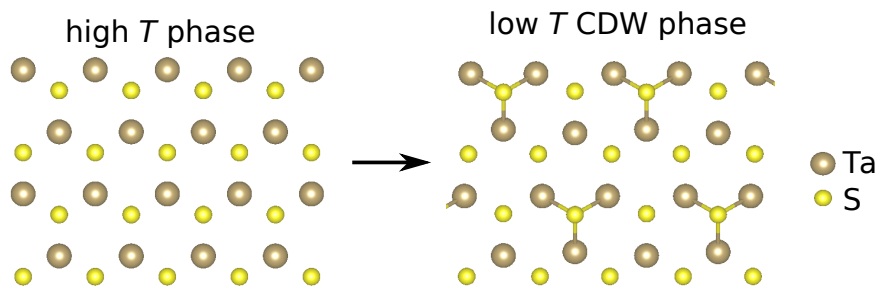


FIGURE 8.7: *The high and low T phases, the latter with $2 \times 2 \times 1$ CDW reconstruction.*

8.7 Interplay between the states

Having established in the previous sections how the novel quantum states in 2D TMDs can be described from first principles, I will discuss here prospective ideas on how the interplay between the different states in these materials might function. This lays the basis for future research.

The Ising state strongly influences the superconducting state, as the spin texture puts restrictions on the coupling between specific spin states, so that Bardeen-Cooper-Schrieffer-like spin singlet pairing (between opposite spin states) is likely not the only mechanism at play. This opens the possibility of unconventional spin-triplet pairing (between equal spin states) in TMDs⁴, especially when the splitting between the bands can be enhanced. Such spin-triplet pairing has topological properties, and can support and stabilize Majorana fermions in hybrid devices based on 2D TMDs [302], holding promise for future quantum computing [314].

In practice, both the singlet and the triplet pairing channels are available in 2D TMDs. To introduce the Ising state into the Eliashberg framework, the electron kinetic energy can be separated into normal and SOC components, with the latter containing the effect of the Ising spin texture. Due to the potentially mixed singlet-triplet pairing both need to be included in the form of coupled equations.

⁴It should be noted that during the superconducting condensation, the direction of the spin expectation values changes from the out-of-plane direction to the in-plane direction [302].

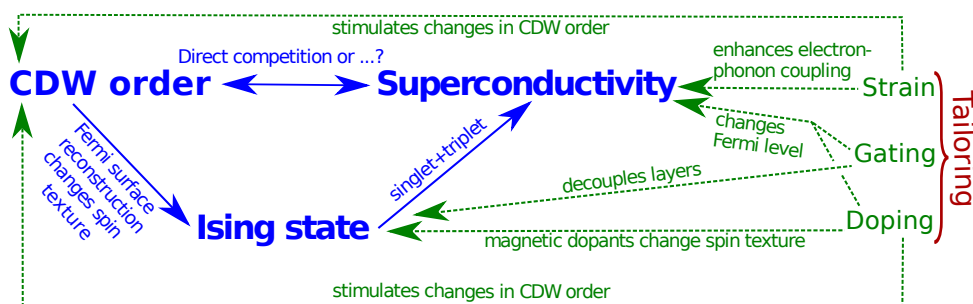


FIGURE 8.8: *Scheme resuming the main questions related to the interplay between the different phases, as well as the pathways aimed at tailoring them.*

As explained in the previous section, the crystal structure reconstructs into a larger unit cell under the influence of the CDW instability. This results in drastic changes in the electronic structure and the e - ph coupling. It is very important to consider whether the CDW gap opening in the electronic structure occurs exactly at the Fermi level, and to what extent the e - ph coupling is affected. This corresponds to the scenario of pure competition between CDWs and superconductivity. Other scenarios are also possible. For instance, a regime may exist where CDWs enhance superconductivity due to decreased electron-electron repulsion as a result of the reconstruction.

While Ising superconductivity and the CDW state can be considered as independent to a first approximation, the CDW state will exert an influence on the Ising state. The Fermi surface reconstruction that CDWs induce affects the electronic structure, and thus also the spin texture.

The interplay between superconductivity, CDWs and the Ising state is summarized in Fig. 8.8.

8.7.1 Tailoring the interplay

Finally, I will discuss some ideas to tailor the interplay between the different states of the preceding sections on the nanoscale. The main conclusions are summarized in Fig. 8.8.

The first route is *gating* the system (i.e., adding or removing electrons), to change the Fermi level, thereby altering the electronic structure. Gating is

moreover required to render the intrinsically semiconducting TMDs (MoS₂, WS₂, etc.) metallic and thus potentially superconducting. Interestingly, gating renders the outermost layer of a few-monolayer stack electrically decoupled from the other layers, thus mimicking a freestanding monolayer – including its Ising state [284]. Changes of the Fermi level and the Fermi surface due to gating can be probed by means of quantum oscillations in applied magnetic fields, in comparison with calculations, as explained in Chapter 4.

A second interesting route is that of *doping*. With doping the Fermi level is altered, but additionally the electronic structure is adapted through hybridization of the electronic states of the dopants with those of the host atoms. Such profound changes in the electronic structure also alter the *e-ph* interaction. Recall, for instance, the results of Chapter 7, where the *e-ph* interaction of 1-ML MgB₂ was strongly enhanced by means of hydrogen adatoms. Also, a strong influence of dopants like Cu in the vdW gap of TiSe₂ has been observed (as explained in the introduction). Magnetic dopants would in addition affect the spin texture and may thus promote the triplet superconducting state. The ultimate goal of this investigation is to realize *local control* of the system through *nanopatterning* with dopants.

A third route for tailoring the properties of the 2D TMDs is *strain*. Owing to recent advances, non-epitaxial 2D materials can be strained by bending the substrate [315]. Since it directly influences the structural properties, strain can significantly affect the CDW order. However, it is also likely to strongly enhance the *e-ph* coupling, similarly to what I reported for ML MgB₂ in Chapter 7 [200]. A closely related route is that of *pressure*, which mainly reduces the vdW gap. The latter has been observed to suppress CDWs and to boost superconductivity [316], although the mechanism is not well understood.

8.8 Conclusions

In conclusion, in this chapter I introduced the different quantum states at play in two-dimensional transition metal dichalcogenides (2D TMDs), resulting from structural, electronic and spin degrees of freedom. This richness in

quantum states makes them a very interesting system for multicomponent superconductivity.

An important property of the crystal structure is that an inversion center is absent in case of an odd number of monolayers, and present otherwise. Due to the heavy mass of the transition metal, TMDs host strong spin-orbit interaction. The combination of this spin-orbit coupling with the lack of an inversion center, leads to a splitting of the electronic bands. By calculating the spin expectation values from the *ab initio* spinor wave functions I demonstrated that in this case the spins are polarized in the out-of-plane direction. Moreover, they are opposite for the two split bands, and they depend on the electronic valley, as a result of time-reversal symmetry. As such, this effect is known as spin-valley locking and the resulting state as the Ising state. Because of the influence of the spin texture on superconducting coupling, the Ising state can lead to mixed singlet-triplet pairing and, thus, to unconventional superconductivity.

A calculation of the phonons and the electron-phonon interaction of the 2D TMDs using density functional perturbation theory (DFPT) revealed potentially very strong superconductivity. However, I showed here that the obtained values give a serious overestimation compared with the experimental values. This discrepancy can be solved by lowering the electronic smearing in the DFPT calculations, which resolves an instability of the longitudinal acoustic phonon mode, in the case of monolayer TaS₂. Such an instability, resulting from strong electron-phonon interaction coupling nested Fermi sheets, is called a charge density wave (CDW). The crystal reconstruction following the eigendisplacements of the CDW mode can be used to correct the electron-phonon interaction at the base of the superconducting state.

All of these quantum states are closely related because they originate from the same degrees of freedom (structural, electronic and spin). Hence, their interplay is a subject of much current interest. A preliminary requirement to study this interplay is a complete *ab initio* description of the Ising and CDW states, as established in this chapter. Because of the importance of the atomic-scale interactions in establishing these states, they are prone to be tailored on the nanoscale, by means of, e.g., gating, doping and strain.

Chapter 9

Summary and outlook

9.1 Summary

Recent years have seen important breakthroughs in superconductivity research, as discussed in Chapter 1. In 2001 a layered material, magnesium diboride (MgB_2), was discovered to host two distinctly different superconducting condensates. The first, strongest condensate originates from the in-plane boron electron states (the σ condensate), the other from the out-of-plane boron states (the π condensate). Therefore, bulk MgB_2 is a four-band, two-gap superconductor. More recently, efforts have been made to reduce superconducting systems spatially in one or more dimensions. Contrary to all expectations – based on limitations on order in low-dimensional systems – superconductivity was realized down to a single monolayer in various systems, ranging from epitaxial monolayers of elemental metals to (doped or gated) atomic sheets of the graphene family.

The quantum confinement in such 2D materials leads to profound changes in the electronic and vibrational properties. For instance, confinement can lead to different subbands at the Fermi level, and is therefore directly linked to multiband superconductivity. Thus, there is a growing interest in the influence of multiple degrees of freedom on the superconducting state – such as multiple bands, spin degrees of freedom, but also different interactions competing with the superconducting state. In general this emergent behavior can be referred to as *multicomponent superconductivity*.

In this thesis it was studied how multicomponent superconductivity behaves in materials ranging from *bulk*-sized to *atomically thin*. For this purpose an appropriate *ab initio framework* was developed here, starting from the basic laws of quantum mechanics without further assumptions. The *ab initio* framework established and employed in this thesis consists of two distinct steps, namely (i) calculations of the *normal-state* properties and (ii) calculations of the *superconducting state* based on quantum-field theory. The first step consists of a full description of the electronic and vibrational properties of the crystal, based on *density functional theory* (DFT). As reviewed in Chapter 2, DFT is based on the existence of a universal energy functional of the electronic density, of which the minimum provides the ground state density (*Hohenberg-Kohn theorems*). In practice, the system of interacting electrons is mapped to an effective system of non-interacting electrons moving in an effective potential, leading to the *Kohn-Sham equations*.

How one includes vibrations in the *ab initio* description was shown in Chapter 3, by taking them into account as perturbations, resulting in a framework called *density functional perturbation theory* (DFPT). Here, a lot of emphasis was put on how the vibrational properties of two-dimensional materials differ from their three-dimensional counterparts, e.g., the emergence of a flexural mode. It was shown that from DFPT the electron-phonon interaction can also be obtained, as matrix elements of the perturbed Kohn-Sham potential. While the normal-state properties – structural, electronic, vibrational and electron-phonon coupling properties – can be obtained from DF(P)T, for the description of the superconducting state an adequate quantum-field theory is employed. This theory is called *Eliashberg theory*, and can be combined with the *ab initio* calculated electron-phonon interaction. In this thesis, the momentum-dependent (i.e., anisotropic) Eliashberg equations are solved, where the anisotropy of the superconducting gap is taken into account to characterize the possible multigap nature of superconductivity.

The first application of this *ab initio* description, presented in Chapter 4, was aimed at clarifying the anomalous behavior of the multiband superconductor *osmium diboride* (OsB_2), with a superconducting gap spectrum and behavior in applied magnetic field that were not well understood. From DFT calculations OsB_2 was found to be a three-band material, harboring two similar quasi-ellipsoidal osmium-derived Fermi sheets and a third anisotropic sheet

with mixed osmium-boron character. I demonstrated that this calculated electronic structure can be validated by means of quantum oscillations, specifically *Shubnikov-de Haas oscillations*. By solving the anisotropic Eliashberg equations, a *single, anisotropic gap* was obtained. The apparent discrepancy with the two-gap fit of the experimental superfluid density evolution with temperature (data of Ref. 222) was elucidated by calculating the superfluid density from the gap spectrum. This yielded the correct convex profile previously exclusively attributed to the two-gap nature, but due to anisotropy of the superconducting gap here. This provides a clear and important caveat for future identifications of multigap superconductors based on superfluid density measurements. It is advisable to supplement these measurements by more direct measurements of the superconducting gap (e.g., using angle-resolved photoemission spectroscopy) and by calculations as performed here. To characterize the behavior of the superconducting state in OsB₂ in applied magnetic field, I calculated the superconducting length scales from its electronic properties using *Ginzburg-Landau relations*. The combination of high Fermi velocities and a limited T_c leads to a very low Ginzburg-Landau parameter in OsB₂, and thus to *type-I behavior* – a very rare property among compound superconductors.

As mentioned above, multicomponent superconductivity can also originate from interactions competing with the superconducting state, for instance, mediated by *spin fluctuations*, i.e., magnetic excitations in materials without long-range magnetic order. A new *ab initio* approach was developed in Chapter 5 to treat lattice vibrations and *ferromagnetic spin fluctuations* (FSFs) on the same footing, within Eliashberg theory. This approach employs the susceptibility to FSFs within the *random phase approximation*, calculated from the *ab initio* band structure and Stoner parameter. The latter is obtained from the band splitting resulting from applied magnetic moments according to *Stoner theory*. Spin-singlet and spin-triplet superconductivity can be treated in a similar way, only in the former the coupling to FSFs is repulsive and in the latter attractive. This novel method was used to study a recently discovered iron-based superconductor, iron tetraboride (FeB₄), in particular to elucidate its lower than expected critical temperature (T_c) [244]. I obtained that FeB₄ has a strong tendency for FSFs, as a result of two nested ellipsoidal Fermi sheets. By solving the anisotropic Eliashberg equations, it

was revealed that the FSFs in FeB_4 reduce T_c by more than an order of magnitude (yielding a value in excellent agreement with the experiment), while not qualitatively changing the anisotropic single-gap spectrum.

In Chapter 6, the formation and evolution of multigap superconductivity in the atomically thin limit was studied, by solving the Eliashberg equations with *ab initio* input. The study was specifically focussed on atomically thin MgB_2 , in view of its bulk two-gap superconductivity. In the atomically thin limit an *emerging surface band*, originating from the magnesium surface, hosts a third gap, in addition to the bulk-like σ and π gaps. In monolayer MgB_2 , the three gaps are very distinct, even at temperatures close to T_c . This calculation thus reveals monolayer MgB_2 as the first known purely *three-gap superconductor*, moreover with a relatively high T_c of 20 K. Here, it needs to be stressed that taking into account multigap effects by solving the fully anisotropic Eliashberg equations is crucial, since the T_c thus obtained is twice that of the isotropic approximation. Moreover, the three gaps translate to three very distinct peaks in the superconducting tunneling spectrum. The gap spectrum was found to change profoundly with every monolayer added to the structure, due to *increased hybridization* between the condensates. This property can be exploited in nano-sized junctions between different superconducting spectra, relying simply on local thickness control of MgB_2 . The theoretical results were subsequently compared to angle-resolved photoemission spectroscopy (ARPES), where the surface band of six-monolayer MgB_2 was indeed observed to host a new superconducting gap in quantitatively good agreement with the theoretical prediction.

Several pathways to *enhance* superconductivity in the monolayer limit were explored in Chapter 7, focussing again on MgB_2 . First, it was found that applying *tensile biaxial strain* leads to significant *phonon softening*, accompanied by strongly enhanced electron-phonon coupling according to Eliashberg theory. By solving the anisotropic Eliashberg calculations it was found that with merely 4–5% tensile strain, T_c is *boosted beyond 50 K*, profiting from the intrinsic enhancement due to the *preservation of three-gap superconductivity* in the strained monolayer. The second route that was explored to enhance the superconductivity is that of *adatoms*, specifically the omnipresent element hydrogen. Under the influence of adatom-host hybrid electron states with a strong coupling to phonons the T_c was found to double at least with

respect to that of pure monolayer MgB_2 , and is boosted further with strain. Using an isotropic approximation to the Eliashberg theory, a T_c above 50 K was attained already at 3% tensile strain, and is expected to increase further when taking into account multiband effects. Both pathways explored in this chapter unequivocally prove the potential of enhancing superconductivity in atomically thin materials using nanoscale manipulations.

In Chapter 8, the study of multicomponent superconductivity in atomically thin materials was extended to the *transition metal dichalcogenides* (TMDs). They display several *novel quantum states* coexisting with superconductivity, as a result of structural, electronic and spin degrees of freedom. The calculation of the electron-phonon interaction within DFPT proved that phonons alone do not suffice to describe the superconducting state in TMDs, in comparison to available experimental data. In particular, the calculated T_c is strongly overestimated. Thus, this analysis proves that the novel quantum states coexisting with superconductivity need to be taken into account. To that end, an *ab initio* description of these states was developed here. Firstly, *spin textures* originating from *strong spin-orbit coupling* are described by a calculation of the spin expectation values from the *ab initio* spinor wave functions. It was shown that this yields an accurate description of the *Ising state* – characterized by spin-valley locking – which can lie at the base of topological and unconventional superconductivity in atomically thin TMDs. Secondly, it was shown that DFPT calculations are able to describe the appearance of structural instabilities in TMDs, called *charge density waves* (CDW). To this end, special care is to be taken of resolving small energy differences (by means of a lowered electronic smearing). I demonstrated that based on the eigendisplacements of the CDW instability the low-temperature *crystal reconstruction* can be performed. The reconstructed unit cell can subsequently be used to study the interplay between the superconducting and CDW state. Finally, a roadmap was provided to study the interplay between superconductivity and the novel quantum states in TMDs in general, based on the established *ab initio* description, able to take into account nanoscale tailoring by means of gating, doping and strain.

9.2 Outlook

The research field of multicomponent superconductivity is rapidly progressing. So, in spite of the effort invested in this thesis to provide a general framework to treat multicomponent superconductivity, applied to several cases of current interest, the investigation is not completed. There are several routes to continue the research initiated in this thesis.

A first route is to include *electronic interactions beyond the generalized gradient approximation* to DFT. For example, the *van der Waals correlations* between different monolayers in certain materials – such as TMDs – can be included in DFT owing to recent advances [317, 318]. Some interactions may even go beyond the DFT description, for instance, the strong correlations indicated by the anomalous Fermi surface of iron selenide (cf. Appendix B). These can be treated using dynamical mean-field theory. Many-body descriptions of the electronic structure may also lead to an improved accuracy. One such description, albeit currently computationally restrictive, is provided by the GW approach (cf. Sec. 2.4.3). Another improvement that can be made is in the description of the *electron-electron interaction* within the Cooper-pair. In the approach to Eliashberg theory employed in the present thesis this was approximated by the isotropic Morel-Anderson pseudopotential (cf. Sec. 3.5.4). Owing to recent advances in the field, *ab initio* calculations of the full, anisotropic interaction kernel based on the random phase approximation have become feasible [84]. This approach is still to be introduced into the UppSC code.

Chapter 5 has provided a new and accurate framework to study superconductivity under the influence of both lattice vibrations and spin fluctuations. The possibility of triplet superconducting pairing in iron tetraboride was investigated, with the result that it is entirely absent. However, using the new framework possible triplet pairing in other material classes with a competing ferromagnetic phase can be explored.

The calculations of Chapters 6–7 were focussed on multigap superconductivity in atomically thin magnesium diboride, yielding concrete pathways to enhance superconductivity in the ultrathin limit by means of biaxial strain and adatoms. These can be explored further in other material classes, e.g., in materials of the graphene family and in MXenes. Other pathways that

can be additionally explored are *uniaxial strain* – i.e., strain applied along one of both in-plane crystal directions – and other geometries such as *one-dimensional nanoribbons*. In addition, for hydrogen-doped monolayer MgB_2 it would be interesting to investigate *nuclear quantum effects* and *phonon anharmonicities* due to hydrogen, as explained in Sec. 3.5.9.

In Chapter 8 of this thesis, a proper *ab initio* description of the novel quantum states coexisting with superconductivity in 2D TMDs (the Ising and CDW states) was developed. Future work will consist of characterizing the behavior of these states further, for different TMD materials, and under the influence of several tailoring methods (strain, doping and gating). The superconducting behavior resulting from the interplay with these states will subsequently be explored by constructing an extended Eliashberg framework, able, for example, to describe Ising superconductivity.

Finally, some prototype ideas have been introduced in this thesis that can be developed into *devices based on atomically thin superconductors*, e.g., the superconducting junction by local thickness control described in Chapter 6. In order to characterize the operation of such devices theoretically, the *ab initio* results presented here can be used as input for Ginzburg-Landau and Bogoliubov-de Gennes simulations describing a larger spatial scale. Such *multi-scale approach* is ideally suited for *in silico design* of new devices.

Chapter 10

Samenvatting en toekomstperspectieven

10.1 Samenvatting

In recente jaren zijn er enkele belangrijke doorbraken in het onderzoek naar supergeleiding verwezenlijkt, zoals besproken in Hoofdstuk 1. In 2001 werd ontdekt dat een gelaagd materiaal, magnesium diboride (MgB_2), twee verschillende supergeleidende condensaten bevat. Het eerste en sterkste condensaat is afkomstig van de elektronische toestanden van boor die in het kristalvlak liggen (het σ -condensaat) en het tweede condensaat van de toestanden van boor die loodrecht op het kristalvlak staan (het π -condensaat). Bulk MgB_2 is dus een vier-band supergeleider met twee verschillende supergeleidende bandkloven. Recenter, werden er succesvolle pogingen ondernomen om supergeleidende materialen ruimtelijk in te perken in één of meerdere dimensies. Tegen alle verwachtingen in – gebaseerd op beperkingen om orde te creëren in laag-dimensionale systemen – werd supergeleiding tot in een enkele monolaag gerealiseerd en dit in uiteenlopende systemen, gaande van epitaxiaal gegroeide monolagen van elementaire metalen tot atomaire monolagen van de grafeenfamilie (gedoteerd of in een aangelegd elektrisch veld).

De kwantuminperking van zulke 2D materialen leidt tot diepgaande veranderingen in de elektronische en vibrationele eigenschappen. Bijvoorbeeld kunnen er verschillende subbanden bij het Fermiverniveau ontstaan, wat direct

gerelateerd is aan multiband supergeleiding. Daarom neemt de interesse voor de invloed van een veelheid aan vrijheidsgraden in de supergeleidende toestand dus alsmaar toe. Deze vrijheidsgraden kunnen niet enkel meerdere banden zijn, maar ook spinvrijheidsgraden en interacties die met de supergeleidende toestand concurreren. In het algemeen worden deze opkomende fenomenen in deze thesis aangeduid als *multicomponent supergeleiding*.

In deze thesis werden de eigenschappen van multicomponent supergeleiding bestudeerd in materialen die variëren van *bulk* tot *atomair dun*. Hiervoor werd een adequaat *ab initio* raamwerk ontwikkeld, dat vertrekt van de basiswetten van de kwantummechanica, zonder verdere aannames. Het *ab initio* raamwerk ontwikkeld en toegepast in deze thesis omvat twee stappen, namelijk (i) het berekenen van de eigenschappen van de *normale (niet-supergeleidende) toestand* en (ii) het berekenen van de supergeleidende toestand door middel van kwantumveldentheorie. De eerste stap bestaat uit een volledige beschrijving van de elektronische en vibrationele eigenschappen van het kristal, gebruik makend van *dichtheidsfunctionaaltheorie* (DFT). Zoals uiteengezet in Hoofdstuk 2 is DFT gebaseerd op het bestaan van een universele energiefunctonaal van de elektronische dichtheid, waarvan het minimum met de grondtoestandsdichtheid overeenkomt (de *Hohenberg-Kohn theorema's*). In de praktijk wordt het systeem van interagerende elektronen gemapt op een effectief systeem van niet-interagerende elektronen bewegend in een effectieve potentiaal, wat leidt tot de *Kohn-Sham vergelijkingen*.

Hoe roostertrillingen aan de *ab initio* beschrijving toe te voegen werd uitgelegd in Hoofdstuk 3, namelijk door hen als perturbaties te beschouwen, resulterend in *dichtheidsfunctionaalperturbatietheorie* (DFPT). Hier werd er bijzondere aandacht gewijd aan hoe de vibrationele eigenschappen van tweedimensionale materialen verschillen van die van driedimensionale materialen, bijvoorbeeld, het tevoorschijn komen van een 'flexural mode'. Er werd aangetoond dat vanuit DFPT de elektron-fonon interactie kan worden bekomen als matrixelementen van de geperturbeerde Kohn-Sham potentiaal. Terwijl de eigenschappen van de normale toestand – structureel, elektronisch en vibrationeel – dus door middel van DF(P)T berekend kunnen worden, wordt voor de beschrijving van de supergeleidende toestand een aangepaste kwantumveldentheorie gebruikt. Deze theorie, Eliashbergtheorie genaamd, kan

gecombineerd worden met de elektron-fonon interactie, bekomen uit *ab initio* berekeningen. In deze thesis worden de impuls-afhankelijke (anisotrope) Eliashbergvergelijkingen opgelost, waarbij de anisotropie van de supergeleidende bandkloof in rekening wordt gebracht om het mogelijke multicomponent karakter van de supergeleiding te ontwaren.

De eerste toepassing van deze *ab initio* beschrijving werd voorgesteld in Hoofdstuk 4 en was gericht op het verhelderen van het abnormale gedrag van de multiband supergeleider *osmium diboride* (OsB_2), waarvan het supergeleidend spectrum en gedrag in aangelegd magnetisch veld helemaal niet goed begrepen waren. Vanuit de DFT berekeningen werd gevonden dat OsB_2 een drie-band materiaal is, bestaande uit twee gelijkaardige quasi-ellipsoïdale Fermi oppervlakken afkomstig van osmium en een derde anisotroop oppervlak met gemengd osmium- en boorkarakter. Ik heb aangetoond dat de berekende elektronische structuur kan worden gevalideerd door middel van kwantumoscillaties, specifiek *Shubnikov-de Haas oscillaties*. Met behulp van de anisotrope Eliashbergvergelijkingen werd een *enkele, anisotrope bandkloof* gevonden. Ik heb vervolgens de schijnbare discrepantie met de dubbele-kloof fit van de experimentele superfluïde dichtheid als functie van de temperatuur (data uit Ref. 222) opgehelderd door de superfluïde dichtheid te berekenen uit het theoretische spectrum. Dit leverde het correcte, convexe profiel op dat voorheen exclusief aan een dubbele-kloof karakter werd toegewezen, maar dat hier voortkomt uit de anisotropie van de supergeleidende bandkloof. Deze analyse levert dus een duidelijke en belangrijke waarschuwing aan voor toekomstige identificaties van supergeleiders met meerdere bandkloven, gebaseerd op metingen van de superfluïde dichtheid. Mijn advies luidt dus om deze metingen steeds aan te vullen met meer directe metingen van de supergeleidende bandkloof (bijvoorbeeld, met behulp van ‘angle-resolved photoemission’ spectroscopie (ARPES)) en met berekeningen analoog aan wat hier werd gedaan. Om het gedrag van de supergeleidende toestand van OsB_2 in aangelegd magnetisch veld te karakteriseren heb ik de supergeleidende lengteschalen berekend vanuit de elektronische eigenschappen met behulp van *Ginzburg-Landau uitdrukkingen*. De combinatie van hoge Fermisnelheden en een beperkte T_c leidt tot een zeer lage Ginzburg-Landau parameter en dus tot *type-I gedrag* – een zeer zeldzame eigenschap voor een samengestelde supergeleidende stof als OsB_2 .

Zoals eerder gesteld, kan multicomponent supergeleiding ook voortkomen uit interacties die met de supergeleidende toestand concurreren, bijvoorbeeld overgebracht door *magnetische spinfluctuaties*, d.w.z. magnetische aangeslagen toestanden in materialen zonder magnetische orde met lange dracht. Hiertoe werd een nieuwe *ab initio* aanpak ontwikkeld in Hoofdstuk 5, waarmee roostertrillingen op gelijke voet in rekening gebracht kunnen worden met *ferromagnetische spinfluctuaties* (FSFs) binnen de Eliashbergtheorie. Deze aanpak maakt gebruik van de susceptibiliteit voor FSFs binnen de ‘*random phase approximation*’ (RPA), berekend met de *ab initio* bandenstructuur en met de Stonerparameter. Die laatste wordt bekomen uit de bandensplitsing onder invloed van aangelegde magnetische momenten volgens *Stoner theorie*. Spin-singlet en spin-triplet supergeleiding kunnen op eenzelfde wijze behandeld worden, enkel is voor de eerste de koppeling met FSFs afstotend en voor de tweede aantrekkend. Deze nieuwe methode werd toegepast om een recent ontdekte ijzerhoudende supergeleider, namelijk ijzer tetraboride (FeB_4), te bestuderen, in het bijzonder om te verklaren waarom de kritische temperatuur (T_c) veel lager ligt dan verwacht [244]. Ik vond dat FeB_4 een sterke neiging vertoont tot FSFs, ten gevolge van twee geneste Fermioppervlakken. Door de anisotrope Eliashbergvergelijkingen op te lossen, toonde ik dat FSFs de T_c van FeB_4 met méér dan een orde van grootte verlagen (wat een waarde oplevert die zeer goed overeenstemt met het experiment), terwijl het anisotrope spectrum met een enkele bandkloof kwalitatief niet verandert.

In Hoofdstuk 6 werd de vorming en de evolutie van supergeleiding met meerdere bandkloven in de atomair dunne limiet onderzocht, op basis van het oplossen van de Eliashbergvergelijkingen met *ab initio* input. Deze studie focuste specifiek op atomair dun MgB_2 omwille van de dubbele-kloof supergeleiding in de bulk. In de atomair dunne limiet werd gevonden dat een *oppervlakteband tevoorschijn komt*, die van het magnesiumvlak stamt. Deze levert een derde bandkloof op, bovenop de σ - en π -bandkloven die ook in de bulk voorkomen. In monolaag MgB_2 zijn de bandkloven duidelijk gescheiden, zelfs bij temperaturen dichtbij T_c . Deze berekening onthult dus dat MgB_2 de eerste als dusdanig gekende supergeleider met een *pure drievoudige bandkloof* is en bovendien een relatief hoge T_c van 20 K heeft. Het moet benadrukt worden dat het in rekening brengen van de meerdere bandkloven – door de volledig anisotrope Eliashbergvergelijkingen op te lossen – cruciaal is, aangezien de T_c die zo gevonden wordt het dubbele is van wat gevonden

wordt binnen de isotrope benadering. De drie bandkloven leiden bovendien tot drie verschillende pieken in het supergeleidende tunnelspectrum. Er werd ook gevonden dat het supergeleidende spectrum drastisch verandert met elke monolaag die aan de structuur toegevoegd wordt, door een *toenemende mate van hybridisatie* tussen de condensaten. Deze eigenschap kan toegepast worden in nanoscopische juncties van verschillende supergeleidende spectra, alle gemaakt van MgB_2 met lokaal gevarieerde dikte. De theoretische resultaten werden vervolgens vergeleken met ARPES metingen. Er werd waargenomen dat de oppervlakteband in MgB_2 met een dikte van zes lagen inderdaad een nieuwe supergeleidende bandkloof voorbrengt, met een kwantitatief goede overeenkomst met de theoretische voorspelling.

In Hoofdstuk 7 worden verschillende paden verkend om supergeleiding in de monolaaglimiet te versterken, waarbij weer gefocust wordt op MgB_2 . Ten eerste werd er gevonden dat het *biaxiaal uitrekken* van het rooster tot een aanzienlijke verzachting van de fononen leidt, gepaard met een sterke toename van de elektron-fononkoppeling volgens de Eliashbergtheorie. Bij het oplossen van de anisotrope Eliashbergvergelijkingen werd gevonden dat slechts 4 – 5% uitrekking nodig is om de T_c te *verhogen tot boven 50 K*. Hierbij wordt ook voordeel gehaald uit de intrinsieke verhoging door koppeling tussen de condensaten, doordat de *drievoudige bandkloof behouden* blijft voor de uitgerekte monolaag. Het tweede pad om de supergeleiding te versterken dat gevolgd werd is dat van de adatomen, specifiek het alomtegenwoordige element waterstof. Er werden hybride elektronische toestanden – gevormd tussen de adatomen en de andere atomen – gevonden, die sterk koppelen met de fononen. Hierdoor verdubbelt de T_c op zijn minst vergeleken met een pure MgB_2 monolaag, wat nog versterkt wordt door uitrekking. Binnen een isotrope benadering van de Eliashbergtheorie werd een T_c boven 50 K gevonden bij slechts 3% uitrekking. Het wordt verwacht dat deze nog verder stijgt wanneer de multibandeffecten volledig in rekening gebracht worden. Beide paden die onderzocht werden in dit hoofdstuk demonstreren dus op ondubbelzinnige wijze het potentieel om supergeleiding te versterken in atomair dunne materialen met behulp van nanoscopische ingrepen.

In Hoofdstuk 8 werd de studie van multicomponent supergeleiding in atomair dunne materialen uitgebreid naar de *transitiemetaaldichalcogeniden* (TMDs).

Deze vertonen verschillende *nieuwe kwantumtoestanden* die samen met supergeleiding optreden, en die voortkomen uit structurele, elektronische en spinvrijheidsgraden. De berekening van de elektron-fonon interactie met behulp van DFPT toonde aan dat enkel fonons niet voldoende zijn om de supergeleidende toestand in TMDs correct te beschrijven, wanneer we vergelijken met beschikbare experimentele data. Meer bepaald is de berekende T_c sterk overschat. Deze analyse toont dus aan dat de nieuwe kwantumtoestanden die samen met de supergeleiding voorkomen ook in rekening gebracht moeten worden. Met dat doel werd hier een *ab initio* beschrijving van deze toestanden ontwikkeld. Ten eerste worden de *spintexturen* die ontstaan uit *sterke spin-baankoppeling* beschreven door de spinverwachtingswaarden te berekenen vanuit de *ab initio* spinor golf functies. Er werd getoond dat dit een accurate beschrijving van de *Isingtoestand* – gekarakteriseerd door ‘spin-valley locking’ – die aan de basis kan liggen van topologische en onconventionele supergeleiding in atomair dunne TMDs. Ten tweede werd aangetoond dat DFPT-berekeningen het verschijnen van structurele instabiliteiten in TMDs, die ‘*charge density waves*’ (CDWs) worden genoemd, kunnen beschrijven. Hiervoor moet speciale aandacht besteed worden om de kleine energiever verschillen waar te nemen (door middel van een verlaagde elektronische ‘smearing’). Ik heb gedemonstreerd dat de *reconstructie van het kristal* bij lage temperaturen uitgevoerd kan worden door gebruik te maken van de eigenverplaatsingen van de CDW-instabiliteit. De gereconstrueerde eenheidscel kan vervolgens gebruikt worden om de wisselwerking tussen de supergeleidende en de CDW-toestand te bestuderen. Tot slot werd een stappenplan gegeven om de wisselwerking tussen supergeleiding en de nieuwe kwantumtoestanden in TMDs in het algemeen te onderzoeken met behulp van de hier ontwikkelde *ab initio* beschrijving. In dit kader kunnen ingrepen op de nanoschaal, door middel van een aangelegd elektrisch veld, van dotering en van deformatie, ook beschouwd worden.

10.2 Toekomstperspectieven

Het onderzoeksdomein van multicomponent supergeleiding kent een snelle ontwikkeling. Hoewel in deze thesis getracht werd om een algemeen kader te voorzien om multicomponent supergeleiding te bestuderen, en dit toe te

passen op verschillende actuele gevallen, is het onderzoek dus niet voltooid. Er zijn verschillende opties om verder te bouwen op het onderzoek dat in deze thesis werd aangevat.

Een eerste mogelijkheid is om *elektronische interacties voorbij de ‘generalized gradient’ benadering* in de DFT mee te nemen. Bijvoorbeeld kunnen *van der Waals correlaties* tussen de monolagen in bepaalde materialen – zoals TMDs – toegevoegd worden dankzij recente ontwikkelingen [317, 318]. Sommige interacties kunnen zelfs de DFT-beschrijving zelf overstijgen, bijvoorbeeld de sterke correlaties aangetoond door anomalieën in het Fermi-oppervlak van ijzerselenide (cf. Appendix B). Deze kunnen behandeld worden met de dynamische gemiddeld-veldtheorie. Veeldeeltjesbeschrijvingen van de elektronische structuur kunnen ook de nauwkeurigheid van de berekeningen verhogen. Eén van deze beschrijvingen is de GW-benadering (cf. Sec. 2.4.3), maar deze is wel computationeel zeer belastend. Ook de beschrijving van de *elektron-elektron interactie* in het Cooperpaar kan verder verfijnd worden. In de aanpak van de Eliashbergtheorie die in deze thesis gebruikt werd, was deze benaderd door de isotrope Morel-Anderson pseudopotentiaal (cf. Sec. 3.5.4). Dankzij recente ontwikkelingen in dit onderzoeksdomein, zijn *ab initio* berekeningen van de volledige, anisotrope interactiekernel binnen de RPA mogelijk geworden [84]. Deze uitbreiding moet nog wel aan de UppSC code toegevoegd worden.

In Hoofdstuk 5 werd een nieuw en accuraat kader ingevoerd om supergeleiding onder de invloed van zowel roostertrillingen als spinfluctuaties te bestuderen. De mogelijkheid tot spin-tripletsupergeleiding in ijzertetraboride werd onderzocht, met als resultaat dat deze geheel afwezig is. Niettegenstaande kan dit nieuwe kader aangewend worden om spin-tripletparing in andere materiaalclassen met een concurrerende ferromagnetische fase te exploreren.

De berekeningen van Hoofdstukken 6–7 waren gefocust op supergeleiding met meerdere bandkloven in atomair dun magnesium diboride, en hebben concrete methodes opgeleverd om supergeleiding in de ultradunne limiet te versterken door middel van biaxiale deformatie en adatomen. Deze paden kunnen verder verkend worden voor andere materiaalklassen, bijvoorbeeld in de grafeenfamilie en in de MXenes. Andere wegen die nog verder verkend kunnen worden zijn die van *uniaxiale deformatie*, d.w.z. deformatie langs één van beide kristalrichtingen – en die van andere geometrieën zoals *ééndimensionale*

nanolinten. Bovendien zou het interessant zijn om *kern-kwantumeffecten* en *fononanharmonieiteit* ten gevolge van waterstof te onderzoeken voor monolaag MgB_2 gedoteerd met waterstof, zoals uitgelegd in Sec. 3.5.9.

In Hoofdstuk 8 van deze thesis werd een aangepaste *ab initio* beschrijving ontwikkeld van nieuwe kwantumtoestanden die samen met supergeleiding voorkomen in 2D TMDs (de Ising- en CDW-toestanden). Toekomstig werk zal toegespitst op het verder karakteriseren van het gedrag van deze toestanden, voor verscheidene TMD materialen, al dan niet onder de invloed van nanoscopische ingrepen (deformatie, dotering en aangelegd elektrisch veld). Het supergeleidende gedrag dat voortkomt uit de wisselwerking met deze toestanden zal vervolgens onderzocht worden door een veralgemeend Eliashbergkader op te stellen dat bijvoorbeeld Isingsupergeleiding kan beschrijven.

Ten slotte werden enkele prototypes voorgesteld in deze thesis die ontwikkeld kunnen worden tot *apparaten die gebruik maken van atomair dunne supergeleiders*, bijvoorbeeld de supergeleidende juncties verkregen door lokale controle van de dikte van de films beschreven in Hoofdstuk 6. Om de werking van zulke apparaten te karakteriseren kunnen de *ab initio* resultaten die hier werden voorgesteld gebruikt worden als input voor Ginzburg-Landau en Bogoliubov-de Gennes simulaties, die een grotere ruimtelijke lengteschaal omvatten. Dergelijke *multi-schaal aanpak* is uiterst geschikt voor het *in silico ontwerpen* van nieuwe apparaten.

Appendix A

Computational details

A.1 Calculations of Chapter 4

The **density functional theory** (DFT) calculations in this chapter make use of the Perdew-Burke-Ernzerhof (PBE) functional, including spin-orbit interaction, implemented within a plane wave basis in the VASP code [172, 176]. Electron-ion interactions are treated using projector augmented wave (PAW) potentials, taking into account Os-5p⁶6s²5d⁶ and B-2s²2p¹ as valence electrons. The energy cutoff for the plane-wave basis is set to 500 eV, to achieve convergence of the total energy below 1 meV per atom. To obtain a very accurate description of the Fermi surface, also needed for accurate calculation of the Fermi velocities and electronic density of states per band, a very dense $40 \times 32 \times 24$ Γ -centered Monkhorst-Pack \mathbf{k} -point grid is used. For high-symmetry \mathbf{k} -points, we use the notational convention established in Ref. 319. The optimized crystal structure was obtained using a conjugate-gradient algorithm so that forces on each atom were below 1 meV/Å. A smearing of $\epsilon = 0.05$ eV was used in the numerical evaluation within the central difference approximation to $\left. \frac{\partial A}{\partial E} \right|_{E=E_F}$ of the cyclotron masses according to Eq. 4.5.

Density functional perturbation theory (DFPT) calculations were carried out within the framework of ABINIT [175], keeping the same valence electrons as in VASP, and also using the PBE functional. The crystal structure was optimized again in ABINIT, with no significant differences with the values reported in Table 4.1. The total number of perturbations due

to atomic displacements (in other words, the number of phonon branches) amounts to $3N = 18$. The summation to obtain the Eliashberg function was carried out over a $21 \times 15 \times 15$ \mathbf{k} -point grid and a $7 \times 5 \times 5$ \mathbf{q} -point grid.

The **Eliashberg calculations** were performed with the Uppsala Superconductivity code (UppSC). The anisotropic Eliashberg equations were solved self-consistently in Matsubara space, starting from the electron and phonon band structures and electron-phonon coupling obtained with DFPT. In this scheme, we iterated until convergence better than 10^{-3} on the relative gap values between each iteration step was reached. In all calculations, we employed standard $\mu^* = 0.215$ for the Coulomb pseudopotential, in order to match the experimental T_c . For the sums over Matsubara frequencies a cut-off energy of up to 0.7 eV was used (total of 2592 Matsubara frequencies). In order to find the superconducting gap-edge, the converged solutions were analytically continued to real frequencies with a Padé approximation procedure.

A.2 Calculations of Chapter 5

The **density functional theory** (DFT) calculations make use of the generalized gradient approximation (GGA), specifically of the Perdew-Burke-Ernzerhof (PBE) functional, implemented within a planewave basis in the ABINIT code [175]. Electron-ion interactions are treated using norm-conserving pseudopotentials [320], taking into account Fe-3d⁷4s¹ and B-2s²2p¹ as valence electrons. The energy cutoff for the plane-wave basis was set to 60 Ha, to achieve convergence of the total energy below 1 meV per atom. To obtain a very accurate description of the Fermi surface, a dense $25 \times 15 \times 15$ Γ -centered Monkhorst-Pack \mathbf{k} -point grid was used. The notational convention established in Ref. 319 is used to denote the high-symmetry \mathbf{k} -points. The optimized crystal structure was obtained using a conjugate-gradient algorithm so that forces on each atom were below 1 meV/Å.

The **density functional perturbation theory** (DFPT) calculations of the phonon dispersion and the electron-phonon coupling coefficients were also carried out using ABINIT. Here, a $25 \times 15 \times 15$ \mathbf{k} -point grid is employed for

the electronic wave vectors and a $5 \times 3 \times 3$ \mathbf{q} -point grid for the phonon wave vectors.

The numerical solution of the **extended Eliashberg equations** (5.6-5.7) along with an efficient calculation procedure of the coupling in equation (5.8) were implemented in the Uppsala Superconductivity Code (UppSC) [39]. Using UppSC, the coupled equations (5.6-5.7), supplemented by the electron and phonon band structure and the electron-phonon and electron-(para)magnon coupling, calculated by first principles, were solved self-consistently in Matsubara space within a strict convergence criterion of $\frac{x_n - x_{n-1}}{x_n} < 10^{-6}$ and with up to 1000 iteration cycles allowed. In all the calculations presented here we set $\mu^*(\omega_c) = 0.1$ for the Coulomb pseudopotential with a sufficient value of ω_c to ensure that the results are well converged.

A.3 Calculations of Chapter 6

The **density functional theory** (DFT) calculations make use of the Perdew-Burke-Ernzerhof (PBE) functional implemented within a plane wave basis in the ABINIT code [175]. Electron-ion interactions are treated using norm-conserving Vanderbilt pseudopotentials [321], taking into account Mg-2s²2p⁶3s² and B-2s²2p¹ as valence electrons. An energy cutoff of 60 Ha for the planewave basis was used, to achieve convergence of the total energy below 1 meV per atom. In order to simulate the atomically thin films, we used unit cells that include 25 Å of vacuum. A dense $22 \times 22 \times 1$ Γ -centered Monkhorst-Pack \mathbf{k} -point grid is used for an accurate description of the Fermi surfaces. The lattice parameters were obtained using a conjugate-gradient algorithm so that forces on each atom were minimized below 1 meV/Å.

In addition, the DFT calculations in Sec. 6.5 and 6.6 make use of the Perdew-Burke-Ernzerhof (PBE) functional implemented within a plane wave basis in the VASP code. Electron-ion interactions are treated using projector augmented wave (PAW) potentials, taking into account Mg-2p⁶3s² and B-2s²2p¹ as valence electrons. An energy cutoff of 450 eV for the planewave basis was used, to achieve convergence of the total energy below 1 meV per atom. To obtain a very accurate description of the Fermi surface, a very dense

$35 \times 35 \times 31$ Γ -centered Monkhorst-Pack \mathbf{k} -point grid is used for bulk MgB_2 , and a $35 \times 35 \times 1$ grid for the few-layer structures.

To calculate phonon dispersions and electron-phonon coupling, **density functional perturbation theory** (DFPT) calculations were carried out, also within the framework of ABINIT. The total number of perturbations due to atomic displacements to be treated (in other words, the number of phonon branches) amounts to $3 \cdot N_{\text{atoms}}$, ranging from 9 for a ML to 54 for 6 MLs. Thus, the phonon spectrum and electron-phonon coupling coefficients, matrix elements of the perturbative part of the Hamiltonian [242], are obtained. We carried out the DFPT calculations on a $22 \times 22 \times 1$ electronic \mathbf{k} -point grid and a $11 \times 11 \times 1$ \mathbf{q} -point grid as phonon wave vectors. Here, an energy cutoff of 60 Ha was used.

Subsequently, the **anisotropic Eliashberg equations**, supplemented by the electron and phonon band structure and the electron-phonon coupling, calculated by first principles, were solved self-consistently in Matsubara space and the converged solutions were then analytically continued to real frequencies. In order to ensure a good accuracy, a strict convergence criterion of $\frac{x_n - x_{n-1}}{x_n} < 10^{-6}$ was imposed and up to 1000 iteration cycles were allowed. In all the calculations presented here $\mu^*(\omega_c) = 0.13$ was set for the Coulomb pseudopotential, with a cut-off frequency $\omega_c > 0.5$ eV. It was checked that ω_c is sufficiently large and that results are well converged with this cut-off. The analytic continuation was performed numerically by employing the high-accuracy Padé scheme based on symbolic computation [39, 203] with a chosen precision of 250 decimal digits. After this procedure, the retarded momentum dependent Green's function, the tunneling spectra and the superconducting gap-edge were calculated.

A.4 Calculations of Chapter 7

The main computational details are identical to those of Sec. A.3. Strain was implemented by changing the in-plane lattice parameter with respect to the equilibrium value. For well-converged results denser \mathbf{k} -point and \mathbf{q} -point grids were found to be required, $40 \times 40 \times 1$ and $20 \times 20 \times 1$ respectively. The plane wave cutoff was also augmented to 65 Ha. For consistency, the

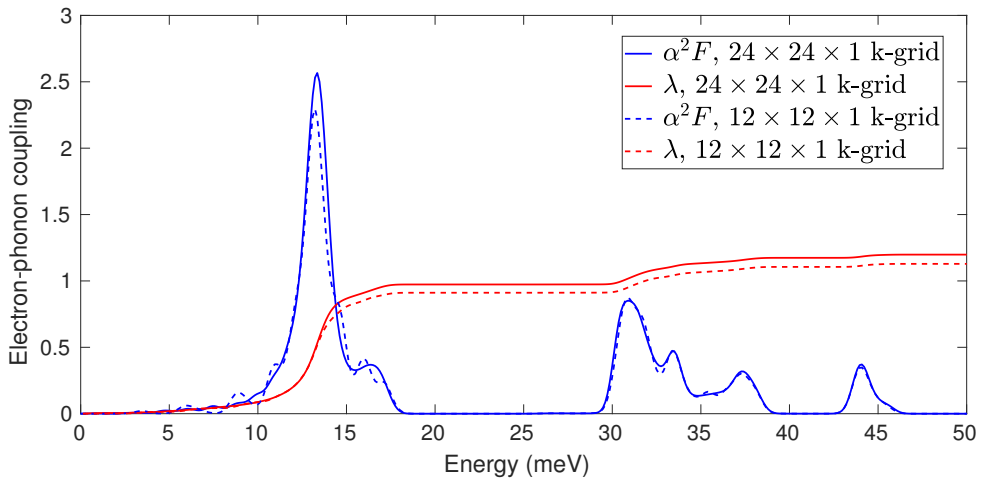


FIGURE A.1: *Eliashberg function ($\alpha^2 F$) and electron-phonon coupling constant (λ) of a monolayer TaS_2 , obtained using a $12 \times 12 \times 1$ q -point grid. The results obtained with a $12 \times 12 \times 1$ and a $24 \times 24 \times 1$ k -point grid are compared, showing a very good convergence with respect to the k -point grid.*

Anderson-Morel pseudopotential describing Cooper pair breaking was chosen as $\mu^*(\omega_c) = 0.13$, the same as for pure atomically thin MgB_2 in Sec. A.3.

A.5 Calculations of Chapter 8

The **density functional theory** (DFT) calculations make use of the Perdew-Burke-Ernzerhof (PBE) functional implemented within a plane wave basis in the ABINIT code [175]. Electron-ion interactions are treated using fully relativistic Goedecker pseudopotentials, taking into account spin-orbit coupling [322, 323]. Here, Nb-4s²4p⁶4d⁴5s¹, S-3s²3p⁴, Se-4s²4p⁴ and Ta-5d³6s² states were included as valence electrons. An energy cutoff of 50 Ha for the planewave basis was used, to achieve convergence of the total energy below 1 meV per atom. In order to simulate the atomically thin films, we used unit cells that include 25 Å of vacuum. A $24 \times 24 \times 1$ Γ -centered Monkhorst-Pack k -point grid was used for the 2D structures and a $16 \times 16 \times 6$ k -point grid for the bulk structures, to achieve an accurate description of the Fermi surfaces. The lattice parameters were obtained using a conjugate-gradient algorithm so that forces on each atom were minimized below 1 meV/Å.

The **density functional perturbation theory** (DFPT) calculations of the phonon dispersion and the electron-phonon coupling coefficients were also carried out using ABINIT. Here, a $24 \times 24 \times 1$ **k**-point grid is employed for the electronic wave vectors and a $12 \times 12 \times 1$ **q**-point grid for the phonon wave vectors in case of the 2D structures. For the bulk structures, a $16 \times 16 \times 6$ **k**-point grid and a $8 \times 8 \times 3$ **q**-point grid were used. To ensure a good convergence of the results with respect to the **k**-point grid a comparison was made between a $24 \times 24 \times 1$ and a $12 \times 12 \times 1$ grid. The results are shown in Fig. A.1, proving that the Eliashberg function and the electron-phonon coupling constant are very well converged.

Appendix B

Shubnikov-de Haas analysis of bulk iron selenide

A Shubnikov-de Haas (SdH) analysis of bulk FeSe is carried out, to investigate its electronic structure. A van der Waals functional is used for an accurate description of the distance between subsequent layers, the so-called vdW gap. The specific functional employed here is the optPBE vdW functional [317, 318], as implemented in VASP [172, 176].

Fig. B.1 shows the crystal structure, Fermi surface, band structure and DOS. There Fermi surface consists of five sheets, three hole pockets around Γ and two electron pockets around M. When a magnetic field is applied in the perpendicular direction to the crystal planes, as indicated in Fig. B.1(b), the maximal areas occur at half of the BZ's z-axis. The corresponding calculated frequencies and cyclotron masses are listed in Table B.1, and compared to available experimental data [224]. The conclusion is that the theoretical results overestimate the cross-sectional areas by more than an order of magnitude in case of the hole pockets and by a factor 4 – 5 in case of the electron pockets. This discrepancy is very likely related to the iron-d character of the bands crossing the Fermi level, as shown in Fig. B.1(c). In addition to the SdH study of OsB₂ in Chapter 4 – where the electronic structure very well described by DFT – this analysis of FeSe proves that SdH oscillations are a powerful tool to probe the Fermi surface, to (dis)prove the DFT prediction.

Sheet	A	B	C	D	E
F_{th} (kT)	0.571	1.282	2.910	3.278	2.836
F_{exp} (kT)	/	0.06	0.20	0.57	0.68
$A_{\text{th}}(E_{\text{F}})$ (% BZ)	1.88	4.23	9.59	10.80	9.35
$A_{\text{exp}}(E_{\text{F}})$ (% BZ)	/	0.20	0.69	2.00	2.30
$m_{\text{c}}/m_{\text{e}}$	0.52	1.66	1.28	1.52	0.87
$m_{\text{c}}^*/m_{\text{e}}$	/	1.9	4.3	7.2	4.2

TABLE B.1: *The theoretical and experimental [224] cyclotron masses m_{c} and m_{c}^* (in units of the free electron mass m_{e}), frequencies F (kT) of the Shubnikov-de Haas oscillations in bulk FeSe, and the corresponding areas as a percentage of the whole Brillouin zone (BZ) plane. Slashes indicate that the corresponding signals were entirely absent in the experiment. The sheets are labeled as in Fig. B.1.*

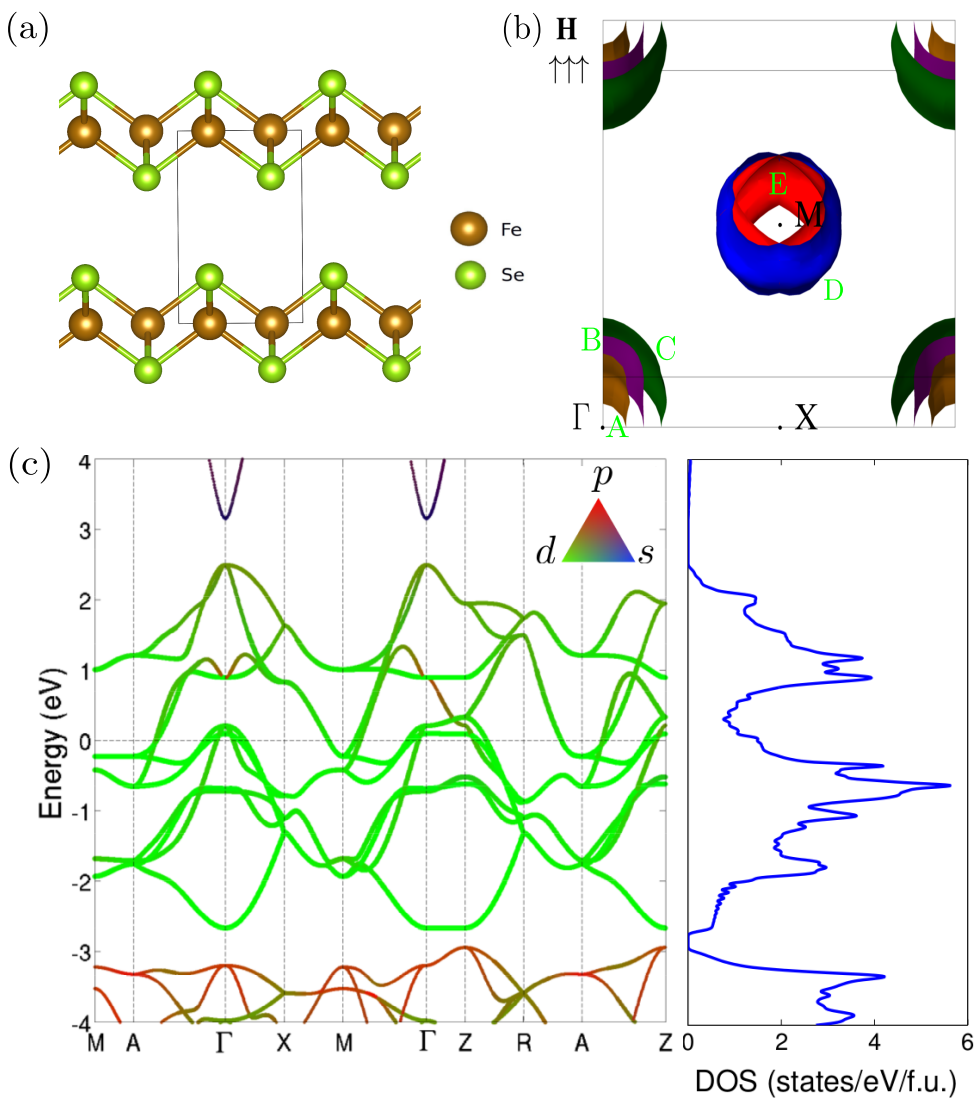


FIGURE B.1: (a) The crystal structure of bulk FeSe. The grey box depicts the unit cell. (b) The Fermi surface of bulk FeSe, calculated using the *vdW*-type *optPBE* functional. There are 3 hole-like pockets around Γ and 2 electron-like pockets around M . From Γ to M the sheets are labeled A to E. (c) The corresponding electronic band structure and DOS. In the band structure the electronic character is indicated in colors, as defined by the color triangle. The contributions of the atomic types are indicated using the line thickness, where thick lines indicate iron character and thin lines boron character.

Appendix C

Relation between susceptibility and nesting in metals

Here, we prove Eq. 5.10, highlighting also the approximations that are made in this framework. The general form of the susceptibility in a crystal within the RPA is [255]

$$\chi_{\mathbf{G},\mathbf{G}'}^0(\mathbf{q},\omega) = \sum_{\mathbf{k}ij} (f(E_{\mathbf{k}+\mathbf{q},j}) - f(E_{\mathbf{k},i})) \times \frac{\langle \mathbf{k},i | e^{-i(\mathbf{q}+\mathbf{G})\cdot\mathbf{r}} | \mathbf{k}+\mathbf{q},j \rangle \langle \mathbf{k}+\mathbf{q},j | e^{i(\mathbf{q}+\mathbf{G}')\cdot\mathbf{r}} | \mathbf{k},i \rangle}{E_{\mathbf{k}+\mathbf{q},j} - E_{\mathbf{k},i} - \omega - i\eta}, \quad (\text{C.1})$$

where $f_{\mathbf{k},i}$ is the Fermi-Dirac distribution for a band i at wave vector \mathbf{k} , \mathbf{G} and \mathbf{G}' are reciprocal lattice vectors and η is an infinitesimally small number.

The dependence of the susceptibility on the reciprocal lattice vectors is a result of crystal symmetry. Often the approximation is made of a **macroscopic susceptibility** $\chi_{\text{mac}}(\mathbf{q},\omega) = \chi_{0,0}(\mathbf{q},\omega)$ (and corresponding macroscopic dielectric function $\epsilon_{\text{mac}}(\mathbf{q},\omega) = \epsilon_{0,0}(\mathbf{q},\omega)$). It means that local effects are ignored, as only the long range ($|\mathbf{G}| \rightarrow 0$ in reciprocal space) is taken into account.

Furthermore, within the **constant matrix element approximation** (CMEA), the dependence on \mathbf{k} and $\mathbf{k}+\mathbf{q}$ of the matrix elements $M_{ij}(\mathbf{k},\mathbf{k}+\mathbf{q}) = \langle \mathbf{k}+\mathbf{q},j | e^{i(\mathbf{q}+\mathbf{G})\cdot\mathbf{r}} | \mathbf{k},i \rangle$ is assumed to be negligible, in which case $M_{ji}^* M_{ij} = 1$.

We obtain thus

$$\begin{aligned}\chi_{\text{mac}}^0(\mathbf{q}, \omega) &= \sum_{\mathbf{k}ij} \frac{f(E_{\mathbf{k}+\mathbf{q},j}) - f(E_{\mathbf{k},i})}{E_{\mathbf{k}+\mathbf{q},j} - E_{\mathbf{k},i} - \omega - i\eta} \\ &= \sum_{\mathbf{k}ij} \frac{f(E_{\mathbf{k}+\mathbf{q},j}) - f(E_{\mathbf{k},i})}{E_{\mathbf{k}+\mathbf{q},j} - E_{\mathbf{k},i} - \omega} + i \sum_{\mathbf{k}ij} \frac{(f(E_{\mathbf{k}+\mathbf{q},j}) - f(E_{\mathbf{k},i})) \eta}{(E_{\mathbf{k}+\mathbf{q},j} - E_{\mathbf{k},i} - \omega)^2 + \eta^2},\end{aligned}\quad (\text{C.2})$$

where in the last step we split the real and the imaginary part into separate terms, which we can denote as $\chi^0 = \chi'^0 + i\chi''^0$. The first, real term is the Lindhard function, while the second term is the imaginary part, χ''^0 , that we want to connect to the Fermi surface topology. Using that

$$\lim_{\eta \rightarrow 0} \left\{ \frac{\eta}{(E_{\mathbf{k}+\mathbf{q},j} - E_{\mathbf{k},i} - \omega)^2 + \eta^2} \right\} = \delta(E_{\mathbf{k}+\mathbf{q},j} - E_{\mathbf{k},i} - \omega) \quad (\text{C.3})$$

we obtain

$$\chi''^0(\mathbf{q}, \omega) = \sum_{\mathbf{k}ij} (f(E_{\mathbf{k}+\mathbf{q},j}) - f(E_{\mathbf{k},i})) \delta(E_{\mathbf{k}+\mathbf{q},j} - E_{\mathbf{k},i} - \omega). \quad (\text{C.4})$$

The difference of Fermi-Dirac functions can be expanded as

$$f(E_{\mathbf{k}+\mathbf{q},j}) - f(E_{\mathbf{k},i}) = \mathbf{q} \cdot \nabla_{\mathbf{k}} f(E_{\mathbf{k},i}) + \mathcal{O}(q^2), \quad (\text{C.5})$$

where band index j can be omitted in case q and ω are small (i.e., only keeping intraband terms). Using $f(E_{\mathbf{k},i}) = \left[e^{\frac{E_{\mathbf{k},i} - E_{\text{F}}}{k_{\text{B}}T}} + 1 \right]^{-1}$ we can rewrite

$$\nabla_{\mathbf{k}} f(E_{\mathbf{k},i}) = -\frac{\partial f(E_{\mathbf{k},i})}{\partial E_{\text{F}}} \nabla_{\mathbf{k}} E_{\mathbf{k},i}. \quad (\text{C.6})$$

This yields

$$\chi''^0(\mathbf{q}, \omega) = -\sum_{\mathbf{k}ij} \frac{\partial f(E_{\mathbf{k},i})}{\partial E_{\text{F}}} \mathbf{q} \cdot \nabla_{\mathbf{k}} E_{\mathbf{k},i} \delta(E_{\mathbf{k}+\mathbf{q},j} - E_{\mathbf{k},i} - \omega), \quad (\text{C.7})$$

whereby the δ -function imposes $E_{\mathbf{k}+\mathbf{q},j} - E_{\mathbf{k},i} = \omega$, so that with an expansion this becomes $E_{\mathbf{k}+\mathbf{q},j} - E_{\mathbf{k},i} = \mathbf{q} \cdot \nabla E_{\mathbf{k},i} + \mathcal{O}(q^2) = \omega$. This assumes again that the curvatures of both bands is equal. At sufficiently small $|\mathbf{q}|$ we find

$\mathbf{q} \cdot \nabla E_{\mathbf{k},i} \simeq \omega$. Therefore, we obtain

$$\chi''^0(\mathbf{q}, \omega) = -\omega \sum_{\mathbf{k}ij} \frac{\partial f(E_{\mathbf{k},i})}{\partial E_{\mathbf{F}}} \delta(E_{\mathbf{k}+\mathbf{q},j} - E_{\mathbf{k},i} - \omega) , \quad (\text{C.8})$$

and at $T = 0$, $\frac{\partial f(E_{\mathbf{k},i})}{\partial E_{\mathbf{F}}} = -\delta(E_{\mathbf{k},i} - E_{\mathbf{F}})$, so that

$$\chi''^0(\mathbf{q}, \omega) = \omega \sum_{\mathbf{k}ij} \delta(E_{\mathbf{k},i} - E_{\mathbf{F}}) \delta(E_{\mathbf{k}+\mathbf{q},j} - E_{\mathbf{k},i} - \omega) , \quad (\text{C.9})$$

which proves Eq. 5.10.

Bibliography

- [1] P. F. Dahl, *Superconductivity: Its historical roots and development from mercury to the ceramic oxides*, American Institute of Physics (New York) (1992).
- [2] D. van Delft and P. Kes, *The discovery of superconductivity*, Physics Today (2010).
- [3] R. G. Sharma, *Superconductivity: Basics and Applications to Magnets*, Springer Series in Materials Science, 2015.
- [4] M. Tinkham, *Introduction to Superconductivity*, Dover Publications, 2004.
- [5] L. D. Landau, *Collected papers of L. D. Landau*, Gordon and Breach, 8th edition, 1965.
- [6] J. F. Annett, *Superconductivity, Superfluids, and Condensates*, Oxford Master Series in Condensed Matter Physics, 2005.
- [7] C. Di Giorgio, D. D'Agostino, A. M. Cucolo, M. Iavarone, A. Scarfato, G. Karapetrov, S. A. Moore, M. Polichetti, D. Mancusi, S. Pace, V. Novosad, V. Yefremenko, and F. Bobba, *Superconducting Vortex-Antivortex Pairs: Nucleation and Confinement in Magnetically Coupled Superconductor-Ferromagnet Hybrids*, InTech, 2017.
- [8] A. A. Abrikosov, *On the Magnetic Properties of Superconductors of the Second Group*, Soviet Physics JETP **5**, 1174 (1957).
- [9] A. A. Abrikosov, *Type-II superconductors and the vortex lattice*, Nobel Lecture, December 8, 2003.

- [10] A. A. Abrikosov, *Fundamentals of the Theory of Metals*, North Holland (Amsterdam), 1988.
- [11] A. L. Fetter and J. D. Walecka, *Quantum Theory of Many-Particle Systems*, Dover Publications, 2003.
- [12] V. M. Vinokur, N. B. Kopnin, A. S. Mel'nikov, I. M. Nefedov, V. I. Pozdnyakova, D. A. Ryzhov, M. A. Silaev, and I. A. Shereshevskii, *Vortex states in mesoscopic superconductors*, Bull. Russ. Acad. Sci.: Phys. **71**, 6 (2007).
- [13] J. R. Kirtley, C. C. Tsuei, M. Rupp, J. Z. Sun, L. S. Yu-Jahnes, A. Gupta, M. B. Ketchen, K. A. Moler, and M. Bhushan, *Direct Imaging of Integer and Half-Integer Josephson Vortices in High- T_c Grain Boundaries*, Phys. Rev. Lett. **76**, 1336 (1996).
- [14] E. Babaev, *Vortices with Fractional Flux in Two-Gap Superconductors and in Extended Faddeev Model*, Phys. Rev. Lett. **89**, 067001 (2002).
- [15] C.-L. Song, Y.-L. Wang, P. Cheng, Y.-P. Jiang, W. Li, T. Zhang, Z. Li, K. He, L. Wang, J.-F. Jia, H.-H. Hung, C. Wu, X. Ma, X. Chen, and Q.-K. Xue, *Direct Observation of Nodes and Twofold Symmetry in FeSe Superconductor*, Science **332**, 1410 (2011).
- [16] L. Kramer and R. J. Watts-Tobin, *Theory of Dissipative Current-Carrying States in Superconducting Filaments*, Phys. Rev. Lett. **40**, 1041 (1978).
- [17] V. V. Moshchalkov, *Ginzburg-Landau theory: a powerful tool to study vortex matter in nanostructured superconductors*, J. Supercond. Nov. Magn. **19**, 409 (2006).
- [18] E.-W. Scheidt, M. Herzinger, A. Fischer, D. Schmitz, J. Reiners, F. Mayr, F. Loder, M. Baenitz, and W. Scherer, *On the nature of superconductivity in the anisotropic dichalcogenide $NbSe_2\{CoCp_2\}_x$* , J. Phys. Condens. Matter **27**, 155701 (2015).
- [19] E. Maxwell, *Isotope Effect in the Superconductivity of Mercury*, Phys. Rev. **78**, 477 (1950).
- [20] B. S. Deaver and W. M. Fairbank, *Experimental Evidence for Quantized Flux in Superconducting Cylinders*, Phys. Rev. Lett. **7**, 43 (1961).

- [21] H. Fröhlich, *Theory of the Superconducting State. I. The Ground State at the Absolute Zero of Temperature*, Phys. Rev. **79**, 845 (1950).
- [22] J. Bardeen, L. N. Cooper, and J. R. Schrieffer, *Microscopic Theory of Superconductivity*, Phys. Rev. **106**, 162 (1957).
- [23] L.-C. Tu, J. Luo, and G. T. Gillies, *The mass of the photon*, Rep. Prog. Phys. **68**, 77 (2005).
- [24] A. J. Leggett, *Number-Phase Fluctuations in Two-Band Superconductors*, Progr. Theor. Phys. **36**, 901 (1966).
- [25] H. Krull, N. Bittner, G. S. Uhrig, D. Manske, and A. P. Schnyder, *Coupling of Higgs and Leggett modes in non-equilibrium superconductors*, Nat. Commun. **7**, 11921 (2016).
- [26] J.-X. Zhu, *Bogoliubov-de Gennes Method and Its Applications*, Springer, 2016.
- [27] F. Giubileo, D. Roditchev, W. Sacks, R. Lamy, D. X. Thanh, J. Klein, S. Miraglia, D. Fruchart, J. Marcus, and P. Monod, *Two-Gap State Density in MgB₂: A True Bulk Property Or A Proximity Effect?*, Phys. Rev. Lett. **87**, 177008 (2001).
- [28] M. Iavarone, G. Karapetrov, A. Koshelev, W. K. Kwok, D. Hinks, G. W. Crabtree, W. N. Kang, E.-M. Choi, H. J. Kim, and S.-I. Lee, *MgB₂ : directional tunnelling and two-band superconductivity*, Supercond. Sci. Technol. **16**, 156 (2003).
- [29] K. Fosshem and A. Sudbø, *Superconductivity: Physics and Applications*, John Wiley & Sons, 2004.
- [30] S. L. Bud'ko, G. Lapertot, C. Petrovic, C. E. Cunningham, N. Anderson, and P. C. Canfield, *Boron Isotope Effect in Superconducting MgB₂*, Phys. Rev. Lett. **86**, 1877 (2001).
- [31] D. G. Hinks, H. Claus, and J. D. Jorgensen, *The complex nature of superconductivity in MgB₂ as revealed by the reduced total isotope effect*, Nature **411**, 457 (2001).
- [32] J. E. Schirber and C. J. M. Northrup, *Concentration dependence of the superconducting transition temperature in PdH_x and PdD_x*, Phys. Rev. B **10**, 3818 (1974).

- [33] B. M. Klein and R. E. Cohen, *Anharmonicity and the inverse isotope effect in the palladium-hydrogen system*, Phys. Rev. B **45**, 12405 (1992).
- [34] D. R. Tilley and J. Tilley, *Superfluidity and Superconductivity*, Institute of Physics Publishing (Bristol and Philadelphia), 3rd edition, 1990.
- [35] J. Nagamatsu, N. Nakagawa, T. Muranaka, Y. Zenitani, and J. Akimitsu, *Superconductivity at 39 K in magnesium diboride*, Nature **410**, 63 (2001).
- [36] H. J. Choi, D. Roundy, H. Sun, M. L. Cohen, and S. G. Louie, *The origin of the anomalous superconducting properties of MgB₂*, Nature **418**, 758 (2002).
- [37] D. Mou, R. Jiang, V. Taufour, S. L. Bud'ko, P. C. Canfield, and A. Kaminski, *Momentum dependence of the superconducting gap and in-gap states in MgB₂ multiband superconductor*, Phys. Rev. B **91**, 214519 (2015).
- [38] E. R. Margine and F. Giustino, *Anisotropic Migdal-Eliashberg theory using Wannier functions*, Phys. Rev. B **87**, 024505 (2013).
- [39] A. Aperis, P. Maldonado, and P. M. Oppeneer, *Ab initio theory of magnetic-field-induced odd-frequency two-band superconductivity in MgB₂*, Phys. Rev. B **92**, 054516 (2015).
- [40] P. J. Ray, *Structural investigation of La_{2-x}Sr_xCuO_{4+y} – Following staging as a function of temperature*, Master Thesis, Niels Bohr Institute, Faculty of Science, University of Copenhagen (2015).
- [41] A. P. Drozdov, M. I. Erements, I. A. Troyan, V. Ksenofontov, and S. I. Shylin, *Conventional superconductivity at 203 kelvin at high pressures in the sulfur hydride system*, Nature **525**, 73 (2015).
- [42] P. Cudazzo, G. Profeta, A. Sanna, A. Floris, A. Continenza, S. Massidda, and E. K. U. Gross, *Ab Initio Description of High-Temperature Superconductivity in Dense Molecular Hydrogen*, Phys. Rev. Lett. **100**, 257001 (2008).
- [43] F. Steglich, J. Aarts, C. D. Bredl, W. Lieke, D. Meschede, W. Franz, and H. Schäfer, *Superconductivity in the Presence of Strong Pauli Paramagnetism: CeCu₂Si₂*, Phys. Rev. Lett. **43**, 1892 (1979).

- [44] C. Pfleiderer, *Superconducting phases of f-electron compounds*, Rev. Mod. Phys. **81**, 1551 (2009).
- [45] Q. Si, R. Yu, and E. Abrahams, *High-temperature superconductivity in iron pnictides and chalcogenides*, Nat. Rev. Mater. **1**, 16017 (2016).
- [46] D. N. Basov and A. V. Chubukov, *Manifesto for a higher T_c* , Nat. Phys. **7** (2011).
- [47] J. G. Bednorz and K. A. Müller, *Possible high- T_c superconductivity in the Ba-La-Cu-O system*, Zeitschrift für Physik B Condensed Matter **64**, 189 (1986).
- [48] Y. Kamihara, H. Hiramatsu, M. Hirano, R. Kawamura, H. Yanagi, T. Kamiya, and H. Hosono, *Iron-Based Layered Superconductor: LaOFeP*, J. Am. Chem. Soc. **128**, 10012 (2006).
- [49] G. Wu, Y. L. Xie, H. Chen, M. Zhong, R. H. Liu, B. C. Shi, Q. J. Li, X. F. Wang, T. Wu, Y. J. Yan, J. J. Ying, and X. H. Chen, *Superconductivity at 56 K in samarium-doped SrFeAsF*, J. Phys. Condens. Matter **21**, 142203 (2009).
- [50] J. Paglione and R. L. Greene, *High-temperature superconductivity in iron-based materials*, Nat. Phys. **6**, 645 (2010).
- [51] X. Liu, L. Zhao, S. He, J. He, D. Liu, D. Mou, B. Shen, Y. Hu, J. Huang, and X. J. Zhou, *Electronic structure and superconductivity of FeSe-related superconductors*, J. Phys. Condens. Matter **27**, 183201 (2015).
- [52] I. I. Mazin, D. J. Singh, M. D. Johannes, and M. H. Du, *Unconventional Superconductivity with a Sign Reversal in the Order Parameter of LaFeAsO $_{1-x}$ F $_x$* , Phys. Rev. Lett. **101**, 057003 (2008).
- [53] D. V. Evtushinsky, D. S. Inosov, V. B. Zabolotnyy, M. S. Viazovska, R. Khasanov, A. Amato, H.-H. Klauss, H. Luetkens, C. Niedermayer, G. L. Sun, V. Hinkov, C. T. Lin, A. Varykhalov, A. Koitzsch, M. Knupfer, B. Büchner, A. A. Kordyuk, and S. V. Borisenko, *Momentum-resolved superconducting gap in the bulk of Ba $_{1-x}$ K $_x$ Fe $_2$ As $_2$ from combined ARPES and μ SR measurements*, New J. Phys. **11**, 055069 (2009).

- [54] R. Peng, X. P. Shen, X. Xie, H. C. Xu, S. Y. Tan, M. Xia, T. Zhang, H. Y. Cao, X. G. Gong, J. P. Hu, B. P. Xie, and D. L. Feng, *Measurement of an Enhanced Superconducting Phase and a Pronounced Anisotropy of the Energy Gap of a Strained FeSe Single Layer in FeSe/Nb: SrTiO₃/KTaO₃ Heterostructures Using Photoemission Spectroscopy*, Phys. Rev. Lett. **112**, 107001 (2014).
- [55] J. Ge, Z. Liu, C. Liu, C. Gao, D. Qian, Q. Xue, Y. Liu, and J. Jia, *Superconductivity above 100 K in single-layer FeSe films on doped SrTiO₃*, Nat. Mater. **14**, 285 (2015).
- [56] I. I. Mazin and D. J. Singh, *Ferromagnetic Spin Fluctuation Induced Superconductivity in Sr₂RuO₄*, Phys. Rev. Lett. **79**, 733 (1997).
- [57] A. P. Mackenzie and Y. Maeno, *The superconductivity of Sr₂RuO₄ and the physics of spin-triplet pairing*, Rev. Mod. Phys. **75**, 657 (2003).
- [58] Y. Maeno, S. Kittaka, T. Nomura, S. Yonezawa, and K. Ishida, *Evaluation of Spin-Triplet Superconductivity in Sr₂RuO₄*, J. Phys. Soc. Jpn. **81**, 011009 (2012).
- [59] M. V. Mazziotti, A. Valletta, G. Campi, D. Innocenti, A. Perali, and A. Bianconi, *Possible Fano resonance for high-T_c multi-gap superconductivity in p-Terphenyl doped by K at the Lifshitz transition*, EPL **118**, 37003 (2017).
- [60] T. Zhang, P. Cheng, W. Li, Y. Sun, G. Wang, X. Zhu, K. He, L. Wang, X. Ma, X. Chen, Y. Wang, Y. Liu, H. Lin, J. Jia, and Q. Xue, *Superconductivity in one-atomic-layer metal films grown on Si(111)*, Nat. Phys. **6**, 104 (2010).
- [61] M. Sato and Y. Ando, *Topological superconductors: a review*, Rep. Prog. Phys. **80**, 076501 (2017).
- [62] M. Iavarone, G. Karapetrov, A. E. Koshelev, W. K. Kwok, G. W. Crabtree, D. G. Hinks, W. N. Kang, E.-M. Choi, H. J. Kim, H.-J. Kim, and S. I. Lee, *Two-Band Superconductivity in MgB₂*, Phys. Rev. Lett. **89**, 187002 (2002).
- [63] Y. Tanaka, *Multicomponent superconductivity based on multiband superconductors*, Supercond. Sci. Technol. **28**, 034002 (2015).

- [64] M. V. Milošević and A. Perali, *Emergent phenomena in multicomponent superconductivity: an introduction to the focus issue*, Supercond. Sci. Technol. **28**, 060201 (2015).
- [65] H. Suhl, B. T. Matthias, and L. R. Walker, *Bardeen-Cooper-Schrieffer Theory of Superconductivity in the Case of Overlapping Bands*, Phys. Rev. Lett. **3**, 552 (1959).
- [66] J. Kondo, *Superconductivity in Transition Metals*, Progr. Theor. Exp. Phys. **29**, 1 (1963).
- [67] D. R. Tilley, *The Ginzburg-Landau equations for pure two band superconductors*, Proceedings of the Physical Society **84**, 573 (1964).
- [68] S. Souma, Y. Machida, T. Sato, T. Takahashi, H. Matsui, S.-C. Wang, H. Ding, A. Kaminski, J. C. Campuzano, S. Sasaki, and K. Kadowaki, *The origin of multiple superconducting gaps in MgB₂*, Nature **423**, 65 (2003).
- [69] M. E. Zhitomirsky and V.-H. Dao, *Ginzburg-Landau theory of vortices in a multigap superconductor*, Phys. Rev. B **69**, 054508 (2004).
- [70] V. G. Kogan and J. Schmalian, *Ginzburg-Landau theory of two-band superconductors: Absence of type-1.5 superconductivity*, Phys. Rev. B **83**, 054515 (2011).
- [71] A. Vagov, A. A. Shanenko, M. V. Milošević, V. M. Axt, and F. M. Peeters, *Two-band superconductors: Extended Ginzburg-Landau formalism by a systematic expansion in small deviation from the critical temperature*, Phys. Rev. B **86**, 144514 (2012).
- [72] N. V. Orlova, A. A. Shanenko, M. V. Milošević, F. M. Peeters, A. V. Vagov, and V. M. Axt, *Ginzburg-Landau theory for multiband superconductors: Microscopic derivation*, Phys. Rev. B **87**, 134510 (2013).
- [73] J. Bekaert, S. Vercauteren, A. Aperis, L. Komendová, R. Prozorov, B. Partoens, and M. V. Milošević, *Anisotropic type-I superconductivity and anomalous superfluid density in OsB₂*, Phys. Rev. B **94**, 144506 (2016).

- [74] S. A. Kuzmichev, T. E. Kuzmicheva, and S. N. Tchesnokov, *Determination of the electron-phonon coupling constants from the experimental temperature dependences of superconducting gaps in MgB₂*, JETP Letters **99**, 295 (2014).
- [75] A. V. Vagov, A. A. Shanenko, M. V. Milošević, V. M. Axt, and F. M. Peeters, *Extended Ginzburg-Landau formalism: Systematic expansion in small deviation from the critical temperature*, Phys. Rev. B **85**, 014502 (2012).
- [76] L. N. Oliveira, E. K. U. Gross, and W. Kohn, *Density-Functional Theory for Superconductors*, Phys. Rev. Lett. **60**, 2430 (1988).
- [77] M. Lüders, M. A. L. Marques, N. N. Lathiotakis, A. Floris, G. Profeta, L. Fast, A. Continenza, S. Massidda, and E. K. U. Gross, *Ab initio*, Phys. Rev. B **72**, 024545 (2005).
- [78] A. Linscheid, A. Sanna, F. Essenberger, and E. K. U. Gross, *Ab initio theory of superconductivity in a magnetic field. I. Spin density functional theory for superconductors and Eliashberg equations*, Phys. Rev. B **92**, 024505 (2015).
- [79] C. Bersier, A. Floris, A. Sanna, G. Profeta, A. Continenza, E. K. U. Gross, and S. Massidda, *Electronic, vibrational, and superconducting properties of CaBeSi: First-principles calculations*, Phys. Rev. B **79**, 104503 (2009).
- [80] A. Floris, A. Sanna, S. Massidda, and E. K. U. Gross, *Two-band superconductivity in Pb from ab initio calculations*, Phys. Rev. B **75**, 054508 (2007).
- [81] M. Ruby, B. W. Heinrich, J. I. Pascual, and K. J. Franke, *Experimental Demonstration of a Two-Band Superconducting State for Lead Using Scanning Tunneling Spectroscopy*, Phys. Rev. Lett. **114**, 157001 (2015).
- [82] J.-J. Zheng and E. R. Margine, *First-principles calculations of the superconducting properties in Li-decorated monolayer graphene within the anisotropic Migdal-Eliashberg formalism*, Phys. Rev. B **94**, 064509 (2016).

- [83] A. Linscheid, A. Sanna, A. Floris, and E. K. U. Gross, *First-Principles Calculation of the Real-Space Order Parameter and Condensation Energy Density in Phonon-Mediated Superconductors*, Phys. Rev. Lett. **115**, 097002 (2015).
- [84] C. Heil, S. Poncé, H. Lambert, M. Schlipf, E. R. Margine, and F. Giustino, *Origin of Superconductivity and Latent Charge Density Wave in NbS₂*, Phys. Rev. Lett. **119**, 087003 (2017).
- [85] V. Moskalenko, A. Ursu, and N. Botoshan, *A method for investigating electronic state densities for superconductors with impurities*, Phys. Lett. A **44**, 183 (1973).
- [86] N. Schopohl and K. Scharnberg, *Tunneling density of states for the two-band model of superconductivity*, Solid State Commun. **22**, 371 (1977).
- [87] Y. Noat, T. Cren, F. Debontridder, D. Roditchev, W. Sacks, P. Toulemonde, and A. San Miguel, *Signatures of multigap superconductivity in tunneling spectroscopy*, Phys. Rev. B **82**, 014531 (2010).
- [88] Y. Noat, J. A. Silva-Guillén, T. Cren, V. Cherkez, C. Brun, S. Pons, F. Debontridder, D. Roditchev, W. Sacks, L. Cario, P. Ordejón, A. García, and E. Canadell, *Quasiparticle spectra of 2H-NbSe₂: Two-band superconductivity and the role of tunneling selectivity*, Phys. Rev. B **92**, 134510 (2015).
- [89] V. Moshchalkov, M. Menghini, T. Nishio, Q. H. Chen, A. V. Silhanek, V. H. Dao, L. F. Chibotaru, N. D. Zhigadlo, and J. Karpinski, *Type-1.5 Superconductivity*, Phys. Rev. Lett. **102**, 117001 (2009).
- [90] M. Silaev and E. Babaev, *Microscopic theory of type-1.5 superconductivity in multiband systems*, Phys. Rev. B **84**, 094515 (2011).
- [91] A. Chaves, L. Komendová, M. V. Milošević, J. S. Andrade, G. A. Farias, and F. M. Peeters, *Conditions for nonmonotonic vortex interaction in two-band superconductors*, Phys. Rev. B **83**, 214523 (2011).
- [92] M. Silaev and E. Babaev, *Microscopic derivation of two-component Ginzburg-Landau model and conditions of its applicability in two-band systems*, Phys. Rev. B **85**, 134514 (2012).

- [93] L. Komendová, Y. Chen, A. A. Shanenko, M. V. Milošević, and F. M. Peeters, *Two-Band Superconductors: Hidden Criticality Deep in the Superconducting State*, Phys. Rev. Lett. **108**, 207002 (2012).
- [94] Y. Tanaka and T. Yanagisawa, *Chiral state in three-gap superconductors*, Solid State Commun. **150**, 1980 (2010).
- [95] V. Stanev and Z. Tešanović, *Three-band superconductivity and the order parameter that breaks time-reversal symmetry*, Phys. Rev. B **81**, 134522 (2010).
- [96] K. S. Novoselov, A. K. Geim, S. V. Morozov, D. Jiang, Y. Zhang, S. V. Dubonos, I. V. Grigorieva, and A. A. Firsov, *Electric Field Effect in Atomically Thin Carbon Films*, Science **306**, 666 (2004).
- [97] A. K. Geim and I. V. Grigorieva, *Van der Waals heterostructures*, Nature **499**, 419 (2013).
- [98] P. K. Sahoo, S. Memaran, Y. Xin, L. Balicas, and H. R. Gutiérrez, *One-pot growth of two-dimensional lateral heterostructures via sequential edge-epitaxy*, Nature **553**, 63 (2018).
- [99] Y. Saito, T. Nojima, and Y. Iwasa, *Highly crystalline 2D superconductors*, Nat. Rev. Mater. **2**, 16094 (2016).
- [100] T. Uchihashi, *Two-dimensional superconductors with atomic-scale thickness*, Supercond. Sci. Technol. **30**, 013002 (2017).
- [101] C. Brun, T. Cren, and D. Roditchev, *Review of 2D superconductivity: the ultimate case of epitaxial monolayers*, Supercond. Sci. Technol. **30**, 013003 (2017).
- [102] N. D. Mermin and H. Wagner, *Absence of Ferromagnetism or Antiferromagnetism in One- or Two-Dimensional Isotropic Heisenberg Models*, Phys. Rev. Lett. **17**, 1133 (1966).
- [103] V. L. Berezinskii, *Destruction of long-range order in one-dimensional and two-dimensional systems possessing a continuous symmetry group. II. Quantum systems*, Sov. Phys. JETP **34**, 610 (1972).
- [104] J. M. Kosterlitz and D. J. Thouless, *Ordering, metastability and phase transitions in two-dimensional systems*, J. Phys. C **6**, 1181 (1973).

- [105] A. F. Hebard and A. T. Fiory, *Evidence for the Kosterlitz-Thouless Transition in Thin Superconducting Aluminum Films*, Phys. Rev. Lett. **44**, 291 (1980).
- [106] K. Epstein, A. M. Goldman, and A. M. Kadin, *Vortex-Antivortex Pair Dissociation in Two-Dimensional Superconductors*, Phys. Rev. Lett. **47**, 534 (1981).
- [107] P. Anderson, *Theory of dirty superconductors*, J. Phys. Chem. Solids **11**, 26 (1959).
- [108] D. B. Haviland, Y. Liu, and A. M. Goldman, *Onset of superconductivity in the two-dimensional limit*, Phys. Rev. Lett. **62**, 2180 (1989).
- [109] H.-M. Zhang, Y. Sun, W. Li, J.-P. Peng, C.-L. Song, Y. Xing, Q. Zhang, J. Guan, Z. Li, Y. Zhao, S. Ji, L. Wang, K. He, X. Chen, L. Gu, L. Ling, M. Tian, L. Li, X. C. Xie, J. Liu, H. Yang, Q.-K. Xue, J. Wang, and X. Ma, *Detection of a Superconducting Phase in a Two-Atom Layer of Hexagonal Ga Film Grown on Semiconducting GaN(0001)*, Phys. Rev. Lett. **114**, 107003 (2015).
- [110] N. Reyren, S. Thiel, A. D. Caviglia, L. F. Kourkoutis, G. Hammerl, C. Richter, C. W. Schneider, T. Kopp, A.-S. Rüetschi, D. Jaccard, M. Gabay, D. A. Muller, J.-M. Triscone, and J. Mannhart, *Superconducting Interfaces Between Insulating Oxides*, Science **317**, 1196 (2007).
- [111] A. T. Bollinger, G. Dubuis, J. Yoon, D. Pavuna, J. Misewich, and I. Bozovic, *Superconductor-insulator transition in $La_{2-x}Sr_xCuO_4$ at the pair quantum resistance*, Nature **472**, 458 (2011).
- [112] C. Tonnoir, A. Kimouche, J. Coraux, L. Magaud, B. Delsol, B. Gilles, and C. Chapelier, *Induced superconductivity in graphene grown on rhenium*, Phys. Rev. Lett. **111**, 246805 (2013).
- [113] G. Profeta, M. Calandra, and F. Mauri, *Phonon-mediated superconductivity in graphene by lithium deposition*, Nat. Phys. **8**, 131 (2012).
- [114] D. M. Guzman, H. M. Alyahyaei, and R. A. Jishi, *Superconductivity in graphene-lithium*, 2D Mater. **1**, 021005 (2014).

- [115] B. M. Ludbrook, G. Levy, P. Nigge, M. Zonno, M. Schneider, D. J. Dvorkak, C. N. Veenstra, S. Zhdanovich, D. Wong, P. Dosanjh, C. Straßer, A. Stöhr, S. Forti, C. R. Ast, U. Starke, and A. Damascelli, *Evidence for superconductivity in Li-decorated monolayer graphene*, Proc. Natl. Acad. Sci. **112**, 11795 (2015).
- [116] K. Kanetani, K. Sugawara, T. Sato, R. Shimizu, K. Iwaya, T. Hitosugi, and T. Takahashi, *Ca intercalated bilayer graphene as a thinnest limit of superconducting C_6Ca* , Proc. Natl. Acad. Sci. U.S.A. **109**, 19610 (2012).
- [117] Y. Cao, V. Fatemi, S. Fang, K. Watanabe, T. Taniguchi, E. Kaxiras, and P. Jarillo-Herrero, *Unconventional superconductivity in magic-angle graphene superlattices*, Nature **556**, 43 (2018).
- [118] X. Xi, Z. Wang, W. Zhao, J.-H. Park, K. T. Law, H. Berger, L. Forro, J. Shan, and K. F. Mak, *Ising pairing in superconducting $NbSe_2$ atomic layers*, Nat. Phys. **12**, 139 (2016).
- [119] M. M. Ugeda, A. J. Bradley, Y. Zhang, S. Onishi, Y. Chen, W. Ruan, C. Ojeda-Aristizabal, H. Ryu, M. T. Edmonds, H.-Z. Tsai, A. Riss, S.-K. Mo, D. Lee, A. Zettl, Z. Hussain, Z.-X. Shen, and M. F. Crommie, *Characterization of collective ground states in single-layer $NbSe_2$* , Nat. Phys. **12**, 92 (2016).
- [120] J. Pan, C. Guo, C. Song, X. Lai, H. Li, W. Zhao, H. Zhang, G. Mu, K. Bu, T. Lin, X. Xie, M. Chen, and F. Huang, *Enhanced Superconductivity in Restacked TaS_2 Nanosheets*, J. Am. Chem. Soc. **139**, 4623 (2017).
- [121] Y. Yang, S. Fang, V. Fatemi, J. Ruhman, E. Navarro-Moratalla, K. Watanabe, T. Taniguchi, E. Kaxiras, and P. Jarillo-Herrero, *Enhanced Superconductivity and Suppression of Charge-density Wave Order in $2H-TaS_2$ in the Two-dimensional Limit*, arXiv:1711.00079 (2017).
- [122] J. T. Ye, Y. J. Zhang, R. Akashi, M. S. Bahramy, R. Arita, and Y. Iwasa, *Superconducting Dome in a Gate-Tuned Band Insulator*, Science **338**, 1193 (2012).

- [123] Y. Saito, Y. Nakamura, M. S. Bahramy, Y. Kohama, J. Ye, Y. Kasahara, Y. Nakagawa, M. Onga, M. Tokunaga, T. Nojima, Y. Yanase, and Y. Iwasa, *Superconductivity protected by spin-valley locking in ion-gated MoS₂*, Nat. Phys. **12**, 144 (2015).
- [124] D. Geng, X. Zhao, L. Li, P. Song, B. Tian, W. Liu, J. Chen, D. Shi, M. Lin, W. Zhou, and K. P. Loh, *Controlled growth of ultrathin Mo₂C superconducting crystals on liquid Cu surface*, 2D Mater. **4**, 011012 (2017).
- [125] M. Yamada, T. Hirahara, and S. Hasegawa, *Magnetoresistance Measurements of a Superconducting Surface State of In-Induced and Pb-Induced Structures on Si(111)*, Phys. Rev. Lett. **110**, 237001 (2013).
- [126] M. M. Ozer, J. R. Thompson, and H. H. Weitering, *Hard superconductivity of a soft metal in the quantum regime*, Nat. Phys. **2**, 173 (2006).
- [127] S. Qin, J. Kim, Q. Niu, and C. Shih, *Superconductivity at the Two-Dimensional Limit*, Science **324**, 1314 (2009).
- [128] J. Noffsinger and M. L. Cohen, *Superconductivity in monolayer Pb on Si(111) from first principles*, Solid State Commun. **151**, 421 (2011).
- [129] R. Saniz, B. Partoens, and F. M. Peeters, *Confinement effects on electron and phonon degrees of freedom in nanofilm superconductors: A Green function approach*, Phys. Rev. B **87**, 064510 (2013).
- [130] Y. Guo, Y.-F. Zhang, X.-Y. Bao, T.-Z. Han, Z. Tang, L.-X. Zhang, W.-G. Zhu, E. G. Wang, Q. Niu, Z. Q. Qiu, J.-F. Jia, Z.-X. Zhao, and Q.-K. Xue, *Superconductivity Modulated by Quantum Size Effects*, Science **306**, 1915 (2004).
- [131] T. Uchihashi, P. Mishra, M. Aono, and T. Nakayama, *Macroscopic Superconducting Current through a Silicon Surface Reconstruction with Indium Adatoms: Si(111)-($\sqrt{7} \times \sqrt{3}$)-In*, Phys. Rev. Lett. **107**, 207001 (2011).
- [132] S. Yoshizawa, H. Kim, T. Kawakami, Y. Nagai, T. Nakayama, X. Hu, Y. Hasegawa, and T. Uchihashi, *Imaging Josephson Vortices on the Surface Superconductor Si(111)-($\sqrt{7} \times \sqrt{3}$)-In using a Scanning Tunneling Microscope*, Phys. Rev. Lett. **113**, 247004 (2014).

- [133] C. Brun, T. Cren, V. Cherkez, F. Debontridder, S. Pons, D. Fokin, M. C. Tringides, S. Bozhko, L. B. Ioffe, B. L. Altshuler, and D. Roditchev, *Remarkable effects of disorder on superconductivity of single atomic layers of lead on silicon*, Nat. Phys. **10**, 444 (2014).
- [134] H. Kim, S.-Z. Lin, M. J. Graf, Y. Miyata, Y. Nagai, T. Kato, and Y. Hasegawa, *Electrical Conductivity through a Single Atomic Step Measured with the Proximity-Induced Superconducting Pair Correlation*, Phys. Rev. Lett. **117**, 116802 (2016).
- [135] D. Roditchev, C. Brun, L. Serrier-Garcia, J. C. Cuevas, V. H. L. Bessa, M. V. Milosevic, F. Debontridder, V. Stolyarov, and T. Cren, *Direct observation of Josephson vortex cores*, Nat. Phys. **11**, 332 (2015).
- [136] A. V. Matetskiy, S. Ichinokura, L. V. Bondarenko, A. Y. Tupchaya, D. V. Gruznev, A. V. Zotov, A. A. Saranin, R. Hobar, A. Takayama, and S. Hasegawa, *Two-Dimensional Superconductor with a Giant Rashba Effect: One-Atom-Layer Tl-Pb Compound on Si(111)*, Phys. Rev. Lett. **115**, 147003 (2015).
- [137] G. C. Ménard, S. Guissart, C. Brun, R. T. Leriche, M. Trif, F. Debontridder, D. Demaille, D. Roditchev, P. Simon, and T. Cren, *Two-dimensional topological superconductivity in Pb/Co/Si(111)*, Nat. Commun. **8**, 2040 (2017).
- [138] A. Brinkman, M. Huijben, M. van Zalk, J. Huijben, U. Zeitler, J. C. Maan, W. G. van der Wiel, G. Rijnders, D. H. A. Blank, and H. Hilgenkamp, *Magnetic effects at the interface between non-magnetic oxides*, Nat. Mater. **6**, 493 (2007).
- [139] J. A. Bert, B. Kalisky, C. Bell, M. Kim, Y. Hikita, H. Y. Hwang, and K. A. Moler, *Direct imaging of the coexistence of ferromagnetism and superconductivity at the LaAlO₃/SrTiO₃ interface*, Nat. Phys. **7**, 767 (2011).
- [140] J. Biscaras, N. Bergeal, A. Kushwaha, T. Wolf, A. Rastogi, R. C. Budhani, and J. Lesueur, *Two-dimensional superconductivity at a Mott insulator/band insulator interface LaTiO₃/SrTiO₃*, Nat. Commun. **1**, 89 (2010).

- [141] T. E. Weller, M. Ellerby, S. S. Saxena, R. P. Smith, and N. T. Skipper, *Superconductivity in the intercalated graphite compounds C_6Yb and C_6Ca* , Nat. Phys. **1**, 39 (2005).
- [142] J. Chapman, Y. Su, C. A. Howard, D. Kundys, A. N. Grigorenko, F. Guinea, A. K. Geim, I. V. Grigorieva, and R. R. Nair, *Superconductivity in Ca-doped graphene laminates*, Sci. Rep. **6**, 23254 (2016).
- [143] R. Zhang, J. Waters, A. K. Geim, and I. V. Grigorieva, *Intercalant-independent transition temperature in superconducting black phosphorus*, Nat. Commun. **8**, 15036 (2017).
- [144] J.-J. Zhang and S. Dong, *Prediction of above 20 K superconductivity of blue phosphorus bilayer with metal intercalations*, 2D Mater. **3**, 035006 (2016).
- [145] S. Medvedev, T. M. McQueen, I. A. Troyan, T. Palasyuk, M. I. Erements, R. J. Cava, S. Naghavi, F. Casper, V. Ksenofontov, G. Wortmann, and C. Felser, *Electronic and magnetic phase diagram of β - $Fe_{1.01}Se$ with superconductivity at 36.7 K under pressure*, Nat. Mater. **8**, 630 (2009).
- [146] Q. Fan, W. H. Zhang, X. Liu, Y. J. Yan, M. Q. Ren, R. Peng, H. C. Xu, B. P. Xie, J. P. Hu, T. Zhang, and D. L. Feng, *Plain s-wave superconductivity in single-layer $FeSe$ on $SrTiO_3$ probed by scanning tunnelling microscopy*, Nat. Phys. **11**, 946 (2015).
- [147] Y. Miyata, K. Nakayama, K. Sugawara, T. Sato, and T. Takahashi, *High-temperature superconductivity in potassium-coated multilayer $FeSe$ thin films*, Nat. Mater. **14**, 775 (2015).
- [148] A. Aperis and P. M. Oppeneer, *Multiband full-bandwidth anisotropic Eliashberg theory of interfacial electron-phonon coupling and high- T_c superconductivity in $FeSe/SrTiO_3$* , Phys. Rev. B **97**, 060501 (2018).
- [149] G. G. Sotelo, D. H. J. N. Dias, R. A. H. de Oliveira, A. C. Ferreira, R. D. A. Jr, and R. M. Stephan, *MagLev Cobra: Test Facilities and Operational Experiments*, J. Phys. Conf. Ser. **507**, 032017 (2014).
- [150] D. S. Holmes, A. L. Ripple, and M. A. Manheimer, *Energy-Efficient Superconducting Computing – Power Budgets and Requirements*, IEEE Trans. Appl. Supercond. **23**, 1701610 (2013).

- [151] W. Magnus and W. Schoenmaker, *Quantum Transport in Submicron Devices*, Springer, 2012.
- [152] T. Golod, A. Iovan, and V. M. Krasnov, *Single Abrikosov vortices as quantized information bits*, Nat. Commun. **6**, 8628 (2015).
- [153] S.-T. Lo, K. Y. Chen, S.-D. Lin, J.-Y. Wu, T. L. Lin, M. R. Yeh, T.-M. Chen, and C.-T. Liang, *Controllable Disorder in a Hybrid Nanoelectronic System: Realization of a Superconducting Diode*, Sci. Rep. **3**, 2274 (2013).
- [154] T. Oortlepp and T. Van Duzer, *Access Time and Power Dissipation of a Model 256-Bit Single Flux Quantum RAM*, IEEE Trans. Appl. Supercond. **24**, 1 (2014).
- [155] M. V. Milošević, A. Kanda, S. Hatsumi, F. M. Peeters, and Y. Ootuka, *Local Current Injection into Mesoscopic Superconductors for the Manipulation of Quantum States*, Phys. Rev. Lett. **103**, 217003 (2009).
- [156] A. Y. Aladyshkin, A. V. Silhanek, W. Gillijns, and V. V. Moshchalkov, *Nucleation of superconductivity and vortex matter in superconductor-ferromagnet hybrids*, Supercond. Sci. Technol. **22**, 053001 (2009).
- [157] S. De Franceschi, L. Kouwenhoven, C. Schönberger, and W. Wernsdorfer, *Hybrid superconductor-quantum dot devices*, Nat. Nanotechnol. **5**, 703 (2010).
- [158] M. H. Devoret and R. J. Schoelkopf, *Superconducting Circuits for Quantum Information: An Outlook*, Science **339**, 1169 (2013).
- [159] M. Springborg, *Methods of electronic structure calculations*, John Wiley & Sons, 2000.
- [160] R. M. Martin, *Electronic Structure: Basic Theory and Practical Methods*, Cambridge University Press, 2008.
- [161] J. Kohanoff, *Electronic structure calculations for solids and molecules: Theory and computational methods*, Cambridge University Press, 2006.
- [162] D. Sholl and J. A. Steckel, *Density functional theory: a practical introduction*, John Wiley & Sons, 2009.

- [163] F. Giustino, *Materials Modelling Using Density Functional Theory: Properties and Predictions*, Oxford University Press, 2014.
- [164] P. Hohenberg and W. Kohn, *Inhomogeneous Electron Gas*, Phys. Rev. **136**, 864 (1964).
- [165] W. Kohn and L. J. Sham, *Self-Consistent Equations Including Exchange and Correlation Effects*, Phys. Rev. **140**, 1133 (1965).
- [166] D. M. Ceperley and B. J. Alder, *Ground State of the Electron Gas by a Stochastic Method*, Phys. Rev. Lett. **45**, 566 (1980).
- [167] J. P. Perdew, K. Burke, and M. Ernzerhof, *Generalized Gradient Approximation Made Simple*, Phys. Rev. Lett. **77**, 3865 (1996).
- [168] L. J. Sham and L. Schlüter, *Density-Functional Theory of the Energy Gap*, Phys. Rev. Lett. **51**, 1888 (1983).
- [169] W. G. Aulbur, L. Jönsson, and J. W. Wilkins, *Quasiparticle Calculations in Solids*, Solid State Phys **54** (1999).
- [170] A. D. Becke, *A new mixing of Hartree-Fock and local density-functional theories*, J. Chem. Phys. **98**, 1372 (1992).
- [171] J. Heyd, G. E. Scuseria, and M. Ernzerhof, *Hybrid functionals based on a screened Coulomb potential*, J. Chem. Phys. **118**, 8207 (2003).
- [172] G. Kresse and J. Furthmüller, *Efficient iterative schemes for ab initio total-energy calculations using a plane-wave basis set*, Phys. Rev. B **54**, 11169 (1996).
- [173] H. J. Monkhorst and J. D. Pack, *Special points for Brillouin-zone integration*, Phys. Rev. B **13**, 5188 (1976).
- [174] P. E. Blöchl, *Projector augmented-wave method*, Phys. Rev. B **50**, 17953 (1994).
- [175] X. Gonze, B. Amadon, P.-M. Anglade, J.-M. Beuken, F. Bottin, P. Boulanger, F. Bruneval, D. Caliste, R. Caracas, M. Côté, T. Deutsch, L. Genovese, P. Ghosez, M. Giantomassi, S. Goedecker, D. Hamann, P. Hermet, F. Jollet, G. Jomard, S. Leroux, M. Mancini, S. Mazevet, M. Oliveira, G. Onida, Y. Pouillon, T. Rangel, G.-M. Rignanese,

- D. Sangalli, R. Shaltaf, M. Torrent, M. Verstraete, G. Zerah, and J. Zwanziger, *ABINIT: First-principles approach to material and nanosystem properties*, *Comput. Phys. Commun.* **180**, 2582 (2009).
- [176] G. Kresse and J. Furthmüller, *Efficiency of ab-initio total energy calculations for metals and semiconductors using a plane-wave basis set*, *Comput. Mater. Sci.* **6**, 15 (1996).
- [177] C. Kittel, *Introduction to solid state physics*, John Wiley & Sons, 8 edition, 2005.
- [178] N. Ashcroft and N. Mermin, *Solid state physics*, Harcourt College Publishers, 1976.
- [179] M. A. Stroschio and M. Dutta, *Phonons in nanostructures*, Cambridge University Press, 2001.
- [180] E. Mariani and F. von Oppen, *Flexural Phonons in Free-Standing Graphene*, *Phys. Rev. Lett.* **100**, 076801 (2008).
- [181] S. K. Pati, T. Enoki, and C. N. R. Rao, *Graphene and Its Fascinating Attributes*, World Scientific, 2011.
- [182] G. Grimvall, *The electron-phonon interaction*, North Holland Publishing Co. (Amsterdam), 1981.
- [183] F. Giustino, *Electron-phonon interactions from first principles*, *Rev. Mod. Phys.* **89**, 015003 (2017).
- [184] S. Baroni, P. Giannozzi, and A. Testa, *Green's-function approach to linear response in solids*, *Phys. Rev. Lett.* **58**, 1861 (1987).
- [185] X. Gonze, D. C. Allan, and M. P. Teter, *Dielectric tensor, effective charges, and phonons in α -quartz by variational density-functional perturbation theory*, *Phys. Rev. Lett.* **68**, 3603 (1992).
- [186] S. Y. Savrasov, *Linear response calculations of lattice dynamics using muffin-tin basis sets*, *Phys. Rev. Lett.* **69**, 2819 (1992).
- [187] P. Giannozzi, S. de Gironcoli, P. Pavone, and S. Baroni, *Ab initio calculation of phonon dispersions in semiconductors*, *Phys. Rev. B* **43**, 7231 (1991).

- [188] X. Gonze, *Adiabatic density-functional perturbation theory*, Phys. Rev. A **52**, 1096 (1995).
- [189] X. Gonze, *First-principles responses of solids to atomic displacements and homogeneous electric fields: Implementation of a conjugate-gradient algorithm*, Phys. Rev. B **55**, 10337 (1997).
- [190] X. Gonze and C. Lee, *Dynamical matrices, Born effective charges, dielectric permittivity tensors, and interatomic force constants from density-functional perturbation theory*, Phys. Rev. B **55**, 10355 (1997).
- [191] P. B. Allen and B. Mitrović, *Theory of Superconducting T_c* , Academic Press, 1983, volume 37 of *Solid State Physics*, pp. 1 – 92.
- [192] G. Ummarino, *Eliashberg theory. In the lecture notes of the autumn school on “Emergent phenomena in correlated matter”*, Schriften des Forschungszentrums Jülich, 2013.
- [193] A. Migdal, *Interaction between Electrons and Lattice Vibrations in a Normal Metal*, JETP **34**, 996 (1958).
- [194] A. A. Abrikosov, *Bad screening and applicability of Migdal’s theorem to layered cuprates*, Physica C Supercond. **424**, 149 (2005).
- [195] G. M. Eliashberg, *Interactions between Electrons and Lattice Vibrations in a Superconductor*, JETP **11**, 696 (1960).
- [196] G. M. Eliashberg, *Temperature Green’s Function for Electrons in a Superconductor*, JETP **12**, 1000 (1961).
- [197] P. Morel and P. W. Anderson, *Calculation of the Superconducting State Parameters with Retarded Electron-Phonon Interaction*, Phys. Rev. **125**, 1263 (1962).
- [198] W. L. McMillan, *Transition Temperature of Strong-Coupled Superconductors*, Phys. Rev. **167**, 331 (1968).
- [199] P. B. Allen and R. C. Dynes, *Transition temperature of strong-coupled superconductors reanalyzed*, Phys. Rev. B **12**, 905 (1975).
- [200] J. Bekaert, A. Aperis, B. Partoens, P. M. Oppeneer, and M. V. Milošević, *Evolution of multigap superconductivity in the atomically*

- thin limit: Strain-enhanced three-gap superconductivity in monolayer MgB₂*, Phys. Rev. B **96**, 094510 (2017).
- [201] J. Bekaert, L. Bignardi, A. Aperis, P. van Abswoude, C. Mattevi, S. Gorovikov, L. Petaccia, A. Goldoni, B. Partoens, P. M. Oppeneer, F. M. Peeters, M. V. Milosevic, P. Rudolf, and C. Cepek, *Free surfaces recast superconductivity in few-monolayer MgB₂: Combined first-principles and ARPES demonstration*, Sci. Rep. **7**, 14458 (2017).
- [202] J. Bekaert, A. Aperis, B. Partoens, P. M. Oppeneer, and M. V. Milošević, *Advanced first-principles theory of superconductivity including both lattice vibrations and spin fluctuations: The case of FeB₄*, Phys. Rev. B **97**, 014503 (2018).
- [203] K. S. D. Beach, R. J. Gooding, and F. Marsiglio, *Reliable Padé analytical continuation method based on a high-accuracy symbolic computation algorithm*, Phys. Rev. B **61**, 5147 (2000).
- [204] M. A. Morales, J. M. McMahon, C. Pierleoni, and D. M. Ceperley, *Nuclear Quantum Effects and Nonlocal Exchange-Correlation Functionals Applied to Liquid Hydrogen at High Pressure*, Phys. Rev. Lett. **110**, 065702 (2013).
- [205] I. Errea, M. Calandra, C. J. Pickard, J. Nelson, R. J. Needs, Y. Li, H. Liu, Y. Zhang, Y. Ma, and F. Mauri, *High-Pressure Hydrogen Sulfide from First Principles: A Strongly Anharmonic Phonon-Mediated Superconductor*, Phys. Rev. Lett. **114**, 157004 (2015).
- [206] R. Bianco, I. Errea, M. Calandra, and F. Mauri, *High-pressure phase diagram of hydrogen and deuterium sulfides from first principles: structural and vibrational properties including quantum and anharmonic effects*, arXiv:1802.07968 (2018).
- [207] S. Yonezawa and Y. Maeno, *Type-I superconductivity of the layered silver oxide Ag₅Pb₂O₆*, Phys. Rev. B **72**, 180504 (2005).
- [208] L. L. Zhao, S. Lausberg, H. Kim, M. A. Tanatar, M. Brando, R. Prozorov, and E. Morosan, *Type-I superconductivity in YbSb₂ single crystals*, Phys. Rev. B **85**, 214526 (2012).

- [209] R. Prozorov, *Equilibrium Topology of the Intermediate State in Type-I Superconductors of Different Shapes*, Phys. Rev. Lett. **98**, 257001 (2007).
- [210] A. D. Hernández and D. Domínguez, *Magnetic properties of the intermediate state in small type-I superconductors*, Phys. Rev. B **72**, 020505 (2005).
- [211] G. R. Berdiyrov, A. D. Hernandez, and F. M. Peeters, *Confinement Effects on Intermediate-State Flux Patterns in Mesoscopic Type-I Superconductors*, Phys. Rev. Lett. **103**, 267002 (2009).
- [212] R. Prozorov, A. F. Fidler, J. R. Hoberg, and P. C. Canfield, *Suprafröth in type-I superconductors*, Nat. Phys. **4**, 327 (2008).
- [213] M. A. Engbarth, S. J. Bending, and M. V. Milošević, *Geometry-driven vortex states in type-I superconducting Pb nanowires*, Phys. Rev. B **83**, 224504 (2011).
- [214] A. Müller, M. V. Milošević, S. E. C. Dale, M. A. Engbarth, and S. J. Bending, *Magnetization Measurements and Ginzburg-Landau Simulations of Micron-Size β -Tin Samples: Evidence for an Unusual Critical Behavior of Mesoscopic Type-I Superconductors*, Phys. Rev. Lett. **109**, 197003 (2012).
- [215] G. R. Berdiyrov, A. D. Hernández-Nieves, M. V. Milošević, F. M. Peeters, and D. Domínguez, *Flux-quantum-discretized dynamics of magnetic flux entry, exit, and annihilation in current-driven mesoscopic type-I superconductors*, Phys. Rev. B **85**, 092502 (2012).
- [216] U. Essmann and H. Träuble, *The direct observation of individual flux lines in type II superconductors*, Phys. Lett. **A24**, 526 (1967).
- [217] J. Auer and H. Ullmaier, *Magnetic Behavior of Type-II Superconductors with Small Ginzburg-Landau Parameters*, Phys. Rev. B **7**, 136 (1973).
- [218] A. E. Jacobs, *First-Order Transitions at H_{c1} and H_{c2} in Type II Superconductors*, Phys. Rev. Lett. **26**, 629 (1971).
- [219] A. E. Jacobs, *Interaction of Vortices in Type-II Superconductors near $T = T_c$* , Phys. Rev. B **4**, 3029 (1971).

- [220] A. Vagov, A. A. Shanenkov, M. V. Milošević, V. M. Axt, V. M. Vinokur, J. A. Aguiar, and F. M. Peeters, *Superconductivity between standard types: Multiband versus single-band materials*, Phys. Rev. B **93**, 174503 (2016).
- [221] V. G. Kogan and R. Prozorov, *Changing the type of superconductivity by magnetic and potential scattering*, Phys. Rev. B **90**, 180502 (2014).
- [222] Y. Singh, C. Martin, S. L. Bud'ko, A. Ellern, R. Prozorov, and D. C. Johnston, *Multigap superconductivity and Shubnikov-de Haas oscillations in single crystals of the layered boride OsB₂*, Phys. Rev. B **82**, 144532 (2010).
- [223] T. Hahn, editor, *International Tables for Crystallography, Vol. A*, Springer, 2005.
- [224] T. Terashima, N. Kikugawa, A. Kiswandhi, E.-S. Choi, J. S. Brooks, S. Kasahara, T. Watashige, H. Ikeda, T. Shibauchi, Y. Matsuda, T. Wolf, A. E. Böhmer, F. Hardy, C. Meingast, H. v. Löhneysen, M.-T. Suzuki, R. Arita, and S. Uji, *Anomalous Fermi surface in FeSe seen by Shubnikov-de Haas oscillation measurements*, Phys. Rev. B **90**, 144517 (2014).
- [225] A. Audouard, F. Duc, L. Drigo, P. Toulemonde, S. Karlsson, P. Strobel, and A. Sulpice, *Quantum oscillations and upper critical magnetic field of the iron-based superconductor FeSe*, EPL **109**, 27003 (2015).
- [226] A. Tamai, A. Y. Ganin, E. Rozbicki, J. Bacsá, W. Meevasana, P. D. C. King, M. Caffio, R. Schaub, S. Margadonna, K. Prassides, M. J. Rosseinsky, and F. Baumberger, *Strong Electron Correlations in the Normal State of the Iron-Based FeSe_{0.42}Te_{0.58} Superconductor Observed by Angle-Resolved Photoemission Spectroscopy*, Phys. Rev. Lett. **104**, 097002 (2010).
- [227] M. Aichhorn, S. Biermann, T. Miyake, A. Georges, and M. Imada, *Theoretical evidence for strong correlations and incoherent metallic state in FeSe*, Phys. Rev. B **82**, 064504 (2010).
- [228] J. Long, L. Yang, and X. Wei, *Lattice, elastic properties and Debye temperatures of ATiO₃ (A = Ba, Ca, Pb, Sr) from first-principles*, J. Alloys Compd. **549**, 336 (2013).

- [229] H. J. Choi, D. Roundy, H. Sun, M. L. Cohen, and S. G. Louie, *First-principles calculation of the superconducting transition in MgB_2 within the anisotropic Eliashberg formalism*, Phys. Rev. B **66**, 020513 (2002).
- [230] H. J. Choi, M. L. Cohen, and S. G. Louie, *Anisotropic Eliashberg theory and the two-band model for the superconducting properties of MgB_2* , Phys. Rev. B **73**, 104520 (2006).
- [231] A. Y. Liu, I. I. Mazin, and J. Kortus, *Beyond Eliashberg Superconductivity in MgB_2 : Anharmonicity, Two-Phonon Scattering, and Multiple Gaps*, Phys. Rev. Lett. **87**, 087005 (2001).
- [232] V. G. Kogan, C. Martin, and R. Prozorov, *Superfluid density and specific heat within a self-consistent scheme for a two-band superconductor*, Phys. Rev. B **80**, 014507 (2009).
- [233] J. Singh, A. Jayaraj, D. Srivastava, S. Gayen, A. Thamizhavel, and Y. Singh, *Possible multigap type-I superconductivity in the layered boride RuB_2* , Phys. Rev. B **97**, 054506 (2018).
- [234] T. Moriya, *Developments of the theory of spin fluctuations and spin fluctuation-induced superconductivity*, Proc. Jpn. Acad., Ser. B **82**, 1 (2006).
- [235] D. Scalapino, *Superconductivity and Spin Fluctuations*, J. Low Temp. Phys. **117**, 179 (1999).
- [236] A. Aperis, P. Kotetes, G. Varelogiannis, and P. M. Oppeneer, *Small- q phonon-mediated unconventional superconductivity in the iron pnictides*, Phys. Rev. B **83**, 092505 (2011).
- [237] N. F. Berk and J. R. Schrieffer, *Effect of Ferromagnetic Spin Correlations on Superconductivity*, Phys. Rev. Lett. **17**, 433 (1966).
- [238] G. Riblet, *Superconductivity and Spin Fluctuations in the Ir-Ni, Ir-Co, and Ir-Fe Alloy Systems*, Phys. Rev. B **3**, 91 (1971).
- [239] A. J. Millis, *Nearly antiferromagnetic Fermi liquids: An analytic Eliashberg approach*, Phys. Rev. B **45**, 13047 (1992).
- [240] O. V. Dolgov, I. I. Mazin, A. A. Golubov, S. Y. Savrasov, and E. G. Maksimov, *Critical Temperature and Enhanced Isotope Effect in the*

- Presence of Paramagnons in Phonon-Mediated Superconductors*, Phys. Rev. Lett. **95**, 257003 (2005).
- [241] L. Ortenzi, S. Biermann, O. K. Andersen, I. I. Mazin, and L. Boeri, *Competition between electron-phonon coupling and spin fluctuations in superconducting hole-doped CuBiSO*, Phys. Rev. B **83**, 100505 (2011).
- [242] S. Y. Savrasov and D. Y. Savrasov, *Electron-phonon interactions and related physical properties of metals from linear-response theory*, Phys. Rev. B **54**, 16487 (1996).
- [243] A. N. Kolmogorov, S. Shah, E. R. Margine, A. F. Bialon, T. Hammerschmidt, and R. Drautz, *New Superconducting and Semiconducting Fe-B Compounds Predicted with an Ab Initio Evolutionary Search*, Phys. Rev. Lett. **105**, 217003 (2010).
- [244] H. Gou, N. Dubrovinskaia, E. Bykova, A. A. Tsirlin, D. Kasinathan, W. Schnelle, A. Richter, M. Merlini, M. Hanfland, A. M. Abakumov, D. Batuk, G. Van Tendeloo, Y. Nakajima, A. N. Kolmogorov, and L. Dubrovinsky, *Discovery of a Superhard Iron Tetraboride Superconductor*, Phys. Rev. Lett. **111**, 157002 (2013).
- [245] A. F. Bialon, T. Hammerschmidt, R. Drautz, S. Shah, E. R. Margine, and A. N. Kolmogorov, *Possible routes for synthesis of new boron-rich FeB and Fe_{1-x}Cr_xB₄ compounds*, Appl. Phys. Lett. **98**, 081901 (2011).
- [246] M. Zhang, M. Lu, Y. Du, L. Gao, C. Lu, and H. Liu, *Hardness of FeB₄: Density functional theory investigation*, J. Chem. Phys. **140**, 174505 (2014).
- [247] K. Kotmool, T. Kaewmaraya, S. Chakraborty, J. Anversa, T. Bovorn-ratanaraks, W. Luo, H. Gou, P. C. Piquini, T. W. Kang, H.-K. Mao, and R. Ahuja, *Revealing an unusual transparent phase of superhard iron tetraboride under high pressure*, Proc. Natl. Acad. Sci. U.S.A. **111**, 17050 (2014).
- [248] Y. Kamihara, T. Watanabe, M. Hirano, and H. Hosono, *Iron-Based Layered Superconductor LaO_{1-x}F_xFeAs (x = 0.05–0.12) with T_c = 26 K*, J. Am. Chem. Soc. **130**, 3296 (2008).

- [249] M. Rotter, M. Tegel, and D. Johrendt, *Superconductivity at 38 K in the Iron Arsenide $Ba_{1-x}K_xFe_2As_2$* , Phys. Rev. Lett. **101**, 107006 (2008).
- [250] X. Wang, Q. Liu, Y. Lv, W. Gao, L. Yang, R. Yu, F. Li, and C. Jin, *The superconductivity at 18 K in LiFeAs system*, Solid State Commun. **148**, 538 (2008).
- [251] F.-C. Hsu, J.-Y. Luo, K.-W. Yeh, T.-K. Chen, T.-W. Huang, P. M. Wu, Y.-C. Lee, Y.-L. Huang, Y.-Y. Chu, D.-C. Yan, and M.-K. Wu, *Superconductivity in the PbO-type structure α -FeSe*, Proc. Natl. Acad. Sci. U.S.A. **105**, 14262 (2008).
- [252] Y. Mizuguchi, F. Tomioka, S. Tsuda, T. Yamaguchi, and Y. Takano, *Superconductivity at 27 K in tetragonal FeSe under high pressure*, Appl. Phys. Lett. **93**, 152505 (2008).
- [253] R. Lortz, Y. Wang, S. Abe, C. Meingast, Y. B. Paderno, V. Filipov, and A. Junod, *Specific heat, magnetic susceptibility, resistivity and thermal expansion of the superconductor ZrB_{12}* , Phys. Rev. B **72**, 024547 (2005).
- [254] Y. Wang, R. Lortz, Y. Paderno, V. Filipov, S. Abe, U. Tutsch, and A. Junod, *Specific heat and magnetization of a ZrB_{12} single crystal: Characterization of a type-II/1 superconductor*, Phys. Rev. B **72**, 024548 (2005).
- [255] M. L. Cohen and S. G. Louie, *Fundamentals of Condensed Matter Physics*, Cambridge University Press, 2016.
- [256] M. Sgrist and K. Ueda, *Phenomenological theory of unconventional superconductivity*, Rev. Mod. Phys. **63**, 239 (1991).
- [257] E. F. Talantsev, W. P. Crump, J. O. Island, Y. Xing, Y. Sun, J. Wang, and J. L. Tallon, *On the origin of critical temperature enhancement in atomically thin superconductors*, 2D Mater. **4**, 025072 (2017).
- [258] J. Kortus, I. I. Mazin, K. D. Belashchenko, V. P. Antropov, and L. L. Boyer, *Superconductivity of Metallic Boron in MgB_2* , Phys. Rev. Lett. **86**, 4656 (2001).

- [259] A. A. Golubov, J. Kortus, O. V. Dolgov, O. Jepsen, Y. Kong, A. O. K., B. J. Gibson, K. Ahn, and R. K. Kremer, *Specific heat of MgB_2 in a one- and a two-band model from first-principles calculations*, J. Phys. Condens. Matter **14**, 1353 (2002).
- [260] K. Szałowski, *Critical temperature of MgB_2 ultrathin superconducting films: BCS model calculations in the tight-binding approximation*, Phys. Rev. B **74**, 094501 (2006).
- [261] H. Tang and S. Ismail-Beigi, *Self-doping in boron sheets from first principles: A route to structural design of metal boride nanostructures*, Phys. Rev. B **80**, 134113 (2009).
- [262] Z. A. Piazza, H.-S. Hu, W.-L. Li, Y.-F. Zhao, J. Li, and L.-S. Wang, *Planar hexagonal B_{36} as a potential basis for extended single-atom layer boron sheets*, Nat. Commun. **5**, 3113 (2014).
- [263] C. Cepek, R. Macovez, M. Sancrotti, L. Petaccia, R. Larciprete, S. Lizzit, and A. Goldoni, *Epitaxial growth of $MgB_2(0001)$ thin films on magnesium single-crystals*, Appl. Phys. Lett. **85**, 976 (2004).
- [264] C.-Y. Moon, Y.-H. Kim, and K. J. Chang, *Dielectric-screening properties and Coulomb pseudopotential μ^* for MgB_2* , Phys. Rev. B **70**, 104522 (2004).
- [265] K. Chen, W. Dai, C. G. Zhuang, Q. Li, S. Carabello, J. G. Lambert, J. T. Mlack, R. C. Ramos, and X. X. Xi, *Momentum-dependent multiple gaps in magnesium diboride probed by electron tunnelling spectroscopy*, Nat. Commun. **3**, 619 (2012).
- [266] T. Morshedloo, M. Roknabadi, and M. Behdani, *First-principles study of the superconductivity in MgB_2 bulk and in its bilayer thin film based on electronphonon coupling*, Physica C Supercond. **509**, 1 (2015).
- [267] L. Petaccia, C. Cepek, S. Lizzit, R. Larciprete, R. Macovez, M. Sancrotti, and A. Goldoni, *Characterization of high-quality $MgB_2(0001)$ epitaxial films on $Mg(0001)$* , New J. Phys. **8**, 12 (2006).
- [268] J. M. Harris, P. J. White, Z. X. Shen, H. Ikeda, R. Yoshizaki, H. Eisaki, S. Uchida, W. D. Si, J. W. Xiong, Z. X. Zhao, and D. S.

- Dessau, *Measurement of an anisotropic energy gap in single plane $Bi_2Sr_{2-x}La_xCuO_{6+\delta}$* , Phys. Rev. Lett. **79**, 143 (1997).
- [269] E. Navarro-Moratalla, J. O. Island, S. Mañas-Valero, E. Pinilla-Cienfuegos, A. Castellanos-Gomez, J. Quereda, G. Rubio-Bollinger, L. Chirolli, J. A. Silva-Guillén, N. Agraït, G. A. Steele, F. Guinea, H. S. J. van der Zant, and E. Coronado, *Enhanced superconductivity in atomically thin TaS_2* , Nat. Commun. **7**, 11043 (2016).
- [270] Y. Cao, A. Mishchenko, G. L. Yu, E. Khestanova, A. P. Rooney, E. Prestat, A. V. Kretinin, P. Blake, M. B. Shalom, C. Woods, J. Chapman, G. Balakrishnan, I. V. Grigorieva, K. S. Novoselov, B. A. Piot, M. Potemski, K. Watanabe, T. Taniguchi, S. J. Haigh, A. K. Geim, and R. V. Gorbachev, *Quality Heterostructures from Two-Dimensional Crystals Unstable in Air by Their Assembly in Inert Atmosphere*, Nano Lett. **15**, 4914 (2015).
- [271] S. K. Das, A. Bedar, A. Kannan, and K. Jasuja, *Aqueous dispersions of few-layer-thick chemically modified magnesium diboride nanosheets by ultrasonication assisted exfoliation*, Sci. Rep. **5**, 10522 (2015).
- [272] T. F. Smith and C. W. Chu, *Will Pressure Destroy Superconductivity?*, Phys. Rev. **159**, 353 (1967).
- [273] N. A. Lanzillo, J. B. Thomas, B. Watson, M. Washington, and S. K. Nayak, *Pressure-enabled phonon engineering in metals*, Proc. Natl. Acad. Sci. U.S.A. **111**, 8712 (2014).
- [274] B. Lorenz, R. L. Meng, and C. W. Chu, *High-pressure study on MgB_2* , Phys. Rev. B **64**, 012507 (2001).
- [275] A. V. Pogrebnyakov, J. M. Redwing, S. Raghavan, V. Vaithyanathan, D. G. Schlom, S. Y. Xu, Q. Li, D. A. Tenne, A. Soukiassian, X. X. Xi, M. D. Johannes, D. Kasinathan, W. E. Pickett, J. S. Wu, and J. C. H. Spence, *Enhancement of the Superconducting Transition Temperature of MgB_2 by a Strain-Induced Bond-Stretching Mode Softening*, Phys. Rev. Lett. **93**, 147006 (2004).
- [276] J.-C. Zheng and Y. Zhu, *Searching for a higher superconducting transition temperature in strained MgB_2* , Phys. Rev. B **73**, 024509 (2006).

- [277] J. Pešić, R. Gajić, K. Hingerl, and M. Belić, *Strain-enhanced superconductivity in Li-doped graphene*, EPL **108**, 67005 (2014).
- [278] C. Si, Z. Liu, W. Duan, and F. Liu, *First-Principles Calculations on the Effect of Doping and Biaxial Tensile Strain on Electron-Phonon Coupling in Graphene*, Phys. Rev. Lett. **111**, 196802 (2013).
- [279] C. Si, Z. Sun, and F. Liu, *Strain engineering of graphene: a review*, Nanoscale **8**, 3207 (2016).
- [280] S. Manzeli, D. Ovchinnikov, D. Pasquier, O. V. Yazyev, and A. Kis, *2D transition metal dichalcogenides*, Nat. Rev. Mater. **2**, 17033 (2017).
- [281] A. Pásztor, A. Scarfato, C. Barreateau, E. Giannini, and C. Renner, *Dimensional crossover of the charge density wave transition in thin exfoliated VSe_2* , 2D Mater. **4**, 041005 (2017).
- [282] O. Zheliuk, J. Lu, J. Yang, and J. Ye, *Monolayer Superconductivity in WS_2* , Phys. Status Solidi (RRL) **11**, 1700245 (2017).
- [283] S. V. Borisenko, A. A. Kordyuk, V. B. Zabolotnyy, D. S. Inosov, D. Evtushinsky, B. Büchner, A. N. Yaresko, A. Varykhalov, R. Follath, W. Eberhardt, L. Patthey, and H. Berger, *Two Energy Gaps and Fermi-Surface “Arcs” in $NbSe_2$* , Phys. Rev. Lett. **102**, 166402 (2009).
- [284] J. M. Lu, O. Zheliuk, I. Leermakers, N. F. Q. Yuan, U. Zeitler, K. T. Law, and J. T. Ye, *Evidence for two-dimensional Ising superconductivity in gated MoS_2* , Science **350**, 1353 (2015).
- [285] D. Costanzo, S. Jo, H. Berger, and A. F. Morpurgo, *Gate-induced superconductivity in atomically thin MoS_2 crystals*, Nat. Nanotechnol. **11**, 339 (2016).
- [286] Q. H. Chen, J. M. Lu, L. Liang, O. Zheliuk, A. Ali, P. Sheng, and J. T. Ye, *Inducing and Manipulating Heteroelectronic States in a Single MoS_2 Thin Flake*, Phys. Rev. Lett. **119**, 147002 (2017).
- [287] R. Zhang, I.-L. Tsai, J. Chapman, E. Khestanova, J. Waters, and I. V. Grigorieva, *Superconductivity in Potassium-Doped Metallic Polymorphs of MoS_2* , Nano Lett. **16**, 629 (2016).

- [288] X. Wang, X. Chen, Y. Zhou, C. Park, C. An, Y. Zhou, R. Zhang, C. Gu, W. Yang, and Z. Yang, *Pressure-induced iso-structural phase transition and metallization in WSe_2* , Sci. Rep. **7**, 46694 (2017).
- [289] Z. Chi, X. Chen, F. Yen, F. Peng, Y. Zhou, J. Zhu, Y. Zhang, X. Liu, C. Lin, S. Chu, Y. Li, J. Zhao, T. Kagayama, Y. Ma, and Z. Yang, *Superconductivity in Pristine $2H_a-MoS_2$ at Ultrahigh Pressure*, Phys. Rev. Lett. **120**, 037002 (2018).
- [290] X. Xi, L. Zhao, Z. Wang, H. Berger, L. Forró, J. Shan, and K. F. Mak, *Strongly enhanced charge-density-wave order in monolayer $NbSe_2$* , Nat. Nanotechnol. **10**, 765 (2015).
- [291] S. Kolekar, M. Bonilla, Y. Ma, H. C. Diaz, and M. Batzill, *Layer- and substrate-dependent charge density wave criticality in $1T-TiSe_2$* , 2D Materials **5**, 015006 (2018).
- [292] E. Morosan, H. W. Zandbergen, B. S. Dennis, J. W. G. Bos, Y. Onose, T. Klimczuk, A. P. Ramirez, N. P. Ong, and R. J. Cava, *Superconductivity in Cu_xTiSe_2* , Nat. Phys. **2**, 544 (2006).
- [293] B. Hildebrand, C. Didiot, A. M. Novello, G. Monney, A. Scarfato, A. Ubaldini, H. Berger, D. R. Bowler, C. Renner, and P. Aebi, *Doping Nature of Native Defects in $1T-TiSe_2$* , Phys. Rev. Lett. **112**, 197001 (2014).
- [294] A. M. Novello, M. Spera, A. Scarfato, A. Ubaldini, E. Giannini, D. R. Bowler, and C. Renner, *Stripe and Short Range Order in the Charge Density Wave of $1T-Cu_xTiSe_2$* , Phys. Rev. Lett. **118**, 017002 (2017).
- [295] L. J. Li, E. C. T. O'Farrell, K. P. Loh, G. Eda, B. Özyilmaz, and A. H. Castro Neto, *Controlling many-body states by the electric-field effect in a two-dimensional material*, Nature **529**, 185 (2015).
- [296] T. Ritschel, J. Trinckauf, K. Koepf, B. Büchner, M. v. Zimmermann, H. Berger, Y. I. Joe, P. Abbamonte, and J. Geck, *Orbital textures and charge density waves in transition metal dichalcogenides*, Nat. Phys. **11**, 328 (2015).
- [297] H. Ryu, Y. Chen, H. Kim, H.-Z. Tsai, S. Tang, J. Jiang, F. Liou, S. Kahn, C. Jia, A. A. Omrani, J. H. Shim, Z. Hussain, Z.-X. Shen,

- K. Kim, B. I. Min, C. Hwang, M. F. Crommie, and S.-K. Mo, *Persistent Charge-Density-Wave Order in Single-Layer TaSe₂*, *Nano Lett.* **18**, 689 (2018).
- [298] M. Spera, A. Scarfato, E. Giannini, and C. Renner, arXiv:1710.04096 (2017).
- [299] D. Xiao, G.-B. Liu, W. Feng, X. Xu, and W. Yao, *Coupled Spin and Valley Physics in Monolayers of MoS₂ and Other Group-VI Dichalcogenides*, *Phys. Rev. Lett.* **108**, 196802 (2012).
- [300] J. R. Schaibley, H. Yu, G. Clark, P. Rivera, J. S. Ross, K. L. Seyler, W. Yao, and X. Xu, *Valleytronics in 2D materials*, *Nat. Rev. Mater.* **1**, 16055 (2016).
- [301] Y. Xing, K. Zhao, P. Shan, F. Zheng, Y. Zhang, H. Fu, Y. Liu, M. Tian, C. Xi, H. Liu, J. Feng, X. Lin, S. Ji, X. Chen, Q.-K. Xue, and J. Wang, *Ising Superconductivity and Quantum Phase Transition in Macro-Size Monolayer NbSe₂*, *Nano Lett.* **17**, 6802 (2017).
- [302] B. T. Zhou, N. F. Q. Yuan, H.-L. Jiang, and K. T. Law, *Ising superconductivity and Majorana fermions in transition-metal dichalcogenides*, *Phys. Rev. B* **93**, 180501 (2016).
- [303] Y.-T. Hsu, A. Vaezi, M. H. Fischer, and E.-A. Kim, *Topological superconductivity in monolayer transition metal dichalcogenides*, *Nat. Commun.* **8**, 14985 (2017).
- [304] G. C. Ménard, S. Guissart, C. Brun, S. Pons, V. S. Stolyarov, F. Debontridder, M. V. Leclerc, E. Janod, L. Cario, D. Roditchev, P. Simon, and T. Cren, *Coherent long-range magnetic bound states in a superconductor*, *Nat. Phys.* **11**, 1013 (2015).
- [305] P. Manchanda, V. Sharma, H. Yu, D. J. Sellmyer, and R. Skomski, *Magnetism of Ta dichalcogenide monolayers tuned by strain and hydrogenation*, *Appl. Phys. Lett.* **107**, 032402 (2015).
- [306] Y. Guo, H. Deng, X. Sun, X. Li, J. Zhao, J. Wu, W. Chu, S. Zhang, H. Pan, X. Zheng, X. Wu, C. Jin, C. Wu, and Y. Xie, *Modulation of Metal and Insulator States in 2D Ferromagnetic VS₂ by van der Waals Interaction Engineering*, *Adv. Mater.* **29**, 1700715 (2017).

- [307] H. Shi, H. Pan, Y.-W. Zhang, and B. I. Yakobson, *Strong ferromagnetism in hydrogenated monolayer MoS₂ tuned by strain*, Phys. Rev. B **88**, 205305 (2013).
- [308] V. Kochat, A. Apte, J. A. Hachtel, H. Kumazoe, A. Krishnamoorthy, S. Susarla, J. C. Idrobo, F. Shimojo, P. Vashishta, R. Kalia, A. Nakano, C. S. Tiwary, and P. M. Ajayan, *Re Doping in 2D Transition Metal Dichalcogenides as a New Route to Tailor Structural Phases and Induced Magnetism*, Adv. Mater. **29**, 1703754 (2017).
- [309] P. B. Littlewood and C. M. Varma, *Amplitude collective modes in superconductors and their coupling to charge-density waves*, Phys. Rev. B **26**, 4883 (1982).
- [310] M. D. Johannes, I. I. Mazin, and C. A. Howells, *Fermi-surface nesting and the origin of the charge-density wave in NbSe₂*, Phys. Rev. B **73**, 205102 (2006).
- [311] M. S. Dresselhaus, G. Dresselhaus, and A. Jorio, *Group Theory: Application to the Physics of Condensed Matter*, Springer, 2008.
- [312] M. Calandra, I. I. Mazin, and F. Mauri, *Effect of dimensionality on the charge-density wave in few-layer 2H-NbSe₂*, Phys. Rev. B **80**, 241108 (2009).
- [313] O. R. Albertini, A. Y. Liu, and M. Calandra, *Effect of electron doping on lattice instabilities in single-layer 1H-TaS₂*, Phys. Rev. B **95**, 235121 (2017).
- [314] V. Mourik, K. Zuo, S. M. Frolov, S. R. Plissard, E. P. A. M. Bakkers, and L. P. Kouwenhoven, *Signatures of Majorana Fermions in Hybrid Superconductor-Semiconductor Nanowire Devices*, Science **336**, 1003 (2012).
- [315] M. A. Bissett, M. Tsuji, and H. Ago, *Strain engineering the properties of graphene and other two-dimensional crystals*, Phys. Chem. Chem. Phys. **16**, 11124 (2014).
- [316] D. C. Freitas, P. Rodière, M. R. Osorio, E. Navarro-Moratalla, N. M. Nemes, V. G. Tissen, L. Cario, E. Coronado, M. García-Hernández, S. Vieira, M. Núñez Regueiro, and H. Suderow, *Strong enhancement*

- of superconductivity at high pressures within the charge-density-wave states of 2H-TaS₂ and 2H-TaSe₂*, Phys. Rev. B **93**, 184512 (2016).
- [317] M. Dion, H. Rydberg, E. Schröder, D. C. Langreth, and B. I. Lundqvist, *Van der Waals Density Functional for General Geometries*, Phys. Rev. Lett. **92**, 246401 (2004).
- [318] J. Klimeš, D. R. Bowler, and A. Michaelides, *Van der Waals density functionals applied to solids*, Phys. Rev. B **83**, 195131 (2011).
- [319] W. Setyawan and S. Curtarolo, *High-throughput electronic band structure calculations: Challenges and tools*, Comput. Mater. Sci. **49**, 299 (2010).
- [320] M. Fuchs and M. Scheffler, *Ab initio pseudopotentials for electronic structure calculations of poly-atomic systems using density-functional theory*, Comput. Phys. Commun. **119**, 67 (1999).
- [321] D. R. Hamann, *Optimized norm-conserving Vanderbilt pseudopotentials*, Phys. Rev. B **88**, 085117 (2013).
- [322] S. Goedecker, M. Teter, and J. Hutter, *Separable dual-space Gaussian pseudopotentials*, Phys. Rev. B **54**, 1703 (1996).
- [323] M. Krack, *Pseudopotentials for H to Kr optimized for gradient-corrected exchange-correlation functionals*, Theor. Chem. Acc. **114**, 145 (2005).

Publication list

Publications related to this thesis

1. **J. Bekaert**, S. Vercauteren, A. Aperis, L. Komendóva, R. Prozorov, B. Partoens, and M. V. Milošević, *Anisotropic type-I superconductivity and anomalous superfluid density in OsB₂*, Phys. Rev. B **94**, 144506 (2016).
2. **J. Bekaert**, A. Aperis, B. Partoens, P. M. Oppeneer, and M. V. Milošević, *Evolution of multigap superconductivity in the atomically thin limit: Strain-enhanced three-gap superconductivity in monolayer MgB₂*, Phys. Rev. B **96**, 094510 (2017).
3. **J. Bekaert**, L. Bignardi, A. Aperis, P. van Abswoude, C. Mattevi, S. Gorovikov, L. Petaccia, A. Goldoni, B. Partoens, P. M. Oppeneer, F. M. Peeters, M. V. Milošević, P. Rudolf, and C. Cepek, *Free surfaces recast superconductivity in few-monolayer MgB₂: Combined first-principles and ARPES demonstration*, Sci. Rep. **7**, 14458 (2017).
4. **J. Bekaert**, A. Aperis, B. Partoens, P. M. Oppeneer, and M. V. Milošević, *Advanced first-principles theory of superconductivity including both lattice vibrations and spin fluctuations: The case of FeB₄*, Phys. Rev. B **97**, 014503 (2018).

Other publications

5. **J. Bekaert**, R. Saniz, B. Partoens, and D. Lamoen, *Native point defects in Cu(In,Ga)Se₂: hybrid density functional calculations predict*

- the origin of p- and n-type conductivity*, Phys. Chem. Chem. Phys. **16**, 22299 (2014).
6. M. Buffière, G. Brammertz, S. Oueslati, H. El Anzeery, **J. Bekaert**, K. Ben Messaoud, C. Köble, S. Khelifi, M. Meuris, and J. Poortmans, *Spectral current-voltage analysis of kesterite solar cells*, J. Phys. D: Appl. Phys. **47**, 175101 (2014).
 7. **J. Bekaert**, R. Saniz, B. Partoens, and D. Lamoen, *First-principles study of carbon impurities in CuInSe₂ and CuGaSe₂, present in non-vacuum synthesis methods*. J. Appl. Phys, **117**, 015104 (2015).
 8. G. Brammertz, S. Oueslati, M. Buffière, **J. Bekaert**, H. El Anzeery, K. Ben Messaoud, S. Sahayaraj, T. Nuytten, C. Köble, M. Meuris, and J. Poortmans, *Investigation of properties limiting efficiency in Cu₂ZnSnSe₄-based solar cells*, IEEE J. Photovolt. **5**, 649 (2015).
 9. S. Oueslati, G. Brammertz, M. Buffière, H. El Anzeery, O. Touajar, C. Köble, **J. Bekaert**, M. Meuris, and J. Poortmans, *Physical and electrical characterization of high-performance Cu₂ZnSnSe₄ based thin film solar cells*, Thin Solid Films **582**, 224 (2015).
 10. G. Brammertz, M. Buffière, C. Verbist, S. Oueslati, **J. Bekaert**, H. El Anzeery, K. Ben Messaoud, S. Sahayaraj, M. Batuk, J. Hadermann, C. Köble, M. Meuris, and J. Poortmans, *Process variability in Cu₂ZnSnSe₄ solar cell devices: Electrical and structural investigations*, The conference record of the IEEE Photovoltaic Specialists Conference (2015).
 11. R. Saniz, **J. Bekaert**, B. Partoens, and D. Lamoen, *Structural and electronic properties of defects at grain boundaries in CuInSe₂*, Phys. Chem. Chem. Phys. **19**, 14770-14780 (2017).

Curriculum vitæ

NAME: Jonas BEKAERT
BORN: 28/06/1990, Lier, Belgium
CONTACT: Campus Groenenborger (G.U.305)
Groenenborgerlaan 171
2020 Antwerpen, Belgium
EMAIL: jonas.bekaert@uantwerpen.be,
jonasdbekaert@gmail.com



Education

- 2014-2018 Department of Physics, University of Antwerp
PhD study in the Condensed Matter Theory group
- 2012-2014 Department of Physics, University of Antwerp
Master of Science in Physics, with highest distinction (88%)
Thesis title: "First-principles electronic structure calculations of Cu(In,Ga)Se₂ photovoltaic absorber materials"
Internship at IMEC, Alternative Thin Film Photovoltaics group
- 2008-2012 Department of Physics, University of Antwerp
Bachelor of Science in Physica, with distinction (74%)
Thesis titles: "Temperature-dependent Raman spectroscopy of empty and water-filled carbon nanotubes" & "Numerical GPU simulations of the magnetization reversal in mesoscopic 3D ferromagnets"
- 2002-2008 Sint-Ursula Lyceum, Lier
Latin-Mathematics

Societies

- Member of the Belgian Physical Society (BPS), 2014-current
- Antwerp section of the European Physical Society *Young Minds* programme. Responsible for the organization of regular colloquia on new physics, a biennial alumni evening, etc.

2015-2017 President

2017-CURRENT Vice-president

Computer skills

OPERATING SYSTEMS: Linux, Windows

TEXT AND TYPESETTING EDITORS: vi, nano, Microsoft Word,
L^AT_EX

PROGRAMMING LANGUAGES (BASIS): C/C++, CUDA, Python

SOFTWARE FOR AB INITIO CALCULATIONS: ABINIT, VASP,
Quantum Espresso

MATHEMATICAL SOFTWARE: MATLAB, Mathematica

Languages

Dutch (*native*), English (*fluent*), French (*fluent*), German (*basis*)

Public presentations

1. Talk at the E-MRS Conference, entitled “Native point defects in Cu(In, Ga)Se₂: hybrid density functional calculations predict the origin of p- and n-type conductivity”, Lille (France), May 26-30, 2014.
2. Talk on “Native point defects in Cu(In,Ga)Se₂”, University of Luxembourg (Luxembourg), October 8, 2014.
3. Talk in the General Scientific Meeting of the Belgian Physical Society, entitled “OsB₂: a unique multiband superconductor”, University of Liège (Belgium), May 13, 2015.
4. Talk in the International Conference of Physics Students (ICPS), entitled “OsB₂: a unique multiband superconductor”, University of Zagreb (Croatia), August 12-19, 2015.

5. Poster presentation in the Ninth International Conference on “Vortex Matter in nanostructured Superconductors”, entitled “Type-I behavior in the multiband superconductor OsB₂”, Rhodes (Greece), September 12-17, 2015.
6. Talk in the “Materials for the future” workshop, entitled “Bulk to atomically thin multiband superconductors: combined *ab initio* & mean-field approach”, Uppsala (Sweden), December 2-4, 2015.
7. Talk in the ‘Theory at Sea’ meeting for theoretical physics in Flanders, entitled “Multigap superconductors in the atomically thin limit”, Oostende (Belgium), May 25-26, 2016.
8. Talk in the CECAM conference on ‘Superconductivity in atomically thin materials and heterostructures’, entitled “Strain-enhanced three-gap superconductivity in atomically thin MgB₂”, Lugano (Switzerland), November 20-24, 2017.
9. Talk in the Young Speakers Contest of the General Scientific Meeting of the Belgian Physical Society, entitled “Monolayer materials as an ideal platform for enhanced superconductivity”, Antwerpen (Belgium), April 11, 2018.

Teaching

- Practicals of ‘Analytical Mechanics’ (BA Physics, University of Antwerp), 2014-2015, 2015-2016.
- Practicals of ‘Electronic Structure Calculations’ (MA Physics, University of Antwerp), 2014-2015, 2015-2016, 2016-2017.
- Practicals of ‘Advanced Quantum Mechanics’ (MA Physics, University of Antwerp), 2016-2017.

Refereeing

Journal of Applied Physics, Journal of Physics: Condensed Matter, Materials Research Express, Solid State Communications, Thin Solid Films.

Scientific awards

1. ‘Umicore Materials Technology Award 2015’, awarded by Research Foundation-Flanders, for my Master’s thesis entitled “First-principles electronic structure calculations of Cu(In,Ga)Se₂ photovoltaic absorber materials”.
2. First poster prize in the Ninth International Conference on ‘Vortex Matter in nanostructured Superconductors’, 12-17 September 2015, Rhodes (Greece) for the presentation entitled “Type-I behavior in the multi-band superconductor OsB₂”.
3. First prize for best speaker at the 2018 Young Speaker Contest of the Belgian Physical Society for a seminar on “Monolayer materials as an ideal platform for enhanced superconductivity”.